MULTIMODAL DEGRADATION INTERACTIONS IN ELECTRODES FOR ENERGY STORAGE

by

Ankit Verma

A Dissertation

Submitted to the Faculty of Purdue University

In Partial Fulfillment of the Requirements for the degree of

Doctor of Philosophy

School of Mechanical Engineering

West Lafayette, Indiana

May 2020

THE PURDUE UNIVERSITY GRADUATE SCHOOL
STATEMENT OF COMMITTEE APPROVAL

Dr. Partha P. Mukherjee, Chair

School of Mechanical Engineering

Dr. Xiulin Ruan

School of Mechanical Engineering

Dr. Vilas Pol

Davidson School of Chemical Engineering

Dr. Vikas Tomar

School of Aeronautics and Astronautics

Approved by:

Dr. Nicole Key

Dedicated to my beloved parents, brother, sister-in-law and my teachers…

ACKNOWLEDGMENTS

I have felt immense pleasure and satisfaction in working under the tutelage of Prof. Partha P. Mukherjee who has provided excellent guidance and generous support throughout my thesis work. He introduced me to the world of quality research, helped me in understanding the subject matter leading to conclusions through constant cooperation, assistance and encouragement. Furthermore, the collaborative research environment fostered by him within the group, in conjunction with opportunities to interface with leading researchers outside has contributed to the sum total of my holistic development.

I am thankful to the seasoned scientists at national labs, academia and industry, in particular, Dr. Kandler Smith (NREL), Dr. Yuichiro Tabuchi (Nissan), Prof. Perla Balbuena (TAMU) and Prof. Sarbajit Banerjee (TAMU); their insights, both research and otherwise, have sustained me through my doctoral journey. I am grateful to my thesis committee members, Prof. Xiulin Ruan, Prof. Vilas Pol and Prof. Vikas Tomar for their detailed inputs and assistance. I am also thankful to the teachers of mechanical engineering department of Purdue University as well as Texas A&M University whose invaluable contributions in the courses have helped me immensely throughout the research period.

I am thankful to all my friends here, especially Aashutosh and Daniel, and my lab mates for being there with me in times of need and making my stay at Purdue University enjoyable. In the second leg of my doctoral journey, I did gratifying research collaborations with Feng and Sabarish; my sincere thanks to them. Also, I am indebted to my delightful friends back home, Arjun, Rakesh and Jaiprakash, who always managed to lift up my spirits even at somber times.

I would like to express my sincere gratitude to my parents, brother and sister-in-law whose struggles and insurmountable love have encouraged me always and helped me to cope with all the difficulties in life so far.

TABLE OF CONTENTS

LIST OF TABLES

LIST OF FIGURES

LIST OF SYMBOLS

Symbols

c_s	Molar concentration of lithium in solid phase
$c_{s.\max}$	Maximum Li solid phase concentration
D_s	Solid phase diffusivity of Li
DD_{total}	Total damage density
DD_{Gr}	Damage density in graphite
DD_{film}	Damage density in film
$\vec{f}$	Force vector
$\vec{u}$	Displacement vector
E	Young's modulus
i	Current density
$I_{applied}$	Total current applied to the system
k_n	Axial spring stiffness
k_s	Shear spring stiffness
n_{Gr}	Total number of springs in graphite
n_{film}	Total number of springs in film
$n_{broken,total}$	Total number of broken springs in graphite + film
$n_{broken,Gr}$	Total number of broken springs in graphite
$n_{broken,\,film}$	Total number of broken springs in film
ν	Poisson's ratio
ω	Active material expansion coefficient
ψ	Fracture threshold energy
R	Particle radius
σ	Stress
S	Active area
t	Time variable
T	Temperature
F	Faraday's constant
${}^{t}A$	Area at previous configuration
c_s	Molar concentration of lithium in solid phase
$c_{s.\max}$	Maximum Li solid phase concentration
$\hat{c}_s$	Normalized concentration of Li in solid phase
D_s	Solid phase diffusivity of Li
DD_{total}	Total damage density

DD_{Si}	Damage density in silicon
DD_{film}	Damage density in film
$\Delta\vec{f}$	Incremental force vector
$\Delta\vec{u}$	Incremental displacement vector
${}^{t+\Delta t}_{\ \ t}\varepsilon_{ij}$	Green-Lagrange strain tensor
E	Young's modulus
${}^{t+\Delta t}_{\ \ t}F_i$	External force
i	Current density
$I_{applied}$	Total current applied to the system
M_{Li}	Mobility of lithium in solid phase
n_{Si}	Total number of springs in silicon
n_{film}	Total number of springs in film
$n_{broken,total}$	Total number of broken springs in silicon + film
$n_{broken,Si}$	Total number of broken springs in silicon
$n_{broken,\,film}$	Total number of broken springs in film
κ	Gradient energy coefficient
R	Universal gas constant
R_p	Particle radius
${}^{t+\Delta t}R$	Residual
S	Active area
${}^{t+\Delta t}_{\ \ t}S_{ij}$	2nd Piola-Kirchoff stress tensor
t	Time variable
T	Temperature
F	Faraday's constant
r	Radial coordinate
${}^{t+\Delta t}_{\ \ t}u_i$	Displacement
${}^{t}V$	Volume at previous configuration
ω	Non-dimensional enthalpy of mixing
ψ_e^n	Strain energy of spring in old state
ψ_e^{n+1}	Strain energy of spring in current state
x_i	Spatial coordinate
L_a	Anode thickness
L_{sep}	Separator thickness
L_c	Cathode thickness
A	Electrode area
A_{surf}	Cell surface area
η	Overpotential

j	Volumetric current density
i	Current density
i_o	Exchange current density
σ_s	Electronic conductivity
σ_s^{eff}	Effective electronic conductivity
a_s	Specific surface area of electrode
c_e	Electrolyte concentration
R_s	Particle radius
c_s	Concentration of Li in solid phase
c_s^{max}	Maximum Li solid phase concentration
θ_s	Surface stoichiometry of spherical particle
h	Heat transfer coefficient
ϕ_s	Solid phase potential
D_s	Solid phase diffusivity
F	Faraday's constant
D_e	Electrolyte diffusivity
D_e^{eff}	Effective electrolyte diffusivity
κ	Ionic conductivity
κ_D	Diffusional conductivity
t^+	Transference number
U_a	Anode open circuit potential
k	Reaction rate constant
R	Universal gas constant
T	Temperature
ϕ_e	Electrolyte phase potential
dU_{eq}/dT	Entropic coefficient
$\dot{Q}$	Total heat generation
U_c	Cathode open circuit potential

Operator

d	Total derivative
∂	Partial derivative
∇	Gradient

Superscripts

eff	Effective property
max	Maximum concentration

Subscripts

s	Solid
a	Anode
sep	Separator
e	Electrolyte
c	Cathode
surf	Surface

LIST OF ABBREVIATIONS

AM	Active Material
B	Binder
BC	Boundary Conditions
CA	Conductive Additive
CC	Current Collector
NMC	Nickel-Manganese-Cobalt
OCP	Open Circuit Potential
P	Pore
SE	Solid Electrolyte
SEI	Solid Electrolyte Interphase
SOC	State of Charge

ABSTRACT

Energy storage electrodes exhibit significant capacity and performance degradation with cycling owing to extensive decrepitation of anodes associated with lithiation-delithiation induced volumetric expansion and contraction. Microcrack formation in the active material and solid electrolyte interphase layer contribute to deleterious effects including hindered diffusion, particle isolation, and loss of cyclable active material inventory, with detrimental performance ramifications. Unabated solid electrolyte interphase growth in conjunction with irregular plating on metal/intercalation electrodes can also pose serious safety issues like short-circuit, compromising the integrity of the system. In this work, degradation originating from coupled mechano-electrochemical-transport interactions have been identified with detailed insights into the physical mechanisms contributing to this degradation. Strategies to ameliorate degradation damage inside these systems have been enumerated, with emphasis on graphite and silicon intercalation anodes and lithium metal anode.

1. INTRODUCTION

This chapter provides a description of the coupled degradation mechanisms in electrodes for energy storage and establishes the current state of the art in degradation modeling for lithium-ion and lithium metal systems.

1.1 Lithium-Ion and Lithium Metal Batteries

Lithium-ion batteries (LIBs) are ubiquitous in portable electronics and are making their way to large-scale applications, such as electric vehicles and grid storage, owing to their high energy and power density[1]. Li-ion cells are an intercalation chemistry where Li^+ ions shuttle back-and-forth between the two electrodes via liquid electrolyte. The electrode microstructures are porous to enhance the surface area for electrochemical reaction. This interfacial area between electrode and electrolyte represent the active interface at which electrochemical reactions take place.

A schematic of a typical Li-ion unit cell is shown in Figure 1.1. The cell contains porous separator sandwiched between two porous electrodes. The electrodes are classified as anode (negative) and cathode (positive) depending on the material and thermodynamic potential of individual material. The void space is saturated by the liquid electrolyte. During the discharge operation of this cell, Li ions stored in anode deintercalate and jump to electrolyte, generating electrons in the process. The generated electron travels from anode to cathode via external circuit through the solid phase. These electrons cannot move internally from anode to cathode due to the presence of electronically insulating separator. The Li^+ ions generated at anode-electrolyte interface due to deintercalation move towards the cathode under the concentration and potential gradient set up in the electrolyte. The ions will experience electric field established in electrolyte due to electrolyte phase potential gradient, and eventually intercalate back at the cathode. The usual choice for anode materials is graphite $\left(LiC_6\right)$ and a typical cathode is often a transitional metal oxide host $\left(LiMO,\ MO = \text{metal oxide}\right)$. Recently, considerable research efforts are being put into the utilization of high energy density Li metal as the anode paired with liquid as well as solid electrolytes. Lithium metal batteries (LMBs) with liquid electrolytes can suffer from deleterious dendritic growth, consequently, all solid-state batteries (ASSBs) providing a rigid barrier against the dendrite growth have been the focus of current state-of-the-art research as well.

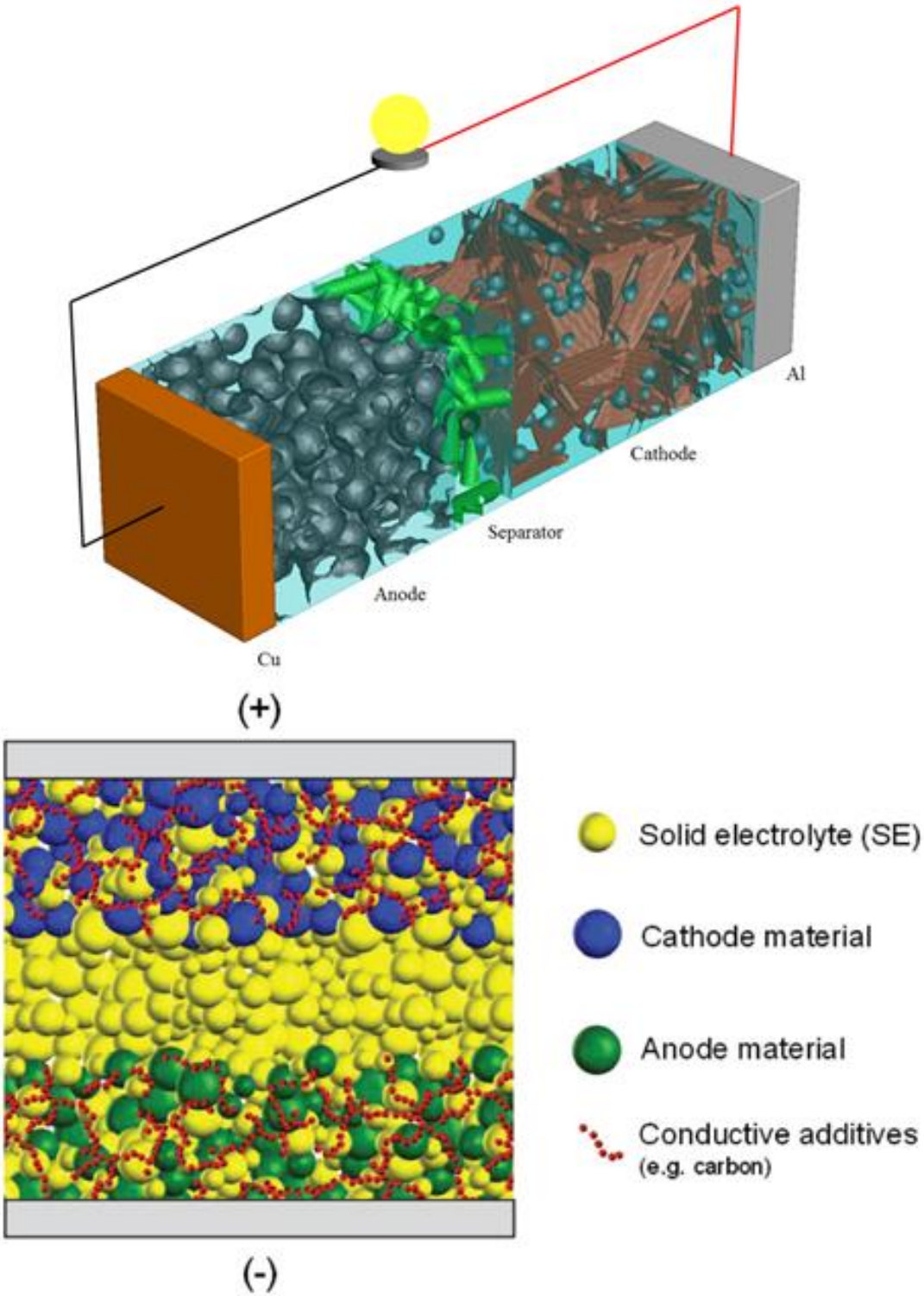

Figure 1.1 Schematic diagram illustrating components of a typical Li-ion battery unit cell with liquid electrolyte[2] (top) and solid electrolyte (bottom)[3].

1.2 Degradation Mechanisms

Lithium-ion battery systems, although, holding great promise for the future of environmentally friendly transportation and energy storage, suffers from service life limitations owing to the degradation of active electrode material upon repeated charge-discharge cycling [4, 5]. Coupled electro-chemo-mechanical interactions in LIB electrodes have been identified as the pivotal factors constraining the life and performance of LIBs. Primarily, microcrack formation in the active material due to diffusion-induced stress (DIS), large volumetric strain and chemical/electrochemical solid-electrolyte interphase (SEI) formation constitute the degradation modes exacerbating capacity fade and impedance growth which leads to cell performance and life decline [6-8]. High current rate operation during fast charge of LIBs can also lead to irreversible plating at the anode which can further react with the liquid electrolyte to form SEI contributing to exacerbated capacity fade. Under extreme scenarios, the plated Li metal can pierce through the separator and reach the cathode with the subsequent internal short leading to total failure of the cell. Figure 1.2 gives an overview of the myriad degradation mechanism in Li-ion cells.

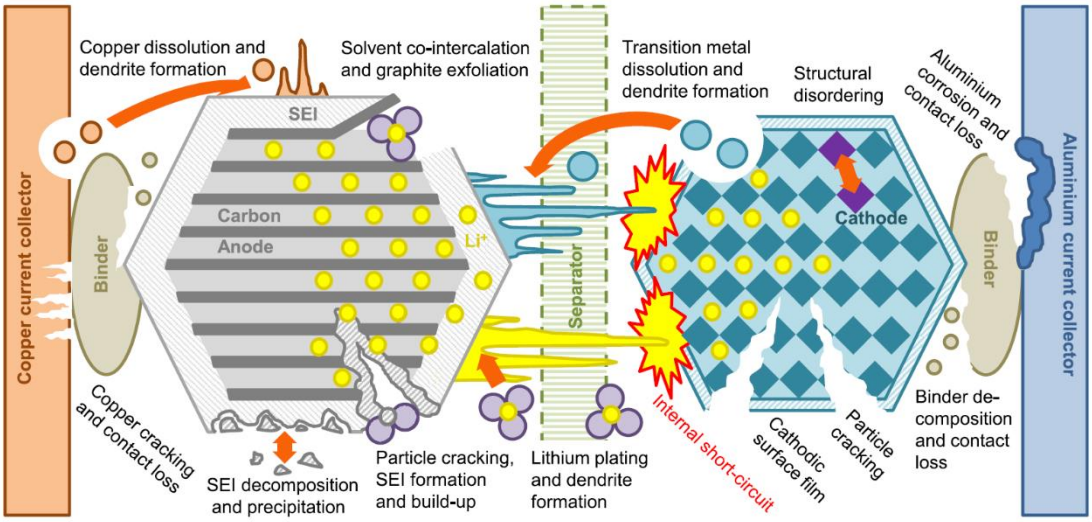

Figure 1.2 Degradation mechanisms in Li-ion cells[9].

For lithium metal batteries, controlling the immense volumetric change of the anode during cycling as part of the plating/stripping process is a challenge. Drastic capacity fading due to the continuous formation of solid electrolyte interphase as well as dead lithium limits the usage of Li metal in secondary batteries. Figure 1.3 compares the schematics of LIB and LMB and exhibits

the problems associated with dendrites, dead lithium and thick SEI leading to poor Coulombic efficiency of the lithium metal battery.

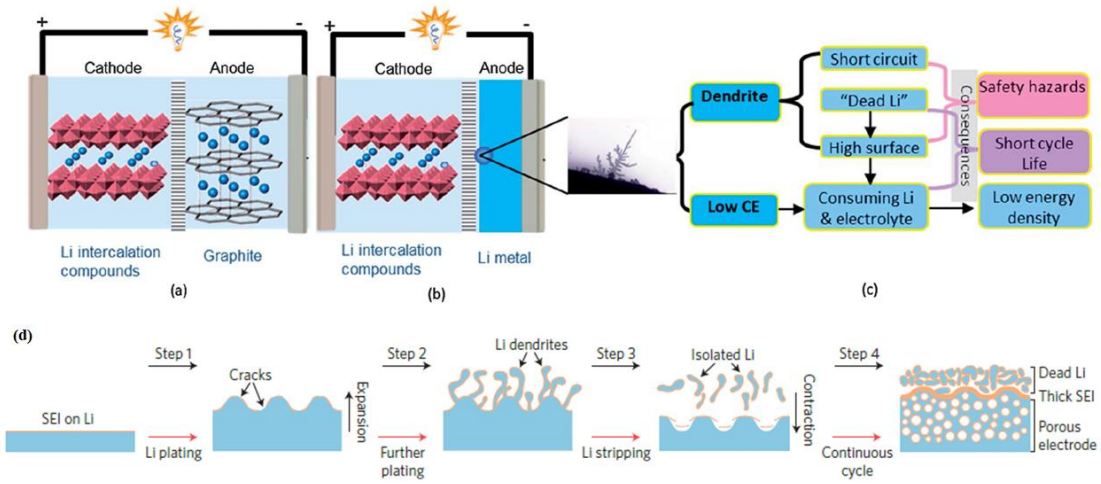

Figure 1.3 Schematic of (a) Li-ion battery, (b) Li-metal battery. (c) Li dendrite morphology eventually leads to safety hazards and severe capacity fade. (d) Stepwise demonstration of the Li plating and stripping process[10, 11].

All-solid-state batteries (ASSBs) are also afflicted with interfacial delamination during extended cycling leading to enhanced interfacial impedance due to contact loss. Furthermore, unmitigated Li dendrite growth beyond critical current densities for both amorphous and polycrystalline solid electrolytes (SEs) has been observed notwithstanding the rigid barrier induced mechanical stresses. Figure 1.4 contrasts the mechanism of lithium deposition in liquid and solid electrolytes. Lithium ions preferentially plate at the peaks of the dendritic protrusions in liquid electrolyte due to higher ion concentration in its vicinity as well as due to warping of the electric field towards the dendrite tip. Failure mode in the solid electrolyte is through the propagation of the Li metal along pre-existing Griffith flaws.

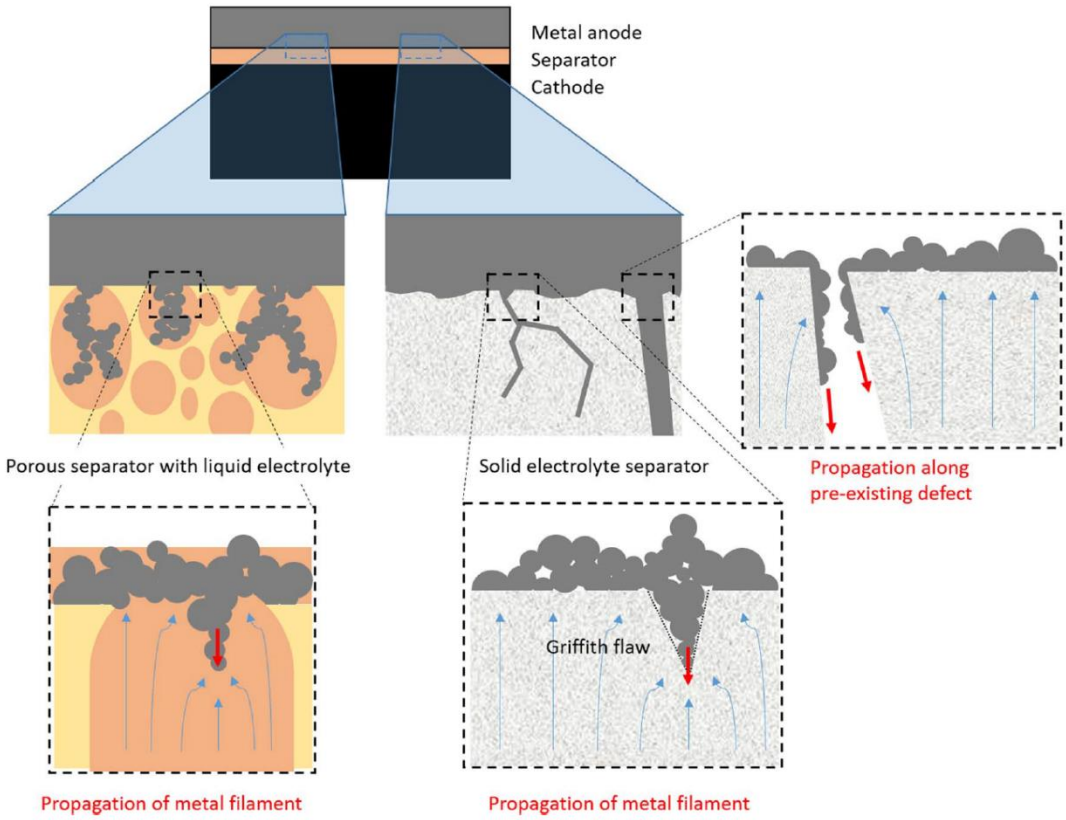

Figure 1.4 Illustration of Li metal electrodeposition in liquid electrolytes and solid-state electrolytes. Defects in solid electrolytes provide pathways for dendrite propagation[12].

1.2.1 Mechanical Degradation

Fracture and decrepitation of electrodes result from lithium diffusion induced concentration gradients and strain during charging and discharging operations [13, 14]. Insertion of lithium in the negative electrodes can induce significant volume change of the order of a few to several hundred percent. Commercially used graphite anodes exhibits volumetric expansion of around 10% during lithiation while next-generation high capacity anodes like silicon and tin show massive lithiation induced volumetric change of the order of 300% [15]. The resulting stresses, aptly named as diffusion-induced stress (DIS), can cause nucleation and growth of cracks, leading to mechanical degradation of the electrode materials (see Figure 1.5 and Figure 1.6). This pulverization may lead to particle isolation and reduced lithium intercalation ability contributing to capacity fade.

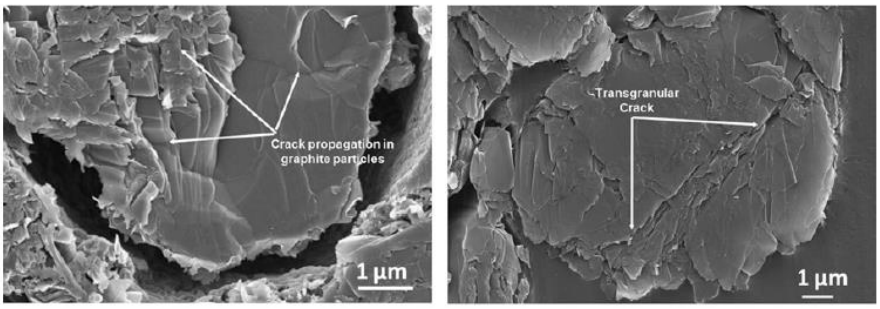

Figure 1.5 Scanning electron microscopic images of typical hairline crack propagation (left) and transgranular crack (right) in a graphite particle[16].

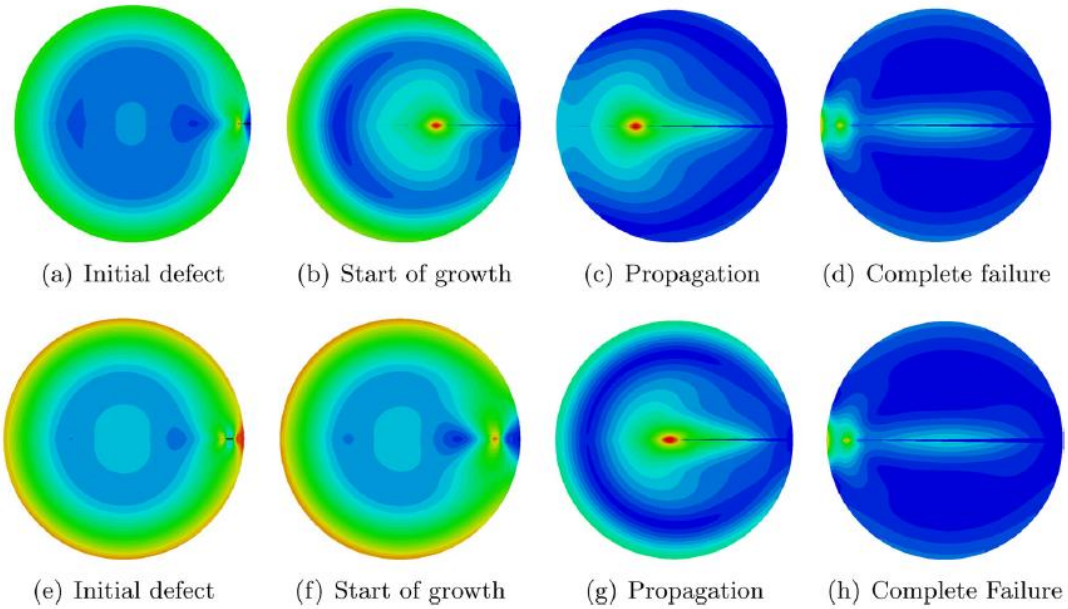

Figure 1.6 Crack propagation sequences for radially aligned defects located at the periphery of the particle (a-d) and embedded close to the surface of the particle (e-f). Red corresponds to cohesive damage initiation stress and blue corresponds to zero stress [17].

1.2.2 Chemical/Electrochemical Degradation

Solid-electrolyte interphase (SEI) is a thin layer that primarily forms at the active material-electrolyte interface from electrolyte decomposition during the initial formation cycling of lithium-ion batteries with dimensions of the order of tens to hundreds of nanometers [18]. This SEI layer is beneficial in preventing further undesired loss of electrolyte and cyclable Li^+ ions by acting as a buffer between the electrolyte and the electrode surface. However, the total amount of SEI that

forms on top of active material increases slowly on further cycling, and lithium gets consumed due to deleterious SEI electrochemical reduction reactions during charging phase, effectively leading to capacity fade and increased interfacial impedance. Furthermore, diffusional stress and high volumetric strain induced microcracks in the particle and SEI layer result in fresh contact between electrolyte and active material particle surface leading to more loss of cyclable lithium inventory (see Figure 1.7)[19]. Irreversible lithium plating under fast charge also contributes to non-linear aging aggravated by high charging currents, high depths of discharge and low temperatures.

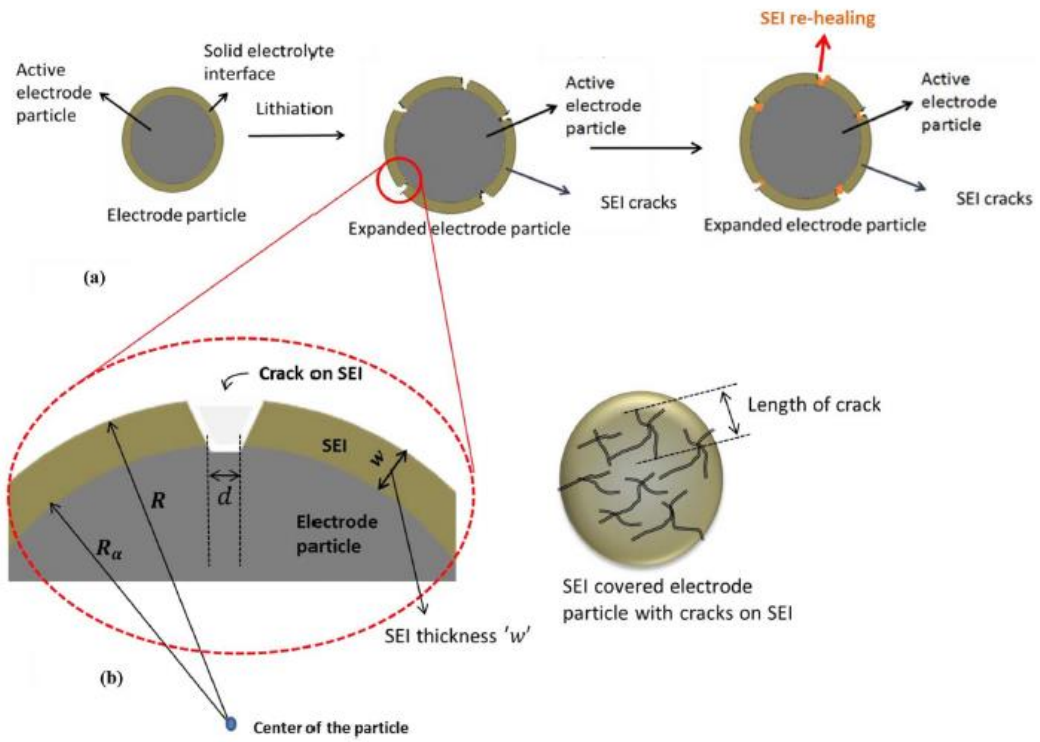

Figure 1.7 Schematic representation of surface fracture depicting an electrode particle encapsulated with an SEI layer [20].

1.2.3 Thermal Degradation

Safety and performance of lithium-ion batteries over a wide temperature window are of paramount importance, especially for electric vehicles. The safety concerns are predicated on the thermal behavior as the occurrence of local temperature excursions may lead to thermal runaway. Previous studies have shown that an increase in cell temperature may diminish capacity loss and favorably affect the power ability [21-23] In addition, temperature increase may also abate mechanical degradation (i.e. micro-crack formation) and prevent lithium deposition in the anode.[24] However,

an increase in the cell temperature beyond a critical limit may also initiate undesirable exothermic decomposition reactions, which may lead to extreme thermal events such as thermal runaway.[25-27] The electrode microstructure of LIBs has a profound impact on its performance-safety-degradation interactions. Figure 1.8 presents the maximum temperature and capacity obtained from the 18650 cells with a different porosity of cathode (i.e. different amount of active material) during the discharging process with varying discharge currents. It provides a guideline for optimal tuning of the cathode microstructure (porosity) towards safe LIBs.

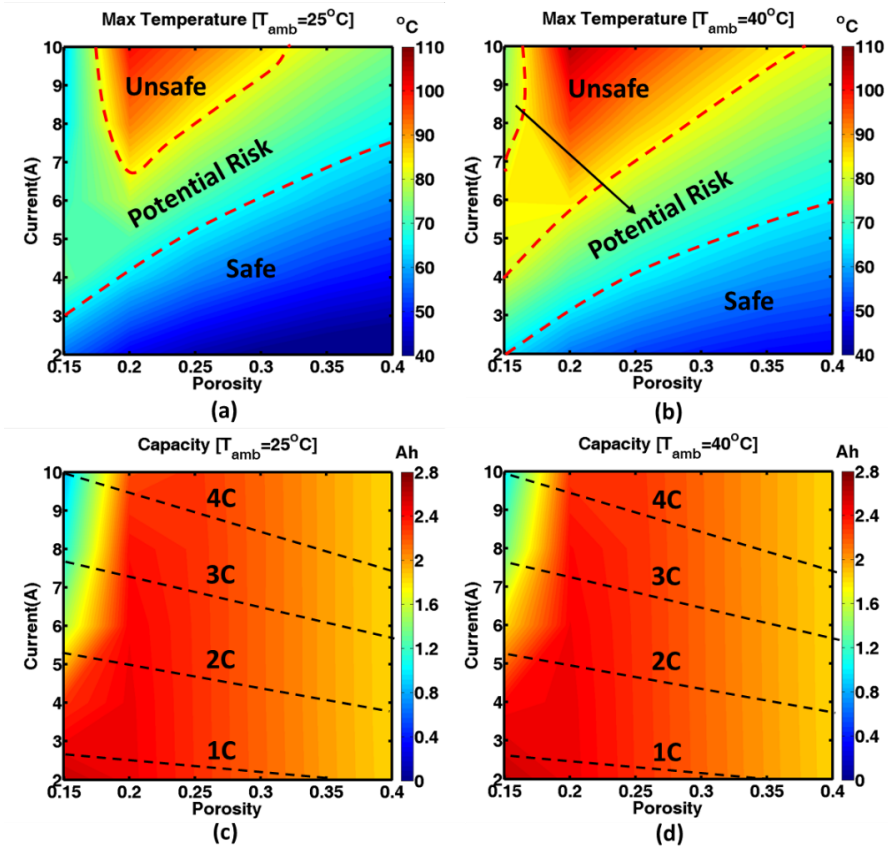

Figure 1.8 The influence of discharge current and cathode porosity on the max temperature obtained at the end of discharge when (a) T_{amb} = 25°C (b) T_{amb} = 40°C. The *Safe* region corresponding to T < 60 °C. The *Potential Risk* region corresponding to 60 °C < T < 80 °C. The unsafe region corresponding to T > 80 °C. The influence of discharge current and cathode porosity on the cell capacity obtained at the end of discharge when (a) T_{amb} = 25°C (b) T_{amb} = 40°C[28].

1.3 Detailed Literature Review

As mentioned above, electrochemical and mechanical degradations in LIB electrodes have been

identified as the key factors limiting the life and performance of LIBs[29-31]. Diffusion of lithium atoms inside the electrode active particles is an inherently slow process with diffusivity magnitudes of the order of 10^{-14} m^2/s. This results in the formation of appreciable concentration gradients inside the electrode particles resulting in diffusion induced stress. The phenomena of DIS can be thought analogous to thermal gradients induced stress. Thermal gradients, ΔT (K), cause inhomogeneous material expansion leading to strain proportional to the coefficient of thermal expansion, α (K^{-1}). Similarly, Li concentration gradients, Δc ($mol/m^{3)}$, inside the active material host lead to diffusion induced strain proportional to the molar expansion coefficient, Ω (m^3/mol). If the resulting stress exceeds the fracture threshold energy of the material, evolution and propagation of microcracks occur leading to damage. Furthermore, active particles are tightly jammed in the electrode alongside secondary phase inclusions like binder and conductive additives, consequently, stress from particle-particle and particle-inclusions contact can exacerbate mechanical damage inside the electrodes. Prediction of the extent of mechanical damage due to DIS requires a modeling methodology capable of capturing microcrack evolution and crack front propagation alongside diffusional transport such as the coupled lattice-spring model (see Figure 1.9 and Figure 1.10).

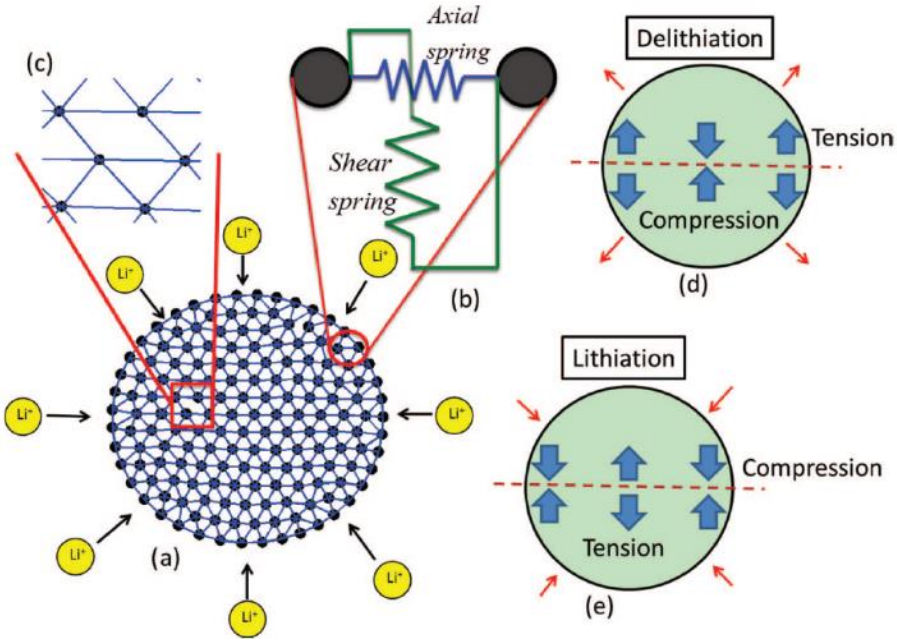

Figure 1.9 Schematic representation of the lattice spring model for coupling mechanical fracture with transport [32].

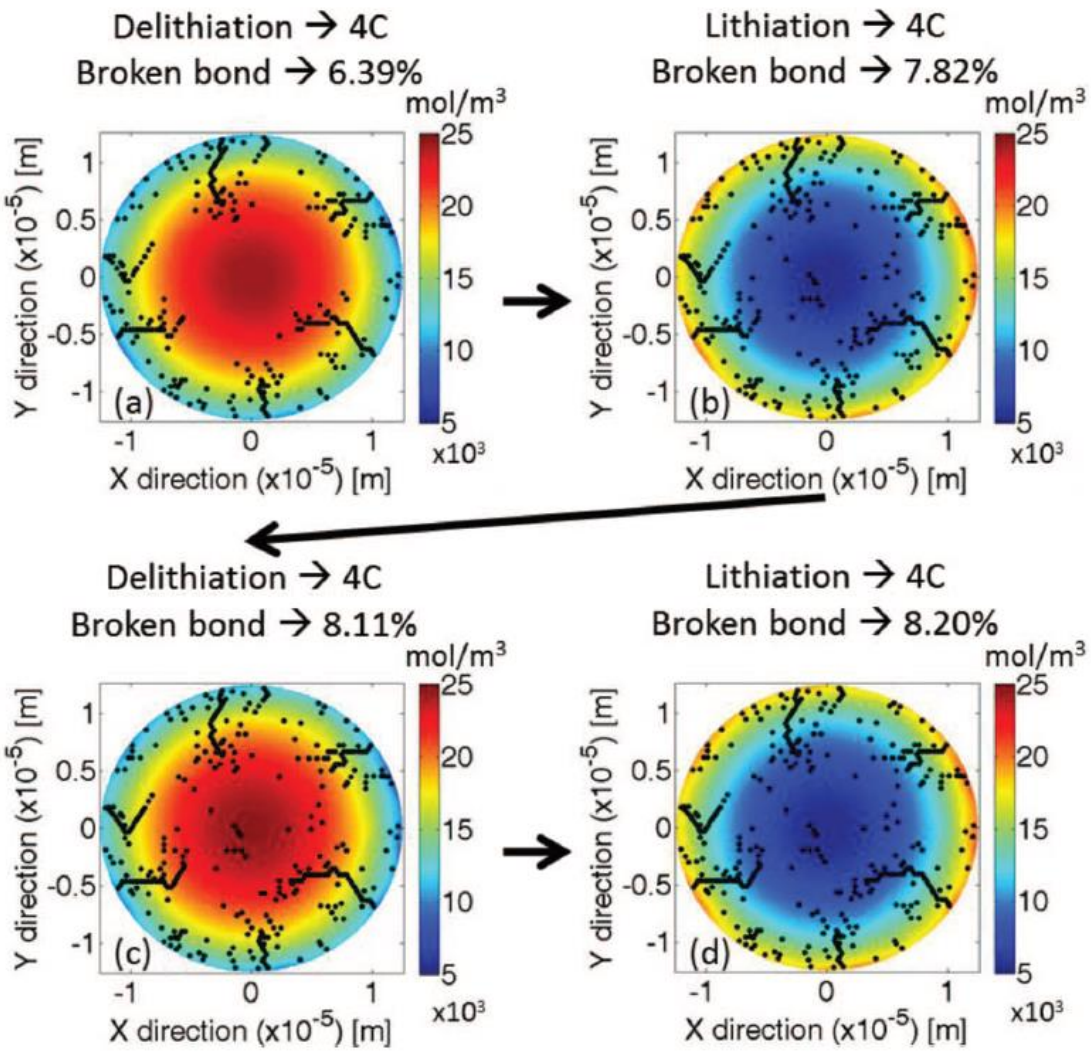

Figure 1.10 Fracture pattern superimposed on the concentration profile for delithiation and lithiation of graphite particle [33].

The gradient in concentration profile that develops within the electrode active particles during the transport of lithium, gives rise to diffusion-induced stress (DIS)[34, 35]. Mechanical degradation is the formation of microcracks and subsequently spanning cracks within the active particle due to the DIS[36]. On the other hand, for proper stabilization of active material with respect to the electrolyte, formation of a SEI layer is essential[37]. However, the total amount of SEI that forms on top of graphite cannot be controlled, and cyclable lithium gets consumed within the SEI layer effectively leading to capacity fade[37, 38]. This continued growth of SEI layer has been considered as the major contributor to the electrochemical degradation. However, the

mechanical and electrochemical degradations within LIBs are not completely isolated from each other[22, 39].

The microcracks can affect the cell performance in two opposing ways:

a) *Positive effect*: Microcracks spanning from the surface of the particle are exposed to electrolyte and are electrochemically active thereby reducing the diffusion length and facilitating the transport of lithium; thus improving cell performance.
b) *Negative effect*: Microcracks that are interior to the active particle are electrochemically inactive and obstruct lithium diffusion; deteriorating cell performance. Also, microcracks connected to the surface provides fresh domain for SEI formation and subsequently loss of cyclable lithium, which eventually leads to loss of capacity.

Depending on the microcrack pattern formed, either of the above effects can dominate. Upon repeated charge-discharge cycles, there also exists a possibility of the active particle breaking off into smaller particles, which may get electronically isolated from the electrode microstructure due to poor contact with conductive additives. However, in the present research particle-isolation has not been taken into consideration. Thus, disintegration of the active particle can lead to significant irreversible loss of capacity[40, 41].

Improving the energy and power density as well as life span of lithium-ion battery systems has been the key research emphasis lately. In that direction, fundamental understanding of the mechanisms underlying the degradation phenomena observed in the battery electrodes is of prime importance[42]. Several studies to understand the chemical and mechanical degradation mechanisms have been carried out over the last few decades. To understand the capacity fade observed in LIBs over hundreds of cycles, scientists had a fair amount of idea about the formation of SEI films on top of the active materials[39]. However, more detailed models to incorporate the impact of SEI film formation on the performance of the battery has been developed later[25, 43-45]. There also exist models that incorporate the transport of reactive species through the SEI film and subsequent impact on the performance of LIBs [34, 46]. Christensen and Newman conducted the pioneering work for quantifying mechanical stress generation in active particles during lithium intercalation [47, 48]. It was observed that smaller particle size and larger aspect ratio reduces the DIS in the particle resulting in better performance[42, 49, 50]. Presence of transgranular cracks in graphite and $LiCoO_2$ active particles was pointed out by the SEM and TEM images of cycled electrodes [51-53], which has also been demonstrated in Figure 1.5. An electrochemical shock

map, developed by Woodford *et al*., helped to predict the onset of failure based on the C-rate, particle size and the fracture toughness of the active material (see Figure 1.11) [54]. Cheng and Verbrugge proposed a dimensionless number, which is equivalent to Biot number in heat-transfer, and demonstrated that the microcrack initiation is solely governed by this dimensionless number (see Figure 1.12)[37]. The fracture of electrodes of LIBs operated at high currents was investigated by Zhao *et.al*[51]. Impacts of SEI growth and mechanical degradation on the electrochemical impedance spectra (EIS) have also been investigated by Chen *et al.* [55, 56].

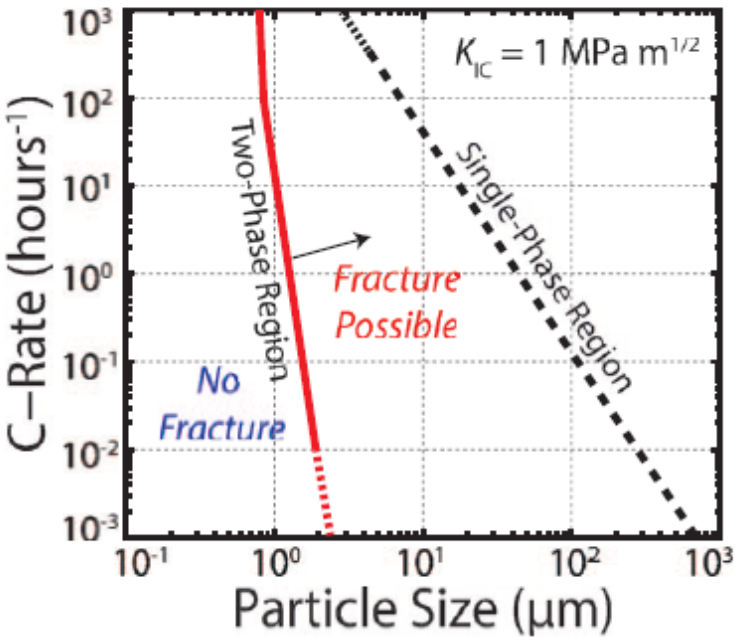

Figure 1.11 Electrochemical shock map for $Li_XMn_2O_4$, accounting for both concentration gradient stresses and coherency stresses [57] .

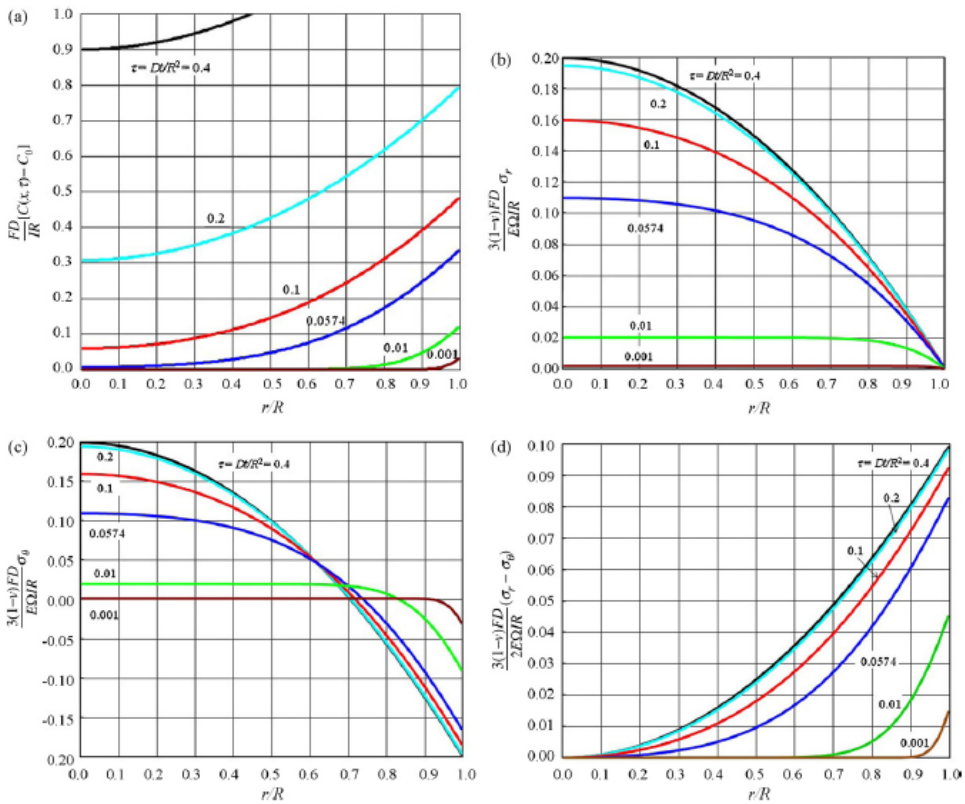

Figure 1.12 Concentration profile (a) and the corresponding radial (b), tangential (c), and shear stress (d) for galvanostatic operation[38].

Most of the computational models developed to study mechanical degradation so far neglect the electrochemical reactions taking place in the newly formed microcracks linked to the particle surface. But as the SEM images of graphite and TEM images of $LiCoO_2$ show, the microcracks give rise to large new surface areas, which if exposed to the electrolyte can significantly contribute to the lithium generating/consuming electrochemical reactions[58, 59]. Most of the computational models developed for analyzing the formation and growth of SEI layer does not incorporate the increase in active particle surface area due to microcrack formation. However, few computational techniques have been implemented in the recent past, that incorporates the coupled impact of mechanical degradation and SEI formation on the overall capacity fade experienced by LIBs, in a phenomenological fashion. Among them, Deshpande *et al.* developed a model that simulates the loss of capacity owing to the formation and growth of SEI layer over the microcrack surface (see Figure 1.13) [60]. Xu *et al.* adopted the model developed by Deshpande *et al.* and investigated the loss of capacity due to crack propagation on the negative

electrode [57]. Narayanrao *et al.* developed a phenomenological model to capture the increase in electrochemically active surface area due to microcrack formation, and incorporated it within a porous electrode model for investigating the capacity fade over multiple cycles [61]. While all the models mentioned above rudimentarily account for the increase in the solid particle – electrolyte interfacial area, they do not account for the electrochemical reactions at the microcrack surfaces that contribute to the lithium flux acting on the particle.

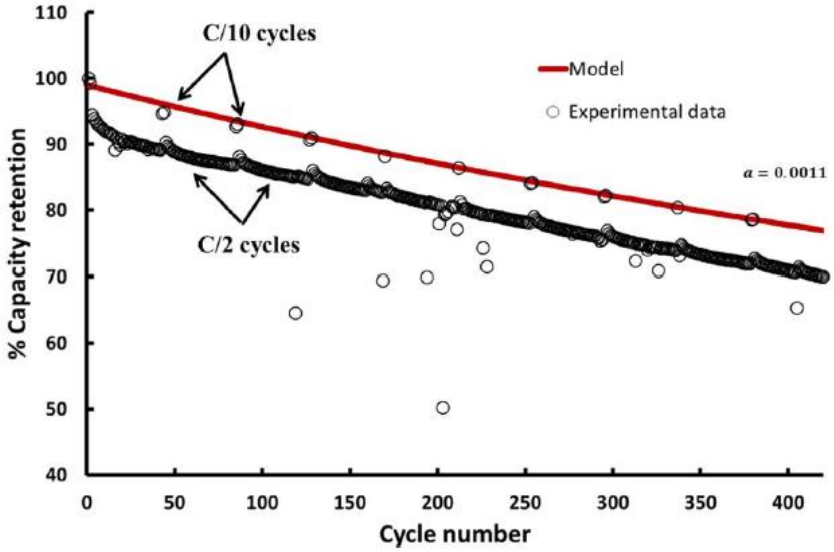

Figure 1.13 Cell capacity retention as a function of cycle number. Black circles represent experimental data and red curve represents model fitting [51].

During lithiation-delithiation processes, transport of lithium within the solid active particle gives rise to large concentration gradients, which imparts huge diffusion induced tensile/compressive force on the particle[39, 56, 62]. Microcracks evolve in domains of the active particle that experience tensile force[63]. Coalescence of these microcracks gives rise to spanning cracks within the active particles. Nucleation of microcracks is usually not observed under compressive force. Flow of electrolyte is possible through the crack fronts that are connected to the surface of the active particle[25, 37]. Penetration of electrolyte inside the active particle not only leads to reduction in diffusion length for lithium transport, but also facilitates the growth of SEI at these fresh active particle surfaces[38].

Quantification of stresses in electrode particles coupled with electrochemistry has been investigated, from the standpoint of single particles, by several groups[38, 39, 64]. Dependence of

diffusion-induced stress on particle geometry has been demonstrated by Sastry and coworkers for isolated particles [62, 65]. Few works have incorporated phase change, anisotropic swelling and grain boundary effects to understand its effects on the mechanics of single particles[22, 38, 66]. In a functioning electrode, the particles are combined into a complex network of particles that provide significant mechanical constraint to any given particle. On swelling, these network constraints can significantly increase the stress in the particle, impacting fracture behavior. Consequently, recent works have focused on analyzing realistic electrode microstructures incorporating particle contact, binder morphology and its effects on stress [53, 67, 68]. The advancement of synchrotron X-ray tomographic reconstruction techniques as well as focused ion-beam scanning electron microscopy (FIB-SEM) have enabled accurate reconstruction of electrode architectures on which coupled electrochemistry-mechanics simulations can be performed to scale up particle level stress analyses to the electrode level [66, 69-76].

The impact of coupled electro-chemo-mechanical degradation in realistic electrodes can also be probed virtually through utilization of acoustic emission spectroscopy[77] and electrochemical impedance spectroscopy modeling for both single particle and porous electrodes (see Figure 1.14 and Figure 1.15) [78, 79]. With appropriate calibration, these techniques can be used for early detection and diagnosis of degradation and safety concerns in lithium-ion batteries.

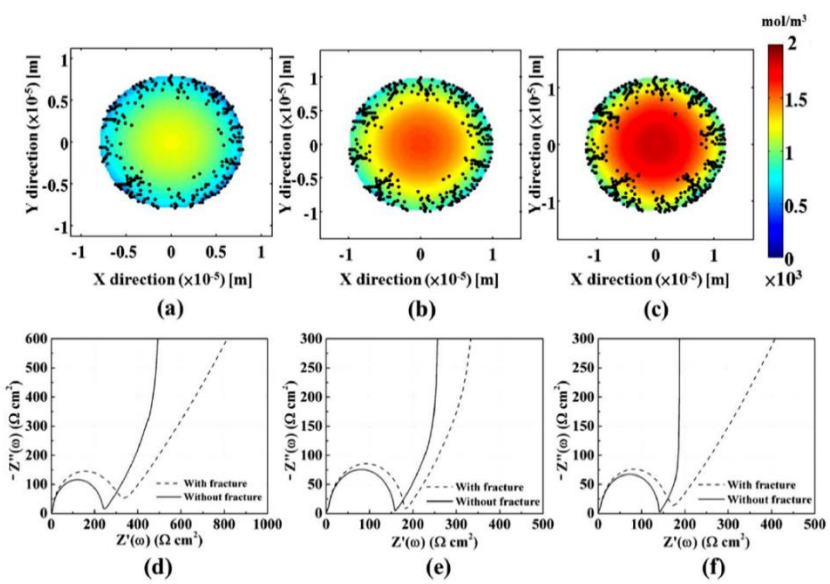

Figure 1.14 (a-c)Fracture and concentration distribution and corresponding impedance response (d-f) for graphite particles [80].

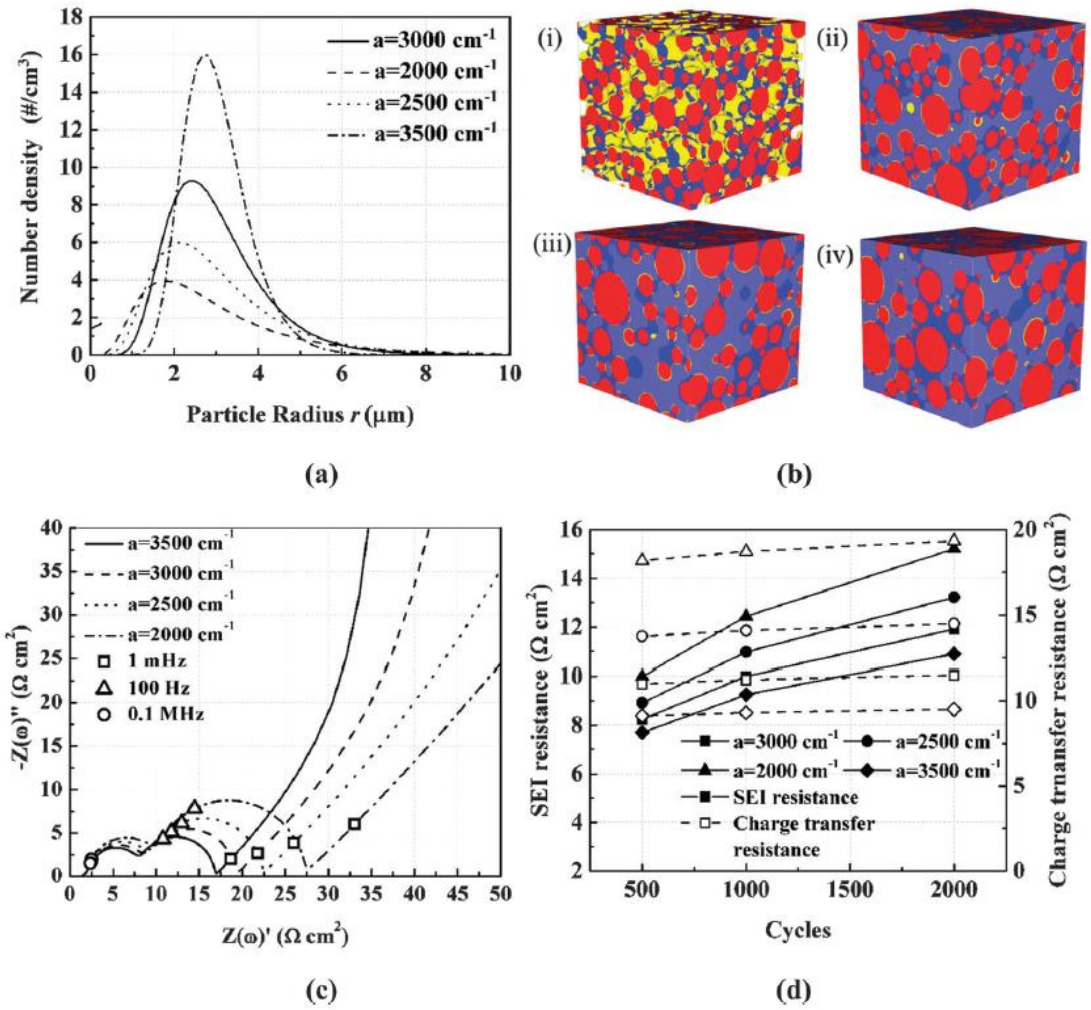

Figure 1.15 Porous electrode impedance response variation with microstructure inclusive of solid electrolyte interphase layer resistance [81].

Recently, lithium metal as a negative electrode has attracted tremendous interest due to the burgeoning demand for electrical energy storage.[82-84] Universally considered in the scientific community as the "Holy Grail" anode, Li metal surpasses current commercial Li-ion intercalation anodes with regards to specific gravimetric capacity (~3862 mAh/g for Li metal vs. 372 mAh/g for graphite), low density (~0.534 g/cm^3 for Li metal vs. ~2.2 g/cm^3 for graphite), and the lowest negative electrochemical potential (0 V vs. Li/Li$^+$ for Li metal against stoichiometrically varying 0 - 1.5V vs. Li/Li$^+$ for graphite).[59, 60] Consequently, Li metal offers a realistic perspective for high energy density rechargeable batteries; also evidenced by the resurgent research focus in beyond Li-ion chemistry, such as Li-sulfur and Li-air battery systems.[10, 82, 85] A critical

challenge for Li metal anodes centers around unmitigated Li dendrite growth, which degrades cell performance and causes safety concerns, such as low cycling efficiency, thermal runaway, and short circuit.[11, 86, 87] Several approaches have been proposed to enable dendrite-free electrodeposition, for example, utilizing solid electrolytes with high toughness to prevent dendrite propagation,[88-90] employing highly concentrated electrolytes to prevent electrolyte depletion,[91] and electrolyte additives to slow dendrite growth kinetics,[12, 92] as well as patterning nano/microscale electrolyte transport channels to regulate Li-ion flux distribution,[93-95] amongst other techniques.[96-98]

A common feature of intercalation (such as, graphite) and Li metal anodes for liquid electrolyte systems is the formation of a passivating layer known as the solid electrolyte interphase (SEI) through the reduction of electrolyte solvent and salt with Li, intercalated or otherwise. The SEI layer allows for the transport of Li-ion from the electrolyte to the anode surface while preventing further deleterious reactions between the anode and electrolyte.[99-101] The mechanism of SEI formation in intercalation anodes (e.g., graphite) is well established; SEI is predominantly formed during the initial formation cycles, growing continuously with further electrochemical cycling, albeit at a much slower rate, which contributes to the capacity fade of the Li-ion battery system.[102, 103] For state-of-the-art Li metal anode, extensive efforts have been made to unravel the SEI formation mechanisms.[23, 103-105] Similar to the case of graphite, the SEI on Li anode is multicomponent, of which the major inorganic constituents include Li_2O, Li_2S/Li_2S_2, LiF, Li_2CO_3, and LiOH, depending on the battery system and operating conditions (see Figure 1.16).[106]

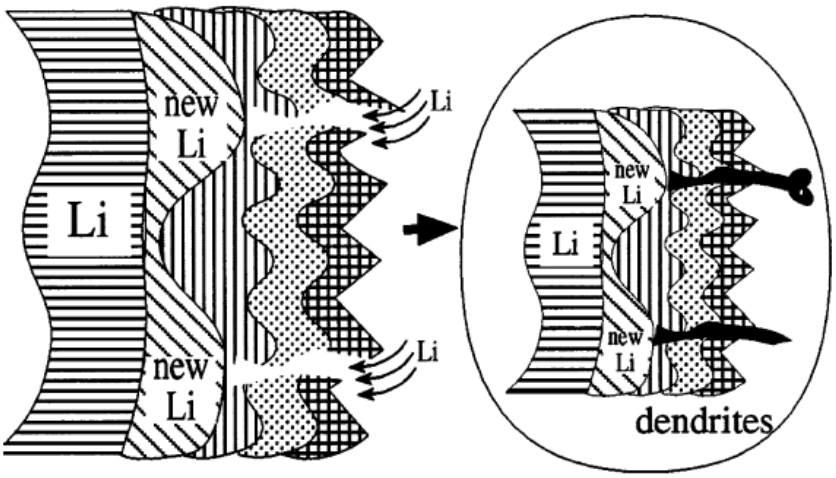

Figure 1.16 Schematic illustration of surface film formation on lithium electrodes in alkyl carbonates[107].

For commercially used intercalation anodes (e.g., graphite), the SEI exhibits good chemical and mechanical stabilities under small volumetric changes (~10%) of the active material.[108] In contrast, the immense volume change of Li metal renders the SEI unstable, eventually resulting in disintegration of the SEI layer. The fracture of the SEI layer decreases local Li-ion transfer resistance, thereby initiating Li dendrite formation.[109] Also, repetitive fracture of the SEI during Li plating/stripping results in fresh contact of electrolyte with Li metal surface, resulting in unabated parasitic Li depleting reduction reactions leading to faster SEI growth and poor cycling efficiency (see Figure 1.17).[103] Additionally, an inhomogeneous SEI layer can induce Li dendrite formation due to the spatially non-uniform Li-ion flux through the SEI. Therefore, it is imperative to develop fundamental understanding of the lithium metal and SEI interactions.

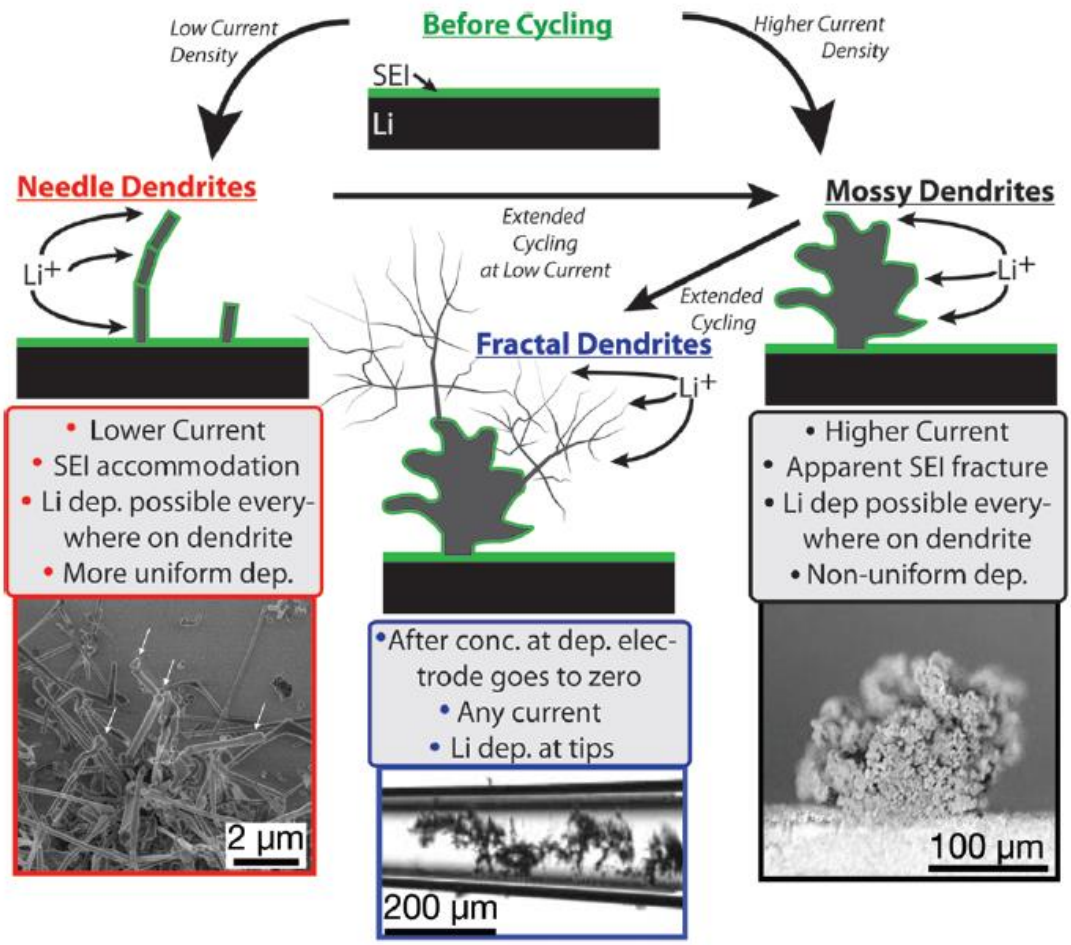

Figure 1.17 Schematic representation of different dendrite morphologies shown with representative micrographs[107].

All solid-state batteries with inorganic solid electrolytes have been advocated in literature, however, Li metal can still penetrate through the grain boundaries of the polycrystalline garnet solid electrolyte, which may lead to short circuit above critical current densities (see Figure 1.18 and Figure 1.19). Intense research efforts have also been devoted to polymer solid electrolytes and inorganic sulfide electrolyte to mitigate dendrite propagation. Accurate characterization of dendrite – SEI – electrolyte transport-mechanics-electrochemistry interactions can help illuminate strategies towards amelioration of substantial capacity fade in Li metal anodes-based systems.

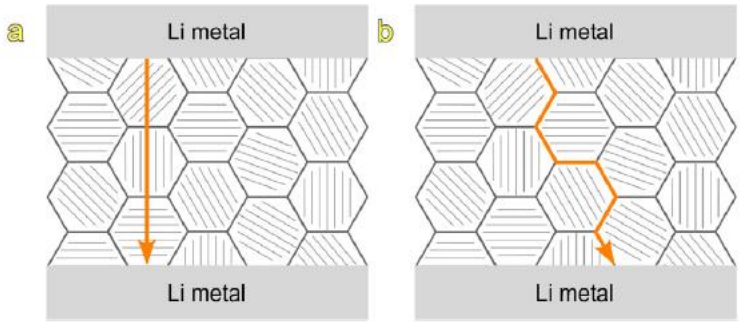

Figure 1.18 Illustration of Li metal plating through polycrystalline LLZO solid electrolyte (a) transgranular, (b) intergranular [110].

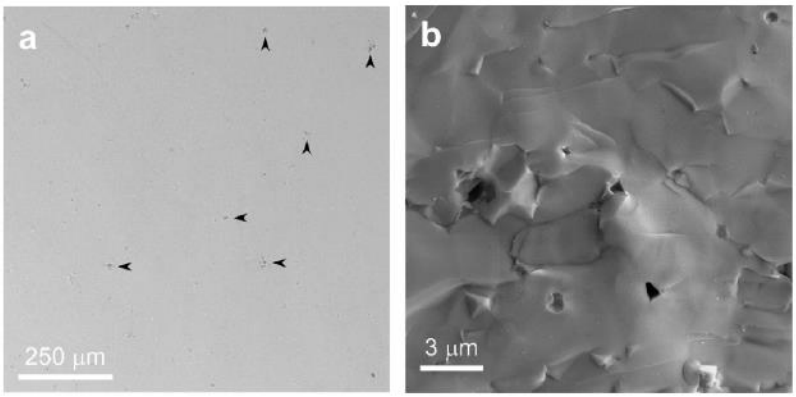

Figure 1.19 Electron micrographs of uncycled LLZO (a) SEM image of a polished surface (arrow heads indicate micron-sized pores), (b) SEM image of a fracture surface[111].

The rigid barriers in ASSBs contribute to mechanical stress at the Li|SE interface which can suppress dendritic growth. An investigation into the complexations between electrolyte ion transport, reaction kinetics at the metal-solid electrolyte interface, mechanical stress induced chemical potential change and damage is necessitated to understand the system (see Figure 1.20). Ion transport in single-ion conductor inorganic solid electrolytes (LPS, LLZO) and dual-ion conductor polymer electrolytes (PEO, SEO) can be characterized by Ohm's law and the Nernst-Plank theory, however, stress effect on ion conduction are yet to be ascertained. In intercalation anodes, stress induced diffusion amplifies Li transport inside the active material; a similar phenomenon is expected for solid electrolytes. [110] This necessitates theoretical/experimental determinations of solid electrolyte ionic transport properties (conductivity, diffusivity) as function of the stress state inside the system. The seminal model of stress-kinetics coupling was provided

by Monroe and Newman, correlating the Butler-Volmer exchange current density to mechanical stresses and molar volumes of the constituent polymer solid electrolyte and Li metal.[11, 77] A static solve on the Li metal-polymer electrolyte system with linear elastic perturbation theory showed that solid electrolytes with shear modulus twice that of Li metal were capable of suppressing dendrites. However, this study did not account for ion transport in the solid electrolyte. The above model was extended by Barai and Srinivasan to account for ion transport through potential and concentration gradients and Li metal plasticity.[112] Stable deposition regimes for inorganic electrolytes have been explored as well, accounting for polycrystalline architecture and anisotropic transport, stiffness parameters. [93, 113-115] Grain boundary softening has been proposed for preferential intergranular Li metal penetration through the boundaries using first principles calculations. [116] Experimental observations of the all solid-state battery operation beyond a critical current density (CCD) exhibit rapid failure of the cell. Polymer electrolyte systems are constrained by the limiting current density beyond which the concentrations at the plating electrode drop to zero at Sand's time limits leading to rapid dendritic growth explaining the CCD for polymer systems. However, single ion inorganic conductors are devoid of mass transport limitations, yet, CCDs are seen for these systems as well which requires detailed investigations.

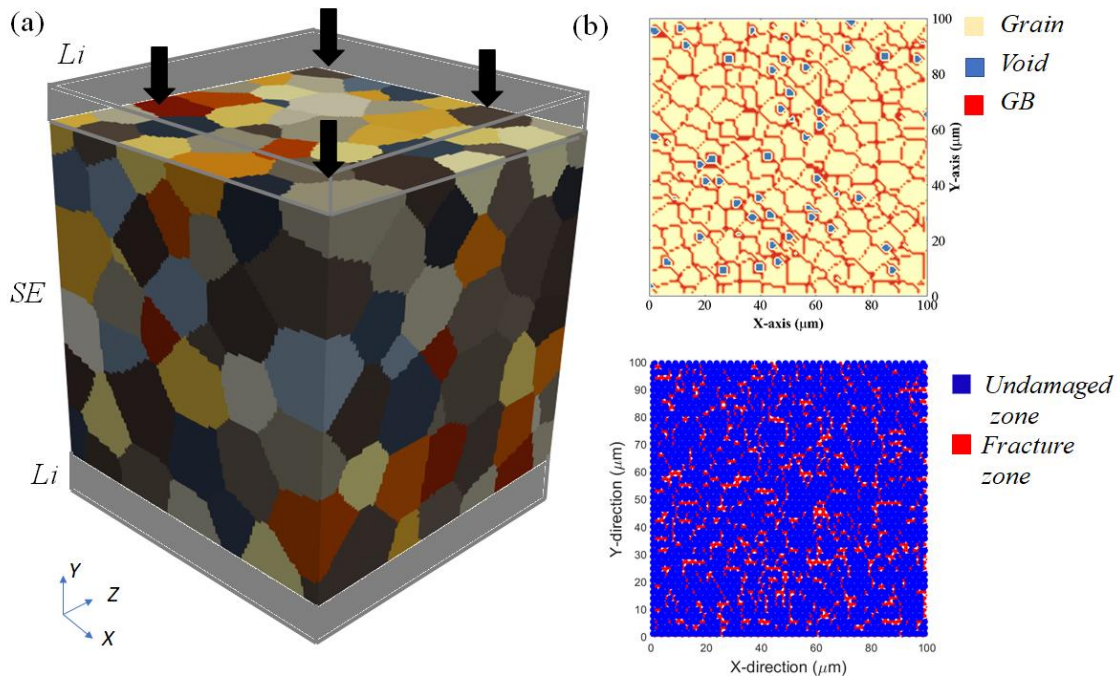

Figure 1.20 (a) Schematic of Li-Li symmetric cell with polycrystalline solid electrolyte architecture. Li^+ ion flux from the stripping electrode redistributes through the solid electrolyte and is directed onto the plating electrode. (b) Cross sectional view of the polycrystalline solid electrolyte with grain, grain boundaries (GB) and voids delineated. Li plating and stripping induces stresses in the system leading to mechanical damage preferentially along the softer grain boundaries of the system.

It is imperative to note that there is an ongoing debate in the scientific community with regards to the molar volume inside the inorganic solid electrolyte. Zero molar volume has been reported for LLZO in literature based on negligible volumetric change with Li^+ incorporation, alongside a wide range of values for different SEs. [117, 118] Ahmad *et al.* has delineated the stability regime of inorganic solid electrolytes as a function of solid electrolyte to Li metal molar volume and shear modulus ratio and has shown that inorganic solid electrolytes with low molar volume and high shear moduli ratios (such as LPS or LLZO) are prone to current instabilities.[119] A bridge needs to be built between the molecular scale definitions of molar volume with those used in continuum models; in particular, there is a lack of consensus as to whether to correlate molar volume to the cationic/anionic radii or to consider it as an inherent part of the crystal structure.

Detailed insights into the performance of SSBs through modeling requires a dynamic model that is capable of temporal tracking of deposition/stripping at the interface which includes

the interactions emanating from elastic-plastic stresses, ion transport, and electrochemistry. Furthermore, incorporation of chemical (surface tension) and mechanical wettability (external pressure), imperfect contact/peeling, and microstructural heterogeneities (e.g., voids, grains, grain boundaries for a polycrystalline electrolyte) into the modeling paradigm will help elucidate the scenarios that limit performance. The presence of an interphase/interlayer between the metal and SE will add to the model complexity, requiring stresses and transport to be solved in an additional layer, while accounting for characteristics of the layer (brittle/ductile deformation, Maxwell/Ohm transport law, Butler-Volmer/Tafel kinetics etc.). First-principles studies catalyzed by machine learning approaches will also be useful in rapid estimation of the transport, mechanical and thermodynamic properties of the SE materials[120]. First-principles atomistic calculations utilizing density functional theory catalyzed by machine learning approaches will also be useful in rapid estimation of the transport (ionic conductivity/diffusivity), mechanical (stiffness tensor), kinetic (exchange current density) and thermodynamic (molar volume) properties of the SE materials[121].In literature, density functional theory has proven useful in estimating the ionic conductivity and Young's modulus of both amorphous and polycrystalline solid electrolyte materials[117, 118] Our conjecture and proposition is that dynamic mesoscale interactions[122, 123], including the interplay between reaction kinetics, interfacial stochasticity, transport, and mechanics, are essential to provide fundamental mechanistic insights into Li-metal-based SSBs.

2. MECHANO-ELECTROCHEMICAL INTERACTION AND DEGRADATION IN GRAPHITE ELECTRODE

Relevant Publications and/or Working Papers

1. **A. Verma,** T. Kotaka, Y. Tabuchi, P.P. Mukherjee, "*Mechano-Electrochemical Interaction and Degradation in Graphite Electrode with Surface Film"*, Journal of Electrochemical Society **165** (10), A2397-A2408 **(2018)**
2. N. Kotak, P. Barai, **A. Verma**, A. Mistry, P.P. Mukherjee, "*Electrochemistry-Mechanics Coupling in Intercalation Electrodes*", Journal of Electrochemical Society **165** (5), A1064-A1083 **(2018)**

2.1 Background

Lithium ion batteries (LIBs) have become pervasive in applications like portable electronics [123]. The energy and power densities afforded by lithium ion batteries are being improved continuously with intense efforts being directed to develop durable batteries with high energy and power densities for usage in electric and hybrid electric vehicles [124-126] and grid energy storage [4, 127]. Active materials used for the anode [7, 128], cathode [129, 130] couple dictate the energy and power densities afforded by LIBs. Graphite [6] is the most commonly used negative electrode material in commercial Li ion batteries while the transition metal oxides belonging to the nickel-cobalt-manganese (NCM) amalgam group have attained considerable popularity as the positive electrode material [131, 132]. The theoretically achievable capacity of graphite is 372 mAh/$g_{graphite}$, with practical attainable capacity around 350 mAh/$g_{graphite}$ [133]. Current cathode materials have realized discharge capacities of 200 mAh/g_{AM}.

A drawback that afflicts anode materials predominantly is significant volumetric expansion/expansion upon lithiation/delithiation of particles. Graphite shows a volumetric expansion of around 10% at full lithium intercalation within the graphene sheets [134]. This expansion manifests as around 3% increase in the linear dimension (radius, in case of spherical graphite active material). Several other materials are being investigated as a potential replacement to graphite anodes with most promising results being shown by silicon [135] and tin [136]. They exhibit much larger lithium storage capacities than currently used graphite electrodes. The theoretical capacity of Si is around 4200 mAh/g when fully lithiated [1, 137]. However, Si lithiation is associated with massive volume expansion of the order of 300% [138]. Larger volume

expansion and the resulting stress within silicon electrodes exacerbates the fracture and mechanical degradation leading to faster capacity fade for silicon electrodes.

Consequently, a critical challenge that needs to be addressed in advancing lithium ion battery technology is fracture and decrepitation of electrodes as a result of the lithium diffusion during charging and discharging operations [139, 140]. Insertion of lithium in the negative electrodes can induce a large volume change of the order of a few to several hundred percent. The resulting stresses, aptly named as diffusion-induced stress (DIS), can cause nucleation and growth of cracks, leading to mechanical degradation of the electrode materials. Several studies [113, 141-146] have investigated the effect of particle size and C-rate on the evolution of stresses in the bare active material and the corresponding fracture map [113, 146-148]. Recently, studies are being focused on investigating the mechanical properties of the anode active material in the presence of a surface film [145, 149, 150] and with core shell structure of active material [151].

Surface film can form on the anode surface in various ways. During electrode preparation, secondary phase inclusions comprising of conductive additive and binder can coat on the electrode particles [148]. Also, during cycling, a film grows on the surface of the anode active material which is termed the solid electrolyte interphase [149, 152]. The film thickness is of the order of nanometers and its growth is found to saturate at the end of first few cycles. Alternatively, some researchers are investigating the role of artificial coatings on electrode particles in mitigating damage and capacity fade experimentally as well [153].

In this work, the lattice spring model from Barai et. al.[154-156] is extended to accommodate a surface film of varying mechanical properties like Young's modulus, Poisson's ratio and fracture energy threshold atop the graphite active material. The geometric aspect of varying film thickness is investigated as well. We perform computational investigations into the effect of a film on the surface of the graphite active material on its mechanical response during electrochemical discharge.

The rest of the chapter is divided into the following sections. The Methodology section gives an overview of the physics and numerical techniques used in our simulations based on the Lattice Spring Model. The Results and Discussion section elucidates the ramifications of varying the film geometric and mechanical properties on the evolution of damage inside the active material. Rate performance studies with and without surface film are presented as well to correlate damage with capacity. The chapter concludes with a section summarizing the simulation results.

2.2 Methodology

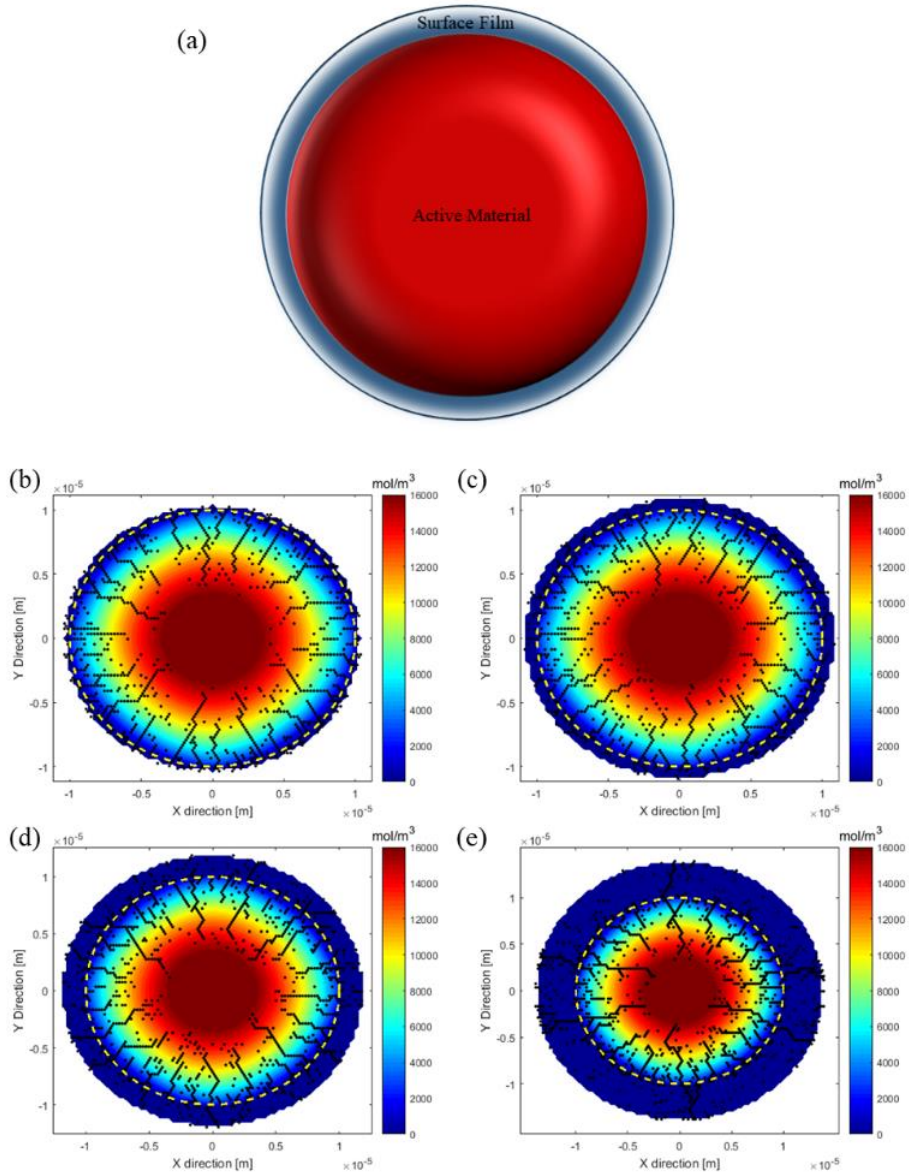

Figure 2.1 (a) Material contour map for spherical active material (red) with surface film (blue) on top. Variation of concentration contour plots as a function of film thickness to graphite particle radius ratio, (b) $\delta / R = 0.05$, (c) $\delta / R = 0.1$, (d) $\delta / R = 0.2$ and (e) $\delta / R = 0.4$. The dashed yellow line indicates the graphite particle boundary. The number of broken bonds (denoted by black dots) inside the active material are relatively unaffected by the increase in film thickness. Hence, fracture inside active material is relatively unaffected by film thickness.

Figure 2.1 (a) shows the active material surrounded by film which is being studied here. The investigation into the mechano-electrochemical interactions of active material + film requires accurate quantification of the mechanical properties of individual layers. These parameters include Young's modulus, Poisson's ratio, mean fracture energy threshold per unit area and expansion coefficient. The mean fracture threshold energy per unit area is an indicator of the amount of strain energy that the material can absorb without breaking. If the strain energy exceeds this threshold, crack nucleation is initiated. The elastic modulus of the material directly relates to the amount of fracture damage inside the material, hence material with high Young's modulus will have a greater propensity for fracture provided the fracture threshold energy for both the materials is the same. Material parameters for graphite active material and surface film (SEI as well as secondary phase) are reported in Table 2-1. In addition, the table also lists the diffusion coefficient for Li in graphite and the nominal spherical graphite active material size.

Table 2-1 Material parameters of graphite active material (AM) and surface film.

AM Young's modulus, E_1	**70.57 Gpa** [157], 10 Gpa [153] , 33 Gpa [158]
AM Poisson's ratio, υ_1	**0.277** [150] , 0.3 [150]
AM mean fracture energy threshold per unit area, ψ_1	2 J/m^2 [37, 152, 159]
AM expansion coefficient, ω	1.14×10^{-6} m^3/mol [37]
AM radius of particle, R	10 µm
AM diffusion coefficient, D_s	3.9×10^{-14} m^2/s [152]
Film Young's modulus, E_2	1.9 Gpa (PVDF+CA) [152] 66.0 Gpa (SEI) [158]
Film Poisson's ratio, υ_2	0.34 (PVDF+CA) [159], 0.3 (SEI)[158]

The problem formulation involves modeling of two coupled physical phenomenon, the mechanical behavior involving deformation, stress and fracture and solid-state diffusion of lithium inside the active material particles. The mechanical behavior is elucidated using a two-dimensional random lattice spring formulation with diffusion behavior computed on a juxtaposed two-dimensional Cartesian grid. The complexity of this approach is in the accurate mapping of field

variables (like concentration) from the Cartesian grid to the spring network and vice versa. The usefulness of this approach has previously been demonstrated for bare active material particles by Barai et. al [37]. In this work, we extend this model to account for the presence of a surface film by adding an additional layer of springs with spring stiffness disparate from the active material to investigate the resulting change in fracture map.

A brief overview of the coupled Lattice Spring Model [152] is given here. The computational domain is discretized into a spring network with coordination number six (Born model) which mimics the properties of the actual material. Both central springs and shear springs are used to accurately replicate the Young's modulus and Poisson's ratio of the material. The Young's modulus and Poisson's ratio are related to the axial and shear spring stiffness according to the following constitutive relations:

$$E(c) = \frac{\sqrt{3}}{4\ell}\left((3-\nu)k_n + (1+\nu)k_s\right)$$
$$\nu = \frac{k_n - k_s}{3k_n + k_s} \tag{2.1}$$

Here, l is the length of the spring used to discretize the domain. Depending on the material encompassing the domain, we will have different stiffness values for the axial and shear springs. For active material with a surface film on top, two different spring constants are used for each of the material domain. Variable spring lengths can also be used to mesh dissimilar material zones.

Force balance is modeled using Newton's second law. Body forces are absent and the assumption of quasi-static equilibrium eliminates the inertial term. The validity of the assumption of quasi-static equilibrium is derived from the fact that the solid-state diffusion of Li ions inside the active material is orders of magnitude smaller than pressure wave propagation inside the material. Consequently, mechanical equilibrium is reached much faster than concentration equalization and hence the stress distribution inside the particle can be obtained by solving for Equation (2.2).

$$\nabla \cdot \sigma = 0 \tag{2.2}$$

with stress free boundary condition applied at the surface of the active material.

Electrochemistry in the electrode is solved using the single particle model (SPM). The rate determining transport mechanism inside the battery is the solid-state diffusion inside the active

material. The electrolyte ionic diffusivity and conductivity is assumed to be high enough to neglect concentration and potential gradients inside the electrolyte. Therefore, the active material is subjected to constant flux from all directions irrespective of its position from the current collector under galvanostatic operation. Under this assumption, the distribution of Li ion concentration inside the solid phase can be determined by solving the diffusion equation given below,

$$\frac{\partial c_s}{\partial t} = \nabla \cdot \left(D \nabla c_s \right) \tag{2.3}$$

with surface flux boundary condition given by the following relation

$$\begin{aligned} -D \frac{\partial c_s}{\partial n} &= \frac{i}{F} \\ I_{app} &= \int_{surface} i \, \mathrm{d}S \end{aligned} \tag{2.4}$$

The concentration equation is solved using finite difference approach on a Cartesian grid. It is only solved for inside the active material domain. The film domain is devoid of concentration gradients and experiences stress from the active material swelling/shrinking during lithiation/delithiation. The diffusion induced stress is then mapped onto the spring network for solution of the stress equation. The stress strain relationship is translated into a force displacement relationship. Stress generated using diffusion is assimilated as an axial displacement in the spring.

$$\begin{Bmatrix} f_{a1} \\ f_{s1} \\ f_{a2} \\ f_{s2} \end{Bmatrix}_{conc} = \begin{bmatrix} k_n & 0 & -k_n & 0 \\ 0 & k_s & 0 & -k_s \\ -k_n & 0 & k_n & 0 \\ 0 & -k_s & 0 & k_s \end{bmatrix} \begin{Bmatrix} \Omega \Delta c_1 l \\ 0 \\ \Omega \Delta c_2 l \\ 0 \end{Bmatrix} \tag{2.5}$$

Correspondingly, the local force displacement relation takes the following form

$$\begin{Bmatrix} f_{a1} \\ f_{s1} \\ f_{a2} \\ f_{s2} \end{Bmatrix} = \begin{Bmatrix} f_{a1} \\ f_{s1} \\ f_{a2} \\ f_{s2} \end{Bmatrix}_{mech} + \begin{Bmatrix} f_{a1} \\ f_{s1} \\ f_{a2} \\ f_{s2} \end{Bmatrix}_{conc} = \begin{bmatrix} k_n & 0 & -k_n & 0 \\ 0 & k_s & 0 & -k_s \\ -k_n & 0 & k_n & 0 \\ 0 & -k_s & 0 & k_s \end{bmatrix} \begin{Bmatrix} u_{a1} \\ u_{s1} \\ u_{a2} \\ u_{s2} \end{Bmatrix} \tag{2.6}$$

The strain energy is calculated in each spring according to $\psi^{[e]} = \frac{1}{2} \vec{f} \cdot \vec{u}$. Once the strain energy exceeds the fracture energy threshold, the spring breaks and is irreversibly removed from the network, resulting in fracture. Furthermore, the two way coupling between stress and diffusion

is ensured by reducing the Li ion diffusivity in the affected region according to $D_{fract} = \alpha D_{pristine}$ [21, 152]. The presence of cracks will make the Li ion diffusion path more tortuous, hence, a parameter α with a value 0.6 is used to scale the pristine material diffusion coefficient value. The choice of this value for the parameter α is reasoned from the work of Barai et al [37]. Thus, concentration is solved on a two-dimensional finite difference Cartesian grid with typical size 60×60. Mechanics and fracture propagation is solved on a triangular lattice spring framework with grid size 60×60 juxtaposed on the Cartesian grid. The grid size chosen is appropriate for striking a balance between accuracy and computational time. For a more detailed information of the methodology and solution algorithm, the reader is directed to the seminal work by Barai et al [37].

Concentration dependent elastic moduli are exhibited by most of the active material used in anodes [160]. Qi et. al.[21] used density functional theory calculations to show that the Young's modulus of graphite increases threefold during lithium intercalation. The increase or decrease in Young's modulus relates to the stiffening or softening of the electrode material. The concentration dependent Young's modulus of the active material is incorporated into the simulations using the following relation:

$$E(c) = E_0 \left(1 + k \frac{c}{c_{max}} \right) \tag{2.7}$$

Here E_0 is the Young's modulus with zero stoichiometric Li concentration, c is the current Li ion concentration and c_{max} is the maximum stoichiometric Li ion concentration within the active material. The stiffening or softening of material with Li insertion relies on the parameter k, with $k > 0$ indicating the former while $k < 0$ indicating the latter. Literature reports values of $k = 2$ for graphite and $k = -0.7$ for silicon [161], indicating that graphite stiffens while Si softens on intercalation. Also, silicon exhibits elastic plastic deformation as compared to brittle fracture exhibited by graphite.

The battery performance is estimated using the single particle model formulation for the LIB cell sandwich pioneered by Guo *et al* [162]. The single particle model couples solid state diffusion in the electrode particles, Eqs. (3, 4), with electrochemical reactions at the electrode-electrolyte interface. As has been discussed previously, electrolyte transport is assumed to be rapid enough so as to not impose any limitations in this model. The validity of this assumption is predicated on operation of the LIB cells at low C-rates (< 2C), however, this premise can be

extended to higher C-rates by using a bulk electrolyte transport resistance model where the resistance of the electrolyte, R_e, is a function of C-rate. Butler-Volmer kinetics formulation is used to describe the electrochemical reactions occurring at the anode and cathode electrodes. Electrode overpotential, η_j (j = p, n for positive and negative electrodes, respectively) is estimated using Equations (2.8-2.10).

$$i_j = i_{0,j}\left[\exp\left(\frac{\alpha_{a,j}F}{\Re T}\eta_j\right) - \exp\left(-\frac{\alpha_{c,j}F}{\Re T}\eta_j\right)\right] \tag{2.8}$$

$$i_{0,j} = k_j(T)Fc_{s,j}^{\max}c_e^{\ 0.5}(1-\theta_{surf,j})^{0.5}\theta_{surf,j}^{\ 0.5} \tag{2.9}$$

$$\theta_{surf,j} = \frac{c_{s,j}(r = R_{s,j})}{c_{s,j}^{\ max}} \tag{2.10}$$

Here, i_j is the applied current density, $i_{0,j}$ is the exchange current density and $\alpha_{a,j}, \alpha_{c,j}$ are the anodic and cathodic transfer coefficients for the j-th electrode, $\Re$ is the universal gas constant, F is Faraday's constant and T is the temperature. For intercalation electrodes, the exchange current density formulation, shown in Equation (2.9), is dependent on the electrode rate constant, k_j, maximum molar concentration of intercalated Li inside the electrode host, $c_{s,j}^{\max}$, Li^+ concentration in the electrolyte phase, c_e, and state of charge at the electrode surface, $\theta_{surf,j}$ (see Equation (2.10)).

The computation of the electrode overpotentials facilitates the estimation of voltage of the LIB cell sandwich, V_{cell} using Equations (2.11, 2.12). Here, U_j , is the open circuit potential of the j-th electrode which takes a unique non-linear functional form dependence on surface state of charge, $\theta_{surf,j}$, for each electrode. In our work, material and electrode parameters for graphite anode and lithium cobalt oxide cathode used to ascertain the effect of surface film on battery performance are imported directly from Guo *et al*. [162]

$$\eta_j = \phi_{s,j} - \phi_e - U_j(\theta_{surf,j}, T) \tag{2.11}$$

$$V_{cell} = \phi_{s,p} - \phi_{s,n} - IR_e = \left(U_p + \eta_p\right) - \left(U_n + \eta_n\right) - IR_e \tag{2.12}$$

2.3 Results and Discussions

2.3.1 Effect of Film Mechanical and Geometric Properties

We first investigate the effect of variation of film thickness, Young's modulus and fracture energy threshold on the fracture inside graphite active material and surface film. A fully charged graphite particle with surface film is delithiated under galvanostatic operation until the surface concentration goes to zero. The base case parameters are defined as film thickness to graphite particle radius ratio, $\delta / R = 0.1$, film to graphite particle fracture threshold energy ratio, $\psi_2 / \psi_1 = 1$, and film to graphite Young's moduli ratio, $E_2 / E_1 = 1$. For each of the variations investigated, the remaining two parameters always correspond to the base case values. Also, the graphite parameters are never varied; all the variations explored are done by changing the properties of the surface film. A nominal graphite particle radius of 10 μm is used and the C-rate chosen is 5 C. High value of C-rate is chosen to highlight the variation in mechanical degradation. It has been proven that large particle size and high C-rate increase propensity for fracture, hence these values are used for underscoring the variation effects.

Quantification of the fracture inside the graphite particle with surface film is done by defining a parameter named total damage density, DD_{total} . It is defined as the ratio of number of broken bonds to the total number of bonds in the particle-film agglomerate. Individual graphite/film damage density, DD_{Gr} and DD_{film}, are also defined as the ratio of number of broken bonds in graphite/film to the total number of bonds in the graphite and film agglomerate. The definitions have been kept as above such that $DD_{total} = DD_{Gr} + DD_{film}$.

$$DD_{total} = \frac{n_{broken,total}}{n_{Gr} + n_{film}} \tag{2.13}$$

$$DD_{Gr} = \frac{n_{broken,Gr}}{n_{Gr} + n_{film}}, \; DD_{film} = \frac{n_{broken,\,film}}{n_{Si} + n_{film}} \tag{2.14}$$

Effect of Film Thickness

Table 2-2 enumerates the fracture extent as film thickness to particle radius ratio, δ / R , is increased from 0.05 to 0.4. The film thickness is 0.5 μm, 1 μm, 2 μm and 4 μm for the shown size ratios

considering a 10 μm radius graphite particle. Since graphite size is the same, we observe that the number of bonds used for discretization of the graphite active material remains the same (=4997) over the range of film thicknesses explored. The number of bonds in the surface film layer exhibits increase from 509 to 4970 mirroring the increase in film thickness from 0.5 μm to 4 μm. Figure 2.1(b-d) gives the concentration contour plots inside the active material, for the size ratios explored, at the end of delithiation juxtaposed with the damage pattern. The dashed yellow line indicates the graphite particle boundary. As discussed before, concentration is not solved for inside the film and is assigned a value of zero for representation purposes. The black dots represent fractured bonds and higher density of these bonds implies higher damage. Figure 2.2 shows the corresponding variation of damage density inside active material, film as well as the total damage density (sum of the previous two).

Table 2-2 Damage density variation with film thickness to particle size ratio for 10 μm graphite particle at 5 C rate for $E_2 / E_1 = 1.0, \psi_2 / \psi_1 = 1.0$. The total number of springs inside the active material is 4997.

δ/R	Damaged bonds in AM	Damaged bonds in film	Total no. of bonds in film	Damage density in AM	Damage density in film	Total damage density
0.05	909	189	509	0.1650	0.0343	0.1994
0.1	936	254	1056	0.1546	0.0419	0.1965
0.2	928	378	2185	0.1292	0.0526	0.1818
0.4	961	545	4790	0.0981	0.0556	0.1538

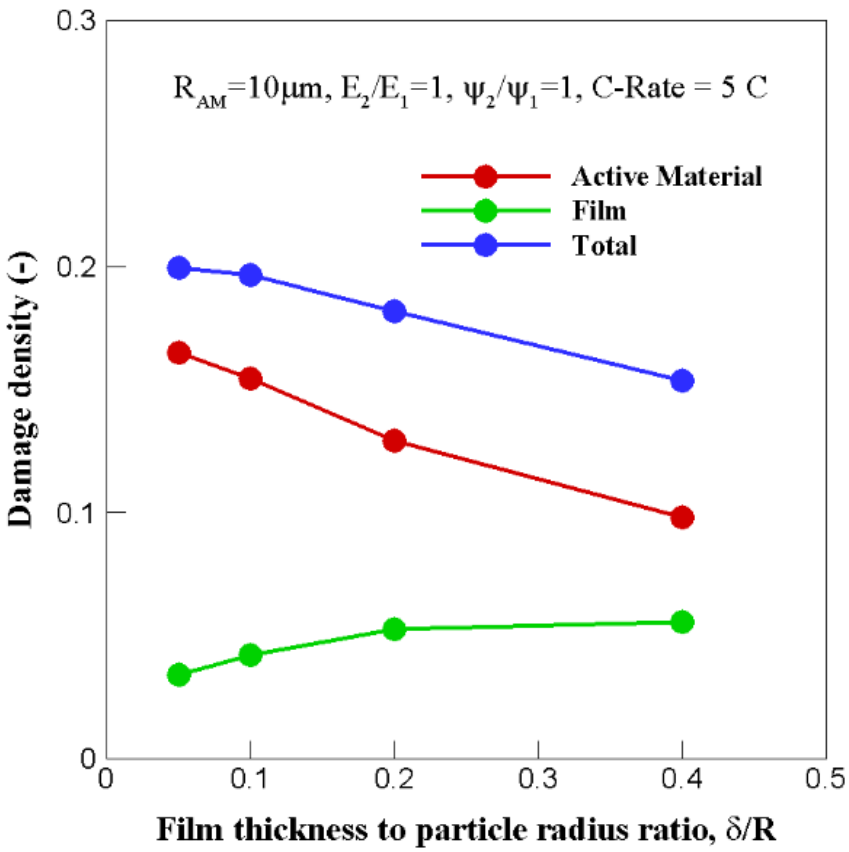

Figure 2.2 Effect of surface film thickness on damage density inside graphite with surface film. Total number of surface film bonds increase with film thickness. Total damage density shows a mild decrease with film thickness increase.

From the results, it can be ascertained that as film thickness is increased, damage density inside the film saturates. This is because there is no diffusion induced stress inside the film. Fracture inside the film will be mostly concentrated close to active material surface and portion of film far from the active material is relatively unaffected. The graphite damage density shows a downward trend with film thickness increase. The decreasing trend of active material damage density is predominated by the increase in the total number of bonds in the agglomerate as the film thickness is increased. Damaged bonds do not rise in the same proportion as total number of bonds; the bonds added to the surface film with thickness increase do not rupture easily because of more support structure and absence of diffusion induced stress. Consequently, the ratio of damaged bonds to total number of bonds keeps on decreasing with thickness increase.

From the above analysis, we can derive an important conclusion. Surface film damage stabilizes beyond a critical thickness. Given, that surface films are generally comprised of inert materials we should aim to use the minimum required thickness to reduce the fraction of non-intercalating phases. This provides an avenue for improving the performance characteristics of lithium ion batteries through less fracture damage while simultaneously keeping the non-contributing components to energy and power density to low levels. Total agglomerate damage density trend is dominated by graphite damage density and hence mirrors the decreasing trend of graphite damage as film thickness increases.

Effect of Film Fracture Threshold Energy

Table 2-3 and Figure 2.3 and Figure 2.4 detail the effect of changing the film fracture threshold energy on the fracture behavior. Figure 2.3 shows the superimposed damage and concentration contours inside the graphite particle with surface film. The detailed breakdown of film, graphite and total damage density variation with fracture threshold energy is displayed in Figure 2.4. Total number of bonds in the graphite active material (4997) and film (1056) remain the same throughout the variations explored since the size of the agglomerate system does not change.

Table 2-3 Damage density variation with ratio of fracture threshold energy for 10 µm graphite particle at 5 C rate for $\delta / R = 0.1,\ E_2 / E_1 = 1.0$. The graphite fracture threshold energy is kept constant and film fracture threshold energy is varied to obtain different ratios. The total number of springs inside the active material is 4997 and film is 1056.

$\psi_2 / \psi_1 = 1.0$	Damaged bonds in AM	Damaged bonds in film	Damage density in AM	Damage density in film	Total damage density
0.1	887	545	0.1465	0.0900	0.2365
0.2	870	448	0.1437	0.0740	0.2177
0.5	919	323	0.1518	0.0533	0.2051
1.0	907	263	0.1498	0.0434	0.1932
5.0	957	110	0.1581	0.0181	0.1762
10.0	957	71	0.1581	0.0117	0.1698

It is observed that as the film fracture threshold energy increases, fraction of broken bonds inside the film decreases considerably. There is a slight increase in the fraction of broken bonds inside the graphite active material as the film fracture threshold energy is increased. The above observations can be explained using our understanding of the physical meaning of fracture threshold energy. Fracture threshold energy dictates the failure criteria of the material. For a low fracture threshold energy, more fracture will occur as lesser amount of strain energy accumulation is enough to nucleate cracks. Correspondingly, the film shows severe cracking at very low fracture threshold energy which reduces as the film fracture energy threshold is increased. To mitigate the fracture inside film, it will be beneficial if we can control the fracture threshold energy, keeping it high. High values of fracture threshold energies are demonstrated by ductile materials undergoing large plastic deformation.

Film fracture threshold energy shows negligible impact on the damage inside the active material. Total damage is dominated by the film damage trend and shows decrease with increase in film fracture threshold energy.

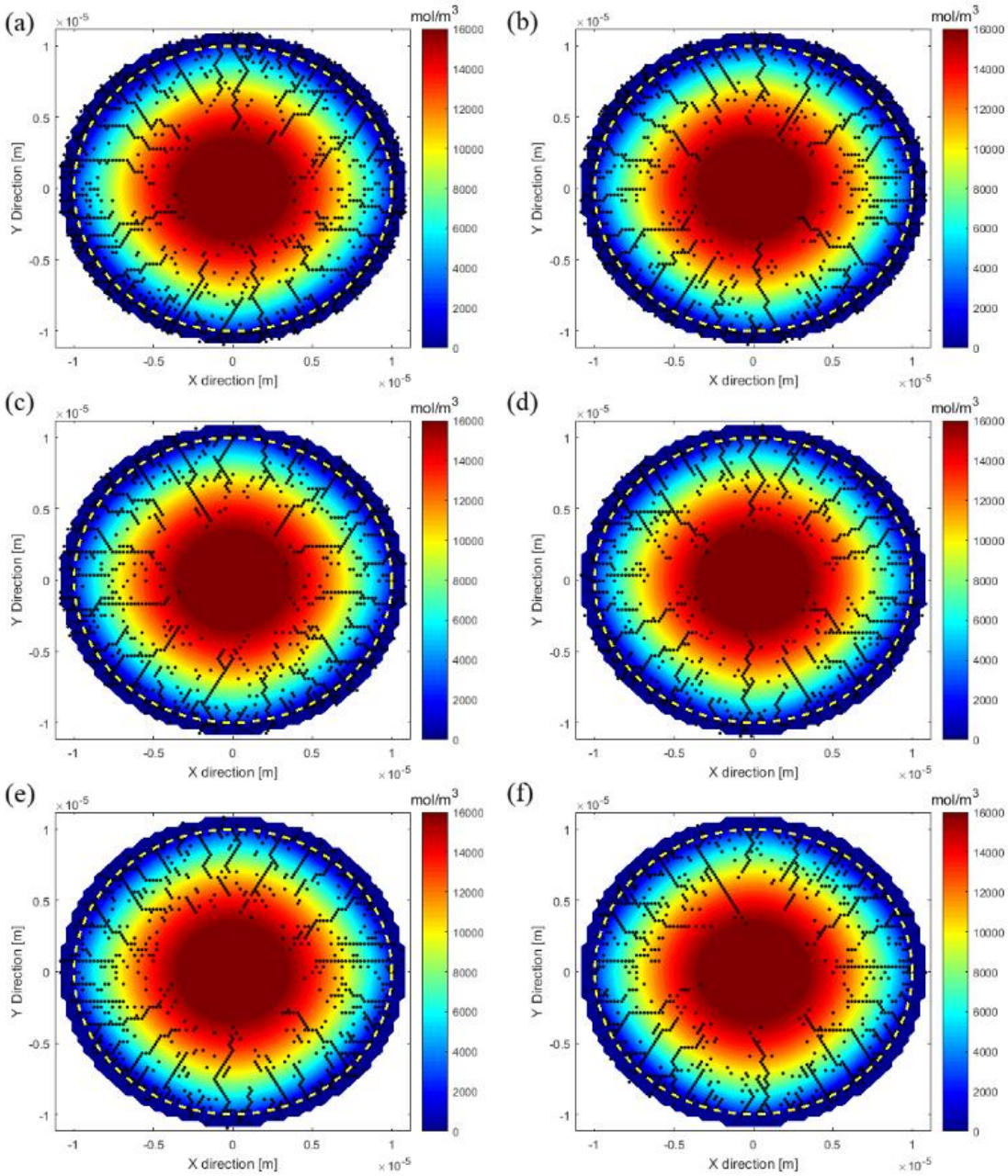

Figure 2.3 Variation of concentration contour plots as a function of film to graphite fracture energy threshold ratio, (a) $\psi_2/\psi_1 = 0.1$, (b) $\psi_2/\psi_1 = 0.2$, (c) $\psi_2/\psi_1 = 0.5$, (d) $\psi_2/\psi_1 = 1.0$, (e) $\psi_2/\psi_1 = 5.0$ and (f) $\psi_2/\psi_1 = 10.0$. The dashed yellow line indicates the graphite particle boundary. The number of broken bonds (denoted by black dots) inside the active material are relatively unaffected by the increase in film threshold energy. Hence, fracture inside active material is relatively unaffected by film threshold energy. Number of broken bonds inside film region shows drastic decrease as film threshold energy increases.

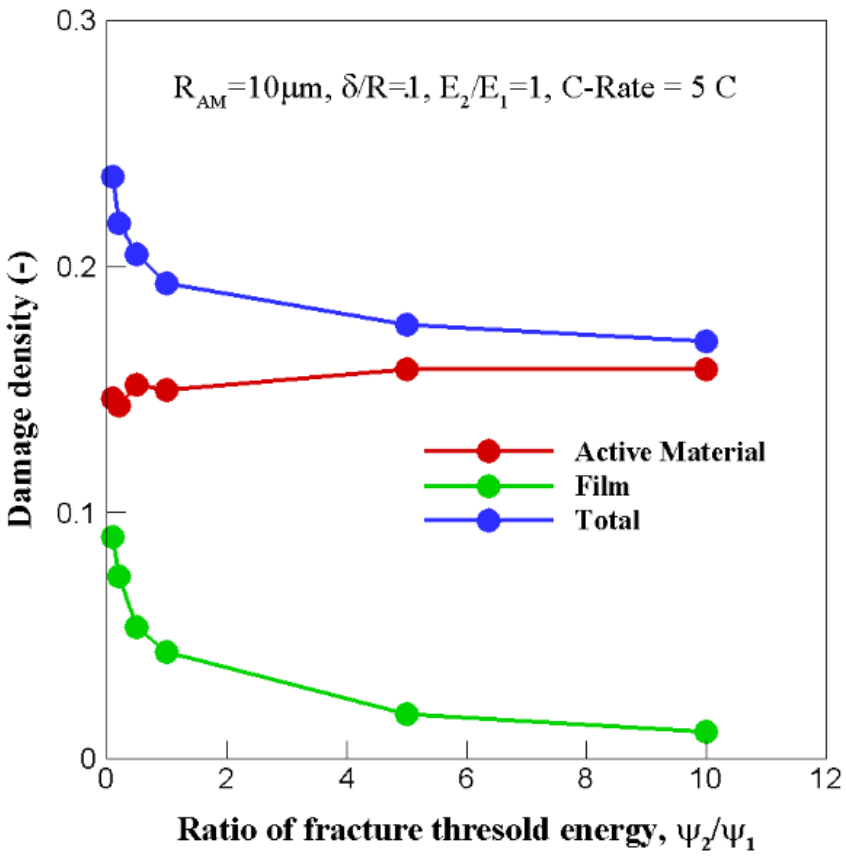

Figure 2.4 Effect of surface film fracture threshold energy on damage density inside graphite with surface film. As the ratio increases, damage density inside film decreases drastically while active material is relatively unaffected.

Effect of Film Young's Modulus

Table 2-4 and Figure 2.5 and Figure 2.6 detail the effect of changing the film Young's modulus on the fracture map. Figure 2.5 shows the superimposed damage and concentration contours inside the particle-film agglomerate. The detailed breakdown of film, graphite and total damage density variation with fracture threshold energy is displayed in Figure 2.6. Again, total number of bonds in the graphite active material (4997) and film (1056) remain the same throughout the variations explored since the size of the agglomerate system does not change.

Table 2-4 Damage density variation with film to graphite Young's modulii ratio for 10 μm graphite particle at 5 C rate for $\delta / R = 0.1, \psi_2 / \psi_1 = 1.0$. The total number of springs inside the active material is 4997 and film is 1056.

E_2/E_1	Damaged bonds in AM	Damaged bonds in film	Damage density in AM	Damage density in film	Total damage density
0.1	831	127	0.1372	0.0209	0.1582
0.2	861	168	0.1422	0.0277	0.1699
0.5	882	188	0.1457	0.0310	0.1767
1.0	938	253	0.1549	0.041	0.1967
5.0	1005	301	0.1660	0.0497	0.2157
10.0	1036	312	0.1711	0.0515	0.2227

As the film Young's modulus is increased, the fraction of broken bonds inside the film increases since more strain energy has to be released. Increased Young's modulus implies increased strain energy accumulation which leads to more number of broken bonds. A very interesting observation is that the fraction of broken bonds inside active material also shows a monotonically increasing trend with increased film's elasticity modulus. Thus, the Young's modulus of the film has a direct impact on fracture inside the active material. As the elastic modulus of film increases, damage inside the film as well as the active material increases. This positive correlation provides us with a way to reduce fracture inside active material. Using a film of lower elastic modulus will help diminish fracture damage inside the active material. Mechanical damage at high C-rates hinders diffusion and causes particle isolation which leads to capacity fade and reduced rate capabilities. Consequently, using a low elastic modulus film will improve the battery capacity and life.

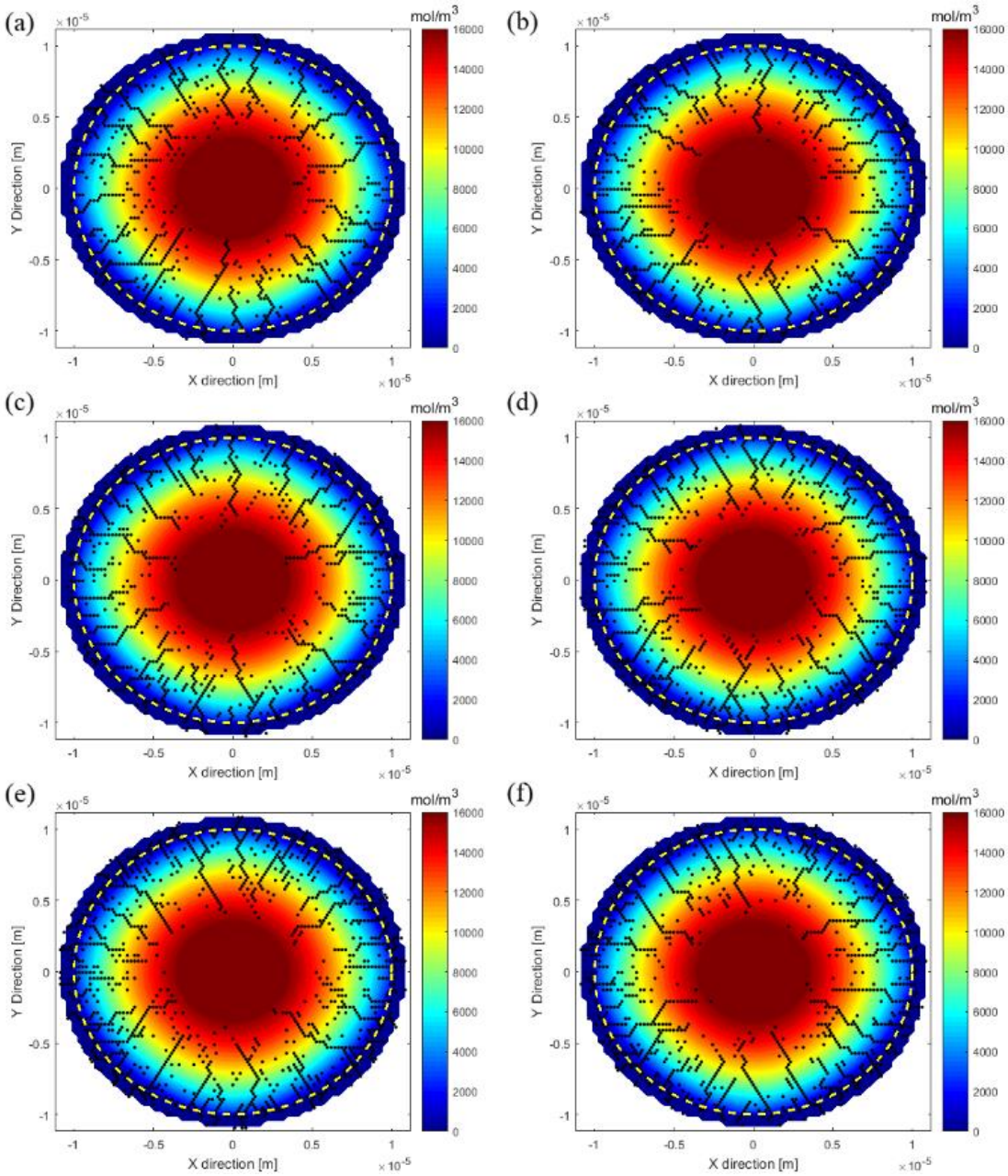

Figure 2.5 Variation of concentration contour plots as a function of film to graphite Young's moduli ratio, (a) $E_2 / E_1 = 0.1$, (b) $E_2 / E_1 = 0.2$, (c) $E_2 / E_1 = 0.5$, (d) $E_2 / E_1 = 1.0$, (e) $E_2 / E_1 = 5.0$ and (f) $E_2 / E_1 = 10.0$. The dashed yellow line indicates the graphite particle boundary. The number of broken bonds (denoted by black dots) inside the active material increases with increase in film stiffness. Hence, fracture inside active material shows a monotonically increasing trend with film Young's modulus. Number of broken bonds inside film region also shows increase with film stiffness.

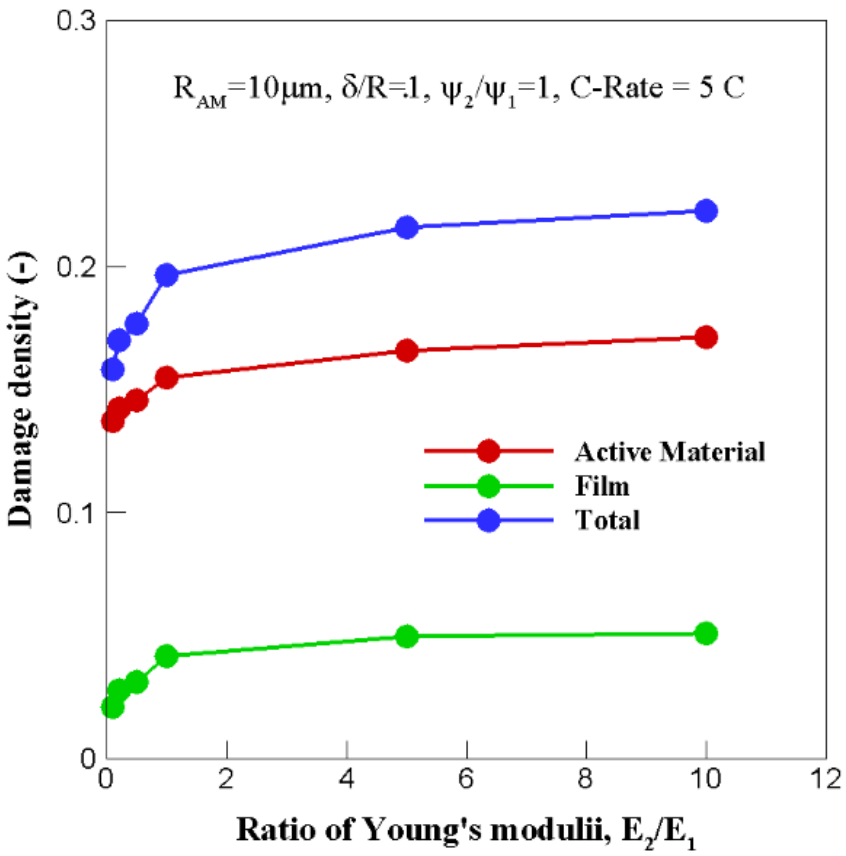

Figure 2.6 Effect of surface film Young's modulus increase on damage density inside graphite with surface film. As the ratio increases, damage density inside film as well as graphite increases.

The above results can be summed up as follows: an ideal surface film on graphite should have high fracture energy threshold and low Young's modulus. The high fracture energy threshold and low Young's modulus will reduce fracture inside film while low Young's modulus also has the additional benefit of reducing fracture inside graphite. The thickness of the film needs to be optimized such that there is a balance between the stability of the surface film (thicker films are more stable) and amount of inert material inside the electrode. Also, another clear conclusion that can be made is that only film Young's modulus has a considerable effect on fracture inside graphite active material. Film thickness and fracture energy threshold has little impact on fracture inside graphite material but dictates the fracture characteristics of the surface film.

2.3.2 Effect of Variation of Graphite Particle Size and C-rate

The variation of graphite particle size and C-rate on fracture inside active material is fairly well established for bare active material. Higher C-rates and larger particle sizes have more predilection for fracture. In this section, we establish what effect the surface film has on this fracture map. For this purpose, extensive datasets were created by doing variations of 5 C-rates (1C, 2C, 3C, 4C, 5C) and 5 particle radii (1μm, 3μm, 5μm, 7μm, 10μm) for 7 different values of $\delta / R,\ \psi_2 / \psi_1,\ E_2 / E_1$. A base case of $\delta / R = 0.5\ \psi_2 / \psi_1 = 1,\ E_2 / E_1 = 1$ is used and then we vary each of these ratios 2 times (one higher than base value and one lower than base value) to create a dataset of 175 values for damage density. The objective behind this work is to see how much the fracture map gets modified when the surface film is present and what is the extent that each of these parametric ratios affect the fracture map. The datasets are then regressed using a functional form for damage density inside graphite as a function of these parameters. Damage density (DD) is assumed to have the following functional form

$$DD = f(R, CRate, \delta / R, \psi_2 / \psi_1, E_2 / E_1) \tag{2.15}$$

The interesting observation that we find is that all the datasets can be regressed with a nice goodness of fit using only three of the above five parameters. These parameters are particle radius (*R*), *C-Rate* and film to graphite modulii ratio E_2 / E_1. This can also be intuitively explained from our observations in the previous section where we concluded that only the film Young's modulus has a considerable effect on the fracture inside graphite while film thickness and fracture threshold energy have negligible impact on graphite fracture. Building on this, we use non-linear least squares fit to find a second-degree polynomial in these parameters which accurately represent our dataset. The functional form is given below,

$$\begin{aligned} DD &= f(R, CRate, E_2 / E_1) \\ &= -0.00078868R^2 + 0.0010623R \times CRate + 0.00028628R \times E_2 / E_1 + 0.013755R \\ &\quad -0.0034473(CRate)^2 + 0.00078652 \times CRate \times E_2 / E_1 + 0.041395 \times CRate \\ &\quad -0.0028905 \times (E_2 / E_1)^2 + 0.014983 \times E_2 / E_1 - 0.062672 \end{aligned} \tag{2.16}$$

The coefficient of determination of the fit for the full dataset is 0.9884 which shows that the fit is nice. Figure 2.7 shows the corresponding fits for each of the 7 datasets varying C-rate and

graphite radius. The coefficient of determination value for each of these individual sets are also given and show that the fit is of good quality.

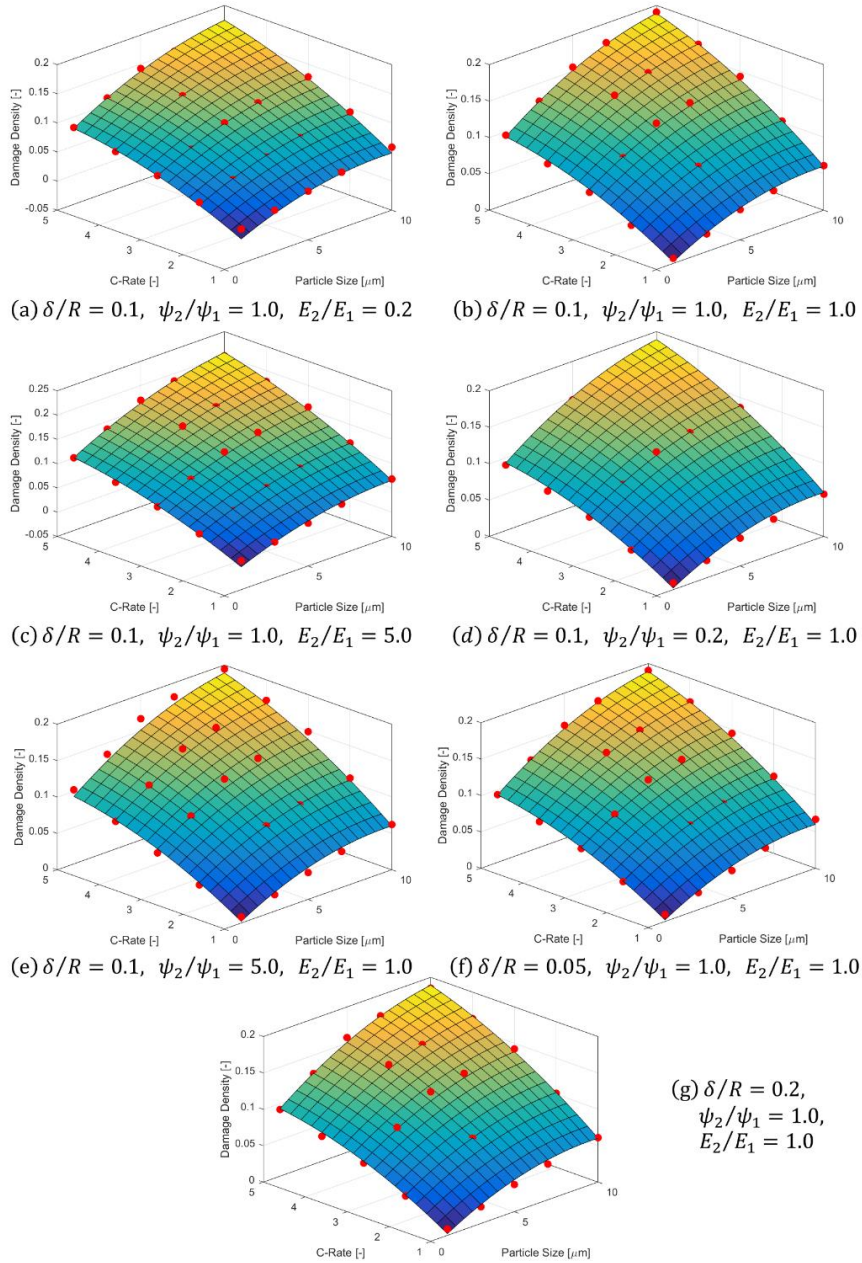

(a) $\delta/R = 0.1,\ \psi_2/\psi_1 = 1.0,\ E_2/E_1 = 0.2$ (b) $\delta/R = 0.1,\ \psi_2/\psi_1 = 1.0,\ E_2/E_1 = 1.0$

(c) $\delta/R = 0.1,\ \psi_2/\psi_1 = 1.0,\ E_2/E_1 = 5.0$ (d) $\delta/R = 0.1,\ \psi_2/\psi_1 = 0.2,\ E_2/E_1 = 1.0$

(e) $\delta/R = 0.1,\ \psi_2/\psi_1 = 5.0,\ E_2/E_1 = 1.0$ (f) $\delta/R = 0.05,\ \psi_2/\psi_1 = 1.0,\ E_2/E_1 = 1.0$

(g) $\delta/R = 0.2,$ $\psi_2/\psi_1 = 1.0,$ $E_2/E_1 = 1.0$

Figure 2.7 Nonlinear regression fit for damage density in graphite active particle as a function of graphite particle radius, C-rate and film to graphite Young's modulus ratio. The coefficient of determination for the explored variations are (a) $R^2 = 0.9799$, (b) $R^2 = 0.9951$, (c) $R^2 = 0.9928$, (d) $R^2 = 0.9831$, (e) $R^2 = 0.9807$, (f) $R^2 = 0.9926$ and (g) $R^2 = 0.9909$ For variation of Young's modulus, we see a change in the level of fracture as can be seen from the maximum damage density axis values variation. For other film property variations, the variation is minimal and hence they do not show up in the regression function.

2.3.3 Fracture Phase Map

Figure 2.8 shows the fracture phase maps in with variation of film to particle Young's modulus ratio, fracture threshold energy ratio and size ratio. Young's modulus has a significant impact on fracture as is evident by the increase in the red zone with increase in Young's modulus ratio. Consequently, controlling the stiffness of the surface film to low values has desirable advantage of mitigating fracture inside the active material. Film thickness and fracture threshold energy have relatively little impact on fracture inside the graphite active material but have direct bearing on the fracture in the surface film.

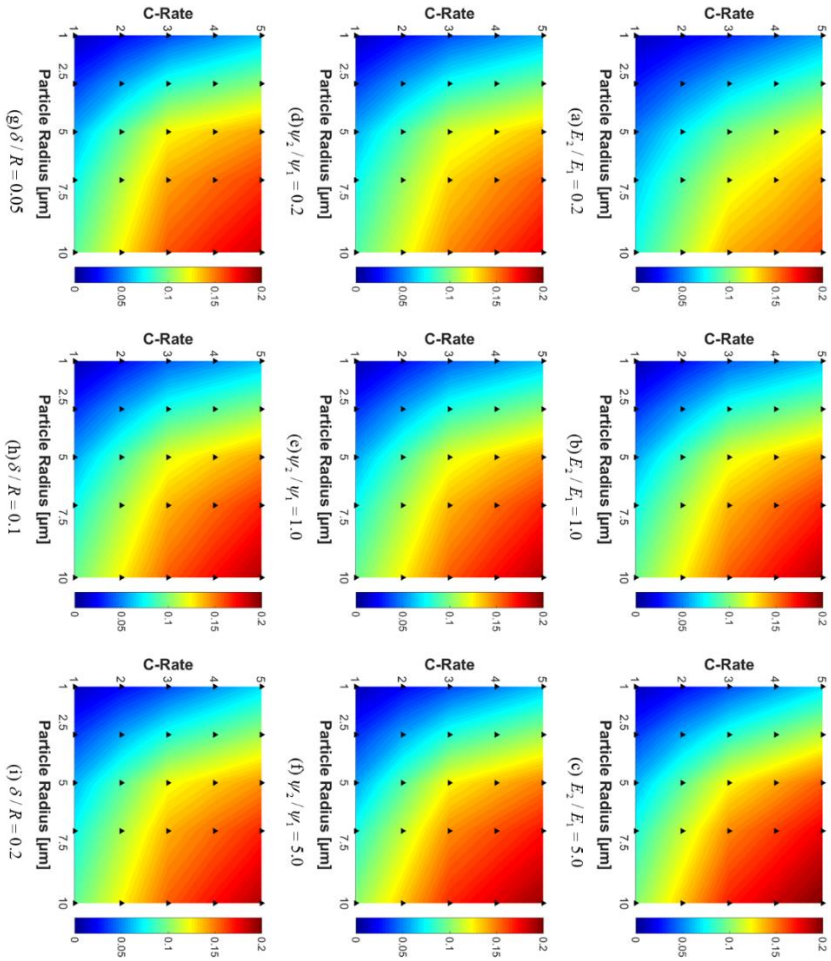

Figure 2.8 Fracture phase map variation with film to graphite Young's moduli ratio, (a) $E_2 / E_1 = 0.2$, (b) $E_2 / E_1 = 1.0$, (c) $E_2 / E_1 = 5.0$, film to graphite fracture threshold energy ratio, (d) $\psi_2 / \psi_1 = 0.2$, (e) $\psi_2 / \psi_1 = 1.0$, (f) $\psi_2 / \psi_1 = 5.0$, film to graphite size ratio, (g) $\delta / R = 0.2$, (h) $\delta / R = 1.0$, (i) $\delta / R = 5.0$. As the Young's modulus of film is increasing, the red zone increases showing higher propensity of damage. Fracture threshold energy and film thickness to particle size ratio have less impact on the phase map.

2.3.4 Performance of Graphite Anode with Surface Film

Figure 2.9 compares the cycling performance of a 10 μm graphite particle with and without surface film. We perform initial cycling of the LCO-graphite system at C/5 for 3 cycles, to mimic the formation cycling protocol for lithium-ion batteries. At the end of the formation cycles, a final charge-discharge cycle at 5C is performed and the discharge performance at first and fourth cycles are compared for the variation of surface film to graphite active material Young's modulus ratio. Positive electrode is taken as lithium cobalt oxide with no fracture assumption inside the positive electrode particle. The Young's moduli ratio is varied by four orders of magnitude to ascertain its impact on performance, $E_{film}/E_{AM} = 0.01$ to $E_{film}/E_{AM} = 100$.

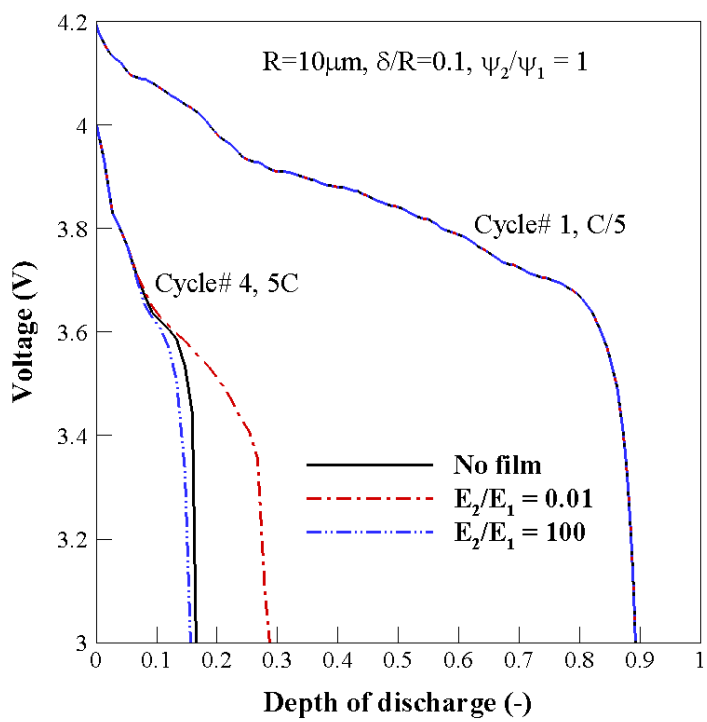

Figure 2.9 Performance of graphite anodes with and without surface film for 10 μm particle for initial low rate C/5 formation cycle discharge and fourth cycle high rate 5C discharge. At high C-rates, low Young's modulus of surface film leads to improved performance due to lesser amount of crack formation.

The results illustrate the negligible impact of fracture at low rate cycling (C/5) where the performance curves with and without surface film show no variation and collapse onto each other.

At low C-rates, the concentration gradient inside the particle is small and consequently diffusion induced stresses are miniscule. Strain energy accumulation is insufficient to break the bonds leading to negligible fracture scenario. Thus, lithium ion battery performance is unaffected by surface film property modification at low C-rates. The fourth cycle discharge performance at 5C shows significant variation with surface film property modification due to the inception of fracture at high C-rates. Low Young's moduli ratio ($E_{film}/E_{AM} = 0.01$) graphite particle- surface film agglomerate performs much better than the graphite particle with no film as well as the high stiffness ratio case $E_{film}/E_{AM} = 100$. This further validates the hypothesis that softer surface film can improve the performance of LIBs as it mitigates the fracture tendencies of the active material.

2.3.5 Effect of Graphite Morphology and Surface Conditions

The results obtained thus far have utilized the spherical particle assumption and traction free boundary conditions on the particle surface. However, in a functioning anode, the particle morphology can show wide variation as well as the particles are combined into a complex network that provide significant mechanical constraint to any given particle. To ascertain the impact of varying particle morphology and boundary effects on fracture characteristics, we have performed mechano-electrochemical simulations for ellipsoidal (oval in 2D) and spherical particles (circle in 2D) and contrasted the obtained results. Further, the network effect is incorporated by considering fixed displacement boundary conditions on the spherical particle surface and the results are juxtaposed alongside the traction free boundary condition simulation results to delineate its impact.

Impact of Particle Morphology on Fracture

Coupled electrochemical-mechanical charge-discharge simulations are performed for spherical particle with radius $R = 12.5\,\mu m$ and an oval particle with major and minor dimensions $A = 15\,\mu m$, $B = 10.4167\,\mu m$ respectively for C-rate 2C and ambient temperature 25˚C. The operating conditions as well as the area of the spherical and oval particles are kept the same so as to ensure homologous geometric $\left(\pi R^2 = \pi AB\right)$ and operating conditions for delineating the impact of aspect ratio. Figure 2.10 shows the obtained damage profile superimposed on the concentration contour plots for the anode (a) spherical particle and (b) oval particle

$(A = 15\,\mu m,\ B = 10.4167\,\mu m)$ at the end of first cycle discharge and charge. Damage is predominantly observed along the major axes in the oval particles (along x axis for oval particle) while the damage shows no preferred directional dependence for the spherical particle. Larger diffusional transport length for the Li atoms along the major axes for the oval particles leads to higher concentration gradients along that direction. Consequently, increased magnitude of diffusion induced stresses along this direction leads to higher propensity for fracture as is evident from the damage contour plots.

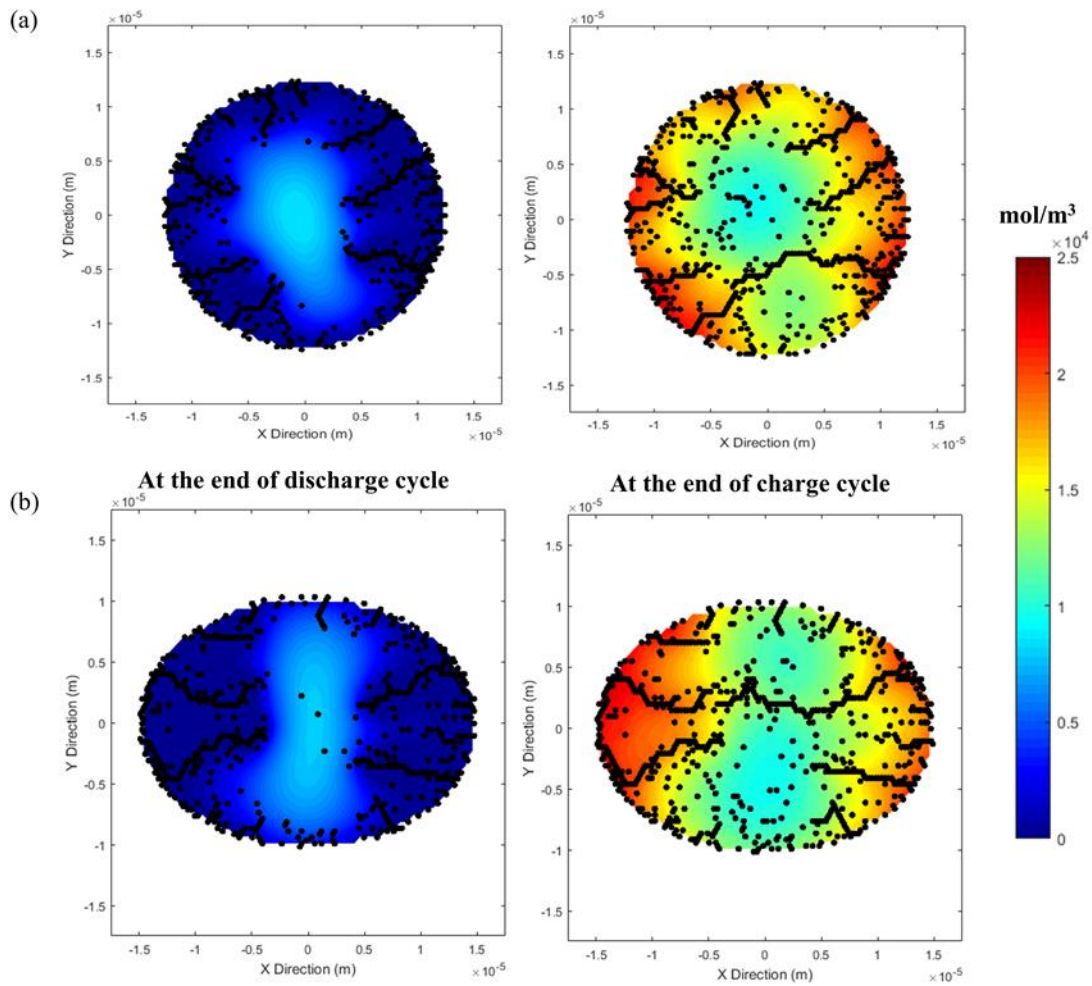

Figure 2.10 Demonstration of coupled electrochemical-mechanical charge discharge simulations performed on: (a) spherical particle of radius $R = 12.5\,\mu m$, and (b) An oval shaped particle with $A = 15\,\mu m$ and $B = 10.4167\,\mu m$ as the major and minor axes, respectively. Discharge and charge steps have been conducted at 2C rate and ambient temperature of 25^0C. The oval particle demonstrates higher microcrack density along the major axis due to larger magnitudes of concentration gradient and diffusion induced stress.

Impact of Particle Surface Boundary Condition on Fracture

Figure 2.11 compares the damage contours superimposed on the concentration profiles for spherical particle with traction free boundary condition prescribed at the surface versus spherical particle with zero displacement boundary condition imposed at the particle surface. The particle radii as well as the operating conditions are the same for both simulations differing only in the implementation of the boundary conditions. With traction free boundary condition, lesser damage is observed in the electrode particle as is evident by the smaller damage density (black dots) inside the electrode particle at the end of the discharge-charge step. Constrained particles develop larger stresses because of additional contact stress in conjunction with the diffusion induced stresses inside the particle.

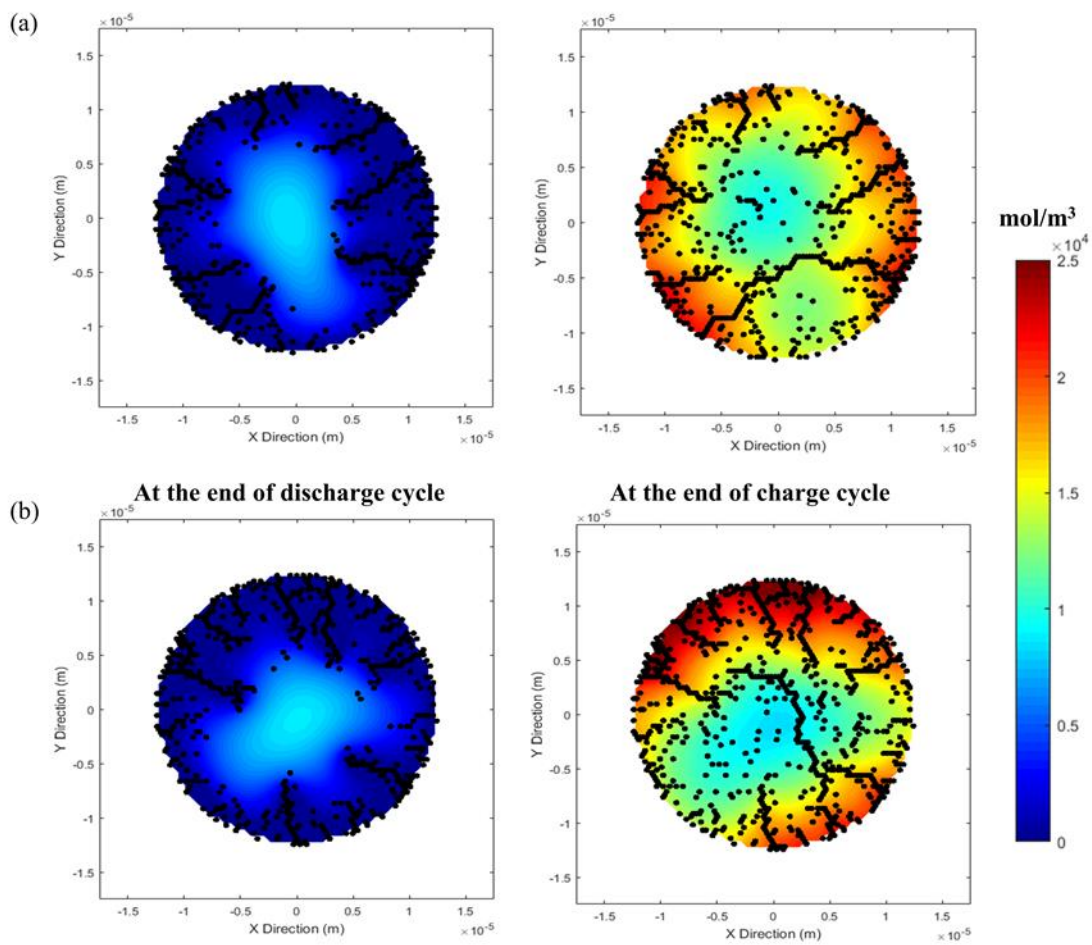

Figure 2.11 Comparison between evolution of concentration and microcracks for: (a) Free boundary, and (b) Fixed boundary case. Two particles of radius 12.5μm have been delithiated and lithiated successively at 2C with the two different free and fixed boundary conditions. Due to the presence of extra boundary constraints, the particle shown in (b) is incapable of releasing its strain energy, which led to enhanced microcrack formation within the active particle.

2.4 Conclusions

The work here elucidates clearly what mechanical effects a surface film has on a graphite active particle during delithiation. It shows that film can have a beneficial effect on avoiding fracture inside the active material if it fulfils certain characteristics like low Young's modulus. In summary, the following deductions can be made:

- Film thickness to particle size ratio and fracture threshold energy ratio of surface film to particle has low impact on fracture inside the active material.
- Low Young's modulus ratio of surface film to active particle is desirable to mitigate fracture inside the active material. Thus, a secondary phase film comprising of binder and conductive additive which exhibits small elastic modulus is beneficial for suppressing mechanical damage inside the active material.
- Damage density inside the active material can be modelled as a function of particle size, C-rate and film to particle Young's modulus ratio. Small particle size, low C-rate operation and low Young's modulus ratio is recommended for reducing fracture damage.
- Film threshold energy should be high so that film breakdown is mitigated.
- Film thickness should be optimized so that film fracture is minimal as well as inert film material is small.

3. MECHANO-ELECTROCHEMICAL INTERACTION AND DEGRADATION IN SILICON ELECTRODE

Relevant Publications and/or Working Papers

1. **A. Verma,** P.P. Mukherjee**,** "*Mechanistic Analysis of Mechano-Electrochemical Interaction in Silicon Electrodes with Surface Film"*, Journal of Electrochemical Society **164** (14), A3570-A3581 **(2017)**
2. D.E. Galvez-Aranda, **A. Verma**, K. Hankins, J.M. Seminario, P.P. Mukherjee, P.B. Balbuena, "*Chemical and Mechanical Degradation and Mitigation Strategies for Si Anodes: Multiscale Modeling*", Journal of Power Sources, **419**, 208-218 **(2019)**
3. **A. Verma,** A. Franco, P.P. Mukherjee, "*Mechanistic Elucidation of Si Particle Morphology on Electrode Performance*", Journal of Electrochemical Society **165** (15), A3852-A3860 **(2019)**

3.1 Mechanistic Analysis of Mechano-Electrochemical Interaction in Silicon Electrodes with Surface Film

3.1.1 Background

Lithium ion battery (LIB) technology has become the prevalent energy storage and supply system for portable electronics [146]. In recent years, the application of LIBs is extending to large scale applications such as electric vehicles [161-163], commercial aircrafts [4, 7] and grid energy storage [128, 129]. The widespread usage of LIBs in high energy and power applications is predicated on robust improvement of energy and power densities afforded by the LIB which is directly correlated with the anode [128, 164] and cathode [6, 165] active materials utilized. Current commercial batteries use graphite [130] as anode and lithium cobalt oxide / lithium nickel manganese cobalt oxide [131, 132] as cathode material . Graphite exhibits a maximum specific capacity of 372 $mAh/g_{graphite}$ while the current cathode materials are limited to a maximum of 200 mAh/g_{AM}. These chemistries have been utilized in electric vehicle batteries, however, the low capacity necessitates use of bulky and expensive battery packs to power the vehicle which form the major impediment to commercialization of electric vehicles.

Extensive efforts have been invested in identifying high capacity anode and cathode materials for usage in next generation lithium ion batteries [134]. Silicon has been the focus of several researchers as an anode material owing to its high theoretical specific capacity of 4200 mAh/g_{Si}, approximately ten times that of graphite [133, 135, 136]. This high capacity is a result of

large lithium intercalation ability of silicon as compared to graphite; a silicon atom can intercalate a maximum of 4.4 atoms of lithium ($Li_{4.4}Si$) while graphite can accommodate a maximum of 1 lithium atom per graphite molecule (LiC_6) [166]. However, experimental analysis of silicon anode lithium ion battery has revealed much lower capacities (~75% of the theoretical capacity) during initial cycles [132] as well as rapid capacity degradation with charge-discharge cycling. Capacity fade of the order of 20% is observed within the first 50 cycles [167, 168].

This severe capacity fade is a direct consequence of the high volumetric expansion and contraction of silicon particles during lithiation and delithiation respectively [169]. While graphite particles exhibit a total volumetric expansion of 10% during lithium insertion [168] , silicon particles can expand up to around 300% with full lithiation [139]. This intercalation induced strain gives rise to crack initiation and fracture within the silicon active material [139]. Additionally, it also leads to rupture of the solid-electrolyte interphase (SEI) layer formed on the silicon surface which is unable to accommodate this high volumetric expansion. This results in fresh contact between the electrolyte and active material particle surface resulting in reformation of the SEI layer leading to loss of cyclable lithium inventory [113, 170, 171]. Severe fracture inside active material also leads to particle isolation and reduced lithium intercalation ability contributing to capacity fade.

Experimental as well as computational methodologies have been used to investigate transport kinetics and stress generation inside high capacity anode active materials [172-175]. Lithium ion transport through two phase diffusion mechanism has been reported to be the contributing factor towards pulverization of silicon anodes [176]. Two phase diffusional lithium transport dictates the first lithiation of the silicon active particle involving the conversion of crystalline silicon (Si) to amorphous lithiated silicon (Li_xSi). Subsequent delithiation-lithiation can be modelled as a single-phase diffusion process governed by the Fick's law of diffusion [174, 177, 178]. The Cahn-Hilliard formulation based two phase transport model has been utilized by Chen et al. to model combined lithium diffusion and motion of the two-phase interface [179]. A similar formulation is adopted to capture two-phase diffusion in silicon in the current study.

Silicon anodes have been extensively probed computationally for the large volume expansion and subsequent stress generation [179-181]. Propagation of nucleated cracks in thin film silicon electrodes and silicon nanowires during the lithiation-delithiation process has been studied to identify the critical size [179, 182]. Deshpande et al. has elucidated the impact of surface

energy in mitigating fracture inside nanowire silicon electrode structures with high surface area to volume ratio [177]. Large elastic-plastic deformation of silicon has been incorporated in a few computational studies [183, 184]. Lattice spring model based high volume expansion modeling has been shown to replicate the deformation of silicon and tin electrodes [185, 186]. However, there are no detailed numerical analyses investigating the effect of the diffusion mechanism on fracture tendencies inside silicon particle with surface film mimicking solid electrolyte interphase or secondary phase layer.

In this work, we have extended the computational methodology developed in our group [51, 182] to analyze and contrast the effect of the diffusion mechanism on the fracture methodology inside silicon active material with a surface film. Lithiation of crystalline silicon via two-phase diffusion process has been reported to cause large strain inhomogeneity between lithium rich and lithium poor phase exacerbating fracture. We investigate if the change in the nature of the diffusion process for completely amorphous silicon can mitigate fracture tendencies inside the silicon particle. Surface film geometry and mechanical properties variation are also scrutinized to delineate their impact on the fracture map. Thus, a comparative analysis has been conducted to determine the changes in fracture pattern attributed to the nature of the diffusion process. Based on the results obtained, different techniques that are capable of minimizing the overall mechanical degradation of high capacity anode materials will also be investigated.

The rest is divided as follows. The details of the model physics are given in the following Methodology section. Two-phase and single-phase diffusion dynamics and corresponding fracture mechanics for silicon particle with film is elaborated. The Results and Discussion section elucidates the effect of diffusion mechanism and surface film geometric and mechanical properties on the fracture behavior. Finally, a fracture phase map for silicon particle as a function of particle size and C-rate is demonstrated and the results are summarized in the Conclusion section.

3.1.2 Methodology

The problem formulation involves modeling of two coupled physical phenomenon, solid-state diffusion of lithium inside the active material particles and the resulting mechanical behavior involving large deformation, stress and fracture. The mechanical behavior is elucidated using a two-dimensional random lattice spring formulation with diffusion transport computed on a juxtaposed spherical coordinates computational grid. The complexity of the approach is in the

accurate mapping of the field variables (like concentration) from the spherical grid to the spring network while accounting for large deformation of the spring network. The approach has previously been demonstrated for pristine low volumetric expansion active material like graphite [17, 19, 151, 178] and high capacity electrode active material particles like silicon and tin with two-phase diffusion [83, 151]. In this work, we extend the model to do a comparative analysis of the fracture map for two-phase versus single phase diffusion inside silicon while accounting for the presence of a surface film by adding an additional layer of springs with spring stiffness different from the active material to investigate the resulting change in fracture map.

At the single particle level, the rate determining transport mechanism is the solid-state diffusion inside the active material. The electrolyte ionic diffusivity and conductivity is assumed to be high enough to neglect concentration and potential gradients inside the electrolyte. Therefore, the active material is subjected to constant flux from all directions irrespective of its position from the current collector under galvanostatic operation. Two-phase diffusion inside the electrode particle is modeled using the Cahn-Hilliard equation provided in Equation (3.1) [59]. The corresponding single-phase diffusion formulation based on Fick's law is given in Equation (3.2) [150].

$$\frac{\partial \hat{c}_s}{\partial t} = \nabla . M_{Li}\left(\hat{c}_s\right)\nabla\left\{c_{s,max}RT\left[\omega\left(1-2\hat{c}_s\right)+\ln\frac{\hat{c}_s}{1-\hat{c}_s}\right]-\kappa\nabla^2\hat{c}_s\right\} \tag{3.1}$$

$$\frac{\partial \hat{c}_s}{\partial t} = \nabla\left(D_s\nabla\hat{c}_s\right) \tag{3.2}$$

Symmetry boundary condition is applied at the particle center (Equation (3.3)) and constant flux boundary condition is applied at the particle surface (Equations (3.4) and (3.5). The particle surface boundary condition form manifests differently for the two-phase and single-phase models while the symmetry boundary condition form is the same for both models.

$$\text{Two-Phase and Single-Phase}: \left.\frac{\partial \hat{c}_s}{\partial r}\right|_{r=0} = 0 \tag{3.3}$$

$$\text{Two-Phase: } M_{Li}\left(\hat{c}_s\right)\nabla\left\{c_{s,max}RT\left[\omega\left(1-2\hat{c}_s\right)+\ln\frac{\hat{c}_s}{1-\hat{c}_s}\right]-\kappa\nabla^2\hat{c}_s\right\}\Bigg|_{r=R_p} = \frac{I_{applied}}{SF} \tag{3.4}$$

$$\text{Single-Phase: } D_s\nabla\hat{c}_s\Big|_{r=R_p} = \frac{I_{applied}}{SF} \tag{3.5}$$

Here $\hat{c}_s$ is the non-dimensional concentration variable, defined as $\hat{c}_s = \frac{c_s}{c_{s,\max}}$, where c_s denotes the molar concentration of lithium within the active material and $c_{s,\max}$ corresponds to the maximum intercalated amount of lithium in the active material. M_{Li} is the mobility of lithium with functional dependence on concentration, defined as $M_{Li} = \frac{D_{Li}}{c_{s,\max} RT}\left(\hat{c}_s\left(1-\hat{c}_s\right)\right)$, where D_{Li} corresponds to the diffusivity of lithium, R is the universal gas constant and T is temperature in Kelvin. The dimensionless parameter ω controls the shape of the double-well energy function characterizing the lithium-rich and lithium-poor phases. The parameter κ modulates the contribution of the large concentration gradient at the two-phase interface to the free energy. Numerical solution of the Cahn-Hilliard model requires simplification of the fourth order governing differential equation into two coupled second order equations which are solved iteratively. Comparatively, the Fick's law formulation for single-phase diffusion is relatively straightforward as it leads directly to a single second order governing differential equation.

The concentration equations are further discretized using finite volume approach on a spherical grid. It is only solved for in the active material domain. The film domain is assumed devoid of concentration gradients and experiences stress from the active material swelling/shrinking during lithiation/delithiation. Consequently, a nominal concentration of zero is assigned to the surface film layer and only mechanics is solved for in the film layer.

A modified lattice spring model capable of incorporating both large and small deformation is utilized to capture mechanical degradation inside the silicon anode with film. Detailed illustration of the lattice spring methodology amalgamating large deformation has been provided in Barai et al [17, 19]. The salient features of this framework are summarized here along with the modifications required to incorporate surface film mechanics.

The governing virtual work expression utilized for this model is given in Equation (3.6)[151].

$$\int_{{}^{t}V} {}^{t+\Delta t}_{\ \ t}S_{ij}\,\delta\,{}^{t+\Delta t}_{\ \ t}\varepsilon_{ij}\,d^{t}V - \int_{{}^{t}A} {}^{t+\Delta t}_{\ \ t}F_{i}\,\delta\,{}^{t+\Delta t}_{\ \ t}u_{i}\,d^{t}A = {}^{t+\Delta t}R \tag{3.6}$$

Here ${}^{t}V$ and ${}^{t}A$ signify the volume and area at the previous equilibrium configuration, ${}^{t+\Delta t}_{\ \ t}S_{ij}$ is the 2nd Piola-Kirchoff stress tensor, ${}^{t+\Delta t}_{\ \ t}\varepsilon_{ij}$ is the Green-Lagrange strain tensor, ${}^{t+\Delta t}_{\ \ t}F_{i}$ is the external force, ${}^{t+\Delta t}_{\ \ t}u_{i}$ is the displacement and ${}^{t+\Delta t}R$ is the residual. First term on the LHS represents

the internal energy while the second term denotes the energy due to external loads. There are no external forces considered $\left({}^{t+\Delta t}_{\ \ t}F_i = 0\right)$ in our present model, with the entire load coming from the internal diffusion and expansion induced stress. Equilibrium configuration is solved for using residual minimization which signifies the balancing of the internal and external forces. The expanded form of the Green-Lagrange strain tensor is given in indicial notation by Equation (3.7) [182].

$$ {}^{t+\Delta t}_{\ \ t}\varepsilon_{ij} = \frac{1}{2}\left(\frac{\partial_t u_i}{\partial x_j} + \frac{\partial_t u_i}{\partial x_j} + \frac{\partial_t u_k}{\partial x_i}\frac{\partial_t u_k}{\partial x_j} \right) \tag{3.7} $$

Here, ${}_t u_i$ signifies the displacement from time step t to $t+\Delta t$ and x_j corresponds to the spatial coordinate. Linear elastic relation is considered between the second Piola-Kirchoff stress and Green-Lagrange strain along the axial direction given by Equation (3.8) [151, 174].

$$ {}^{t+\Delta t}_{\ \ t}S_{11} = E.{}^{t+\Delta t}_{\ \ t}\varepsilon_{11} \tag{3.8} $$

The Young's modulus, denoted by E, assumes different values for the active material and surface film. Other mechanical properties like Poisson's ratio and fracture threshold energy also assumes different values for silicon [17] and film [187]. Correspondingly, an indicator function is used to identify the different material phases. The large volume expansion based lattice spring model is applied to the silicon active material domain while small deformation based lattice spring model mechanics is assigned to the film layer.

Microcrack formation is governed by the strain energy accumulation inside the spring element as the element deforms. If the element energy exceeds its fracture threshold, it is considered broken, and irreversibly removed from the lattice network. The strain energy of a spring element is estimated by Equation (3.9).

$$ \psi_e^{n+1} = \psi_e^n + \frac{1}{2}\Delta\vec{f}\cdot\Delta\vec{u} \tag{3.9} $$

The incremental internal force and displacement of the lattice spring element is denoted by $\Delta\vec{f}$ and $\Delta\vec{u}$ respectively. ψ_e^{n+1} and ψ_e^n represent the strain energy at the current and previous equilibrium configuration. Removal of the spring from the network is accomplished by neglecting its contribution to the stiffness matrix for subsequent force deformation analysis. The load carried by the broken spring is redistributed amongst the neighboring elements resulting in stress concentration effects. In this way, rupturing of the spring elements leads to the nucleation of microcracks which can further coalesce together to form spanning cracks.

3.1.3 Results and Discussion

Figure 3.1(a) shows a representative contour map of the anode active material surrounded by film which is being studied here. The investigation into the mechano-electrochemical interactions of active material and film requires accurate quantification of the mechanical properties of individual layers. These parameters include Young's modulus, Poisson's ratio, mean fracture energy threshold per unit area and expansion coefficient. The mean fracture threshold energy per unit area is an indicator of the amount of strain energy that the material can absorb without breaking. If the strain energy exceeds this threshold, crack nucleation is initiated. The elastic modulus of the material directly relates to the amount of fracture damage inside the material, hence material with high Young's modulus will have a greater propensity for fracture provided the fracture threshold energy for both the materials is the same. Material parameters for silicon active material and surface film (SEI/secondary phase) are reported in Table 3-1. In addition, the table also lists the diffusion coefficient for Li in silicon and the nominal spherical silicon active material size.

Table 3-1 List of transport and mechanical parameters for silicon and surface film.

Parameter	Symbol	Value	Reference
Diffusivity	D_{Li} (m^2/s)	2×10^{-12}	[188]
Maximum lithium concentration	$c_{s,max}$ (mol/m^3)	29.52×10^4	[187]
Density	ρ_{Si} (kg/m^3)	2200	-
Temperature	T (K)	300	-
Non-dimensional enthalpy of mixing	ω (-)	2.6	[188]
Gradient energy coefficient	κ (J/m)	2.0×10^{-9}	[189]
Young's modulus of amorphous silicon	E_{aSi} (GPa)	45.0	[189]
Young's modulus of crystalline silicon	E_{cSi} (Gpa)	90.0	[190]
Young's modulus of surface film	E_{film} (GPa)	66.0	[182]
Fracture threshold energy of amorphous silicon	$\Psi_{t,aSi}$ (J/m^2)	5.0	[182]
Fracture threshold energy of crystalline silicon	$\Psi_{t,cSi}$ (J/m^2)	10.0	[182]
Fracture threshold energy of surface film	$\Psi_{t,film}$ (J/m^2)	10.0	-

Concentration Profile in Amorphous and Crystalline Silicon with Film

Figure 3.1 (b-e) shows the concentration contour plots for lithiation of a 500 nm amorphous silicon particle with 50 nm surface film thickness via the single phase diffusion process at 1C current rate. The 1C current density is computed based on the theoretical specific capacity of silicon (4200mAh/g). Thus, the current density is calculated as

$$i = \frac{4200\left(\frac{\mathrm{A}}{\mathrm{kg}}\right)\cdot \rho_{Si}\left(\frac{\mathrm{kg}}{\mathrm{m}^3}\right)\cdot \frac{4}{3}\pi R_p^{\,3}\left(\mathrm{m}^3\right)}{4\pi R_p^{\,2}\left(\mathrm{m}^2\right)} = 1400\cdot \rho_{Si}\cdot R_p\ (\mathrm{A/m^2}) \tag{3.10}$$

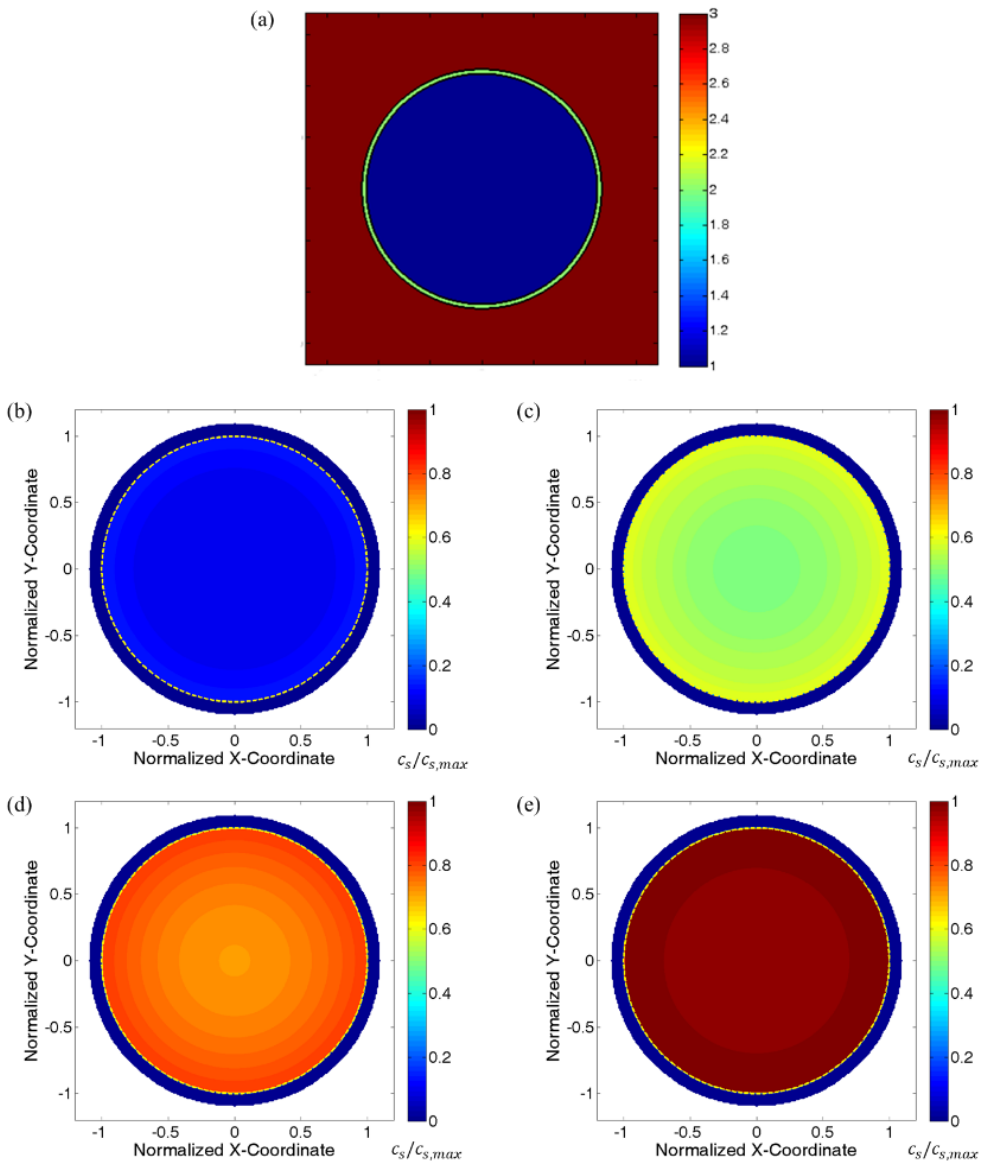

Figure 3.1: (a) Material contour map (indicator function) for spherical active material with surface film on top, 1 – Active Material, 2 – Surface Film, 3 – Electrolyte. (b-e) Concentration contour plots during lithiation of amorphous silicon with film (single phase diffusion) at 1C rate at different times (b) t = 0.05, (c) t = 0.35, (d) t = 0.65 and (e) t = 0.95. The silicon particle boundary is delineated with a dashed yellow line. Smooth transition of concentration with radius inside silicon can be seen due to single phase diffusion mechanism. Film layer is devoid of concentration gradients and is assigned a nominal zero concentration

The silicon particle boundary is delineated by the dashed yellow line beyond which lies the surface film. From the plots, it is evident that the concentration varies across the silicon particle

during lithiation while the surface film layer exhibits a nominal zero concentration. For the completely amorphous silicon particle, smooth transition of concentration with particle radius is observed, thereby revealing the single-phase diffusion mechanism governed by Fick's law. At the end of lithiation $\left(t^{*}=1\right)$, normalized concentration across the entire particle reaches close to unity, thereby indicating that the particle is now full of lithium.

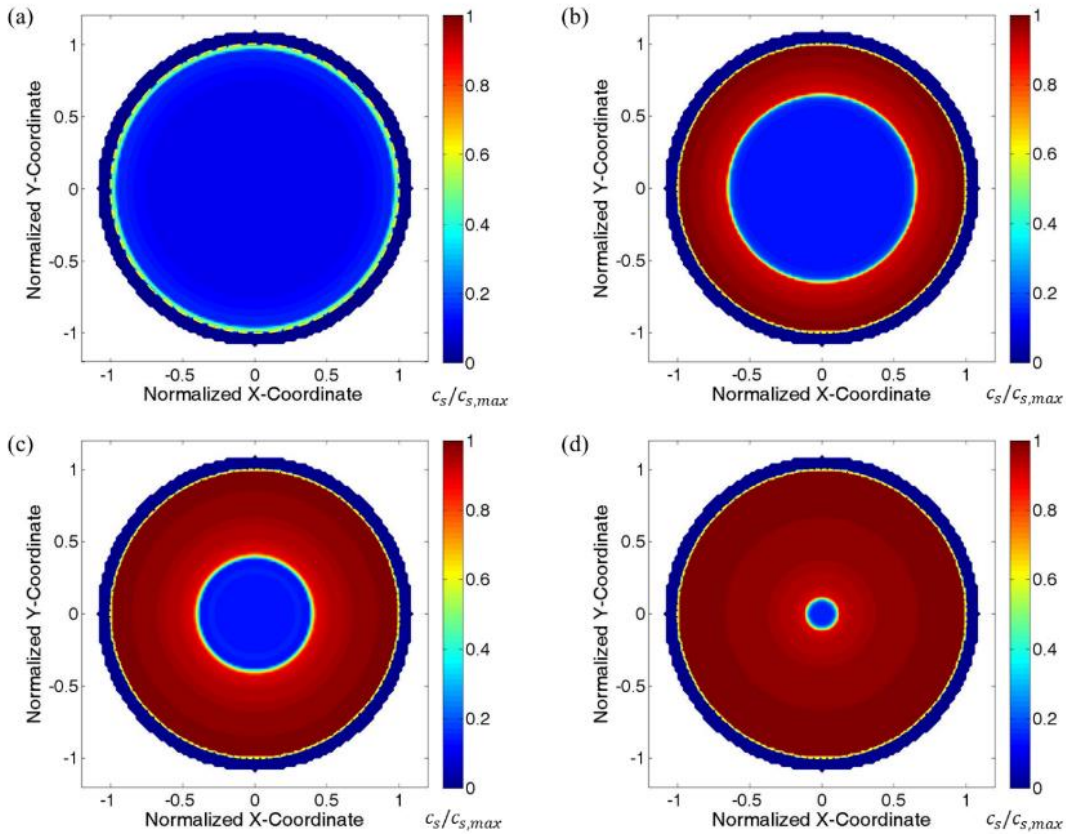

Figure 3.2: Concentration contour plots during lithiation of crystalline silicon with film (two phase diffusion) at 1C rate at different times (a) t = 0.05, (b) t = 0.35, (c) t = 0.65 and (d) t = 0.95. The silicon particle boundary is delineated with a dashed yellow line. Presence of a sharp interface exhibits the two-phase diffusion mechanism. Film layer is devoid of concentration gradients and is assigned a nominal zero concentration.

Figure 3.2 demonstrates the concentration contour plots for lithiation of an equivalent 500 nm crystalline silicon particle with 50 nm surface film through two-phase diffusion mechanism at 1C current rate. The formation of a two-phase interface, across which sharp change in concentration occurs, is observed. As lithium ions move into the silicon particle, lithium rich phase forms at the surface while the lithium poor phase exists beyond the sharp two-phase interface close

to the center of the particle. The interface moves inward as the lithiation progresses and reaches close to the center of the particle at the end of lithiation. The lithiation profile reveals the two-phase diffusion mechanism governed by the Cahn-Hilliard formulation. Again, the surface film (beyond the dashed yellow line) is assigned a nominal concentration of zero. Lithium diffusion inside the surface film is not considered with the focus aimed at understanding the mechanical response of the silicon and film system.

Damage Profile in Amorphous and Crystalline Silicon with Film

Figure 3.3 and Figure 3.4 demonstrate the damage profile within amorphous and crystalline silicon with film respectively during a single lithiation. This corresponds to the single-phase vs two phase lithiation profiles shown in Figure 3.1 and Figure 3.2 respectively and will help in discerning the dominant mechanisms leading to system fracture. The figures show the evolution of the lattice spring representation of the silicon active material (shown in blue) and surface film (shown in red) cluster. Fracture is interpreted as the missing bonds (white space) in the blue and red lattice system. Relatively large magnitude of fracture is observed in the crystalline silicon as compared to amorphous silicon thereby underlining the importance of the diffusion mechanism to fracture. In crystalline silicon, the existence of a sharp two-phase interface during two-phase diffusion leads to the formation of lithium rich and lithium poor phases with large discrepancy in strains. Concentration gradient related stress exists only close to the two-phase interface creating diffusion induced load close to the two-phase interface, however, its magnitude is small compared to the stress due to strain inhomogeneity. As lithiation progresses, the lithium rich phase is pushed outwards inducing tensile stress on the particle surface which leads to the initiation of crack fronts. Thus, the crystalline silicon particle disintegrates at the surface. Fragmentation of the brittle surface film is also observed as it is unable to accommodate the large volumetric expansion of the silicon particle.

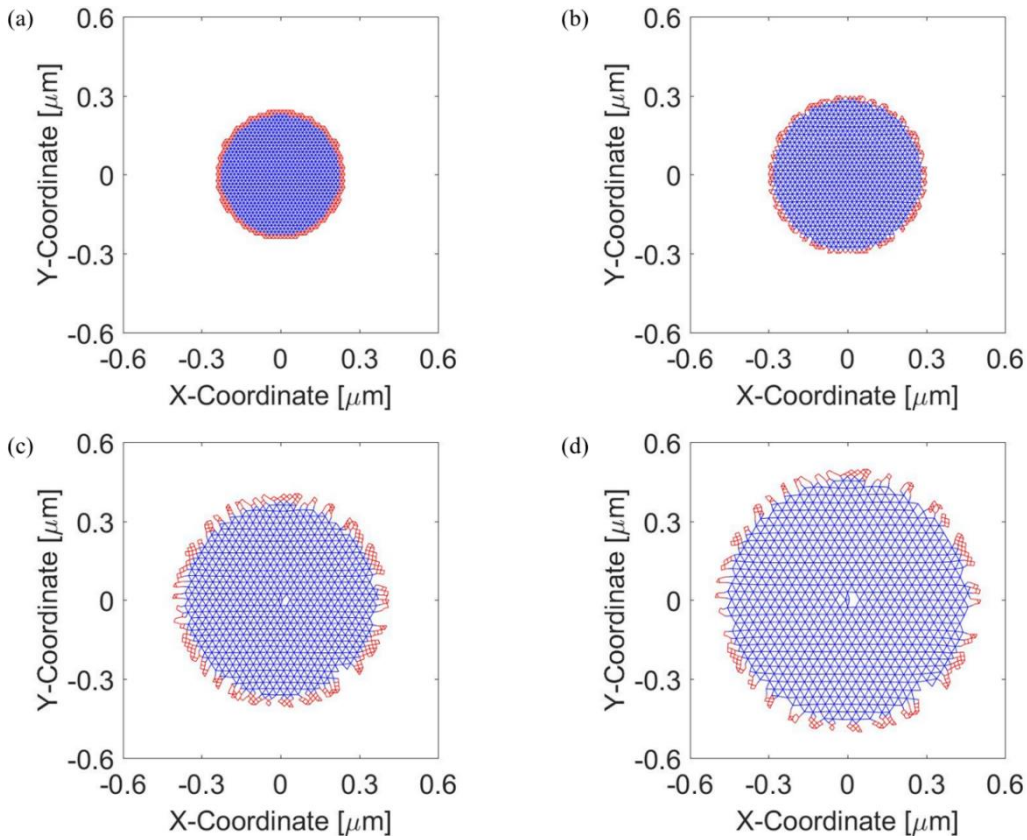

Figure 3.3: Damage contour plots during lithiation of amorphous silicon with film (single phase diffusion) at 1C rate at different times (a) t = 0.05, (b) t = 0.35, (c) t = 0.65 and (d) t = 0.95. Silicon (shown in blue) shows fracture from the center and surface film (red) shows severe fracture.

In the single phase amorphous silicon particle with film, the volumetric strain is homogeneously distributed throughout the particle dimension due to the smoother concentration variation. There is no segregation of lithium rich and lithium poor zones. Thus, the lithium atoms can move to the center of the particle more freely as compared to the crystalline silicon particle where the lithium atoms are constrained by the two-phase interface. The concentration gradient induced stress is present throughout the amorphous silicon particle at all times. Large volumetric strain is observed inside the amorphous Si particle as well, however, the absence of a barrier (like the interface in two phase diffusion process) allows for smoother expansion of the particle. Consequently, the total damage is much lower in amorphous silicon compared to the crystalline silicon because of smaller diffusion induced stress as well as smaller disparity in volumetric strains throughout the radius of the particle.

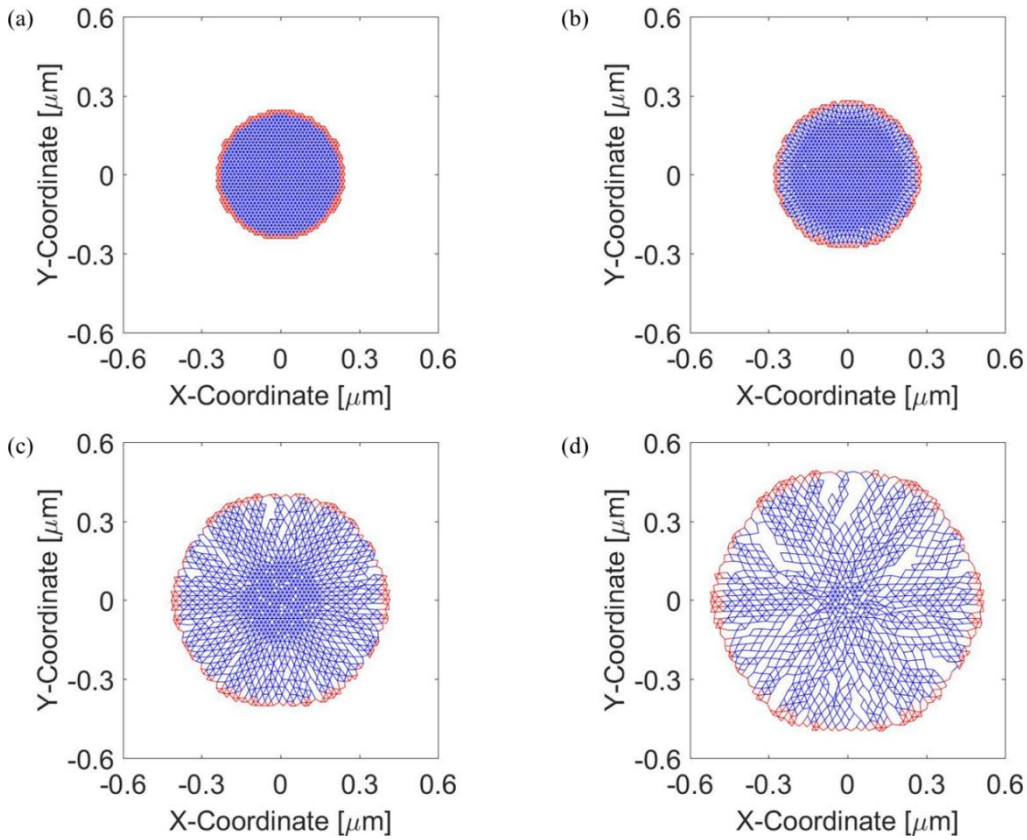

Figure 3.4: Damage contour plots during lithiation of crystalline silicon with film (two phase diffusion) at 1C rate at different times (a) t = 0.05, (b) t = 0.35, (c) t = 0.65 and (d) t = 0.95. Silicon (shown in blue) shows fracture near particle surface due to two-phase lithiation and surface film (red) shows severe disintegration.

Again, fragmentation of the surface film is observed as it is unable contain the large expansion of the silicon particle. Surface film property modification such that it exhibits elastomeric deformation is essential to mitigating surface film fracture in silicon. Elastomers can undergo large elastic deformation, stretching and returning to their original shape in a reversible manner. Thus, changing the nature of the diffusion process can help mitigate fracture inside the silicon particle, however, brittle surface film fracture continues unabated for both crystalline and amorphous silicon due to large volumetric expansion of the particle.

An interesting feature can be observed from the fracture profiles of crystalline versus amorphous silicon. The crystalline silicon particle fractures close to the surface while fracture originates close to the center of the amorphous silicon particle during lithiation. The amorphous silicon particle behavior resembles graphite behavior in the sense that tensile stresses originate at

the center of the particle during lithiation with compressive stress at the surface. During delithiation, tensile stresses occur at the surface while compressive stresses form at the center. As silicon exhibits more strength in compression than tension, higher fracture is observed under tension. Consequently, the particle fractures in regions where tensile stresses originate. Thus, the differing fracture behavior of crystalline versus amorphous silicon is a direct consequence of the diffusion behavior inside the particle. Large volumetric expansion, by itself, cannot explain the fracture behavior as it occurs in both crystalline and amorphous silicon with lithiation. It is the nature of the diffusion process (single phase vs two-phase) that determines the fracture characteristics. Single phase diffusion materials (graphite, amorphous silicon) exhibit tensile fracture close to center of the particle during lithiation while two-phase diffusion materials (crystalline silicon) exhibit tensile fracture close to surface of the particle during lithiation and vice versa.

Quantification of the fracture inside the silicon particle with surface film is done by defining a parameter named total damage density, DD_{total} . It is defined as the ratio of number of broken bonds to the total number of bonds in the silicon active material with surface film. Individual silicon/film damage density, DD_{Si} and DD_{film}, are also defined as the ratio of number of broken bonds in silicon/film to the total number of bonds in the silicon and film agglomerate. The definitions have been kept as above such that $DD_{total} = DD_{Si} + DD_{film}$.

$$DD_{total} = \frac{n_{broken,total}}{n_{Si} + n_{film}} \tag{3.11}$$

$$DD_{Si} = \frac{n_{broken,Si}}{n_{Si} + n_{film}},\ DD_{film} = \frac{n_{broken,\,film}}{n_{Si} + n_{film}} \tag{3.12}$$

Effect of Surface Film Thickness on Damage

Figure 3.5 (a-c) exhibits the effect of film thickness on damage inside the silicon active material and surface film composite for crystalline and amorphous silicon. Figure 3.5 (a) compares the total damage density for crystalline versus amorphous silicon with film as the film thickness is increased. The base silicon particle diameter is kept constant at 500 nm and the lithiation rate is constant as well at 1 C. As demonstrated earlier, for the same base diameter and C-rate, crystalline silicon with film shows higher damage density as compared to amorphous silicon for all the film

thicknesses investigated. Figure 3.5 (b) and Figure 3.5 (c) show the detailed breakdown of the damage density of each layer for crystalline silicon with film and amorphous silicon with film respectively.

The results indicate that as film thickness is increased, damage density inside the film decreases. This is because there is no diffusion induced stress inside the film and hence fracture inside the film will be mostly concentrated close to active material surface and portion of film far from the active material is relatively unaffected. Also, as the film thickness increases there is more support structure for the film. The active material damage density is relatively unaffected by film thickness variation. Hence, a small thickness of surface film is desirable to reduce inert material quantity provided the integrity of the film can be maintained. Total damage density trend is dominated by damage inside film and hence mirrors the decreasing trend of film damage as film thickness increases.

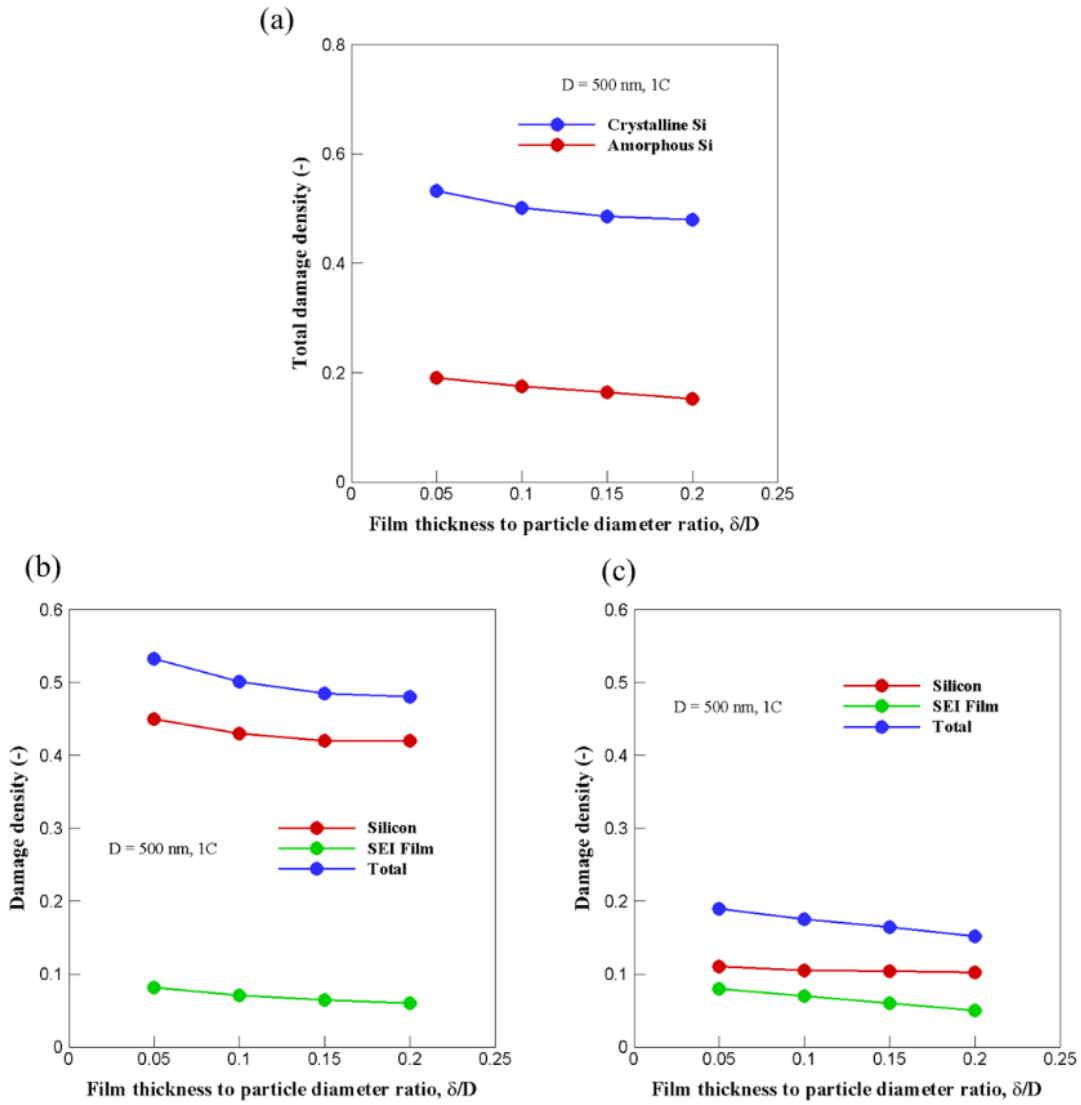

Figure 3.5: Effect of surface film thickness on damage density inside silicon with surface film. (a) Comparison of total damage density in crystalline silicon with film versus amorphous silicon with film. (b) Expanded view of damage density in crystalline silicon with film as a function of film thickness. (c) Expanded view of damage density in amorphous silicon with film as a function of film thickness. High fracture density is seen in crystalline silicon as compared to amorphous silicon. Damage density shows a mild decrease with film thickness increase.

Effect of Surface Film Young's modulus on Damage

Figure 3.6 (a-c) detail the effect of changing the film Young's modulus on damage inside the silicon active material and surface film. Figure 3.6 (a) gives the total damage density for crystalline vs amorphous silicon with film as the film Young's modulus is increased. Base silicon diameter and C-rate are again kept constant at 500 nm and 1 C respectively. Figure 3.6 (b) and Figure 3.7(c)

show the detailed breakdown of the damage density of each layer for crystalline silicon with film and amorphous silicon with film respectively. Crystalline silicon shows consistently higher total damage density than amorphous silicon.

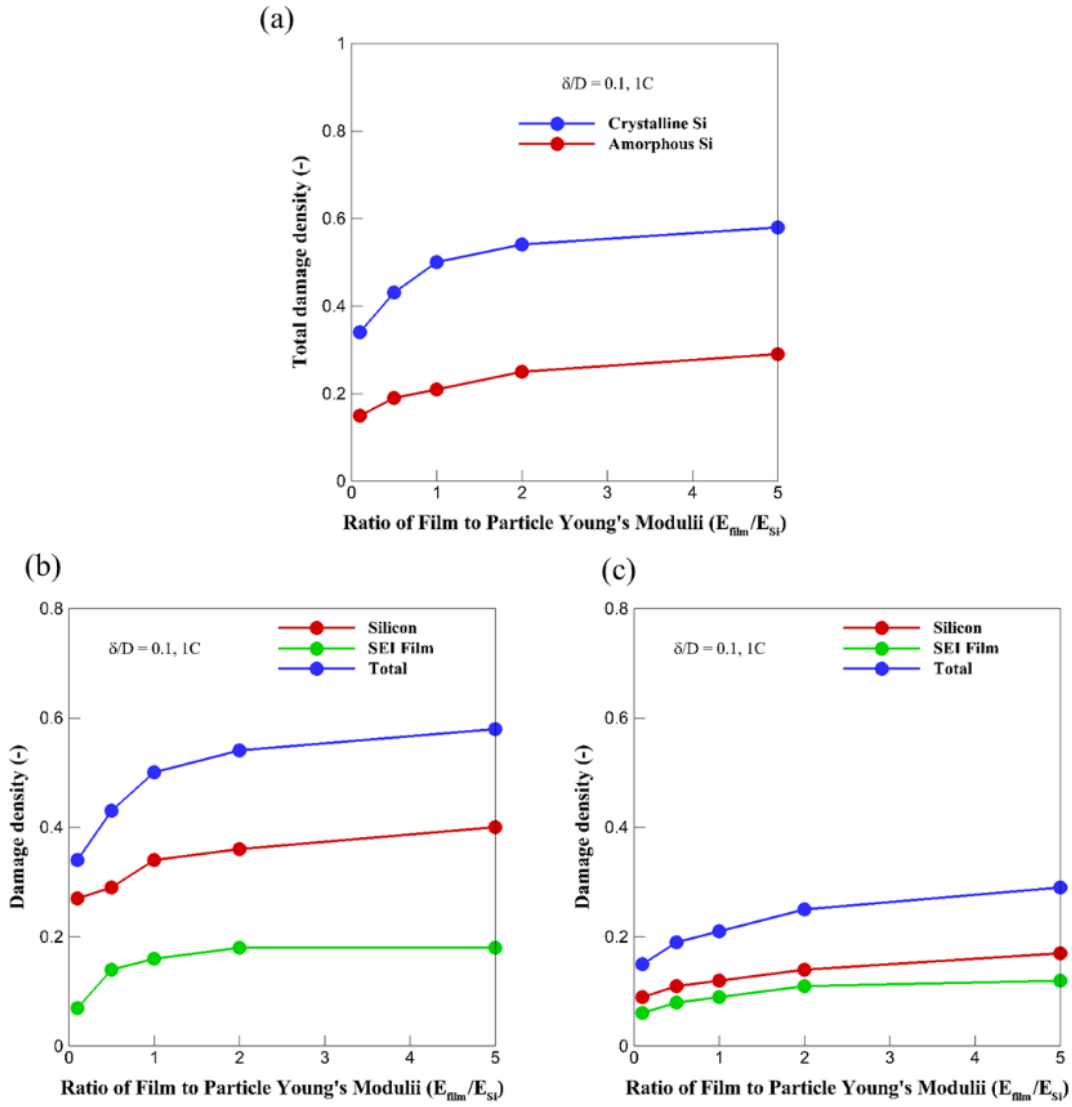

Figure 3.6: Effect of surface film Young's modulus on damage density inside silicon with surface film. (a) Comparison of total damage density in crystalline silicon with film versus amorphous silicon with film. (b) Expanded view of damage density in crystalline silicon with film. (c) Expanded view of damage density in amorphous silicon with film. High fracture density is seen in crystalline silicon as compared to amorphous silicon. Damage density increases with increase in surface film Young's modulus.

As the film Young's modulus is increased, the fraction of broken bonds inside the film increases since more strain energy has to be released. Increased Young's modulus implies

increased strain energy accumulation which leads to higher number of broken bonds. A very interesting observation is that the fraction of broken bonds inside active material also shows a monotonically increasing trend with increased film's elasticity modulus. Thus, the Young's modulus of the film has a direct impact on fracture inside the active material. As the elastic modulus of film increases, damage inside the film as well as the active material increases. This positive correlation provides us with a way to reduce fracture inside active material. Using a film of lower elastic modulus will help diminish fracture damage inside the active material. Mechanical damage hinders diffusion and causes particle isolation which leads to capacity fade and reduced rate capabilities. Consequently, using a low elastic modulus film will improve the battery capacity and life.

Effect of Silicon Particle Diameter and C-rate on Damage

Figure 3.7 (a-c) exhibits the effect of silicon particle diameter on damage. Figure 3.7 (a) compares the total damage density for crystalline versus amorphous silicon with film as the silicon particle diameter is increased. It is established again that amorphous silicon performs much better than crystalline silicon in terms of lower fracture. Figure 3.7 (b) and Figure 3.7 (c) show the detailed breakdown of the damage density of each layer for crystalline silicon with film and amorphous silicon with film respectively.

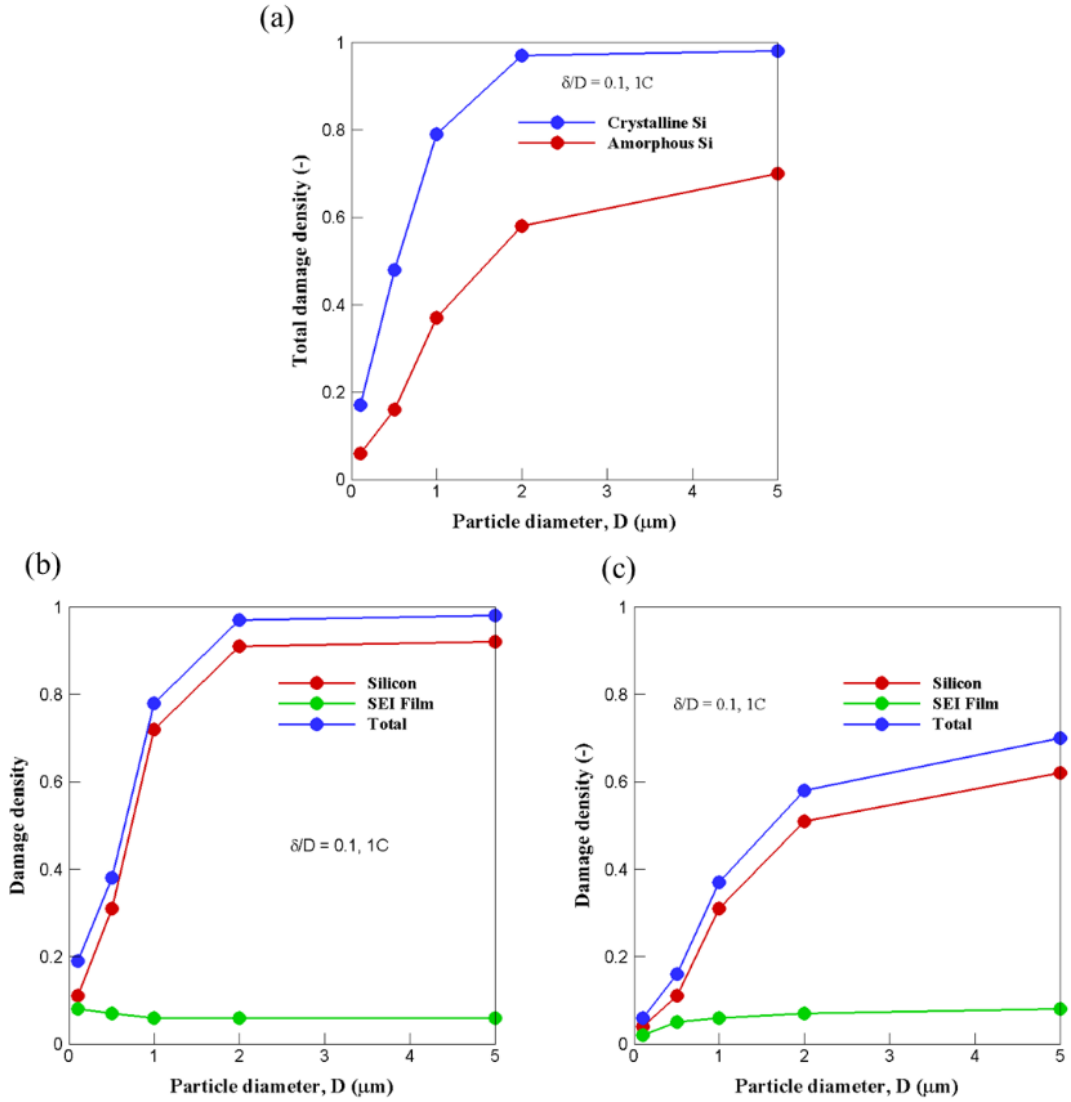

Figure 3.7: Effect of silicon particle diameter on damage density inside silicon with surface film. (a) Comparison of total damage density in crystalline silicon with film versus amorphous silicon with film. (b) Expanded view of damage density in crystalline silicon with film. (c) Expanded view of damage density in amorphous silicon with film. High fracture density is seen in crystalline silicon as compared to amorphous silicon. Damage density shows a rapid increase with increase in particle size.

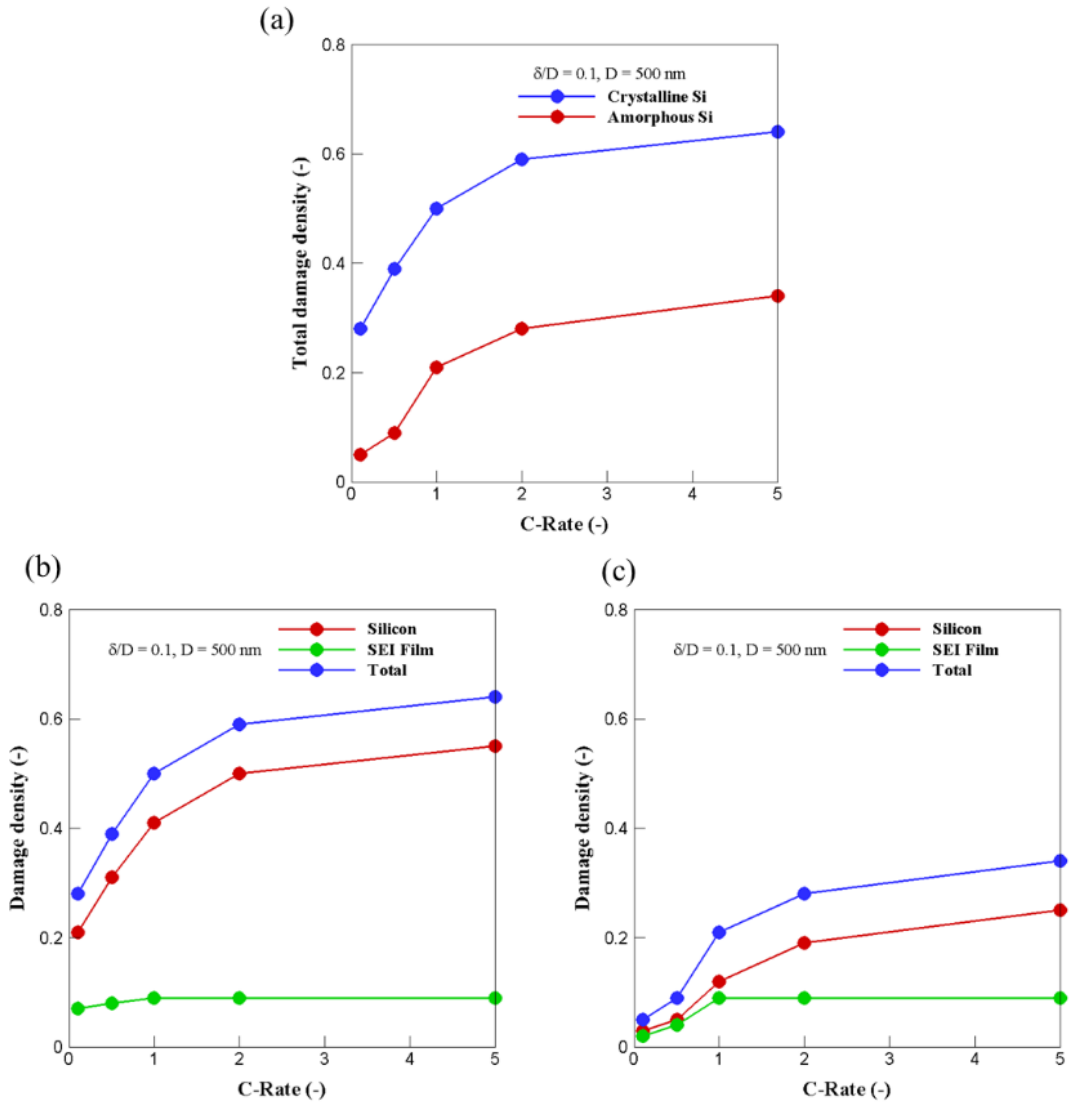

Figure 3.8: Effect of lithiation rate on damage density inside silicon with surface film. (a) Comparison of total damage density in crystalline silicon with film versus amorphous silicon with film. (b) Expanded view of damage density in crystalline silicon with film. (c) Expanded view of damage density in amorphous silicon with film. High fracture density is seen in crystalline silicon as compared to amorphous silicon. Damage density shows a rapid increase with C-rate.

The results indicate that as particle diameter is increased, damage density inside the particle increases rapidly. For large particle sizes, the crystalline silicon particle fractures completely as evidenced by the damage density reaching close to 1. The film also shows significant fracture as the particle size is increased. Larger particles experience higher amount of mechanical degradation

because of higher concentration gradient induced diffusion stress as well as high volume expansion based deformation.

Figure 3.8 (a-c) exhibits the effect of lithiation rate on damage. Figure 3.8 (a) compares the total damage density for crystalline versus amorphous silicon with film as the current rate is increased. Figure 3.8 (b) and Figure 3.8 (c) show the detailed breakdown of the damage density of each layer for crystalline silicon with film and amorphous silicon with film respectively.

The results indicate that as C-rate is increased, damage density inside the particle increases rapidly. The trends are similar to those obtained for particle size and in agreement with literature. Higher C-rates and larger particle sizes have more predilection for fracture.

Fracture Phase Map

Figure 3.9 (a-b) give the fracture phase map for amorphous and crystalline silicon with film clearly demonstrating the need for going towards amorphous silicon to mitigate the fracture tendencies. Crystalline silicon particles beyond 100-200 nm show severe fracture at all C-rates while amorphous silicon particles can sustain reasonably well up to 1-2 μm.

A direction towards improving the performance of silicon electrodes can be gleaned from the discussion presented above. Conversion of crystalline silicon to amorphous silicon is reported to occur over the first few lithiation-delithiation cycles. It is the opinion of the author to introduce extremely slow lithiation and delithiation (<C/100) of crystalline silicon particles with mid-ranged particle size (~ 1-2 μm) for the first few cycles to enable complete conversion into amorphous silicon with minimal fracture. The decreased fracture tendency of amorphous silicon is a desirable characteristic and then can then be utilized to cycle the electrodes at higher C-rates. For amorphous silicon, the damage density for 1-2 μm particle lies within the reasonable limit (<0.2) for C-rates up to 2C. Hence, we recommend an upper limit for C-rate of 2C for cycling of amorphous silicon particles. Thus, fracture inside the silicon active material can be minimized using the above cycling technique.

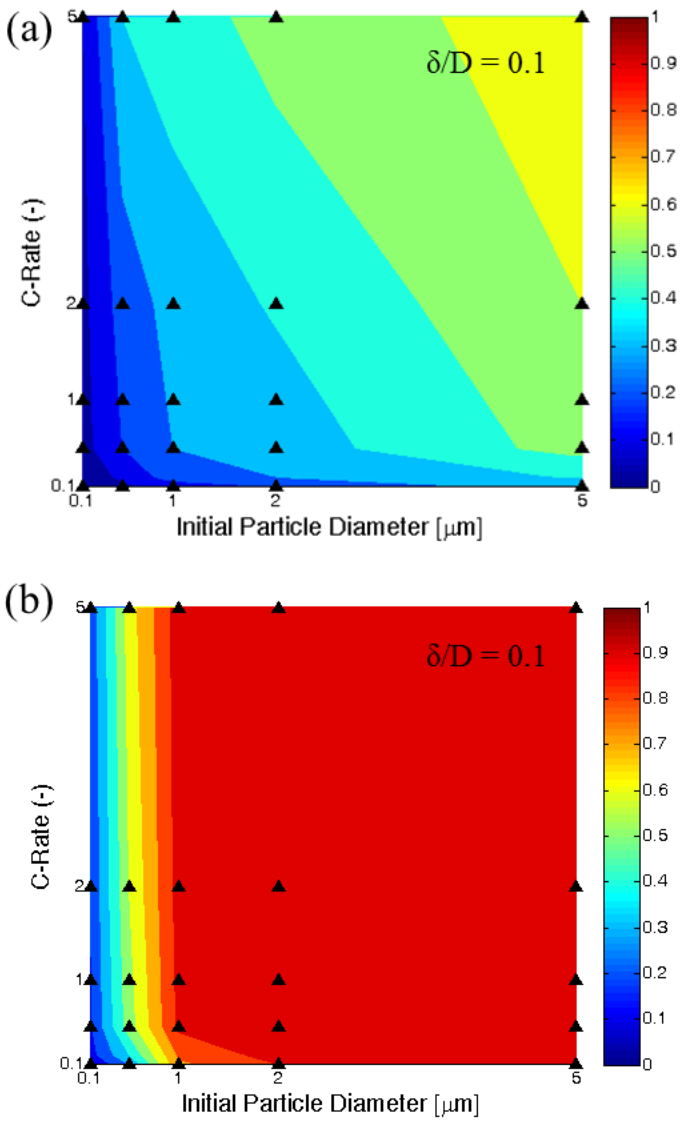

Figure 3.9: Fracture phase map for variation of particle size and C-rate with film thickness to particle size ratio, $\delta / D = 0.1$, for (a) amorphous silicon with film and (b) crystalline silicon with film. Crystalline silicon exhibits much severe fracture as compared to amorphous silicon with increase in particle size and C-rate.

However, surface film rupture is inevitable for both amorphous and crystalline silicon owing to the high volumetric expansion of the silicon particle and brittle mechanics of the film. Consequently, capacity fade due to SEI film breakdown cannot be mitigated unless surface film modification is done to obtain elastomeric films. A small improvement in the fracture characteristics is obtained by decreasing the Young's modulus of the brittle film layer, however,

it is not enough to resolve the capacity deterioration of silicon electrodes due to film breakage and resulting fresh SEI formation.

Figure 3.10 shows the effects of C-rate and film to particle Young's moduli ratio on total damage density in a silicon particle of 500 nm covered with a surface film layer. Both amorphous and crystalline Si particles with film are investigated. Fracture characteristics for amorphous and crystalline Si exhibit wide disparity owing to the nature of the underlying intercalated lithium diffusion process.

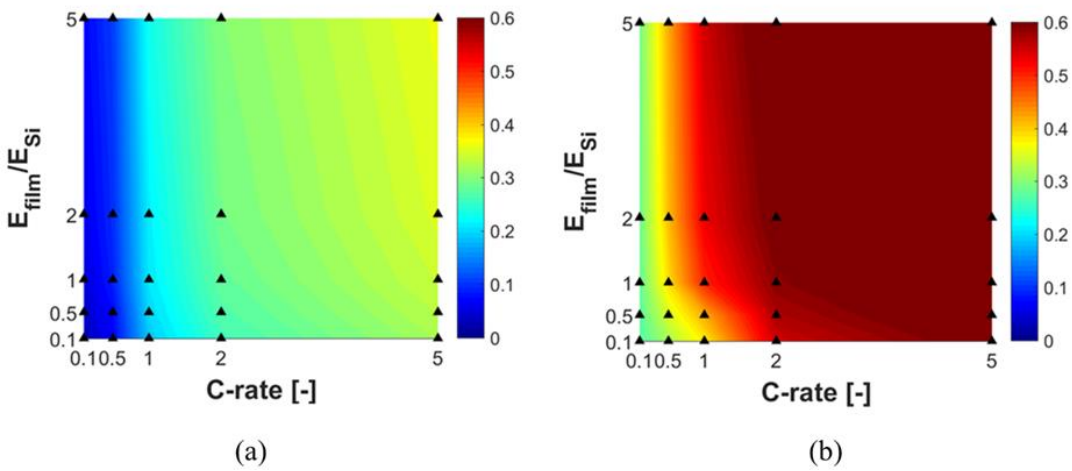

Figure 3.10. Contour plots for total damage density as a function of C-rate and film to Si Young's moduli ratio (E_{film}/E_{Si}) for (a) amorphous Si with film and (b) crystalline Si with film. The Young's moduli ratio is varied by changing the film Young's modulus while keeping the Si Young's modulus constant. Crystalline Si with film exhibits higher damage density as compared to amorphous Si with film. High C-rate and high film's Young modulus contribute to enhanced damage in Si and film composite particle. The effect of C-rate is more pronounced compared to that of the Young's moduli ratio. The Si particle diameter simulated is 500 nm with 50 nm SEI thickness. Here damage density corresponds to the total damage density in the silicon particle and surface film agglomerate.

As the C-rate increases, damage density increases in both crystalline and amorphous Si. Similar trend is observed for increase of surface film to Si particle Young's moduli ratio. However, C-rate variation has a more pronounced effect on the total damage density as compared to Young's moduli change (Figure 3.10). Larger concentration gradients coupled with high volume expansion exacerbate the mechanical damage at high C-rates. Increase in film Young's modulus is reflected in the increases of strain energy accumulation rate. Fracture criterion is dictated by the fracture

threshold energy which is kept fixed for all the variations explored. Faster rate of strain energy accumulation with higher Young's moduli results in larger number of bonds strain energy exceeding the fracture threshold. This is demonstrated by the relatively higher magnitude of damage with increase in film to particle Young's modulus ratio.

Fracture in the silicon with surface film occurs all throughout the simulation time. As fracture progresses, the damaged bonds are removed implying there are no forces in these bonds. For computation of stress variation with time, we plot the stress in an undamaged surface film bond as the lithiation-delithiation progresses. Figure 3.11(a) shows the evolution of stress in an undamaged surface film bond with lithiation-delithiation of an amorphous silicon particle with surface film at multiple C-rates. Here normalized time refers to the time for discharge/charge at a particular C rate divided by 1 hour. For a 1C rate lithiation/delithiation, the total time for charge and discharge will be approximately 2 hours and is normalized to 2. Correspondingly, for 2C current rate the normalized time goes to half of time for 1C rate and so on.

Stress in the surface film increases as lithiation progresses and is a maximum close to the end of lithiation. During delithiation, stress in the surface film relaxes as the particle contracts. There are no concentration gradient-induced stresses inside the surface film; the fracture is due to the film being unable to accommodate the high volumetric expansion of the Si particle. Consequently, we see minor increase in surface film stress with C-rate because a major contribution to stress is due to high volume expansion which is similar for all C-rates at the end of lithiation-delithiation. The C-rate change affects the concentration gradient-induced stress in the Si particle which in turn leads to small variation in stress in the surface film.

Figure 3.11(b) shows the evolution of damage density with lithiation of an amorphous Si particle at 1C rate. The Si particle diameter simulated is 500 nm with 50 nm SEI thickness. Here, we try to characterize the damage that can lead to formation of new sites exposed to electrolyte that can cause irreversible Li loss due to fresh SEI formation. Thus, two types of damage A and B have been defined that can contribute to Li inventory depletion. Type A damage is characterized by fracture of the surface film layer (as simulated by the atomistic model). Here the surface film is treated equivalent to chemical SEI film layer that forms on the Si particle surface. The SEI film layer reformation with cycling contributes to irreversible Li loss during battery operation. Type B damage is characterized by breaking up of the surface Si active material which can lead to fresh

electrolyte flow in the silicon active material cracks and irreversible lithium loss due to SEI formation in these cracks.

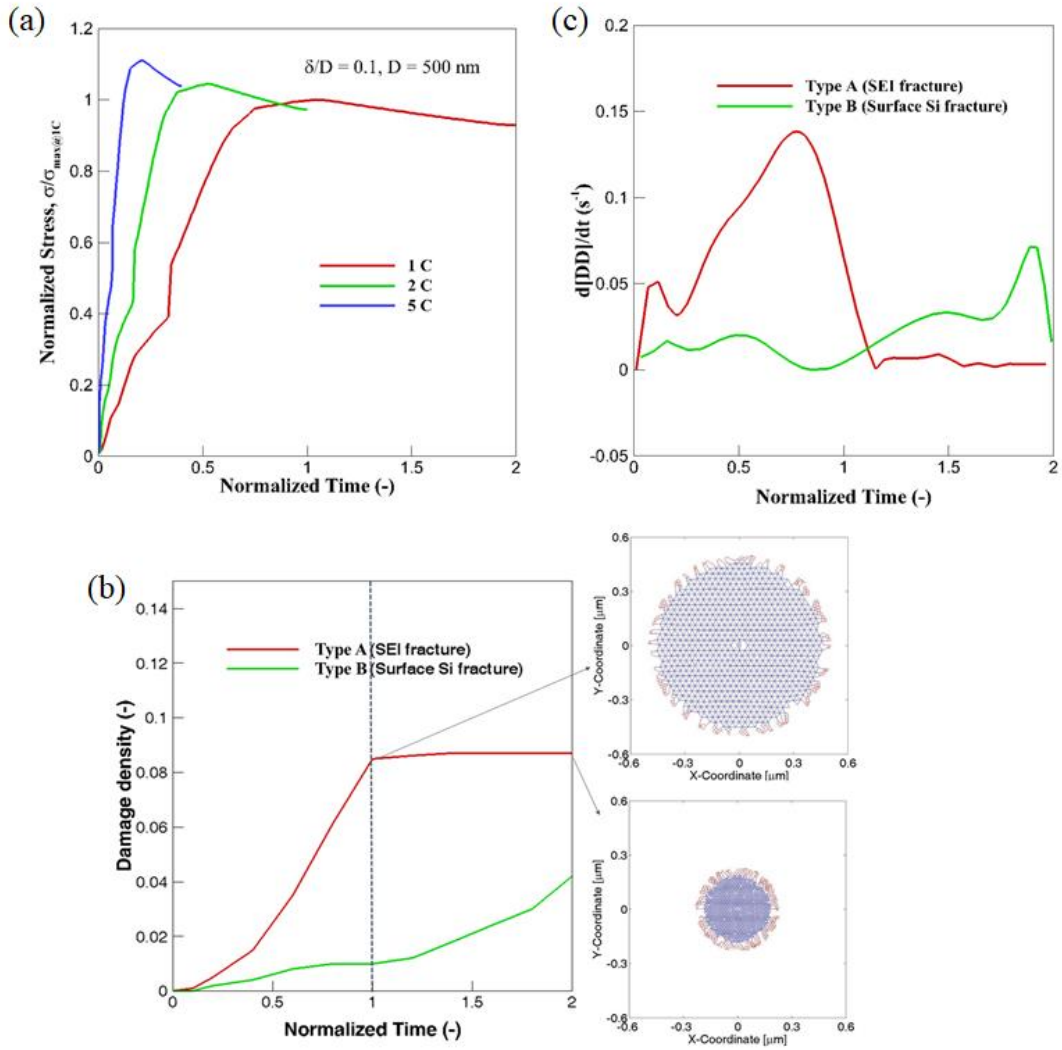

Figure 3.11 (a) Evolution of stress in undamaged surface film bond with lithiation-delithiation of amorphous silicon particle with surface film at multiple C-rates. (b) Damage density vs time for lithiation-delithiation of 500 nm amorphous silicon particle with 50 nm surface film exhibiting single phase diffusion at 1C rate. At t = 1 charging ends and discharge starts. The surface film shows high degradation due to large volumetric expansion of the particle. Cracks are formed in the silicon core during lithiation and close to the silicon surface during delithiation. (c) Evolution of rate of change of total damage density in silicon with surface film agglomerate at 1C rate lithiation-delithiation. The Si particle diameter simulated is 500 nm with 50 nm SEI thickness.

It is evident from Figure 3.11(b) that type A damage supersedes type B damage and thus, the dominant cause of capacity fading can be attributed to brittle SEI layer breakdown. Also, type

A damage is predominant during lithiation of the Si particle leading to high volumetric expansion of Si, which ruptures the surface film. Meanwhile, type B damage due to rupture of the Si surface is higher during delithiation as compared to lithiation. This is due to the formation of compressive stresses at the particle surface during lithiation and tensile stresses at the particle surface during delithiation. Since materials are more resilient to fracture in compression than in tension, we see higher amount of surface Si damage during delithiation.

Figure 3.11(c) plots the rate of change of damage density corresponding to the two modes of damage defined previously (type A and type B) for the same active material and film structure and operating conditions as shown in Figure 3.11(b). Damage density rate is higher in surface film (SEI fracture) during lithiation due to high volumetric expansion and goes close to zero during delithiation owing to stress relaxation due to silicon particle contraction. There is more surface silicon fracture during delithiation as compared to lithiation due to the formation of tensile stresses at the surface during delithiation. This is evident from the higher rate of surface Si damage density increase during delithiation while it hovers close to zero during lithiation.

3.1.4 Conclusions

A stochastic lattice spring methodology coupled with two different diffusion mechanisms inside the silicon particle has been utilized to deduce the effect of large volumetric strain on the fracture tendencies inside the silicon and surface film agglomerate. It is proved that large volumetric strain is not the sole contributing factor for the increased fracture tendencies of high capacity anode materials like silicon. Amorphous silicon with single phase diffusion characteristics exhibits much lower fracture tendency as compared to crystalline silicon with two phase diffusion characteristics. The presence of the two-phase boundary causing large volumetric strain gradient is the primary cause for severe mechanical degradation of crystalline silicon. Since crystalline silicon converts to amorphous silicon during initial cycling, a cycling protocol involving extremely low C-rate lithiation-delithiation of crystalline silicon (for particle sizes > 1μm) can be beneficial to fully convert the crystalline silicon particle to amorphous phase with minimal fracture. Cycling of the amorphous phase silicon particle can then be carried out at moderate to high C-rates with decreased fracture tendencies.

The effect of surface film on the silicon particle has also been elucidated. The surface film can either be composed of the secondary phase materials or be the solid electrolyte interphase layer.

It is shown that a brittle surface film incapable of accommodating the large volumetric strains of silicon particle will disintegrate considerably. Lowering the Young's modulus of the surface film will help decrease the fracture characteristics but will still show considerable damage even for 500 nm sized particles. Consequently, an elastomeric surface film is imperative to mitigate fracture and improve long term cycling of silicon electrodes.

3.2 Mechanistic Elucidation of Silicon Particle Morphology on Electrode Performance

3.2.1 Background

Lithium ion batteries (LIBs) have become the dominant mode of energy storage [189]. In recent years, LIB technology is pervading large scale applications such as electric vehicles [128, 189, 191], commercial aircrafts [4, 7] and grid storage [128, 129]. A robust improvement of energy and power densities afforded by the LIB will drive its rapid adoption in high energy/power operations. This is directly correlated with the specific capacities of anode [128, 164] and cathode [6, 165] active materials utilized in the LIB. Current commercial batteries use graphite [130] and lithium cobalt oxide / lithium nickel manganese cobalt oxide [131, 132] as anode and cathode constituents respectively . Graphite exhibits a theoretical specific capacity of 372 mAh/$g_{graphite}$ while the current cathode materials are limited to 200 mAh/g_{AM} [134]. Electric vehicles have incorporated the aforementioned chemistries, however, rapid escalation in capacity is required to eliminate the use of bulky battery packs in transport applications.

The need for high capacity anode and cathode materials for usage in next generation LIBs has engendered considerable research into new materials[133, 135, 136]. Silicon, with its high theoretical specific capacity of 4200 mAh/g_{Si}, approximately ten times that of graphite [132, 166, 192] is a viable prospect. A silicon atom can imbibe 4.4 atoms of lithium ($Li_{4.4}Si$) while graphite is limited to 1 atom of Li per molecule (LiC_6), outlining the desirability of Si as anode [193]. Unfortunately, experimental cycling datasets reveal low initial capacity (~75% of theoretical) [194] as well as rapid capacity degradation with subsequent lithiation-delithiation. Within the first 50 cycles, 20% capacity fade has been observed [167, 168].

Immense volumetric fluctuations have been found to be the root cause of the capacity loss in silicon [169]. Graphite is constrained to 10% volume expansion [168] , however, silicon particles can expand up to around 400% with full lithiation [139]. This intercalation induced strain

gives rise to crack initiation and subsequent propagation leading to fracture [139]. The protective solid electrolyte interphase (SEI) layer also ruptures, unable to accommodate this large volumetric fluctuation. Subsequent reformation of the SEI layer through contact between exposed particle surface and fresh electrolyte depletes the Li inventory, exacerbating capacity fade. [113, 170, 171]. Particle isolation and diminished diffusivity further reduces the performance.

Silicon anodes have been analyzed computationally for the large volume expansion and subsequent stress generation [172, 173, 184]. Critical size of flaws for crack propagation in thin films and silicon nanowires have been identified [175, 176]. Large elastic-plastic deformation of silicon has been incorporated in a few computational studies [177, 183]. Lattice spring model based high volume expansion modeling has been used to delineate the fracture propensity with particle size and molar volume [184-186].

The propensity of silicon particles to fracture is drastically reduced in the nanometer limit due to lower values of diffusion induced stress[148, 151, 178, 182]. Stress induced diffusion and pressure gradient effects also contribute to the minimization of fracture[146, 147, 195]. Consequently, nanospheres and nanowire configurations are being probed in detail to elucidate the morphological impact on performance[196-200]. Silicon nanospheres, in particular, have been the focus of intensive investigations both experimentally and computationally. Chandrasekaran *et al.* examined lithium insertion/deinsertion in an evolving silicon electrode particle at room temperature under both galvanostatic and potentiostatic control using a single particle model, demonstrating the need for asymmetric transfer coefficients and sluggish kinetics resulting in kinetic hysteresis and potential gap in the Li-Si system [201]. Furthermore, they extended the work to a macrohomogeneous model incorporating porosity variations due to the large molar volume changes [202]. The incorporation of volume changes in porous electrodes through porosity variation for Si anodes has been ably demonstrated [197, 203, 204]. Recently, Mai *et al.* reformulated the macrohomogeneous model coupling large deformations at the particle and electrode level with electrochemistry to simulate the performance of Si anode-NMC532 cathode cell. Chan *et al.* grew silicon nanowires directly on current collector achieving theoretical charge capacity for silicon anodes with minimal capacity fading during cycling [205]. While experimental studies on nanowires are available, computational studies are much sparse as compared to nanospheres. Charge transfer kinetics parameters have been reported by Swamy *et al.* using electrochemical impedance spectroscopy on single crystal silicon wafers [206].

In this work, we have used the single particle formalism with volume evolution to analyze and contrast silicon lithiation in nanospheres and nanorods. The morphological variation requires differing formulations for the two configurations explored and provides insights into the impact of lithiation on the rate performance through diffusive transport and reaction kinetics considerations. Based on the rate performance results obtained, we delineate design guidelines for nanospheres and nanorods for superior performance.

The rest is divided as follows. The details of the model physics are given in the following Methodology section. Spherical and cylindrical diffusive transport in radially evolving systems is outlined alongside the reaction kinetic formulations. The Results and Discussion section elucidates the effect of morphological variation from nanospheres to nanorods on rate performance. A design criterion for the nanospheres and nanorods is given, and material parameters for the silicon anode, in particular, diffusivity and exchange current density are delineated. Finally, the results are summarized in the Conclusion section.

3.2.2 Methodology

The problem formulation involves modeling of coupled solid-state diffusion of lithium inside the silicon nanospheres and nanorods/nanowires active material particles and lithiation reaction kinetics at the surface cognizant of the large volume expansion during lithium insertion in the silicon active material. The single particle model is appropriately adjusted to reflect the dimensional changes for the silicon active material under lithiation. For both nanospheres and nanorods, only radial diffusion is considered. While this approximation is particularly true for the nanospheres because of radial symmetry, its applicability is assumed for the nanorods predicated on theoretical reasoning and experimental dataset. This is justified from the large length to radius ratio of the nanorods ($L/R>>1$) as well as the nature of the manufacturing process of the nanowires. The radial direction provides the shorter diffusion pathway for nanorods with large aspect ratio. Furthermore, the nanorods are grown on the current collectors thereby constraining the Li diffusion through the curved surface area (radial diffusion) and only one of the circular areas pointing towards the separator (axial diffusion). This is reflected in the radial expansion contributing to the bulk of the volume increase. Chan *et. al.* reported a mean diameter increase of the nanowires during lithiation from 89 nm to 141 nm which contributes to around 70% of the final volume coming from radial diffusion with the remaining 30% coming from the length increase through axial diffusion

[207]. The contribution of radial diffusion to volume expansion will increase further towards 100% as the aspect ratio is increased, consequently, radial diffusion is assumed to be the predominant transport pathway for nanorods and the nanorod length is assumed to be invariable throughout the lithiation.

At the single particle level, the rate determining transport mechanism is the solid-state diffusion inside the active material. The electrolyte ionic diffusivity and conductivity is assumed to be high enough to neglect concentration and potential gradients inside the electrolyte. Therefore, the active material is subjected to constant flux from all directions irrespective of its position from the current collector under galvanostatic operation. Single phase diffusion inside the electrode particle is modeled using the Fick's law [208]. In accordance with literature, in particular, Chandrasekaran *et al.*, the final lithiated state of amorphous silicon for single-phase diffusion is considered to be $Li_{15}Si_4$ corresponding to a 280% increase in volume [209]. Thus, the final volume is 3.8 times the initial volume. The electrochemical reaction at the surface of the Si used to model the lithiation process is shown in Equation (3.13).

$$Li^{+} + e^{-} + Si_{4/15} \rightleftarrows LiSi_{4/15} \tag{3.13}$$

This form has been chosen to keep the state of charge of Li between 0 and 1, also allowing for ease of applicability of the Butler-Volmer equation. The state of charge of Li inside the Si particle has a continuous profile between 0 and 1 as we have considered the amorphous silicon particle with single phase diffusion as opposed to the crystalline silicon particle which shows segregation of the Li rich and the Li poor phases which can be treated through the Cahn-Hilliard formalism[139].

Furthermore, the voltage profile having multiple steps in it is seen for Li intercalation in graphite as well, with the plateaus coinciding with the coexistence of multiple phases. Consequently, the open circuit potential of graphite as a function of state of charge shows plateaus as the SOC varies from 0 to 1. In literature, this can be adequately treated with single phase diffusion for the single particle model or the macrohomogeneous pseudo 2D model[139, 210]. The same concept can be extended for lithiation in silicon adequately and thus we have a smooth transition in the concentration profiles throughout the silicon particle and a SOC varying from 0 to 1. We now provide the governing differential equations and constitutive relations for the spherical nanoparticles and nanorods.

Nanospheres

Species balance in the nanosphere is given by the spherical diffusion equation in Equation (3.14).

$$\frac{\partial c_s}{\partial t} = \frac{D_{Li}}{r^2}\frac{\partial}{\partial r}\left(r^2 \frac{\partial c_s}{\partial r}\right) \tag{3.14}$$

Here, c_s is the Li concentration inside the sphere, D_{Li} is the diffusion coefficient of Li into Si, and r, t represent the radial distance within the particle and time respectively. The subscript 's' is used to signify the sphere shape. Symmetry boundary condition is applied at the particle center (Equation (3.15)) and constant flux boundary condition is applied at the particle surface (Equation (3.16)) and the initial condition is given in Equation (3.17).

$$r = 0,\ \frac{\partial c_s}{\partial r} = 0 \tag{3.15}$$

$$r = R_s,\ D_{Li}\frac{\partial c_s}{\partial r} = -\frac{\tilde{i}_s}{nF} \tag{3.16}$$

$$t = 0,\ c_s = 0\,\text{mol/m}^3 \tag{3.17}$$

In the formulation, the apparent current density at the nanosphere surface, $\tilde{i}_s$, can be correlated to the actual current density i_s as shown in Equation (3.18). Here R_0 is the initial radius of the particle prior to lithiation and $R_s(t)$ denotes the temporal evolution of the radius as the volume increases with lithiation, I is the applied current. For a detailed derivation of this formulation, the readers are referred to Chandrasekaran *et al*.

$$\tilde{i}_s = i_s\left[\frac{R_0}{R_s(t)}\right]^3,\ i_s = \frac{I}{4\pi\left[R_s(t)\right]^2} \tag{3.18}$$

We use the Butler-Volmer formulation with symmetric transfer coefficients to describe the charge transfer kinetics at the surface of the silicon nanospheres (Equation (3.19)). Here i_0 is the exchange current density, F is the Faraday's constant, R is the universal gas constant, T is temperature and η is the overpotential for the electrochemical reaction.

$$i_s = i_0\left[\exp\left(\frac{F}{2RT}\eta\right) - \exp\left(-\frac{F}{2RT}\eta\right)\right] \tag{3.19}$$

The exchange current density takes the form shown in Equation (3.20). Here, k is the rate constant, c_e is the Li^+ ionic concentration in the electrolyte phase, c_{max} and $c_{max,0}$ are the maximum concentration of Li in the Si based on the final and initial volume ($V_{s,0}$) of Si respectively while the surface concentration is denoted by the subscript '*surf*'. $\tilde{c}_s$ corresponds to the modified lithium concentration based on the volumetric change during lithiation. The corresponding forms for c_{max} and $c_{max,0}$ are specified in Equations (3.21,3.22) respectively. N_{tot} is the total number of moles of Li that can be inserted into the silicon electrode based on the mass of the pristine Si particle and a maximum molar Li:Si ratio of 3.75:1.

$$i_{s,0} = Fk\left(c_e\right)^{0.5}\left(c_{\max,0} - \tilde{c}_{s,surf}\right)^{0.5}\tilde{c}_{s,surf}{}^{0.5},\ \tilde{c}_{s,surf} = c_{s,surf}\left[\frac{R_s\left(t\right)}{R_0}\right]^3 \tag{3.20}$$

$$c_{max} = \frac{V_{s,0}\dfrac{3.75}{\Omega_{Si}}}{V_{s,0}\left(1+\dfrac{3.75\Omega_{Li}}{\Omega_{Si}}\right)} = 81967\,\text{mol/m}^3 \tag{3.21}$$

$$N_{tot} = V_{s,\max}c_{\max} = \frac{4}{3}\pi\left(3.8R_0^3\right)c_{\max},\ c_{max,0} = \frac{N_{tot}}{V_{s,0}} = \frac{N_{tot}}{\frac{4}{3}\pi R_0^3} = 3.8c_{max} = 311474.6\ \text{mol/m3}$$

(3.22)

The overpotential is correlated to the solid phase potential ϕ_1, electrolyte phase potential ϕ_2 and the open circuit potential (OCP) U of silicon lithiation based on the surface state of charge (SOC) $\theta_{s,surf}$ (Equation (3.23)). The dependence of the OCP on the SOC is obtained from GITT experiments in literature and the surface SOC can be correlated to the current lithiated volume $V_s\left(t\right)$ and surface concentration (Equation (3.24)).

$$\eta = \phi_1 - \phi_2 - U\left(\theta_{s,surf}\right) \tag{3.23}$$

$$\theta_{s,surf} = \frac{V_s\left(t\right)}{N_{tot}}c_{s,surf} = \frac{\frac{4}{3}\pi\left[R_s\left(t\right)\right]^3}{N_{tot}}c_{s,surf} \tag{3.24}$$

Finally, the volume ratio of lithiated, $V_s(t)$, and pristine spherical particle can be correlated to the molar volumes of lithium, Ω_{Li}, silicon, Ω_{Si}, and the average state of charge inside the particle, $\bar{\theta}_s$, to obtain a functional form for the temporal evolution of the nanosphere particle radius (Equation (3.25)).

$$\frac{V_s(t)}{V_{s,0}} = \frac{\frac{4}{3}\pi\left[R_s(t)\right]^3}{\frac{4}{3}\pi R_0^3} = \frac{\Omega_{Si} + 3.75\Omega_{Li}\bar{\theta}_s}{\Omega_{Si}} \Rightarrow \frac{R_s(t)}{R_0} = \left(\frac{\Omega_{Si} + 3.75\Omega_{Li}\bar{\theta}_s}{\Omega_{Si}}\right)^{1/3} \tag{3.25}$$

The average and local state of charge can be obtained from Equations (3.26) and (3.27) respectively. The average state of charge can be directly obtained from the constant current for galvanostatic discharge or can also be obtained from the average concentration field which is easier to evaluate during constant voltage simulations.

$$\bar{\theta}_s = \frac{It}{nFN_{tot}} = \frac{\frac{4}{3}\pi\left[R_s(t)\right]^3}{N_{tot}}\bar{c}_s,\ \bar{c}_s = \frac{\int_0^{R_s(t)} c_s\left(4\pi r^2\right)dr}{\frac{4}{3}\pi\left[R_s(t)\right]^3} \tag{3.26}$$

$$\theta_s = \frac{\frac{4}{3}\pi\left[R_s(t)\right]^3}{N_{tot}}c_s = \frac{c_s}{c_{max}}\left[\frac{R_s(t)}{3.8^{1/3}R_0}\right]^3 \tag{3.27}$$

Nanorods

Species balance in the nanorods is given by the cylindrical diffusion equation. Here the subscript '*n*' denotes the nanorod configuration.

$$\frac{\partial c_n}{\partial t} = \frac{D_{Li}}{r}\frac{\partial}{\partial r}\left(r\frac{\partial c_n}{\partial r}\right) \tag{3.28}$$

The boundary and initial conditions (Equation (3.29)) are similar to the nanosphere configuration differing only in the evaluation of the current densities (Equation (3.30)) based on the cylindrical shape of the nanorods. The curved surface area of the cylinder is the reaction area now (L_0 is the pristine length of the nanorod which is assumed to remain constant throughout lithiation). The volumetric dependence of a cylinder on the square of the radius is reflected in the

equations for the nanorod as compared to the nanosphere which shows a third-degree dependence.

$$r = 0,\ \frac{\partial c_n}{\partial r} = 0;\ r = R_s,\ D_{Li}\frac{\partial c_n}{\partial r} = -\frac{\tilde{i}_n}{nF};\ t = 0,\ c_n = 0\,\text{mol/m}^3 \tag{3.29}$$

$$\tilde{i}_n = i_n\left[\frac{R_0}{R_n(t)}\right]^2,\ i_n = \frac{I}{2\pi R_n(t) L_0} \tag{3.30}$$

Equations (3.31-3.33) give the Butler-Volmer and exchange current density correlation with the corresponding constitutive equations for maximum lithium concentrations. Again, we note the square dependence of the modified concentration on the nanorod radius ratio evolution. Another important point to note is the maximum concentrations based on initial and final volumes have the same value for both nanospheres and nanorods. This is an intrinsic property of lithiated silicon invariant of the morphology which also points to the consistency of the formulation.

$$i_n = i_0\left[\exp\left(\frac{F}{2RT}\eta\right) - \exp\left(-\frac{F}{2RT}\eta\right)\right] \tag{3.31}$$

$$i_{n,0} = Fk(c_e)^{0.5}\left(c_{\max,0} - \tilde{c}_{n,surf}\right)^{0.5}\tilde{c}_{n,surf}{}^{0.5},\ \ \tilde{c}_{n,surf} = c_{n,surf}\left[\frac{R_n(t)}{R_0}\right]^2 \tag{3.32}$$

$$N_{tot} = V_{n,\max}c_{\max} = \pi\left(3.8R_0^2\right)L_0 c_{\max},\ c_{max,0} = \frac{N_{tot}}{V_{n,0}} = \frac{N_{tot}}{\pi R_0^2 L_o} = 3.8c_{max} \tag{3.33}$$

The overpotential equation (Equation (3.34)) is similar to the one for nanospheres differing only in the formulation of the surface state of charge (Equation (3.35)).

$$\eta = \phi_1 - \phi_2 - U\left(\theta_{n,surf}\right) \tag{3.34}$$

$$\theta_{n,surf} = \frac{V_n(t)}{N_{tot}}c_{n,surf} = \frac{\pi\left[R_s(t)\right]^2 L_0}{N_{tot}}c_{n,surf} \tag{3.35}$$

Again, the temporal evolution of the nanorod radius can be correlated to the volumetric evolution and consequently, the molar volumes and average state of charge inside the nanowire (Equations (3.36-3.38). It is to be noted that the nanowire radius increases by the power of 0.50 as

compared to the nanosphere which increases by the power of 0.33. This indicates that, for the same initial radius, the fully lithiated nanorod radius will exceed the fully lithiated nanosphere radius.

$$\frac{V_n(t)}{V_{n,0}} = \frac{\pi\left[R_n(t)\right]^2 L_0}{\pi R_0^2 L_0} = \frac{\Omega_{Si} + 3.75\Omega_{Li}\bar{\theta}_n}{\Omega_{Si}} \Rightarrow \frac{R_s(t)}{R_0(t)} = \left(\frac{\Omega_{Si} + 3.75\Omega_{Li}\bar{\theta}_n}{\Omega_{Si}}\right)^{1/2} \tag{3.36}$$

$$\bar{\theta}_n = \frac{It}{nFN_{tot}} = \frac{\pi\left[R_n(t)\right]^2 L_0}{N_{tot}}\bar{c}_n,\ \bar{c}_n = \frac{\int_0^{R_n(t)} c_n\left(2\pi r L_0\right)dr}{\pi\left[R_n(t)\right]^2 L_0} \tag{3.37}$$

$$\theta_n = \frac{\pi\left[R_n(t)\right]^2 L_0}{N_{tot}} c_n = \frac{c_n}{c_{max}}\left[\frac{R_s(t)}{3.8^{1/2} R_0}\right]^2 \tag{3.38}$$

The aforementioned coupled equations are discretized using the finite volume framework utilizing central differencing spatial scheme with Euler implicit (backward) time stepping scheme. To obtain a good comparison between the nanospheres and nanorods, performance of equal volumes, (and hence mass) are contrasted between the two morphologies. Consequently, nanospheres of pristine radius R_0 are contrasted against nanorods of pristine radius R_0 and length, $L_0 = 4R_0/3$. Furthermore, equivalent volume high aspect ratio nanorods are investigated as well with $L_o / R_0 = 5, 10$ and contrasted with the aforementioned cases to delineate the effect on the performance.

3.2.3 Results and Discussion

Figure 3.12(a) shows the schematic of the volume expansion of the silicon nanospheres and nanowires respectively. Radial diffusion in both cases leads to temporal increase of the radius with lithiation and the length remains constant for the nanorod. Material parameters for silicon active material, in particular, the transport, kinetic and thermodynamic properties are reported in Table 3-2. Furthermore, Table 3-3 lists the equivalent volume forms of the nanospheres and nanorods with $L_o / R_o = 1.33, 5, 10$ respectively. The corresponding 1C current density for each of these configurations is also reported.

Table 3-2 List of baseline geometric, kinetic and transport parameters for silicon nanosphere and nanorods.

Parameter	Symbol	Value	Reference
Initial Radius	R_0 (nm)	30	[174]
Diffusivity	D_{Li} (m^2/s)	10^{-18}	[205]
Rate Constant	k [(m/s)(mol/m^3)$^{-0.5}$]	2.5×10^{-9}	[195]
Molar volume of Li	Ω_{Li} (m^3/mol)	9×10^{-6}	[162]
Molar volume of Si	Ω_{Si} (m^3/mol)	1.2×10^{-5}	[211]
Maximum lithium concentration based on final radius	c_{max} (mol/m^3)	81967	Calculated
Maximum lithium concentration based on initial radius	$c_{max,0}$ (mol/m^3)	311474.6	Calculated
Density	ρ_{Si} (kg/m^3)	2329	[205]
Temperature	T (K)	300	Assumed

Table 3-3 Dimensions of nanospheres and nanorods based on equivalent volume.

Nanosphere	Nanorod		Nanorod5		Nanorod10		1C Current (A)
R_0 (nm)	R_0 (nm)	L_0 (nm)	R_0 (nm)	L_0 (nm)	R_0 (nm)	L_0 (nm)	
10	10	13.33	6.44	32.20	5.11	51.09	3.4916×10^{-17}
30	30	40.00	19.31	96.55	15.33	153.26	9.4272×10^{-16}
50	50	66.67	32.18	160.90	25.54	255.43	4.3645×10^{-15}
75	75	100.00	48.27	241.35	38.31	383.15	1.4730×10^{-14}
100	100	133.33	64.37	321.85	51.09	510.87	3.4916×10^{-14}

Nanospheres vs Nanorods with Same Volume and Same Initial Diameter

Figure 3.12 (b) and (c) showcase the silicon local state of charge as a function of particle radius at 5C lithiation rate for the nanosphere and nanorods of same initial radius, R_0 = 30 nm. For equivalent volume comparison, the silicon nanorod has an initial length, L_0 = 39.90 nm. During lithiation as the Li enters the surface, the surface concentration is higher as compared to the concentration at the particle center. This results in a positive concentration gradient inside the particle as we go from the particle center to the surface. For 5C lithiation corresponding to a discharge of the Li-Si half-cell, the total nominal time of discharge is 720s and correspondingly the concentration profiles are shown at 100s, 200s, 400s and 600s. As the silicon particle gets filled,

the concentration inside the particle increases resulting in the upwards shift of the concentration profiles with lithiation time. An important observation is that surface state of charge of the silicon nanorods increases at a faster pace as compared to the silicon nanosphere of the same diameter. This is directly correlated to the swifter increase of the nanorod radius as compared to the nanosphere radius. Comparing equations (3.25) and (3.36), we observe that the nanorod radius increases by the power of 0.50 as compared to the smaller power of 0.33 exhibited by the nanosphere radius. Diffusion limitations are exacerbated at larger particle radius as Li has to diffuse through a longer distance in the nanorod as it reaches end of discharge. Consequently, the Li concentration shows a steeper concentration gradient in the nanorod as compared to the nanosphere. Although the larger surface area of the nanorod as compared to the nanosphere results in smaller effective current density (and hence lithium flux) at the nanorod surface as compared to the nanosphere, this advantage of the nanorod is overshadowed by the extra diffusion limitations.

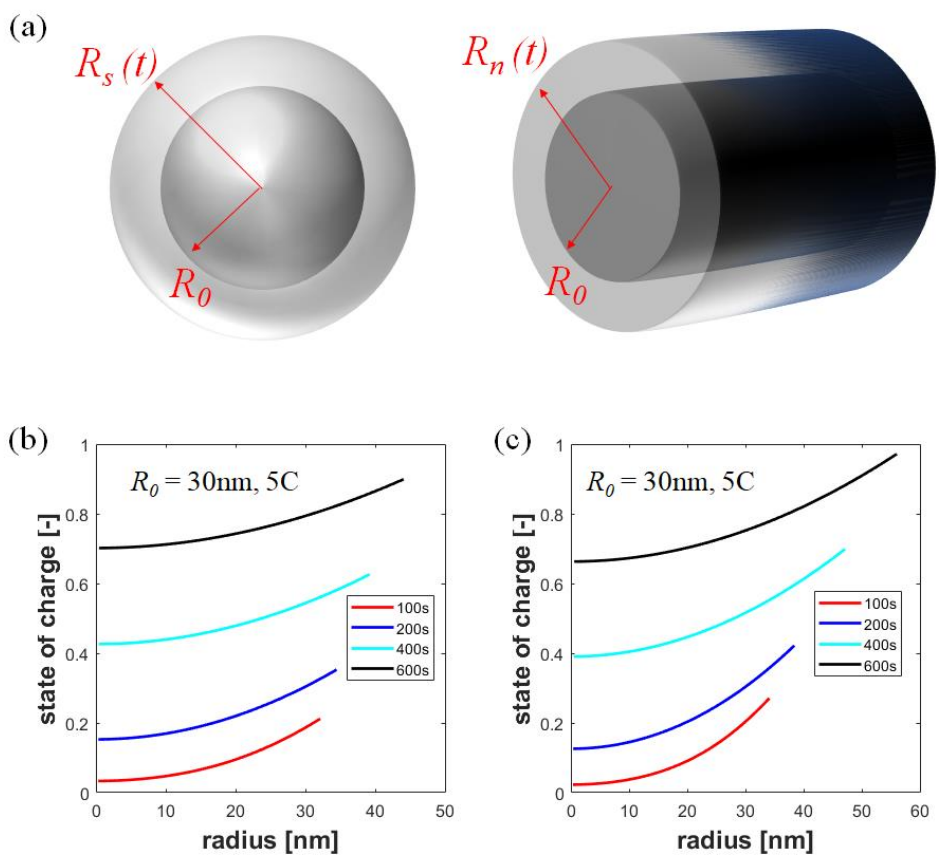

Figure 3.12(a) Schematic of lithiation of nanosphere (left) and nanorod (right). Only radial diffusion is considered and the length of the nanorod remains the same during lithiation. Dimensionless concentration profile as a function of radius for (b) nanosphere and (c) nanorod of equivalent volumes. Both the nanosphere and nanorod have initial radius 30 nm and the current

rate of operation is 5C. The concentration profiles are shown at 100s, 200s, 400s and 600s. Nanorods have steeper concentration gradient than nanospheres.

Figure 3.13 (a) and (b) compare the rate performance of the two morphologies at different C-rates (1C, 3C, and 5C). As the C-rate increases, the voltage vs specific capacity curves shift downwards for both the silicon nanospheres and nanowires. As the C-rate increases, the reaction current density at the particle surface increases resulting in larger overpotentials at the surface. This results in lower voltage with increase of current density. Again, the performance of the silicon nanospheres overshadows the performance of the silicon nanorods. At 1C, 3C and 5C the obtained specific capacity for nanospheres are 3536.4 mAh/g, 3444.5 mAh/g and 3349.8 mAh/g respectively. The corresponding specific capacities for the nanorods are 3485.1 mAh/g, 3288.5 mAh/g and 3085.9 mAh/g respectively. As the C-rate increases, the divide between the nanosphere and nanorod performance increases. The larger surface area of the silicon nanorod is not enough to help its performance surpass that of the silicon nanosphere. Particle radius is the dominant factor here with the nanorod radius increasing more rapidly than the nanosphere radius. This is further exemplified by (c) which shows the temporal evolution of radius at 5C rate for both the nanosphere and nanorod. At the end of lithiation, the nanosphere with initial radius 30 nm has the fully lithiated radius close to 46 nm. In comparison, the nanorod with initial radius 30 nm has the fully lithiated radius close to 57 nm. Furthermore, Figure 3.13(d) exhibits the effect of the current rate on the fully lithiated particle radius towards the end of lithiation. At slower current rates, the particle concentration is homogeneously distributed resulting in uniform lithiation throughout the silicon material. The degree of utilization of the silicon material achieved is higher at low rates, consequently, net amount of Li entering the silicon host at small current rates is considerably larger as opposed to high C-rate operation. The aforementioned dynamics results in larger volume change of both the silicon nanospheres and nanowires at low rates; this is represented in the Figure 3.13(d) by the gently downward sloping fully lithiated radius curves.

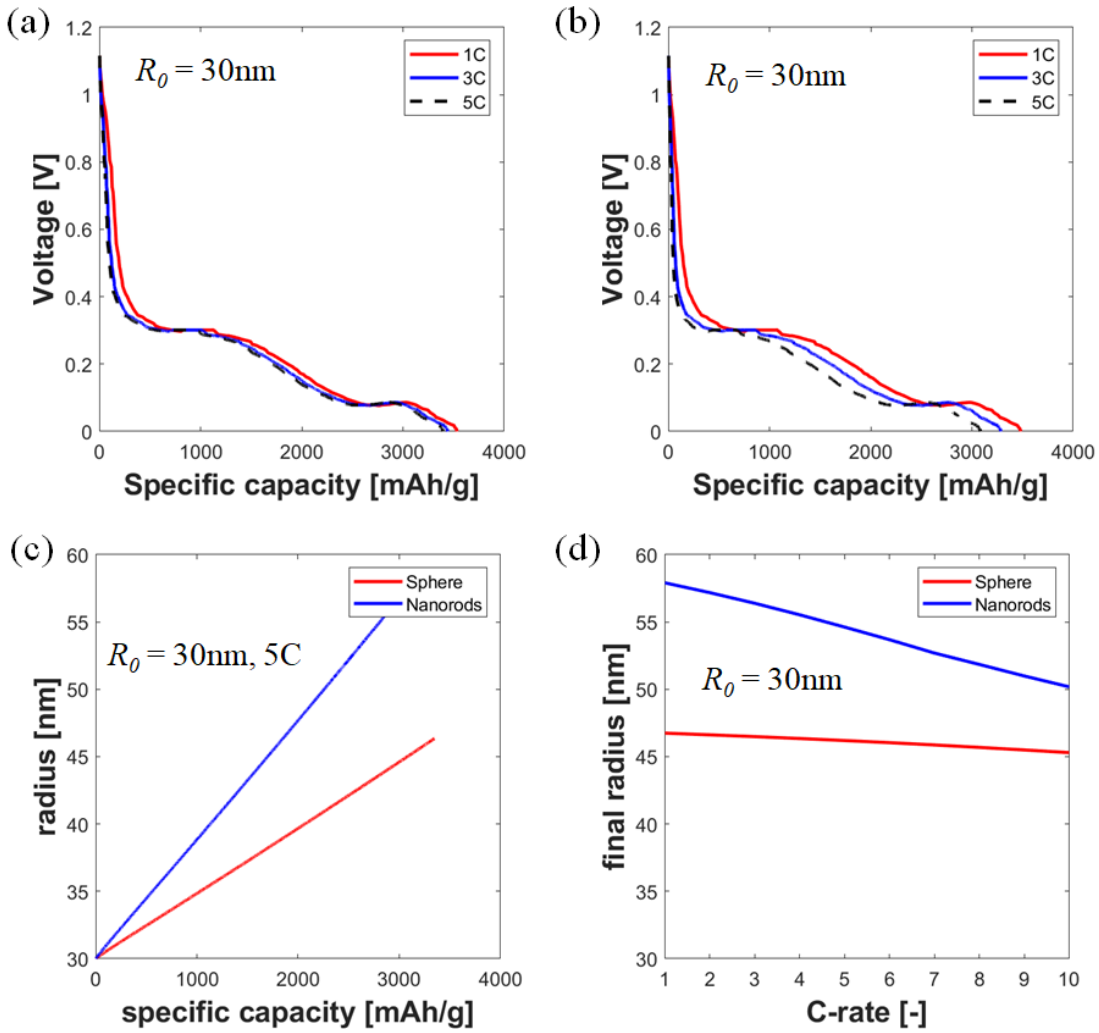

Figure 3.13 Voltage vs specific capacity rate performance curves for (a) nanosphere and (b) nanorod of equivalent volumes. Both the nanosphere and nanorod have initial radius 30 nm and the current rates of operation shown are 1C, 3C and 5C. Nanospheres have better rate performance than nanorods. (c) Temporal evolution of radius as a function of specific capacity nanosphere and nanorod of equivalent volumes. Both the nanosphere and nanorod have initial radius 30 nm and the current rate of operation here is 1C. Nanorods show rapider radial growth as compared to nanospheres. (d) Final lithiated radius for nanospheres and nanorods as a function of C-rate. As C-rate increases, the degree of utilization of the particle decreases because of steeper concentration gradients resulting in lesser increase in the total particle size.

The aforementioned insights point to the fact the nanowires are not always better as compared to nanospheres. In literature, experimental investigations of nanowire silicon have reported superior performance as compared to nanosphere silicon. This dichotomy can be explained by considering nanowires with larger aspect ratios. There is an optimum threshold of

the nanorod length to radius ratio beyond which the nanorod rate performance exceeds the nanosphere rate performance for the same equivalent volume. In the following section, we investigate this phenomenon to delineate this threshold.

Nanospheres vs Nanorods with Same Volume and Varying Diameter

Table 3-3 lists the nanorods of equivalent volume to nanospheres of radius 10 nm, 30 nm, 50 nm, 75 nm and 100 nm for aspect ratio $L_0 / R_0 = 1.33, 5, 10$. The corresponding 1C current density is also tabulated for all the scenarios. Figure 3.14 (a-d) displays contour plots of the obtained specific capacity in mAh/g as a function of the equivalent sphere diameter and C-rate for the nanospheres, nanorods with aspect ratio $L_0 / R_0 = 1.33$, nanorods with aspect ratio $L_0 / R_0 = 5$ and nanorods with aspect ratio $L_0 / R_0 = 10$ respectively. As we go from Figure 3.14 (a) - nanospheres to Figure 3.14 (b) – nanorods with $L_0 / R_0 = 1.33$, we see an increase in the low specific capacity region (red) at high C-rates and particle sizes. This is a direct consequence of the diffusion limitations overshadowing the active area increase. Consequently, nanorods with aspect ratio close to 1.33 are inferior to the nanospheres for all radii and C-rates. Moving on, if we compare Figure 3.14 (a) - nanospheres and Figure 3.14 (c) – nanorods with $L_0 / R_0 = 5$, the specific capacity map is almost identical for all the C-rates and particle sizes. As we increase the aspect ratio, for the same equivalent volume, nanorod has a smaller initial radius as compared to the nanospheres. Consequently, the diffusion limitations start to diminish. In conjunction with the beneficial impact of additional surface area afforded by the nanowires, the nanowire performance begins to supersede that of the nanosphere. As the initial nanorod radius decreases with aspect ratio increase, the fully lithiated nanorod radii also remains smaller than the fully lithiated nanosphere radii. Consequently, throughout the entire lithiation process the nanorod experiences inferior diffusion limitations as compared to the nanosphere. The alliance of inferior diffusion limitations and larger active area enabled minor kinetic limitations allows the nanorod performance to trump the nanosphere rate performance. This is further exemplified in Figure 3.14 (d) – nanorods with aspect ratio $L_0 / R_0 = 10$ which has the least amount of low specific capacity (red) zones. Thus, it is imperative to go for nanorods with aspect ratio $L_0 / R_0 \geq 5$ in order to achieve high performance

silicon anodes. Nanospheres can trump nanorods with aspect ratios less than 5 in performance based on diffusion limitations.

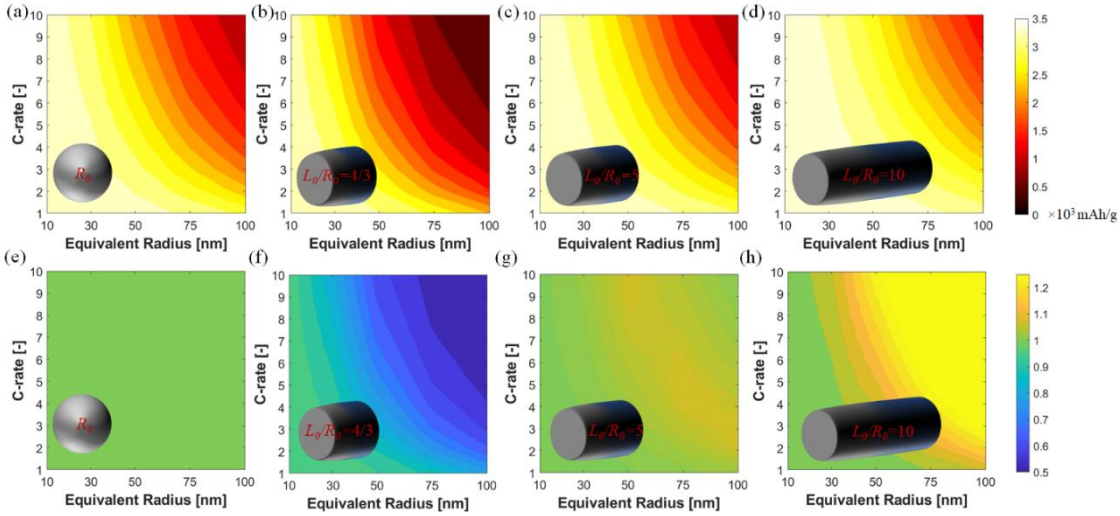

Figure 3.14 Specific capacity contour plots as a function of equivalent spherical particle radius and C-rate for (a) nanosphere, (b) nanorods with same initial diameter as the nanosphere, aspect ratio L_0/R_0=1.33, (c) nanorods with aspect ratio L_0/R_0=5 and (d) nanorods with aspect ratio L_0/R_0=10.0. Ratio of specific capacity obtained to the specific capacity of nanospheres for (e) nanosphere, (f) nanorods with same initial diameter as the nanosphere, aspect ratio L_0/R_0=1.33, (g) nanorods with aspect ratio L_0/R_0=5 and (h) nanorods with aspect ratio L_0/R_0=10.0. Nanorods outperform nanospheres when its aspect ratio is greater than 5.

Figure 3.14 (e-h) further highlights this insight in a more compelling fashion. Here, we have shown the rate performance capacity contour maps for the aforementioned morphologies normalized by the nanospheres specific capacity. Figure 3.14 (e) corresponds to the nanospheres, hence, normalized by its own capacity it exhibits a ratio of 1 throughout. Figure 3.14 (f) corresponds to the nanorods with $L_0 / R_0 = 1.33$ and it displays blue zones with ratio < 1 at high C-rates and particle sizes, exemplifying its inferior performance. Figure 3.14 (g) shows the performance ratio for nanorods with $L_0 / R_0 = 5$ and we see a performance ratio very close to or just greater than 1 for the entire range of particle radii and C-rates investigated. This further demonstrates $L_0 / R_0 = 5$ as the threshold beyond which the nanorod performance starts to surpass that of the nanosphere. Finally, Figure 3.14 (h) compares the performance of nanorods with $L_0 / R_0 = 10$ to that of the nanospheres, and it exhibits a ratio value greater than 1, sometimes as

high as 1.2-1.4, for the entire span of C-rates and particle radius. This cements the fact that larger aspect ratio nanorods are viable candidates for silicon anodes.

The results shown above consider only radial diffusion in the nanowires. Short nanowires will have considerable areal contributions from the nanowire ends and axial diffusive transport can induce substantial concentration gradients in the axial direction. We perform a simple calculation to find the ratio of the curved surface ($A_{s,n} = 2\pi RL$) area to the circular end area $A_{c,n} = \pi R^2$. Note that we are still considering only one end, as in the experiments for the nanowires, the nanowires were grown directly from the current collector, so one end is not subject to any flux. This ratio comes out to be $A_s / A_c = 2L/R$. For *L/R* ratio changing from 1 to 10, the corresponding active area ratio changes from 2 to 20, thereby showing that the assumption of lithiation occurring primarily across the radial direction is strictly accurate for larger aspect ratios. Furthermore, for *L/R* ratio changing from 1 to 10, the corresponding diffusion lengths ratio that the Li^+ ions need to travel in the axial and radial directions go from 1 to 10 as well. As we go for larger aspect ratios, the diffusion length along the axial direction increases to much larger values as compared to the radial direction, thereby assuming radial diffusion being predominant very valid for long nanorods. The shortest nanorods that we consider have a *L/R* ratio 1.33, so we have an active area ratio 2.66 and diffusion length ratio 1.33 correspondingly. Allowing for axial diffusion as well and if diffusivity magnitudes in both the radial and axial direction are the same, we can predict that the nanorod will start outperforming spherical morphology at *L/R* ratios slightly less than 5 as well.

For short cylinder with both radial and axial diffusion contributions, concentration solve cognizant of both the diffusion modes is required (a 2D solve). The final expansion ratio in the radial direction (R_f/R_i) and axial direction (L_f/L_i) needs to be ascertained apriori as well which will be dependent on the magnitudes of the diffusivity magnitudes in the radial (D_r) and axial direction (D_z). Furthermore, the state of charge dependence of the radius ratio and length ratio needs to be ascertained. The assumption of unchanged length allowed for easier treatment of the radius ratio as a function of state of charge and is applicable for large aspect ratio nanorods. The inclusion of axial diffusion will be part of the future work.

Experimental Validation and Delineation of Silicon Specific Material Parameters

The erstwhile study delved deep into the mathematical formalism/results of the morphological evolution of the silicon nanospheres and nanorods with lithiation and its impact on the corresponding rate performance. The results have been derived assuming the diffusivity and exchange current density values reported in the seminal article by Chandrasekaran *et al.* giving the single particle formalism for high expansion materials [205]. We scoured through the silicon literature for its material values and found that a wide range of diffusivity and exchange current density magnitudes has been reported. The results of this survey are tabulated in Table 3-4. Diffusivity magnitudes range from 10^{-16} m^2/s to 10^{-18} m^2/s, spanning three orders of magnitude are provided in literature. The spread in the exchange current density data is even wider, ranging from 10^{-9} A/m^2 to 10 A/m^2, spanning ten orders of magnitude. For the kinetics data, either the exchange current density or the rate constant is reported generally. The variation in the magnitudes is evident even in contiguous works by the same authors; Chandrasekaran *et al.* report the lithiation rate constant to be of the order of 10^{-9} $(m/s)(mol/m^3)^{-0.5}$ for the single particle model analysis and later on use the value of 10^{-13} $(m/s)(mol/m^3)^{-0.5}$ in the macrohomogenous model analysis[205]. To arrive at a clear consensus on the correct magnitude range for the diffusivity and exchange current density values, it is essential to compare experimental datasets with the corresponding simulated counterparts. In this regard, the single particle formalism for nanospheres and nanorods holds great promise. Nanorods and nanospheres, owing to their miniscule size are devoid of crack formation. Consequently, experimental performance datasets for silicon nanospheres/nanorods should have a good match, ideally, with simulations cognizant of the evolving morphology paradigm. Intuitively, this match should be even better at low C-rates when the transport limitations are negligible, an assumption inherent to the single particle formalism.

Table 3-4 Diffusivity, exchange current density/rate constant values of silicon lithiation reported in literature.

Year	Reference	Diffusivity D_{Li} (m^2/s)	Exchange Current Density i_0 (A/m^2)	Rate Constant k [(m/s)(mol/m^3)$^{-0.5}$]
2009	Srinivasan[205]	-	10^{-9}	-
2009	Ding *et al.*[205]	10^{-16}	-	-
2009	Baggeto *et al.*[205]	-	10	-
2010	Xie *et al.* [205]	3×10^{-17} – 3×10^{-16}	-	
2010	Chandrasekaran *et al.* [206]	10^{-18}	-	2.5×10^{-9}
2010	Chandrasekaran *et al.* [212]	10^{-16}	-	10^{-13}
2011	Li *et al.* [213]	7.7×10^{-18} – 1.4×10^{-17}	0.7 – 1.3	-
2012	Pharr *et al.* [214]	2.0×10^{-16}	-	-
2013	Sethuraman *et al. [215]*	-	8.5×10^{-7}	-
2015	Swamy *et al.[205]*	-	1.0	-
2019	Mai *et al.* [206]	10^{-16}	1.0	-

To this effect, we identify two seminal experimental silicon articles in literature pertaining to the rate performance of nanospheres and nanowires. Wu *et al.* synthesized stable silicon anodes consisting of conductive hydrogel coated silicon nanoparticle, providing rate performance datasets ranging from C/12 to C/1.2 current rates with maximum specific capacity around 2500 mAh/g [216]. The average diameter of the spherical silicon nanoparticles was reported to be 60 nm. Furthermore, Chan *et al.* was able to grow silicon nanowires on the current collector with initial average diameter around 89 nm[217]. These nanowires had large aspect ratios, as evident from the SEM micrographs, with nanowire length larger than 5 µm on an average. The silicon nanowires outperformed the nanospheres from the preceding article with lithiation rate performance reported close to 3600 mAh/g at C/20 current rate. Using these two articles as our experimental basis, we performed our single particle model computations to obtain the exchange current density and diffusivity values providing a good match between the two. Figure 3.15(a) and (b) presents the comparison between the experimental and simulated datasets for the nanowires and nanospheres

respectively, achieving a decent congruence between them. The corresponding diffusivity and rate constant values are tabulated in Table 3-5. In an ideal scenario, a single value of the silicon diffusivity and exchange current density should be able to provide a match for both morphological variations. While this posed a formidable challenge, we were able to discern a much smaller range of the diffusivity and rate constant values satisfying both the scenarios. The results exhibit good coherence for silicon diffusivity ranging between 10^{-17} and 10^{-18} m^2/s, and the kinetic rate constant values 1.8×10^{-15} to 1.4×10^{-14} $(m/s)(mol/m^3)^{-0.5}$. The kinetic rate constant magnitudes reported here are especially important, as it narrows the order of magnitude range reported in literature from 10 to 1. Any differences in between the experiments and the simulation results can be attributed to differing experimental conditions, transport limitations at high C-rates and neglecting of any contact/SEI film resistance in the model formulation.

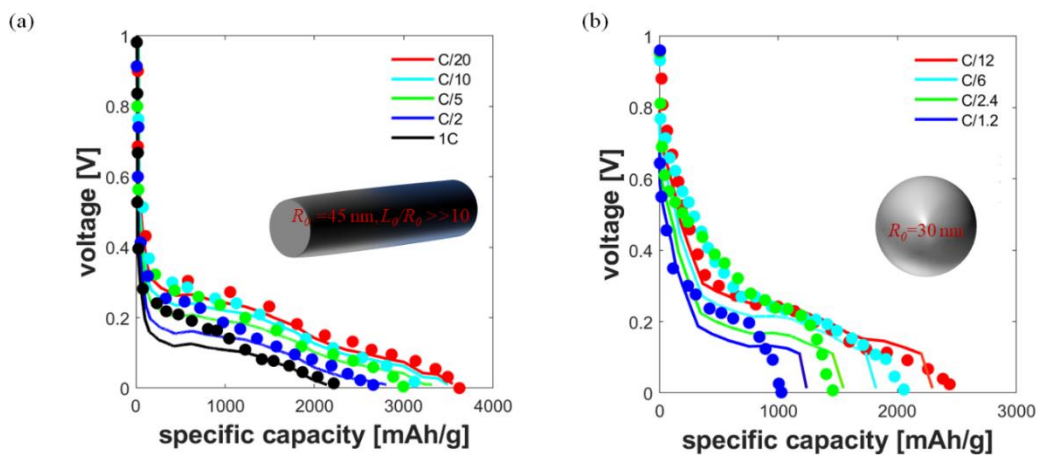

Figure 3.15 Rate performance comparison in between model and experiments for (a) nanorods and (b) nanospheres. Experimental data is shown as symbols and simulation data is shown as lines. For nanorods, we compare against the experimental dataset of Chan *et al.* [218] For nanospheres, we compare against the experimental dataset of Wu *et al.* [210] Good match is obtained in between the experimental and simulation dataset for both the morphological variations investigated.

Table 3-5 Property values used in this study to obtain the match between experimental and computational datasets.

Parameter	Symbol	Nanospheres	Nanorods
Initial Radius	R_0 (nm)	30	45
Length	L_0 (μm)	-	5
Diffusivity	D_{Li} (m^2/s)	10^{-17}	10^{-18}
Rate Constant	k [$(m/s)(mol/m^3)^{-0.5}$]	1.8×10^{-15}	1.4×10^{-14}

3.2.4 Conclusion

A coupled diffusive transport-reaction kinetics study cognizant of large volume expansion of the silicon active material is performed to delineate the variation in rate performance of silicon nanospheres and nanorods during lithiation. The single particle model is reformulated to account for the radial evolution of silicon nanospheres/nanorods while accounting for the ramifications on reaction area and transport. It has been found that silicon nanowires do not always perform superior to silicon nanospheres. For the same volume and initial radius, nanorods rate performance specific capacity is below nanospheres. The criterion for better performance of the silicon nanorods as compared to nanospheres is dictated by the aspect ratio of the nanorods (length to radius) with the threshold value located at $L_0 / R_0 = 5$. This is a consequence of exacerbated rate of diffusion limitations increase in nanorods trumping the beneficial impact of larger surface area. Upon lithiation, nanorods swell at a faster rate as compared to nanospheres resulting in enhanced diffusion limitations. Furthermore, the kinetic rate constant and diffusivity parameters are reported for the silicon anode and they provide a decent match with the experimental nanospheres and nanowires rate performance dataset.

4. ELECTROCHEMICAL AND THERMAL INTERACTION IN LITHIUM PLATING AND SAFETY

Relevant Publications and/or Working Papers

1. (joint first author) B.S. Vishnugopi, **A. Verma**, P.P. Mukherjee, *"Fast Charge of Lithium-Ion Batteries via Electrode Engineering*"
2. C-F. Chen., **A. Verma**, P.P. Mukherjee., "*Probing the Role of Electrode Microstructure in the Lithium-ion Battery Thermal Behavior*", Journal of Electrochemical Society **164** (11), E3146 – E3158 **(2017)**.

4.1 Background

Battery electric vehicles (BEVs) are gradually pervading the commercial light-duty vehicles market. However, wider endorsement of BEVs requires tackling of the prolonged charge duration bottleneck, such that it reaches parity with internal combustion engine vehicle (ICEV) refueling times.[219] The proliferation of vehicle electrification technology is predicated on rapid advancement of lithium-ion battery (LIB) science in conjunction with ancillary support systems, most critical of which is extreme fast charging infrastructure.[139, 220] Existing fast charge stations capabilities of 50-kW and 120-kW have improved the charging times considerably, plateauing around 20 minutes for a 200-mile range. Charging at 400kW, or extreme fast charging (XFC), has been proffered as an attractive upgrade to enabling a 200-mile charge in less than 10 minutes, rivaling ICEV refueling times. However, the path to widespread adoption of XFC is rife with scientific and engineering barriers, requiring significant in-depth analysis for remedial strategies.

On the battery front, technology gaps and thermal considerations form the crux of the scientific challenges surrounding fast charge technology deployment. Lithium-ion batteries generally comprise of intercalation electrodes and electricity is produced as a result of shuttling of Li-ions between an anode (e.g. graphite)[4, 221-223] and a cathode (e.g. metal oxide)[224, 225] through an electrolyte (usually organic solvent with a Li-salt),[226] with electrons moving in the external circuit. LIB physics encompass a multitude of coupled transport processes (species, charge and thermal transport), electrochemical (Li-intercalation, Li-plating, electrochemical solid-electrolyte interphase) and chemical reactions (chemical solid-electrolyte interphase, electrolyte reduction, side reactions) as well as mechanical effects (diffusion induced stress) and a delicate

balance between all these phenomena is essential to good performance and long life of a LIB.[227-229] Fast charging necessitates operation of the LIB at increased current rates which can exacerbate the deleterious effects and adversely impact the performance, safety and life of the battery. Chief amongst these effects are increased propensity for lithium plating at the anode, enhanced rate of side reactions, amplified heat generation causing spike in battery temperatures which may elevate to thermal runaway scenario, and larger diffusion induced stress inside the Li-ion active material (AM) host increasing fracture tendencies.

Li^+ ion transport from the cathode to anode during charge and subsequent intercalation of the ion into the crystal structure voids of the negative electrode material is governed by migration and diffusion in the electrolyte phase and diffusive transport inside the AM phase. Diffusion limited transport in the AM phase is considerably slow, thus, operation of LIBs at higher rates will lead to discrepancy in the rates of lithium transport to the anode surface (much higher) and intercalation inside the anode material. This results in Li plating at the anode surface.[230-236] It can also occur if the negative electrode potential goes below 0V (vs Li/Li^+) which is exacerbated at higher cell voltages (> 4V) and for lower anode to cathode capacity ratio (close to 1.1). Furthermore, diffusive transport becomes increasingly sluggish at low temperatures, as is evident by occurrences of plating at charge rates as low as C/6 at -20˚C.[237-241] Defects, such as pore closure in the separator, can create localized current hotspots with large overpotential, increasing the propensity for Li plating.[242] The deposited Li metal is found to be electronically disconnected from the negative electrode material and hence does not participate in any further electrochemical reactions, as is evidenced by non-removal of the plated Li-metal during any subsequent slow discharges.[243] Consequently, LIB operation at large current rates as well as high capacity loading contributes to faster capacity fade due to loss of electrochemically active Li in the form of deposited Li metal. Li metal deposits at the anode also pose a safety risk as they can penetrate through the separator to the cathode leading to catastrophic internal short of the cell. This phenomenon is aggravated in LIBs with Li metal anode, owing to the formation of dendritic protrusions at the anode during charging, which reach the cathode through the separator even at low current densities.[244, 245] For fast charging operations devoid of plating, lithium titanate has been found to be a viable negative electrode active material owing to higher potential at fully lithiated state (0.05V vs Li/Li^+) and better kinetics.[246-254]

The enhancement of energy density of LIBs through electrode thickness increase is also at loggerheads with power density increase due to aforementioned problems.[255-257] For thick electrodes, current density for a C-rate is higher as compared to thin electrodes, leading to larger overpotentials and Li plating tendencies. Furthermore, at the large current densities associated with extreme fast charging ($\geq$ 6C), electrolyte transport limitations also become evident leading to drastic reduction in charge capacity. Fast charging causes enlarged concentration gradients in the electrolyte leading to severe Li^+ depletion close to the anode surface. Consequently, the cell voltage reaches the upper voltage during constant current charge at exceedingly low charge capacities, rendering the fast charge process ineffective.

Battery thermal considerations also come to the forefront for enabling XFC. LIB systems exhibit robust performance within a narrow temperature window and are susceptible to wide temperature variation during operation. High temperatures (> 80˚C) can lead to rapid battery degradation while low temperatures (< 0˚C) diminish available capacity and power density.[258-260] Heat generation inside the LIB originates from ohmic contributions due to resistance to ionic and electronic transport inside electrolyte and electrode respectively, kinetic contributions due to electrochemical reaction at the electrode-electrolyte interface and entropic contributions from thermodynamics of the intercalation reactions.[261] This heat generation approximately scales positively with current density, and thus, increases remarkably at high current operations. Consequently, with usage of high current rates in XFC, thermal management of the LIBs operating around normal temperatures, say 30˚C, gains additional significance, since LIB temperatures can accelerate beyond the temperature bounds faster as compared to low current operation. At low operating temperatures, XFC can prove to be a boon from a thermal standpoint, since the increased heat generation can push the battery temperature upwards to jumpstart the sluggish transport and kinetics characteristics associated with sub-zero temperatures.

In this work, we aim to derive insights into the fast charge performance of lithium-ion batteries comprised of graphite anode and lithium nickel-manganese-cobalt oxide (NMC333) cathode, cognizant of plating kinetics, electrode microstructure and thermal considerations. We delineate optimal operating conditions (current rate) and anode design criteria for a 2.2Ah cylindrical cell, conducive to a diverse set of ambient temperatures. The rest of the article is divided as follows. The Methodology section provides the governing differential equations for modeling intercalation and plating dynamics during fast charge, alongside a description of the virtual

electrode microstructure reconstruction and effective property characterization technique. The Results and Discussion section elucidates the effect of plating-thermal interactions during cell operation. Based on this, performance-safety maps are generated for ambient operating temperatures of -10˚C, 0˚C and 25˚C to outline desirable anode porosities and current rate zones for fast charge.

4.2 Methodology

In this work, we model the electrochemical-thermal performance of lithium-ion batteries, cognizant of additional plating dynamics and microstructural considerations. The algorithmic flow follows generation of virtual microstructures on which effective geometric and transport parameters including active area, tortuosity, ionic conductivity are computed. The computed parameters serve as input to the performance model to discern the voltage and thermal characteristics of the cylindrical 18650 Li-ion cell. We present the governing differential equations for modeling the electrochemical-thermal performance of the LIB followed by a summary of the virtual microstructure generation and characterization paradigm.

4.2.1 Intercalation and Plating Dynamics

Our system of choice comprises of graphite [LiC_6] anode and NMC333 [$Li(Ni_{1/3}Mn_{1/3}Co_{1/3})O_2$] cathode. The governing equations and the design parameters are presented here.

Butler-Volmer kinetics with symmetric charge transfer coefficients is used to describe the lithium intercalation reaction at both the anode and cathode.

$$i_1 = i_{0,1}\left[\exp\left(\frac{0.5F}{RT}\eta_1\right) - \exp\left(-\frac{0.5F}{RT}\eta_1\right)\right] \tag{4.1}$$

$$\eta_1 = \phi_s - \phi_e - U_1(\theta, T) - i_1 R_{film} \tag{4.2}$$

$$i_{0,1} = k_1(T) c_s^{0.5} c_e^{0.5} \left(c_{s,\max} - c_{se}\right)^{0.5} \tag{4.3}$$

The functional relationships of OCP for graphite and NMC are readily available in literature and have been taken from [262]. The exchange current density $i_{0,1}$ is a function of temperature dependent rate constant k_1 and solid surface lithium concentration c_s and electrolyte

phase concentration c_e. Here, R_{film} is the resistance of the film comprising of the SEI and plated Li that evolves at the anode surface. R_{film} is assumed to be zero for the cathode particles. In addition, plating kinetics at the graphite anode during charge is modeled with asymmetric charge transfer coefficients given by:

$$i_2 = \min\left\{0, i_{0,2}\left[\exp\left(\frac{0.3F}{RT}\eta_2\right) - \exp\left(-\frac{0.7F}{RT}\eta_2\right)\right]\right\} \tag{4.4}$$

$$\eta_2 = \phi_s - \phi_e - U_2 - i_2 R_{film};\ U_2 = 0.0\ \text{V};\ \ i_{0,2} = k_2 F c_e^{0.3} \tag{4.5}$$

The minima function ensures occurrence of plating only when $\eta_2 < 0$ at locations inside the anode in accordance with Ge *et al.*[263] The anode film resistance is correlated to the film thickness, δ_{film}, and the plating current, i_2, and its temporal evolution is given by:

$$R_{film} = \frac{\delta_{film}}{\kappa_{film}};\ \frac{d\delta_{film}}{dt} = -\frac{i_2 M_{Li}}{\rho_{Li} F} \tag{4.6}$$

Here, κ_{film} is the ionic conductivity of the surface film and M_{Li} and ρ_{Li} correspond to the molar mass and density of lithium respectively, with the values taken from Ge *et al.*[28]

We assume spherical geometry for the active material particles and use Fick's law to describe atomic Li transport inside the particles.

$$\frac{\partial c_s}{\partial t} = \frac{1}{r^2}\frac{\partial}{\partial r}\left(D_s r^2 \frac{\partial c_s}{\partial r}\right) \tag{4.7}$$

$$\text{BC:}\ \left.\frac{\partial c_s}{\partial r}\right|_{r=0} = 0\ ,\ \left.\frac{\partial c_s}{\partial r}\right|_{r=R_s} = -\frac{i_1}{D_s F}\ ,\ \text{IC:}\ c_s = const$$

Diffusion of lithium ions inside the electrolyte is modeled using Nernst-Planck equation with D_e^{eff} giving the effective diffusion rate of lithium ions in the electrolyte phase. The volumetric source term in the equation represents the production/destruction of lithium ions in the electrolyte due to the reaction current. t_+ is the transference number of lithium ions and represents the fraction of current carried by the lithium ions, usually taken to be a constant. The relation

between volumetric current density j and reaction current density i at the particle surface is given by Equation (4.9). Here, a_s is the electrode active area per unit volume.

$$\varepsilon \frac{\partial c_e}{\partial t} = \nabla.\left(D_e^{eff} \nabla c_e\right) + \frac{1-t_+}{F} j \tag{4.8}$$

$$j = a_s \left(i_i + i_2\right) \tag{4.9}$$

Electric potential in the solid phase ϕ_s can be determined using Ohm's law. At the electrode-current collector interface, the current flux BC is prescribed. Here, I is the total current coursing through the cell and A is the electrode-current collector interface area. The separator hinders electronic current flow, as such, the flux of electronic current is zero at the electrode-separator interface.

$$\nabla \cdot \left(\sigma_s^{eff} \nabla \phi_s\right) - j = 0 \tag{4.10}$$

Charge motion in the electrolyte phase is driven by gradients of electrolyte potential ϕ_e and ionic concentration c_e . The total ionic current has contribution from two components that the first term represents the migration current due to Ohm's law while the second term represents the diffusional current arising from differences in concentration of ions throughout the length of the cell. The diffusional conductivity κ_D is related to ionic conductivity κ and is given by Equation (4.12).

$$\nabla \cdot \left(\kappa^{eff} \nabla \phi_e\right) + \nabla \cdot \left(\kappa_D^{eff} \nabla \ln c_e\right) + j = 0 \tag{4.11}$$

$$\kappa_D^{eff} = \frac{2RT\kappa^{eff}}{F}\left(t_+ - 1\right)\left(1 + \frac{d \ln f_\pm}{d \ln c_e}\right) \tag{4.12}$$

Energy conservation in the cell can be described using a lumped thermal model owing to low Biot number characteristics of an 18650 cell under natural convection conditions. The heat generation rate $\dot{Q}$ comprises of kinetic (intercalation/plating reaction overpotentials), reversible (entropic) and ohmic (resistance to ion/electron transport) contributions. The total rate is calculated by integrating the source terms over the entire length of the cell and multiplying with the electrode area A. The resulting equation can be solved for temporal evolution of temperature.

$$mC_p \frac{dT}{dt} = \dot{Q} - hA_s \left(T - T_\infty \right) \tag{4.13}$$

$$\dot{Q} = A \int_0^{L_a+L_s+L_c} \left(j_1\eta_1 + j_2\eta_2 + j_1\left(T\frac{dU_1}{dT} \right) + \sigma_s^{eff} \nabla\phi_s \cdot \nabla\phi_s + \kappa^{eff} \nabla\phi_e \cdot \nabla\phi_e + \kappa_D^{eff} \nabla \ln c_e \cdot \phi_e \right) dx \tag{4.14}$$

For a major portion of this work, we assume natural convection conditions corresponding to h=28.4 W/m^{2}K which can be justified as a case of battery operation without an active thermal management system.[211] In a dense battery pack with small cell-to-cell spacing and no active thermal management, free convection is the primary mechanism of heat transfer away from the individual cells. We also present a special case using the adiabatic (h=0) and isothermal ($h \to \infty$) boundary conditions presenting us with the best-case (all internal heat generation utilized in heating up the cell) and worst case (all heat generation lost to the environment) scenario for performance respectively.

Table 4-1 Design parameters of 18650 cells [264]

Parameters	Separator	Cathode (NCM333)
L (m)	20×10^{-6}	80×10^{-6}
ε (-)	0.46	0.25
τ	1.4744	4.5823
a_s (m^2/m^3)	-	6.9177×10^4
σ^{eff} (S/m)	-	14.4572
$c_{e,init}$ (mol/m^3)	1200	
A (m^2)	0.06	
c_p (J/kg-K)	823	
h (W/m^2-K)	28.4	

The nominal parameters for the cell are listed in Table 4-1. Table 4-2 and Table 4-3 delineate the electrode and electrolyte properties respectively. Finally, Table 4-4 lists the boundary conditions for the governing differential equations describing ion and charge transport along the thickness of the electrode.

Table 4-2 Electrode Properties [28, 211, 265]

Parameter	Values		
	Anode	Cathode	Plating
k ($m^{2.5}$ $mol^{-0.5}$ s^{-1}/ $m^{1.1}$ $mol^{-0.7}$ s^{-1})	2.3238×10^{-10}	2.4177×10^{-11}	2.23×10^{-7}
c_s^{max} (mol/m^3)	30900	49500	-
$E_{act}(i_0)$ (J/mol)	68000	50000	35300
D_s (m^2/s)	$1.6\times10^{-14}(1-\theta)^{1.545}$	3.0×10^{-14}	-
$E_{act}(D_s)$ (J/mol)	30000	30000	-
U_{eq} (V)	$0.1493+0.8493\exp(-61.79\theta)+0.3824\exp(-665.8\theta)-\exp(-39.42\theta-41.92)-0.03131\tan^{-1}(25.59\theta-4.099)-0.009434\tan^{-1}(32.49\theta-15.74)$ $(0\le\theta\le1)$	$-10.72\theta^4+23.88\theta^3-16.77\theta^2+2.595\theta+4.563$ $(0.3\le\theta\le1)$	0.0
$\frac{dU_{eq}}{dT}$ (mV/K)	$-58.294\theta^6+189.93\theta^5-240.40\theta^4+144.32\theta^3-38.87\theta^2+2.8642\theta+0.1079$	$-190.34\theta^6+733.46\theta^5-1172.6\theta^4+995.88\theta^3-474.04\theta^2+119.72\theta-12.457$	0.0
R_c (Ohm-m^2)	6×10^{-4}		-
κ_{film} (S/m)	-		1.078×10^{7}

Table 4-3 Electrolyte Properties [211]

Parameters	Value
D_e (m^2/s)	$10^{-4}c\times\left(10^{-4.43-\frac{54}{T-229.0-0.005c}-2.2\times10^{-4}c}\right)$
κ (S/m)	$10^{-4}c\times\left(\begin{array}{l}-10.5+0.074T-6.69\times10^{-5}T^2+6.68\times10^{-4}c-1.78\times10^{-5}cT\\+2.8\times10^{-8}cT^2+4.94\times10^{-7}c^2-8.86\times10^{-10}c^2T\end{array}\right)^2$
V (-)	$0.601-0.24\left(10^{-3}c\right)^{0.5}+0.982\left(1-0.0052\left(T-294\right)\right)\left(10^{-3}c\right)^{1.5}$
t^+ (-)	0.363

Table 4-4 Boundary Conditions [28]

Parameters	CC - anode $x=0$	Anode – separator $x=L_a$	Separator-cathode $x=L_a+L_s$	Cathode-CC $x=L_a+L_s+L_c$
c_e	$\frac{\partial c_e}{\partial x}=0$	$\left(D_e^{eff}\frac{\partial c_e}{\partial x}\right)_{x=L_a-\delta}=\left(D_e^{eff}\frac{\partial c_e}{\partial x}\right)_{x=L_a+\delta}$	$\left(D_e^{eff}\frac{\partial c_e}{\partial x}\right)_{x=L_a-\delta}=\left(D_e^{eff}\frac{\partial c_e}{\partial x}\right)_{x=L_a+\delta}$	$\frac{\partial c_e}{\partial x}=0$
ϕ_e	$\frac{\partial \phi_e}{\partial x}=0$	$\left(\kappa^{eff}\nabla\phi_e+\kappa_D^{eff}\nabla\ln c_e\right)_{L_a-\delta}=\left(\kappa^{eff}\nabla\phi_e+\kappa_D^{eff}\nabla\ln c_e\right)_{L_a+\delta}$	$\left(\kappa^{eff}\nabla\phi_e+\kappa_D^{eff}\nabla\ln c_e\right)_{L_a+L_s+\delta}=\left(\kappa^{eff}\nabla\phi_e+\kappa_D^{eff}\nabla\ln c_e\right)_{L_a+L_s+\delta}$	$\frac{\partial \phi_e}{\partial x}=0$ $\phi_e=0$
ϕ_s	$\sigma_s^{eff}\frac{\partial \phi_s}{\partial x}=-\frac{I}{A}$	$\frac{\partial \phi_s}{\partial x}=0$	$\frac{\partial \phi_s}{\partial x}=0$	$\sigma_s^{eff}\frac{\partial \phi_s}{\partial x}=-\frac{I}{A}$

4.2.2 Virtual Microstructure Generation and Effective Property Calculations

Figure 4.1(a) and Figure 4.1 (b) show the representative anode and cathode electrode microstructure for porosities 30%. The 3D microstructures are generated using GeoDICT and in-house codes are used to characterize the effective transport properties and active area.[211, 265] In general, the electrodes comprise of active material (AM), binder (B) and conductive additive (CA); CA+B is referred to as the conductive binder domain (CBD). For cathode, the AM:B:CA weight fraction ratio is fixed to 90:5:5 while for the anode the AM:B:CA weight fraction ratio corresponds to 95:5:0. Conductive additives are not essential in the anode owing to the high intrinsic electronic conductivity of the graphite active material. We utilize the property regression correlations delineated in Mistry *et al.*[240] for computing the effective parameters with a morphology factor $\omega = 1$ correlating to a film-like conductive binder domain coating. We calculate the active area $a\left(m^2/m^3\right)$, pore-phase tortuosity $\tau\left(-\right)$ and effective electronic conductivity σ^{eff}; the effective pore-phase parameters are correlated to the pristine properties through $D_e^{eff} = D_e \frac{\varepsilon}{\tau}, \kappa^{eff} = \kappa \frac{\varepsilon}{\tau}$ and $\kappa_D^{eff} = \kappa_D \frac{\varepsilon}{\tau}$. The nominal capacity of cell is fixed to 2.2 Ah with anode to cathode (N/P) loading ratio of 1:1.[28] Since our primary focus is on fast charge capabilities, we keep the cathode microstructure fixed with porosity 25% and thickness 80µm corresponding to the NCM333 active material fraction of 0.5843. The anode porosity and correspondingly graphite active material fraction is varied along with the anode length to maintain the 1:1 N/P capacity loading ratio. In particular, the anode porosity is varied from 15% to 45% with the corresponding anode lengths varying from 66.42µm to 94.09µm to achieve the nominal capacity of 2.2Ah for the anode and the cathode. The anode lengths are computed using Equation (4.15).

$$c_{s,n}^{\max} \varepsilon_{s,n} L_n \Delta_{SOC,n} = c_{s,p}^{\max} \varepsilon_{s,p} L_p \Delta_{SOC,p} \tag{4.15}$$

Here the subscripts *n* and *p* correspond to the negative (anode) and positive (cathode) electrode correspondingly. ε_s is the active material volume fraction, L is the length of the electrode and Δ_{SOC} is the allowed state of charge change of the active material. For NCM333 cathode, Δ_{SOC} takes a value of 0.7 as NCM cathodes are rarely delithiated below 0.3 because of structural instabilities below this SOC. Graphite undergoes complete lithiation/delithiation in the range of 0 and 1, resulting in $\Delta_{SOC} = 1$ for the graphite anode. Table 4-5 lists material properties for the

anode/cathode system for the computation of effective properties. Table 4-6 delineates the anode microstructural, geometric variations in terms of porosity and thickness corresponding to the nominal cathode with 25% porosity and 80μm length.

Table 4-5 Material properties of cathode and anode system [28]

Parameter		Particle diameter (μm)	Bulk conductivity (S m^{-1})	Mass density (g cm-3)
Cathode	$Li(Ni_{1/3}Mn_{1/3}Co_{1/3})O_2$	10[a]	0.00106	4.8
	Graphite	4[a]	16700	1.95
	PVDF/C	–	760	1.86[a]
Anode	Graphite	20[a]	16700	1.95
	PVDF/C	–	760	1.86[a]

Table 4-6 Graphite Anode Microstructure and Geometric Parameters

Porosity, ε_n (-)	AM Fraction, $\varepsilon_{s,n}$ (-)	Length, L_n (μm)	Tortuosity, τ_n	Active Area, $a_{s,n}$ (m^2/m^3)	Electronic Conductivity, σ_n^{eff} (S/m)
0.15	0.7981	66.42	11.3875	6.3920×10^4	10380.1743
0.20	0.7511	70.57	6.9453	7.0006×10^4	8921.1390
0.25	0.7042	75.27	4.7617	7.5721×10^4	7594.565
0.30	0.6572	80.66	3.5184	8.1034×10^4	6395.6836
0.35	0.6103	86.86	2.7392	8.5911×10^4	5319.6188
0.40	0.5654	94.09	2.2167	9.0318×10^4	4361.3843

4.3 Results and Discussion

We aim to identify anode microstructure regimes and operating conditions (C-rate, in particular) that foster fast charge/discharge of lithium ion batteries in varying thermal environments. The complexity in identifying such regimes arises due to a trade-off that exists in the key considerations: safe-to-operate temperatures and desired capacities. In addition, undesirable electrochemical side

reactions (e.g. lithium plating) can take place at the active surface of graphite. This can potentially result in capacity fade (on cycling) and pose severe safety concerns. We investigate how these aforementioned factors are influenced by the microstructure of the electrode, which is closely intertwined with the coupled transport processes and electrochemical reactions occurring at the active interface.

In order to mitigate the electrodeposition of lithium metal on graphite, commercial cells are usually designed with an additional anode capacity (as compared to the cathode) giving N/P capacity ratios ranging from 1.1 to 1.2. This requires either increasing the anode length or packing more active material fraction into the anode. In our work, the capacities of cathode and anode have been kept equal to enable a fair comparison of the plating propensities at different porosities as well as getting rid of the additional unused capacity. It is to be noted that the cathode specifications have been kept constant throughout. The length and active material volume fractions of the anode have been varied in order to maintain a constant capacity.

4.3.1 Impact of Ambient Temperature, Current Rate and Electrode Microstructure on Charge Performance

We investigate the effect of operating conditions and anode microstructure on full cell charge performance. Figure 4.1 (c-h) gives the full cell charge performance (voltage vs capacity) and thermal effects (temperature vs capacity) for varying C-rates (top), anode porosities (bottom) and ambient cell temperatures of -10˚C, 0˚C and 25˚C (left to right). In each figure, the voltage curves are clubbed towards the top while the temperature curves are consolidated towards the bottom. The ordinate axis on the left corresponds to the voltage while that on the right corresponds to the temperature rise. Figure 4.1 (c-e) reveals the impact of the current rate (1C-4C) while keeping a fixed anode porosity of 30%. At low temperatures (-10˚C and 0˚C), the charging profiles at higher C-rates reveal an important ‘voltage rebound’ trend. The voltage ascends quickly near to the upper cutoff of 4.2V and then swings back down allowing for charging to occur for a sustained time period. For -10˚C, the voltage rebound effect is present up to the threshold current rate of 2.5C and can allow for nearly 60% (~1.3 Ah) charging capacity. This current threshold is increased to 4C when the starting temperature is raised to -0˚C and we see improved capacity as well (~1.8Ah). The rebound effect is minimal for the operation temperature of 25˚C and best charge performance of the cell is observed with a full charge capacity close to the nominal 2.2Ah for current rates as

high as 4C. It is evident that the improvement in charge performance with a rise in cell temperature can be attributed to the enhanced electrolyte transport (ionic diffusivity, conductivity ↑), electrode kinetics (exchange current density ↑) and transport (solid state diffusivity ↑) properties at high temperatures resulting in smaller kinetic and ohmic overpotentials. Furthermore, the electrolyte ionic diffusivity is a monotonically decreasing function of Li^+ concentration while the ionic conductivity exhibits a non-monotonic trend with Li^+ concentration; it has a maximum at the 1.2M Li^+ concentration and decreases as we go towards lower (< 1.2M) or higher (> 1.2M) concentrations. The curious voltage rebound trend can be physically interpreted through an understanding of the temperature and concentration dependence of these properties. For low temperature charge, during the initial phase of charging, the electrolyte phase exhibits poor ionic conductivity, diffusivity owing to its strong temperature dependence. Hence, there must be a significant potential, concentration drop in the electrolyte phase in order to sustain the high applied current. Further, this increased transport resistance also results in an accumulation of Li^+ ions at near the cathode current collector and a synchronized depletion of Li^+ ions at the anode. The concentrations of both these regions lie outside the optimal concentration (1200 mol/m^3) for achieving the highest ionic conductivity. At low salt concentrations, the ionic conductivity is poor due to a deficit of charge carrying species. At very high concentrations (beyond a certain limit), the solvation shells of neighboring ions overlap with each other, thereby causing a hindrance to their movement (concentrated solution effects). Hence, the steep potential gradients that ensue result in an increased voltage polarization and the steep upward curvature of the voltage profile towards 4.2V. Simultaneously, the large heat generation inside the cell afforded by the steep potential and concentration gradients as well as large kinetic overpotentials tips the cell temperature to 10˚C/20˚C (a temperature rise of nearly 20˚C) at the voltage maxima point from the initial -10˚C/0˚C temperature. Once these temperatures are reached, particle/cell level transport gets enhanced through a decrease in the kinetic and ohmic resistances allowing for the continued charge of the system and the downward voltage slant. Further charging follows the usual voltage trend following the difference between the open circuit potentials of the NCM333 cathode and graphite anode; graphite OCP goes to 0V upon lithiation while NCM333 OCP moves upward to 4.2V upon delithiation; alongwith the corresponding overpotentials.

An important insight can be gleaned from the voltage rebound phenomena: *at low temperatures on or below 0˚C, it is beneficial to operate the cell at high C-rates which affect a*

large temperature rise due to augmented heat generation and lead to better charge capacity of the cell. For 30% porous electrodes, this C-rate is 2.5C and 4C (can go close to 5C as well) for ambient temperatures of -10˚C and 0˚C respectively. To summarize, high C-rate has important can have beneficial implications manifesting as follows: increased concentration polarization and transport phase resistance → high heat generation → large temperature rise → improved transport properties → low transport resistance → low overpotential → better charge capacity.

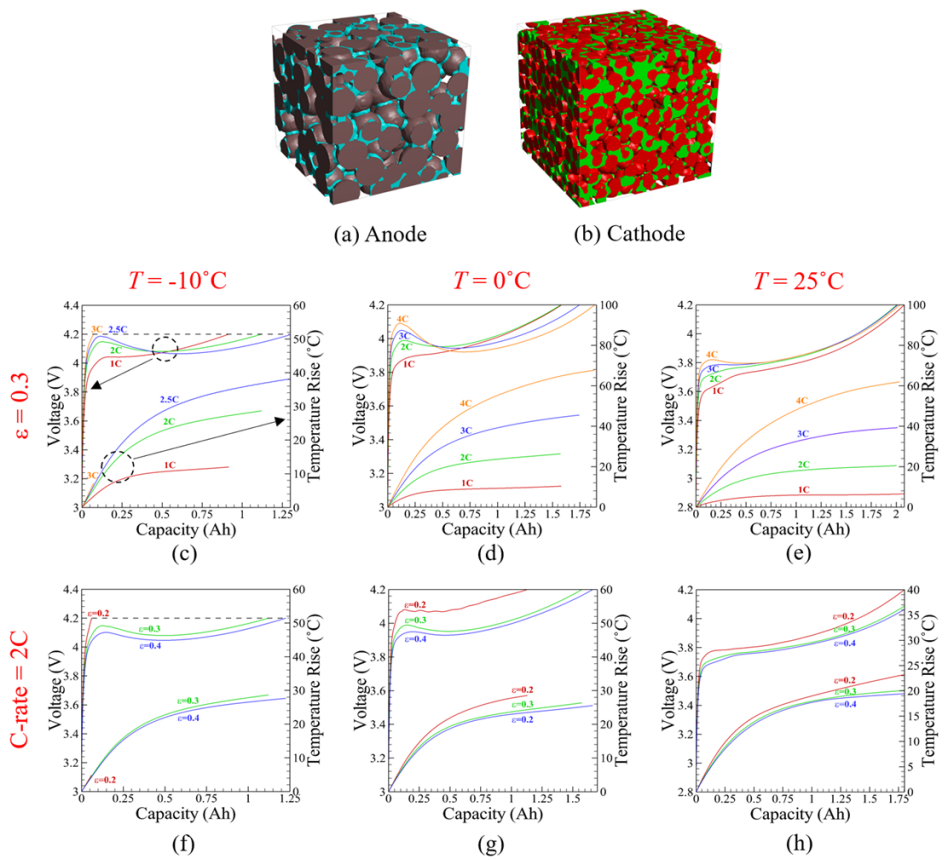

Figure 4.1 Representative (a) anode and (b) cathode microstructures. Both anode and cathode active material particles are assumed to be spherical with anode having larger size particle as compared to cathode. The conductive additive and binder domain (CBD) is shown in light blue and green respectively. Anode has smaller CBD content as compared to cathode. Full cell rate performance (voltage vs capacity) and thermal effects (temperature vs capacity) for porosity 30% and C-rates ranging from 1C - 4C at ambient cell temperatures (c) T = -10˚C, (d) T = 0˚C and (e) T = 25˚C. Full cell rate performance (voltage vs capacity) and thermal effects (temperature vs capacity) for current rate 2C and anode porosity varying from 20% - 40% at ambient temperatures (f) T = -10˚C, (g) T = 0˚C and (h) T = 25˚C. In each figure, the voltage curves are clubbed towards the top while the temperature curves are clubbed towards the middle of the figure. The y-axis on the left corresponds to the voltage while the y-axis on the right corresponds to the temperature rise.

While the transport/kinetic losses get alleviated due to an improvement in the electrolyte/electrode properties caused by self-heating at high C-rates we cannot increase the C-rate beyond a threshold. At even higher C-rates (for example, 0˚C - 3C case), the deleterious effects of the high pore phase resistance cannot be compensated with improved properties. The voltage directly hits the cut-off mark, causing a self-shutdown of the cell. Hence, it is important to find an intermediate value of applied current that not only eludes self-shutdown but also utilizes the self-heating properties to achieve an enhanced capacity. Another detrimental effect arising from combined high C-rate - high ambient temperature operation (T = 25˚C) can be observed. It leads to a significant increase in the cell temperature, thus creating unsafe operating conditions. A temperature rise of 60˚C is possible at 4C current rate, bringing the cell temperature to 85˚C which can trigger SEI decomposition reactions and thermal runaway scenarios. A detailed explanation of this temperature rise and delineation of safe operating regimes (with respect to temperature rise) will be performed in a subsequent section.

Similarly, Figure 4.1 (f-h) demonstrate how the anode porosity variation (20% - 40%) impacts the charge capacity at a fixed current rate of 2C. High porosity is associated with low transport resistance and overpotentials, consequently we see the following charge capacities trend: 40% > 30% > 20%. The voltage rebound is visible again at low temperatures, which is a case of the overpotentials decreasing as charge progresses due to high heat generation induced temperature rise. We see that anode porosity has a lesser impact on the voltage and temperature profiles as compared to the C-rate. While low porosities also have higher heat generation due to large transport resistance, the heat generation is not enough at 2C for it to outperform the high porosity anodes with low resistance. Consequently, the usual trend is obtained: high porosity anodes exhibit better performance due to lower transport resistance.

4.3.2 Heat Rates and Plating Maps

The evolution of heat generation rates and plating magnitudes throughout the full cell can provide us insights into the thermal and degradation response of the cell. Figure 4.2(a-f) gives the heat generation, plating magnitude contour maps as a function of the cell through-plane thickness and state of charge (SOC) for the 20% porosity anode microstructure at 3C current rate and ambient temperature of 25˚C. Operating conditions and microstructure have been chosen to show representative heat rate and plating maps. The anode-separator-cathode dimensions are 70.57μm -

20µm - 80µm respectively. An SOC of 0 corresponds to fully discharged state and an SOC of 1 corresponds to the fully charged state when the voltage reaches 4.2V. An SOC < 1 indicates that charging stops through reaching of the upper voltage cutoff before the charge capacity of 2.2Ah is reached. The contour maps reveal the temporal trend of the kinetic, ohmic, reversible and total heat generation alongside the full length of the cell. The plating heat generation and plating thickness exists only in the anode towards the end of charge (beyond an SOC of 0.6), primarily close to the separator, hence only the 50µm - 70µm anode zone is shown for Figure 4.2 (e) and Figure 4.2 (f). Initially, heat generation is larger close the anode-separator and cathode-separator interfaces as the lithiation and delithiation reaction currents are concentrated close to these interfaces respectively. As the charging progresses, the heat generation distributes throughout the cell as the reaction current, concentration and potential gradients become significant throughout the cell thickness.

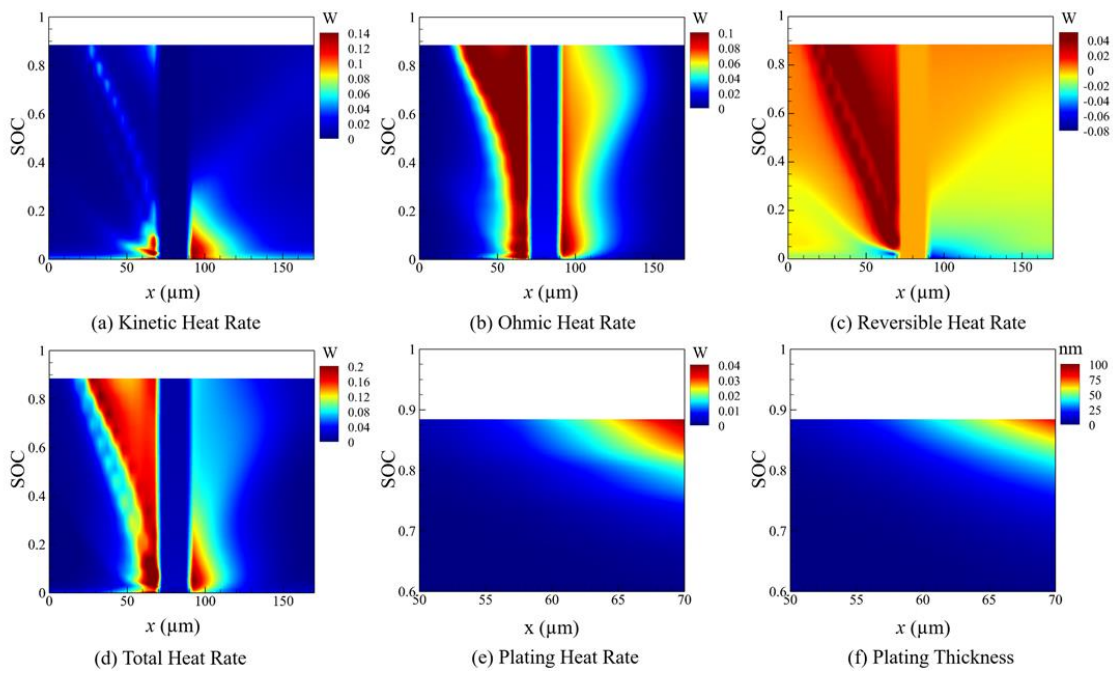

Figure 4.2 (a) Kinetic heat rate, (b) ohmic heat rate, (c) reversible heat rate and (d) total heat rate as a function of unit cell thickness (0µm to 160µm) and state of charge. (e) Plating heat rate and (f) thickness of plated Li film near the anode-separator interface (from 50µm to 70µm where 70µm corresponds to the anode-separator interface). The anode microstructure corresponds to a porosity of 20% with a current rate of 3C at an ambient temperature of 25˚C.

Figure 4.2 (a) shows the kinetic/reaction (intercalation/deintercalation + plating) heating rate. Intercalation overpotential, η_1, is the primary contributor to the reaction heat rate

$\left(j_1\eta_1 + j_2\eta_2\right)$ in the anode, as the plating reaction occurs in a tiny zone for a small portion of the charging time period (see Figure 4.2 (e)). The cathode kinetic heat rate slightly exceeds the anode reaction heat rate as the cathode intercalation exchange current density (2A/m^2) is lower as compared to anode intercalation exchange current density (12A/m^2). Hence, cathode overpotentials are larger leading to higher heat generation. Active surface area in the cathode is smaller as well owing to the larger CBD content which results in larger reaction overpotentials and kinetic heat generation magnitudes. Furthermore, the reaction heat rates become miniscule (predominantly blue zone in the contour map) beyond a SOC of 0.2; cell temperature rise results in an increase of the exchange current densities via the Arrhenius correlations and further decrease in kinetic overpotentials. It is to be noted that the separator zone exhibits zero reaction heat which is consistent with the fact that no reactions occur inside the separator. Figure 4.2 (b) shows the ohmic/joule heating rate $\left(\sigma_s^{eff}\nabla\phi_s\cdot\nabla\phi_s + \kappa^{eff}\nabla\phi_e\cdot\nabla\phi_e + \kappa_D^{eff}\nabla\ln c_e\cdot\phi_e\right)$ emanating from resistance to ion and electron transport in the electrolyte and solid phase. Here, anode exhibits slightly larger heat generation magnitudes (red zone on contour map). This is attributed to the lower anode porosity (20%) as compared to cathode (25%). Thus, anode pore-phase transport resistance is larger, leading to larger electrolyte concentration/potential gradients and hence higher heat generation magnitudes. Also, the separator exhibits ohmic heat generation, however, its large porosity (46%) results in much smaller magnitudes as compared to the anode and cathode. Figure 4.2 (c) exhibits the reversible/entropic heating rate $\left(j_1 T\dfrac{dU_1}{dT}\right)$ whose nature depends directly on the entropic coefficient (dU_1/dT) behaviour which is material specific. Again, the separator has zero entropic heat owing to no reactions occurring in the separator zone. Graphite exhibits relatively larger entropic coefficient magnitudes as compared to NMC333 manifesting as higher heat generation magnitudes inside the anode. The entropic heat can take negative values, exhibiting heat sink behaviour, depending on the sign of dU_{eq}/dT. We see that at high current rates (3C here), magnitudes of the entropic heat (max 0.04W) are smaller as compared to the corresponding reaction (max 0.14W) and transport rates (0.10W). Kinetic and ohmic heat rates are always positive, while reversible heat rates can take both positive/negative values. Finally, we see the total heat generation rates in Figure 4.2 (d), a summation of the kinetic, ohmic and reversible heat

rates. The total heat rates closely follow the joule heat rate trend showcasing that transport resistance is the primary contributor to the heat generation at high current rates.

Finally, the plating heat rate and plating thickness in the anode are displayed in Figure 4.2 (e) and Figure 4.2 (f) respectively. In this scenario, plating reaction becomes active close to the end of charge (around 70% SOC) and propagates to around 15μm away from the anode-separator interface into the anode. Maximum plating is seen close to the anode-separator interface (~100 nm plating thickness), and it decreases as we move away from the interface. As pointed earlier, the plating heat rate provides only a small contribution to the total reaction heat. Thus, even with the addition of a second reaction, the total heat rate is predominantly comprised of the joule heating rate with marginal contributions from the kinetic heat rate.

4.3.3 Plating Fundamentals

We aim to get a deeper insight into the plating-thermal interactions. Lithium plating (formation of metallic lithium) is one of the degradation mechanisms that occur at the anode of lithium ion batteries. Metallic lithium can cover the electrochemically active surface area of the electrode and react with the electrolyte, thus forming insoluble products. (e.g. Li_2CO_3). Over cycling, this may lead to severe capacity fade, and in extreme cases, can also cause a catastrophic internal short of the cell.

Lithium plating is favoured under the following circumstances:

- When the anode solid phase concentration reaches its maximum value (negative electrode is completely saturated with lithium), lithium ions will deposit at the interface, and are unable to diffuse into the full graphite host eventually forming metallic lithium.
- During fast charge events (> 1C), a large kinetic over-potential is required to sustain the high applied current. The anode overpotential can drop below zero, generally during the final stages of cell operation. Thermodynamically, the electrode's (local) electrochemical potential dropping below zero (vs Li/Li^+) favours the formation of lithium metal.
- A large kinetic overpotential is required to compensate for the sluggish reaction kinetics during low temperature (< 0˚C) charging. This can cause plating to occur even during the initial stages of cell operation.

We discern the root cause of plating in our work to be a combination of the latter two reasons because of the larger current rates and low temperature charging protocol investigated. Figure 4.3(a) gives the potential profiles in electrode and electrolyte phase, along with the ion concentration profile in the electrolyte phase at the onset of plating for 1C current rate, ambient temperature -10˚C and anode porosity 35%. Again, operating conditions and anode microstructure have been chosen accordingly to be representative of plating scenarios. Plating occurs once the solid phase potential (blue line) drops below the electrolyte phase potential (green line) resulting in plating overpotential, $\eta_2 < 0$, while the electrolyte ionic concentration lies above zero, allowing for ions to participate in the kinetic reactions. It is to be noted that the electrolyte phase potential is set to zero at the cathode-current collector interface for solution of the elliptic potential equations. Note that the solid phase potential profiles are horizontal in both the anode and the cathode, owing to the high electronic conductivity of the solid phases. Solid phase potential is non-existent in the separator zone and has been portrayed as zero in the figure for visualization purposes. The pore phase potential and concentration profiles show more variation along the cell thickness due to the finite ionic conductivity and diffusivity of the electrolyte. The electrolyte concentration profile shows steep gradients in the cathode phase owing to lower porosity (25%) as compared to anode (35%) resulting in more tortuous pathway. Furthermore, the accumulation of ions in the cathode lowers the ionic diffusivity; ionic diffusivity is a monotonically decreasing function of concentration, this contributes to steeper gradients in the cathode. Figure 4.3 (b) exhibits the temporal evolution of plating overpotential when the current rates are increased from 1C to 3C for the same microstructure at -10˚C. It reveals that an increase in the current rate is associated with a slightly earlier onset of plating, with the blue line (3C) dropping below zero earlier as compared to the red line (1C). However, we see a beneficial impact related to the temperature rise (shown in inset). Plating continues for an extended period with $\eta_2 < 0$ at lower C-rates, e.g., 1C, and it exhibits a monotonically decreasing behaviour. This period is reduced at 3C due to the larger heat generation magnitude induced temperature rise pushing the plating overpotential above zero, $\eta_2 > 0$, and we see the "overpotential rebound" effect. At 1C, the temperature rise is not large enough to elevate the plating overpotential above zero, hence plating continues for a longer time duration. We highlight this strategy for mitigating plating induced cell degradation: *high current rates can be*

beneficial in reducing the duration of the plating regime owing to high self-heat induced temperature rise. In literature, high current rates are predominantly associated with large plating propensity; we challenge this notion showing above that the high current rates can be utilized beneficially upon informed electrode engineering, owing to their inherent temperature rise implication.

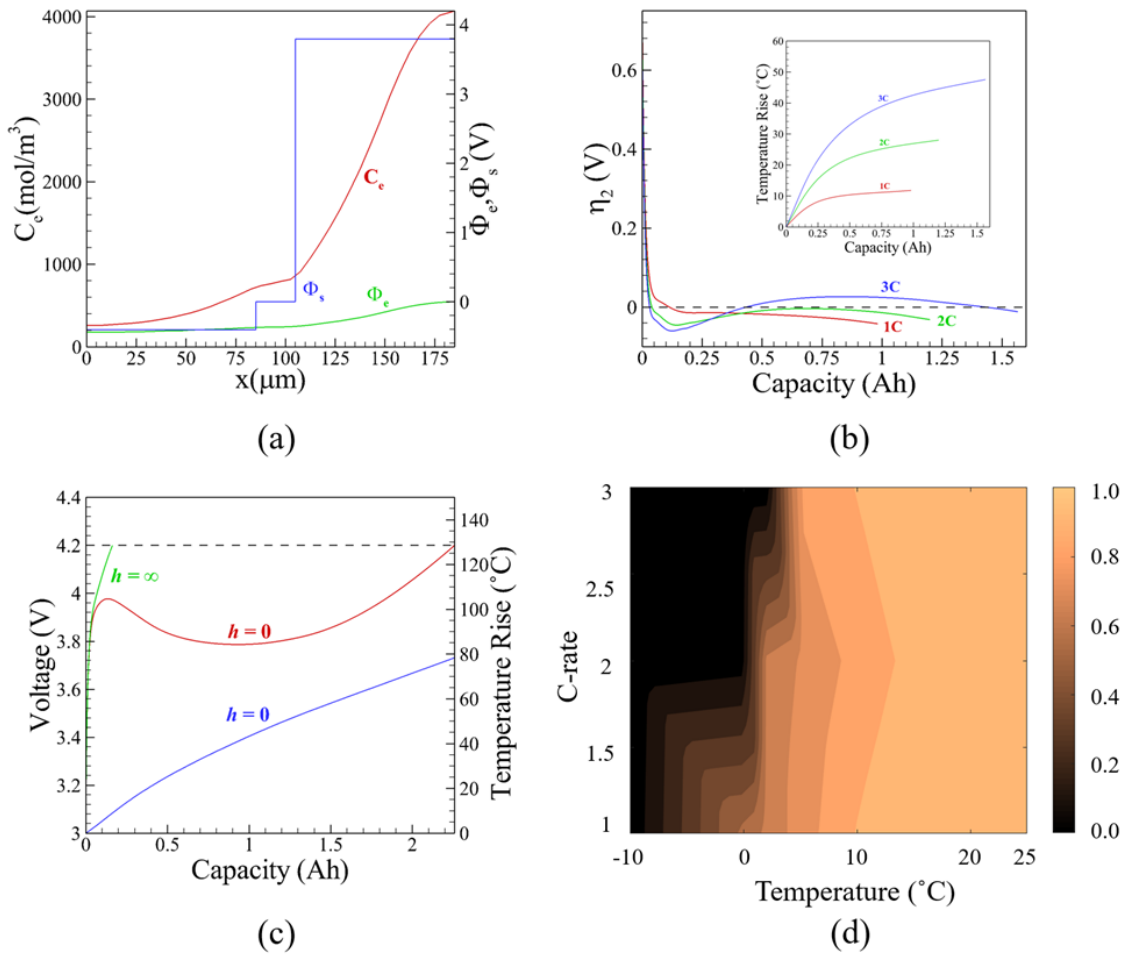

Figure 4.3 (a) The potential and concentration profiles at plating onset and (b) plating overpotential at anode-separator interface and temperature rise (inset) as a function of cell capacity for ambient temperature -10˚C, current rate 1C and anode porosity 35%. (c) Difference in isothermal and adiabatic operation (green: isothermal voltage, red: adiabatic voltage) for same conditions as above. (d) Variation of state of charge at which plating begins as a function of current rate and initial temperature for anode porosity of 30%.

Figure 4.3(c) shows the effect of the ambient convection heat transfer coefficient on the cell charge performance, keeping other conditions same. It is to be noted that adiabatic

performance ($h = 0$) supersedes isothermal operation $(h \to \infty)$ as all the heat generated is allowed to warm up the cell in the former while all the generated heat is lost to the surroundings in the latter. We see that even at 1C, the temperature rise can reach high magnitudes ~80 K, with the adiabatic operating conditions. The voltage rebound effect is visible for adiabatic heat transfer conditions, while the isothermal operation reaches the voltage cut off instantaneously. Finally, in Figure 4.3 (d) we show the plating onset state of charge for anode with 30% porosity as a function of current rate and state of charge. At low temperatures (-10˚C to 0˚C), plating starts from the beginning of charge (SOC~0), more so at high current rates. As we move towards the higher temperatures, we see a delayed onset of plating which moves closer to the end of charge (SOC~1) at 25˚C.

4.3.4 Performance-Safety-Degradation Maps

With the successful incorporation and demonstration of the plating and thermal physics in our model, the objective of this section is to design an optimal anode that promotes fast charge/discharge capabilities cognizant of the thermal operating window. We aim to discern the operating current rate and anode porosity for our lithium ion battery of choice with nominal capacity 2.2Ah capable of working in temperature range -10˚C to 25˚C. To this end, we delineate two performance indicators, namely, charge capacity and discharge capacity, two safety indicators, namely, temperature rise and plated capacity to generate our performance-safety map at all temperatures. Figure 4.4(a-c) shows the charge capacity (Q_c), discharge capacity (Q_d), temperature rise (ΔT) and percentage of capacity contributing to plating reaction (Q_p) as a function of anode porosity ranging from 15% to 40% and current rate ranging from 1C to 5C for varying ambient temperatures. From left to right, the temperature varies from -10˚C to 0˚C to 25˚C. The contour colour scheme grades from black (low) to red (medium) to white (high) with the appropriate scale provided for each set of maps. Charge and discharge capacity vary from 0 to 2.25Ah. Temperature rise takes values from 0 to 80˚C, while plating capacity maxima reaches up to 10% of the total charge capacity. Figure 4.4 (a-c) show the charge capacity and Figure 4.4 (d-f) exhibit the discharge capacity at multiple ambient temperatures. High current rates and low ambient temperature foster large kinetic and transport overpotentials resulting in low capacities and inferior performance. For low temperature charging at -10˚C, widespread presence of the black zone

indicates self-shutdown of the cell through voltage hitting the upper cut-off for those combinations of anode porosity and current rates. The self-shutdown zone shrinks as the ambient temperature is increased, a direct consequence of the enhanced kinetic, transport properties allowing for sustained charge. At ambient temperature 25˚C, the 15% porous anode microstructure exhibits self-shutdown (decreased electrolyte percolation pathways) close to 5C current rate showcasing the difficulties in anode design for fast charge beyond 5C with high packing fractions. Another interesting observation can be delineated from the charge/discharge capacity contours; the constant current discharge capacities in the voltage range 3.0 - 4.2V consistently surpass the constant current charge capacities obtained in the same voltage window. This is a direct consequence of the state of charge dependence of the graphite and NCM333 OCP profiles as well as relatively lower internal heat generation during charge as compared to discharge. A larger thermal excursion during discharge results in enhanced transport and kinetic properties for the solid as well as electrolyte phase resulting in more achievable capacity (larger yellow-white zone). Figure 4.4 (g-i) shows the associated temperature rise during charge for the current rates and anode porosity range investigated; its nature closely mimics the charge capacity contours. This is obvious since a cell that charges for a long period of time exhibiting good charge capacity will also have sustained heat generation for a long period of time showing larger temperature rise. We use the temperature rise during charge instead of discharge as our safety indicator to focus a bit more on fast charge considerations. Again, as the current rate is increased, the temperature rise generally increases, unless it shuts off completely at low temperatures (e.g. self-shutdown beyond 4C at 35% anode porosity for ambient temperature -10˚C). The voltage reaches the upper cut-off with minimal charge at low temperatures due to the sluggish transport and kinetics, and consequently the temperature rise is also minimal (black zone). Similarly, as the anode porosity is decreased from 40% to 15%, the enhanced resistance leads to larger heat generation induced temperature rise unless self-shutdown is achieved at low porosities (e.g. self-shutdown at all current rates for 15% anode porosity and ambient temperature -10˚C). Finally, Figure 4.4 (j-l) depicts contour maps of the plated capacity percentages as function of anode porosity and current rates to be used as our second safety indicator. At -10˚C, the plating induced degradation is observed at low current rates (< 2C) and porosity range 20% to 30% which shifts more towards the left (low porosity zone) and top (high current rate) as the ambient temperature is increased. This is a direct consequence of the thermal-plating interactions as well as self-shutdown of the cell at low temperatures and high C-

rates. It is interesting to note that more lithium plating is observed at 25˚C in the low porosity zone (15% - 20%) for current rates ranging from 1C to 5C. The increased transport and kinetic resistance from the porosity reduction lowers the kinetic overpotential for plating to less than 0.0V resulting in plating magnitudes close to 10% of the charge capacity.

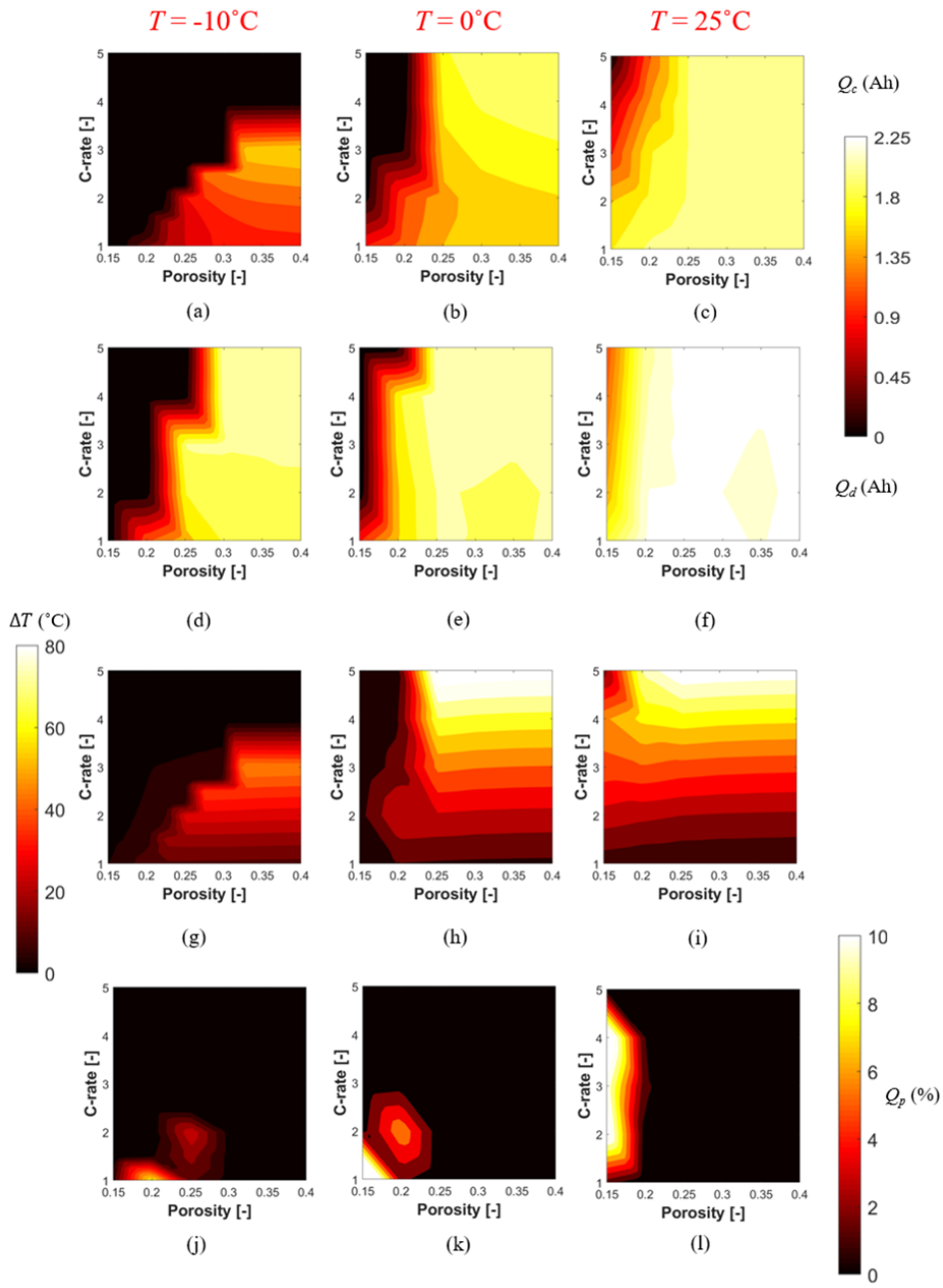

Figure 4.4(a-c) Charge capacity (Q_c), (d-f) discharge capacity (Q_d), (g-i) temperature rise (ΔT) and (j-l) percentage of capacity contributing to plating reaction (Q_p) as a function of anode porosity and current rate for different ambient temperatures. From left to right, the temperature varies from -10˚C to 0˚C to 25˚C.

Figure 4.5, Figure 4.6 and Figure 4.7 demarcate the desirable operating zone as function of C-rate and porosity for the ambient temperature -10˚C, 0˚C and 25˚C respectively. The contour maps are divided into three zones depending on the two performance and safety indicators. Charge and discharge capacity maps are divided into *low:* 0 - 0.5 Ah, *medium:* 0.5 - 1 Ah and *high:* > 1 Ah. Cell temperature is designated as *safe:* < 60˚C, *at risk:* 60˚C - 80˚C and *unsafe:* > 80˚C. Finally, plating capacity maps are delineated into *safe:* < 2.5%, *at risk:* 2.5% - 5% and *unsafe:* > 5%. An intersection of the attributes in each of the four performance indicators is used to generate the final performance-safety map at each temperature, with the blue zone indicating the desirable regime. At the ambient temperature of -10˚C (see Figure 4.5), the charge capacity is the limiting indicator (large low magnitude pink zone) determining the boundaries of the desirable zone. The desirable zone exists only at high porosities (> 30%) where the transport limitations are less severe, and the upper voltage cut-off is not reached instantaneously till 3C current rate. It is evident that fast charge beyond 3C at sub-freezing temperatures is hard to achieve with just anode microstructure tuning.

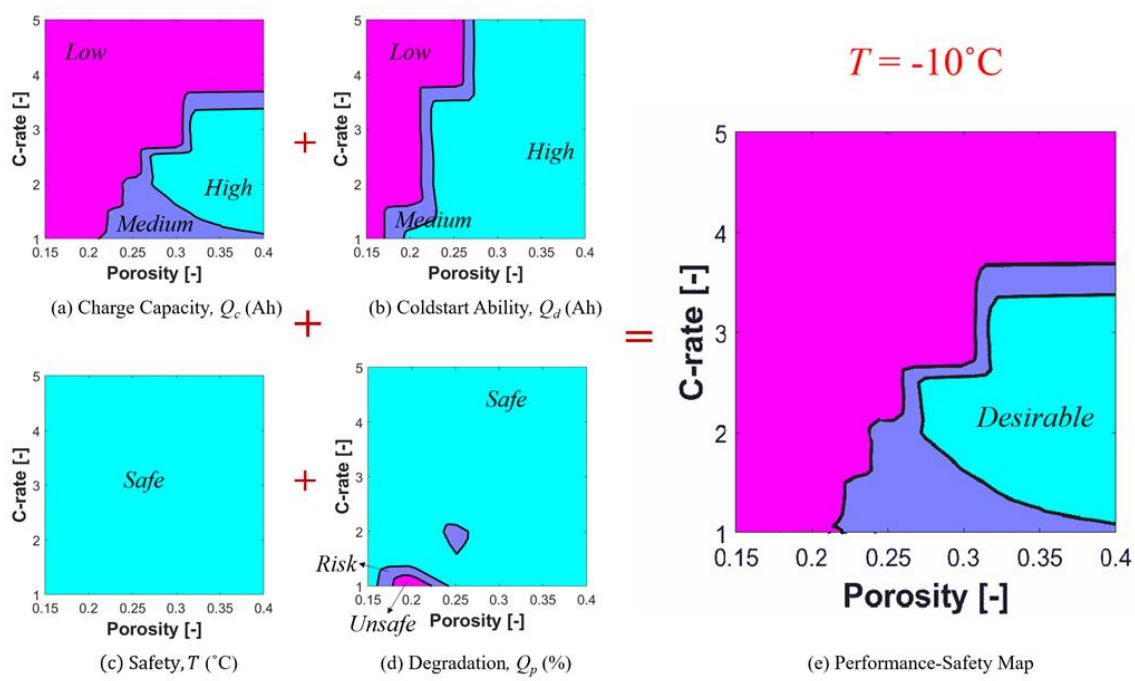

Figure 4.5 Contour maps for (a) charge capacity, (b) discharge capacity/coldstart ability (*low:* 0 - 0.5 Ah, *medium:* 0.5 - 1 Ah and *high:* >1 Ah), (c) cell temperature (*safe:* <60˚C, *at risk:* 60˚C - 80˚C *and unsafe:* >80˚C) and (d) plating capacity (*safe:* <2.5%, *at risk:* 2.5% - 5% and *unsafe:* >5%) as a function of current rate and porosity at ambient temperature -10˚C. (e) Performance-safety map combining all these features giving the desirable zone for initial temperature -10˚C**.**

For the intermediate ambient temperature operation of 0˚C, an intersection of the charge capacity, temperature rise, and degradation indicators delineate the desirable zone (see Figure 4.6);

hence all performance and safety indicators play a role. As compared to the -10˚C operation, the optimal zone is enlarged allowing for larger current rates going up to 5C for anode porosities ~ 25%. It is interesting to note that the plating degradation indicator has a larger safe zone for T = 0˚C as compared to T = -10˚C. This is a direct consequence of earlier shutdown of the cell at T = -10˚C; if the cell charge capacity is low the resulting plated capacity will also be low showing less degradation. Consequently, plating is not always worse at lower temperatures, self-shutdown of the cell plays limits the plated capacity.

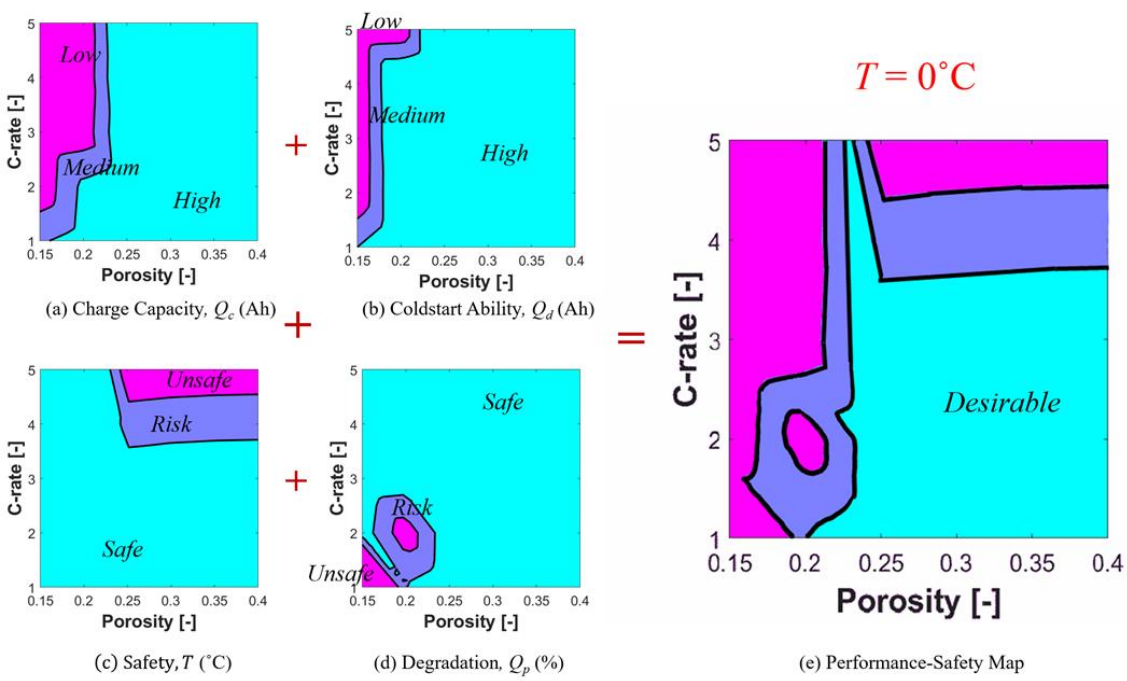

Figure 4.6 Contour maps for (a) charge capacity, (b) discharge capacity/coldstart ability (*low:* 0 - 0.5 Ah, *medium:* 0.5 - 1 Ah and *high:* >1 Ah), (c) cell temperature (*safe:* <60˚C, *at risk:* 60˚C - 80˚C and *unsafe:* >80˚C) and (d) plating capacity (*safe:* <2.5%, *at risk:* 2.5% - 5% and *unsafe:* >5%) as a function of current rate and porosity at ambient temperature 0˚C. (e) Performance-safety map combining all these features giving the desirable zone for ambient temperature 0˚C.

For the high ambient temperature operation of 25˚C, the temperature rise and degradation safety indicators (see Figure 4.7) become the primary limiting mechanisms, resulting in a desirable zone enlargement in the porosity direction but a reduction in the maximum applicable charge current rate direction. At high current rates, the temperatures can increase fast up to the risk (60˚C < T < 80˚C) and unsafe (beyond 80˚C) zones making it the deciding factor. Also, the plating

degradation indicator exhibits unsafe regions in the 15% - 20% anode porosity zones eliminating these microstructure arrangements from the desirable zone.

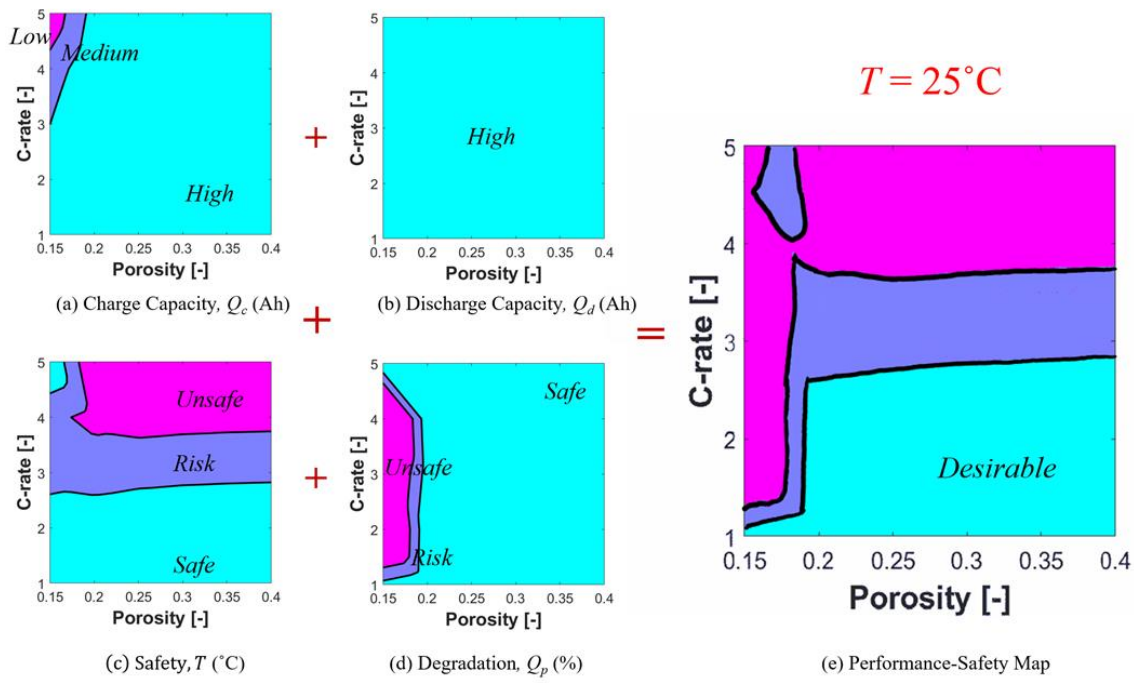

Figure 4.7 Contour maps for (a) charge capacity, (b) discharge capacity *(low:* 0 - 0.5 Ah, *medium:* 0.5 - 1 Ah and *high:* >1 Ah), (c) cell temperature *(safe:* <60˚C, *at risk:* 60˚C - 80˚C and *unsafe:* >80˚C) and (d) plating capacity *(safe*: <2.5%, *at risk:* 2.5% - 5% and *unsafe:* >5%) as a function of current rate and porosity at ambient temperature 25˚C. (e) Performance-safety map combining all these features giving the desirable zone for ambient temperature 25˚C.

Finally, the combined electrode operating zone at all ambient temperatures is shown in Figure 4.8. It is interesting to note that the final desirable zone is primarily an amalgamation of the desirable zones at the low (-10˚C) and high (25˚C) temperatures. It is seen that porosities in excess of 30% with a maximum allowable current rate of 3C for the 2.2Ah cylindrical lithium-ion battery with graphite anode and NCM333 cathode should be used as design constraints for a battery capable of charging at all temperatures. The operation guidelines can be made less stringent for operations in thermal environments above 0˚C, with anode porosities of 25% preferable up to current rates of 3C. It is evident that for fast charge beyond 3C, the electrolyte and solid phase transport properties as well as interfacial kinetic properties need to be enhanced so that low temperature charge is possible as well as the temperature rise is smaller during fast charge as the enhanced properties result in marginal concentration and potential gradients generating less heat.

Also, the external heating strategy for the all climate battery pioneered by CY Wang and co-workers[28, 211, 234, 266-268] can be used in conjunction with the self-heat-based anode and cathode design to improve the performance of the lithium-ion batteries. If external heating can be used to bring the cell temperature up to 0˚C or 25˚C, we can use the corresponding desirable zones in Figure 4.6 and Figure 4.7 to design the corresponding optimal anode for fast charge up to 5C.

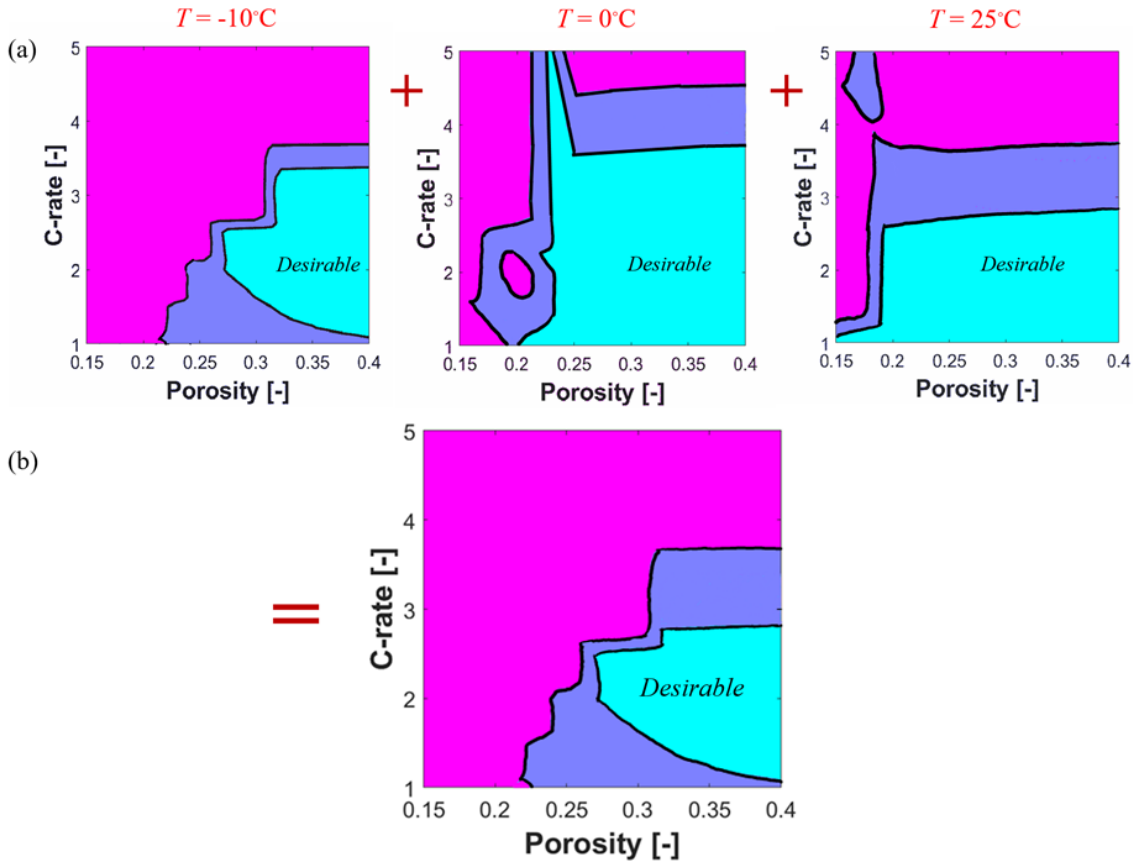

Figure 4.8 Electrode operating zone for (a) T = -10˚C, T = 0˚C, and T = 25˚C and (b) combined operating zone for all temperatures.

4.4 Conclusion

We aimed to elucidate the plating-thermal interactions during fast charge and delineate anode microstructure designs capable of fast charge for medium energy density 2.2Ah cylindrical lithium ion cells comprising of graphite anode and NMC333 cathode. It is shown that self-heat during electrochemical charge can be utilized to supplement any external heating strategies to enable fast charge at low temperatures. Anode porosities of 35%, 25% and 20% can enable fast charge up to 3C for ambient thermal environments of -10˚C, 0˚C and 25˚C respectively utilizing only self-heat.

Larger anode porosities compensate for the sluggish intrinsic electrolyte properties as the ambient temperature is reduced. While these design guidelines are specific for above cell chemistry and design, we propose that the qualitative nature of the desirable zones for other chemistries and cell design will follow similar trends and carefully designed experiments can unravel the optimal porosity for each cell chemistry and configuration. Furthermore, we find the following physical insights into the plating-thermal interactions during fast charge:

- At sub-zero temperatures, it is beneficial to operate the cell at high current rates (provided self-shutdown is evaded) upon informed electrode engineering, which produce a large temperature rise due to augmented heat generation leading to better charge capacity of the cell.
- High current rates can be beneficial in reducing the duration of the plating regime owing to high self-heat induced temperature rise shifting the plating overpotential above zero.
- Sub-zero temperature charge improves with adiabatic thermal conditions allowing for all internal heat generation to increase the cell temperature while high temperature charge ($\geq$ 25˚C) improves with forced convection thermal conditions restricting cell temperature rise below 60˚C for safer operation.

Consequently, alongside the engineering of optimal electrodes, battery management systems should supply larger currents to the cell as the ambient temperature decreases, since it has a beneficial impact on the charge capacity as well as results in less severe degradation. In addition, the thermal management system should allow for switching from natural convection to forced convection based on the ambient thermal environments. The current study can be extended to multiple cell chemistries, cell design configurations (cylindrical vs pouch cell) for thicker high energy density (high capacity) cells which will be the subject of future investigations. Generation of large amount of desirable zone datasets will open the avenue for machine learning based approaches as well.

5. ELECTRODEPOSITION STABILITY OF METAL ELECTRODES WITH LIQUID ELECTROLYTES

Relevant Publications and/or Working Papers

1. F. Hao, **A. Verma**, P.P. Mukherjee, "*Mesoscale Complexations in Lithium Electrodeposition*", ACS Applied Materials and Interfaces, **10** (31), 26320-26327 **(2018)**
2. (joint first author) F. Hao, **A. Verma**, W. Wang, B.S. Vishnugopi, P.P. Mukherjee, *"Ion Channel Assisted Uniform Deposition in Li Metal Batteries*"
3. R. Davidson, **A. Verma**, D. Santos, F. Hao, C. Fincher, S. Xiang, J. van Buskirk, K. Xie, M. Pharr, P. P. Mukherjee, S. Banerjee, "*Mapping Mechanisms and Growth Regimes of Magnesium Electrodeposition at High Current Densities"*, Materials Horizons, DOI: 10.1039/C9MH01367A **(2019)**
4. R. Davidson, **A. Verma**, D. Santos, F. Hao, C. Fincher, S. Xiang, J. van Buskirk, K. Xie, M. Pharr, P. P. Mukherjee, S. Banerjee, "*Formation of Magnesium Dendrites during Electrodeposition"*, ACS Energy Letters, **4**, 375-376 **(2019)**

5.1 Background

The burgeoning demand for electrical energy storage has led to the resurgence of research efforts into utilizing Li-metal as the anode in the Li-ion battery system. Commercial Li-ion battery systems utilizing intercalation chemistries such as graphitic anodes are reaching their upper limits of achievable capacity, thus paving the path for the recent revival of Li metal anode[269]. Li- metal based rechargeable batteries possess prominent advantages over state-of-the-art commercial Li-ion batteries, emanating from its high theoretical specific capacity (3860 mAh g^{-1}) and lowest negative electrochemical potential (-3.04 V *vs*. the standard hydrogen electrode). The prospect of Li-metal as the anode material also offers significant opportunities for sustainable battery systems beyond Li-ion chemistries, including Li-S batteries[270-272], and Li-air batteries.

Despite the remarkable progress, key challenges remain to the practical applications of Li-metal anodes, primarily related to battery safety and cyclability. Due to high chemical reactivity and large volumetric changes from repeated Li stripping and deposition during cycling, Li deposition tends to be in dendritic form which decreases the cycling efficiency, eventually leading to exacerbated capacity fading effects and even short circuit[87, 273]. Extensive research efforts have been devoted to developing dendrite-free depositions, for instance, approaches are proposed to improve the uniformity of solid-electrolyte interphase (SEI)[274-278] and increase dendrite growth resistance by using solid electrolytes[23, 103, 277, 279-281].

Depending on the operating conditions, various morphologies of electrodeposited metal are observed in experiments[282, 283]. Imaging techniques like scanning electron microscopy, magnetic resonance imaging, tomography etc. have been used to capture the deposition process[93, 282-290]. and In an earlier study, Yoshimatsu *et al*. found that particulate and needle-like Li were deposited on the Li electrode, and the needle-like Li was the dominant factor in creating "dead Li" that is responsible for the capacity loss[291]. Using a glass capillary, Bai *et al*. visualized a transition from root-growing mossy lithium to tip-growing dendritic lithium[292]. In addition to experiments, theoretical studies are focused on illuminating the growth mechanism of deposited metal[114, 115, 279, 293-302] , especially on dendrite growth. Since spherical diffusion conditions dominate at the hemispherical tips, the dendrite growth models by Barton and Bockris[303], and Monroe *et al*.[304] revealed that dendrites accelerate across cells.

Li deposition encompasses a complex interplay between coupled physical phenomena associated with SEI microstructure, composition and concentration of Li salts, composition and concentration of solvents, Li wetting with substrate, and battery working conditions [305, 306]. Therefore, a comprehensive understanding of Li deposition mechanism is challenging, although essential in guiding material design for good battery performance. In metal-ion systems, the transport-electrochemistry-mechanics interactions differ widely from intercalation systems. Usage of metal anodes presents several challenges and it is necessary to first elucidate the complex electrodeposition-transport interactions prior to coupling mechanics into the system. Electrodeposition encompasses a complex interplay between coupled physical phenomena associated with SEI microstructure, composition and concentration of salts, composition and concentration of solvents, metal wetting with substrate, and battery working conditions.[297, 307] Therefore, a comprehensive understanding of metal deposition mechanism is challenging, although essential in guiding material design for good battery performance. In this regard, we aim to address the mechanism of metal electrodeposition morphologies using a mesoscale model capable of bridging multiple length and time scales. Two different anodes, lithium and magnesium are investigated for their proclivity for varying deposition morphologies.

5.2 Lithium Electrodeposition

5.2.1 Methodology

A macro-homogeneous deposition model is developed to study lithium electrodeposition. Coupled species and charge transport inside the electrolyte and electronic transport is solved on the two-dimensional computational domain shown in. The domain dimensions are 50 µm × 50 µm for each phase in the vertical and horizontal direction respectively, thus the overall dimension becomes 100 µm × 50 µm in the vertical and horizontal directions respectively. The boundary conditions for the species and charge conservation equations are shown explicitly in the Figure 5.1 . Governing equations in the electrolyte and solid phase are given in Equations (5.1), (5.2) and (5.3) respectively.

$$\nabla.\left(\kappa\nabla\phi_e\right)+\nabla.\left(\kappa_D\nabla\phi_e\right)=0 \tag{5.1}$$

$$\frac{\partial c_e}{\partial t}=\nabla.\left(D_e\nabla c_e\right) \tag{5.2}$$

$$\nabla\cdot\left(\sigma\nabla\phi_s\right)=0 \tag{5.3}$$

Here, κ is the ionic conductivity, κ_D is the diffusional conductivity, D_e is the ionic diffusivity in the electrolyte, σ is the electronic conducitivity of Li metal, ϕ_e and ϕ_s are the potential in electrolyte and solid phase respectively and $c_e$is the concentration of Li^+ ions in the electrolyte phase. Electrolyte property correlations (conductivity, diffusivity, transference number, thermodynamic factor) are taken from Valoen and Reimers[301] for $LiPF_6$ in propylene carbonate/ethylene carbonate/dimethyl carbonate. The initial electrolyte concentration is taken to be 1200 mol/m^3 and the system is assumed to be at 25˚C.

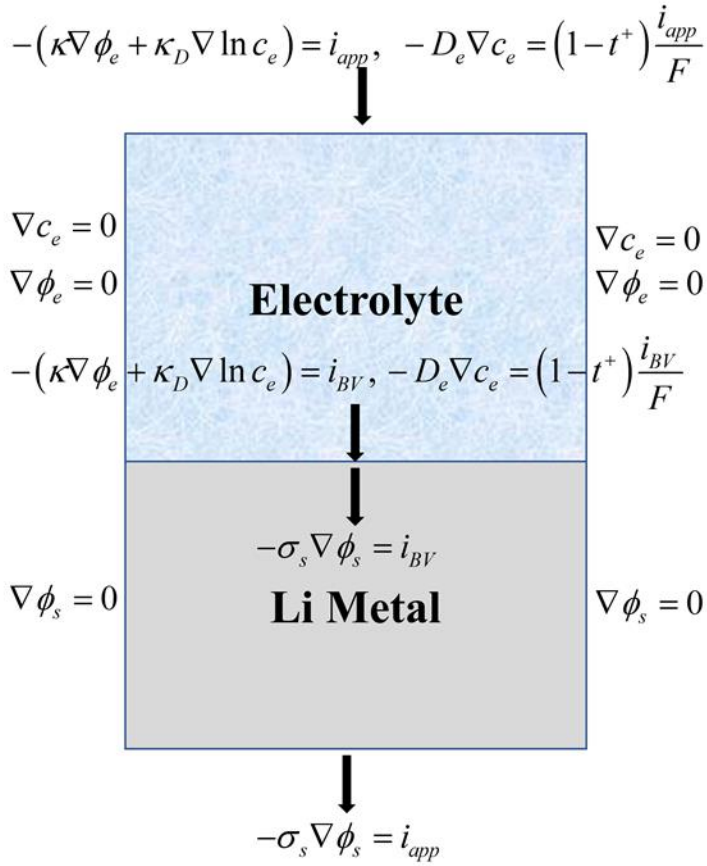

Figure 5.1 Computational domain and boundary conditions for macro-homogeneous model. Here, i_{app} is the applied current density, i_{BV} is the reaction current density at the electrode-electrolyte interface and t^+ is the Li^+ transference number in the electrolyte.

The equations are coupled through the electrochemical reaction occurring at the electrolyte-electrode interface which is given by the Butler-Volmer correlation. A slight modification is made to the correlation used for exchange current density which is reported to have dependence on concentration.[308] The exchange current density formula is given by:

$$i_o = kF\left(c_e\right)^{\alpha} \tag{5.4}$$

Here, k is the deposition rate coefficient. The coupled equations need to be solved iteratively until steady- state conditions persist throughout the computational domain. The validation of the numerical study performed is obtained through monitoring of the Butler-Volmer current density values. For the uniform interface, applied current density should equal the Butler-Volmer current density at the interface to ensure charge conservation and is readily obtained from the simulation results. Similar computational analyses are performed for the rough interface with

protrusion in the center of the domain of dimensions 5 μm × 5 μm. Here again, we ensure that the total current entering and leaving the electrolyte phase is the same (charge conservation). However, the presence of surface roughness ensures that current density will change at the surface features, although the net summation of current density at the interface will still equal the applied current density.

5.2.2 Results and Discussions

Electrochemical reaction rate, Li self-diffusion and ionic diffusion rates determine the nature of deposition. While the relative influence of reaction rate and electrolyte transport limitations has been elucidated in the past through the means of the dimensionless Wagner number *(Wa)*,[308, 309] analysis of Li self-diffusion needs to be incorporated to provide a holistic picture. In this regard, we define a non-dimensional electrochemical Damkohler number (*Da*) as the ratio of electrochemical reaction rate to diffusion rate and classify the observed regimes as a function of this number. $Da \gg 1$ implies that the electrochemical reaction occurs at a much faster pace as compared to surface self-diffusion. This leads to the formation of dendritic structures since the deposited Li will not have enough time to diffuse on the substrate. For $Da \sim 1$, formation of Li islands should be observed due the equivalence of the reaction and self-diffusion rates. Finally, for $Da << 1$, Li self-diffusion eclipses the reaction rate and uniform deposition is obtained.

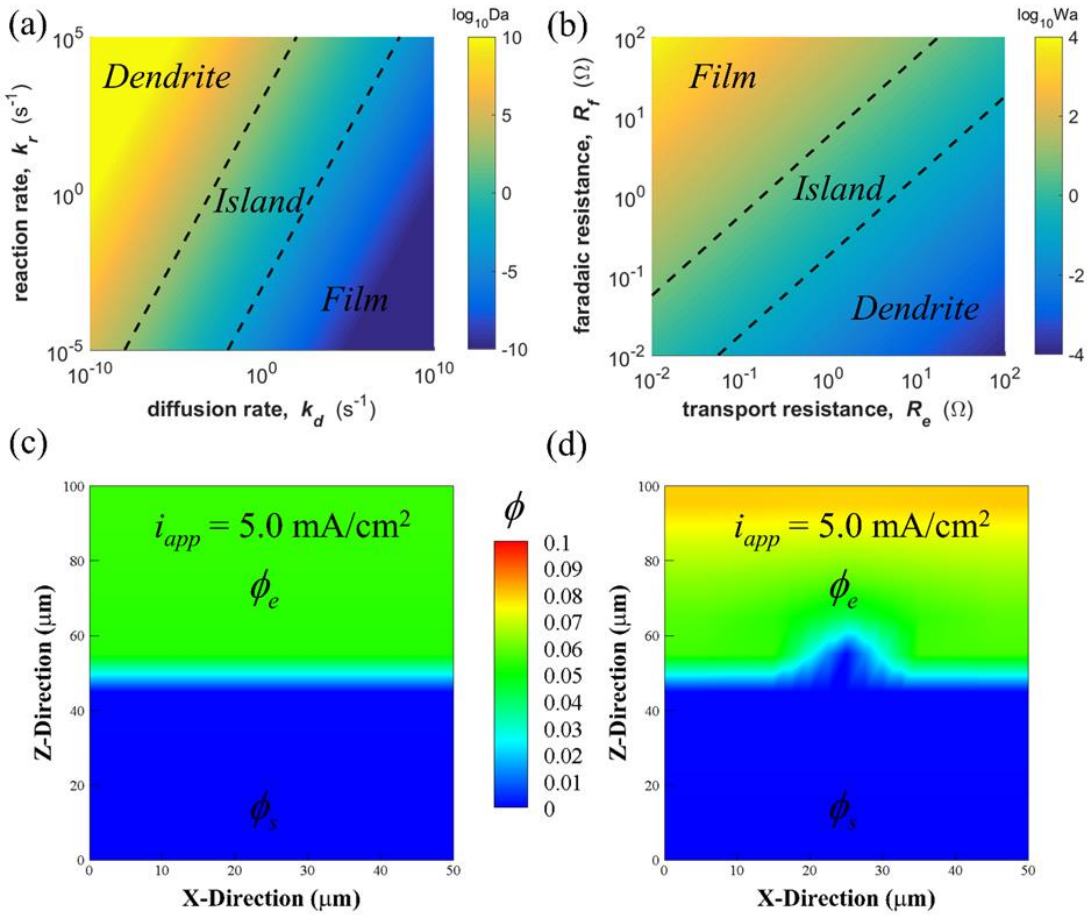

Figure 5.2 Deposition morphology phase map as a function of (a) Damkohler number and (b) Wagner number. High Damkohler number and low Wagner number leads to dendritic deposits. (c) Potential profile in liquid electrolyte and solid Li for uniform substrate. (d) Potential profile in liquid electrolyte and solid Li for rough substrate with protrusion at the middle of electrode-electrolyte interface. Here, ϕ_e is the potential in the electrolyte phase and ϕ_s is the potential in the solid phase.

Figure 5.2(a) shows the aforementioned regimes of deposition morphology for Li as a function of the electrochemical reaction and surface diffusion rate. Different isovalues of the Damköhler number are represented by the contour colors. As mentioned earlier, transition from high to low Damkohler number results in the morphological variation from dendritic to film type structure. Figure 5.2 (b) contrasts the Wagner number criteria for deposition outlining the relative influence of charge transfer resistance (faradaic resistance) and electrolyte transport resistance on deposition morphology. Large Wagner numbers (high faradaic resistance and low transport resistance) imply substrate conformal deposition while increased transport resistance can cause

depletion of Li^+ ions close to the substrate surface resulting in dendritic protrusions. It is evident that both these numbers are pertinent to quantification of the deposition regime and are correlated through the reaction rate/faradaic resistance term. Accurate prediction of the deposition regime requires detailed investigations into both quantities. Generating a combined deposition map based on the Damkohler and Wagner numbers incorporating cell geometric features and operating conditions is the logical way forward and will be the focus of future investigations.

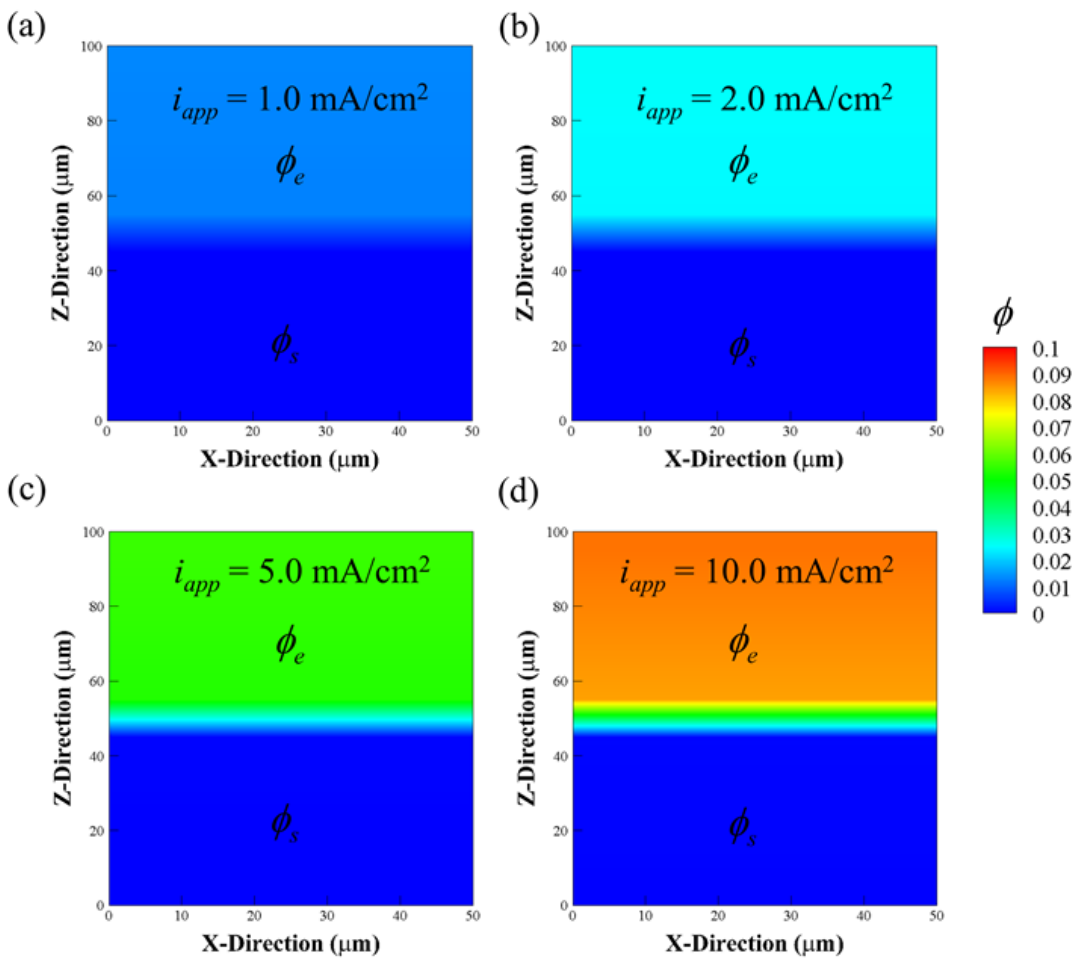

Figure 5.3 Effect of applied current density on potential profile inside electrolyte and Li metal for uniform surface. The current density values are (a) 1.0 mA/cm^2, (b) 2.0 mA/cm^2, (c) 5.0 mA/cm^2 and (d) 10.0 mA/cm^2.

Figure 5.2 (c) and Figure 5.2 (d) illustrate the effect of uniform substrate versus rough substrate on the resulting potential profiles inside the electrolyte and Li metal. Charge and species transport inside the electrolyte is coupled with electrochemical reaction kinetics at the electrolyte-Li metal interface and subsequent electronic transport inside the solid Li. The presence of structural

inhomogeneities (see Figure 5.2 (d)) results in a non-uniform potential profiles resulting in varying reaction rates at the electrode-electrolyte interface with higher local current density near the protrusion (near the middle). This further justifies the findings from the mesoscale model (see Figure 5.2) where preferential deposit of Li was observed on the substrate ridges. For low operating current densities, substrate roughness effects diminish and both uniform and rough substrate show similar behavior (Figure 5.4). Thus, at low current rates preferential deposition is minimal.

Figure 5.3 displays the potential profile in the electrolyte and solid phase for the uniform interface as a function of current density. Potential variation is only obtained in the vertical direction because of the enforcement of adiabatic boundary conditions on the left and right boundaries and the absence of any geometric perturbations. The potential in the solid phase stays close to 0, owing to the extremely high electronic conductivity of solid Li ($\sim 10^7$ S/m). As the current density increases from 1.0 mA/cm^2 to 10.0 mA/cm^2, the potential gradient in the electrolyte increases. The uniformity of current density at the electrolyte-Li metal interface will ensure homogeneous deposition. The above findings show that substrate roughness has a deleterious impact on the interfacial instability with Li^+ ions being directed onto the protrusions resulting in a predilection towards formation of dendritic structures.

Figure 5.4 contrasts the potential profiles in the solid and electrolyte phase for uniform versus rough Li surface at low applied current. Here, (a) and (b) are for the uniform interface while (c) and (d) are for the interface with protrusion in the center of the domain. The presence of the surface protrusion does not have much effect at low current densities as is evidenced by the obtained potential profiles for both uniform and rough surface. So, homogeneous deposition can still be expected at the electrode-electrolyte interface.

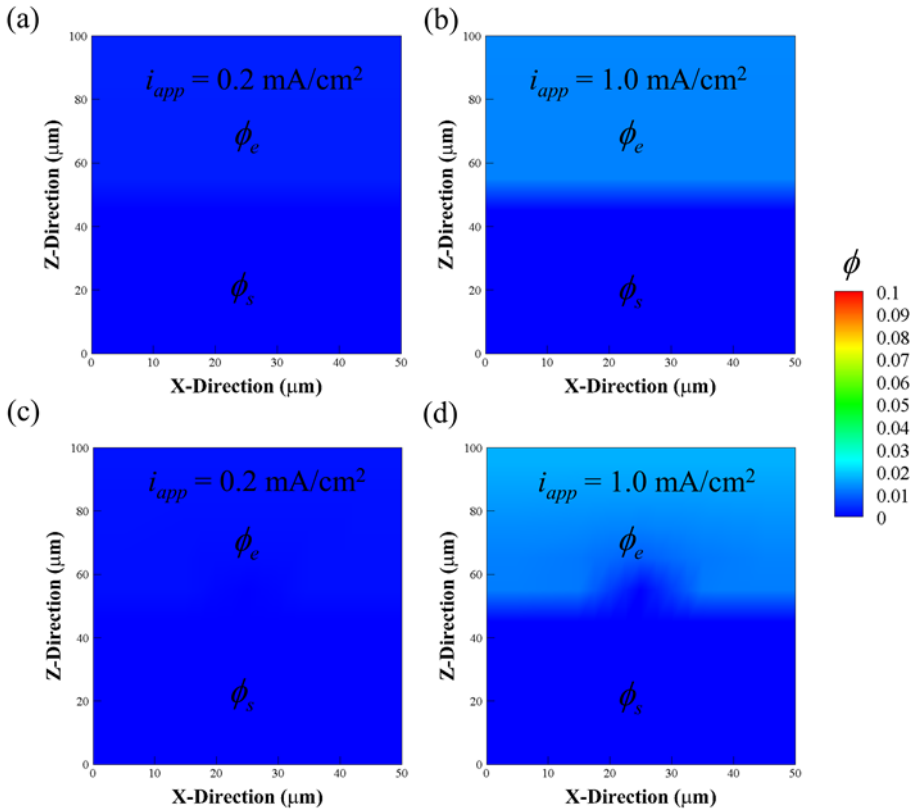

Figure 5.4 Comparison of potential profiles in electrolyte and Li metal at low applied current densities for uniform versus rough surface. Uniform surface with current density (a) 0.2 mA/cm^2 and (b) 1.0 mA/cm^2 . Rough surface with current density (c) 0.2 mA/cm^2 and (d) 1.0 mA/cm^2

5.3 Dendrite Suppression via Ion Flux Regulation

Dendrite formation could originate from the spatial inhomogeneity in Li-ion distribution. Therefore, homogenizing Li-ion flux is an effective strategy to obtain dendrite-free deposition, such as regulating Li-ion flux distribution in channels [18,19]. For instance, Wu et al. reported that uniform Li deposition could be achieved by confining Li-ion pathways in the nanochannels [20]. In this regard, we use our mesoscale model to design the ion-channels for efficient ion-flux regulation and dendrite suppression. Figure 5.5 exemplifies the warping of the electric field around a central protrusion resulting in peak current density eclipsing the valley current density as the current density is increased. In the following, we will investigate the impact of through ion-channels on minimizing this electrodeposition instability.

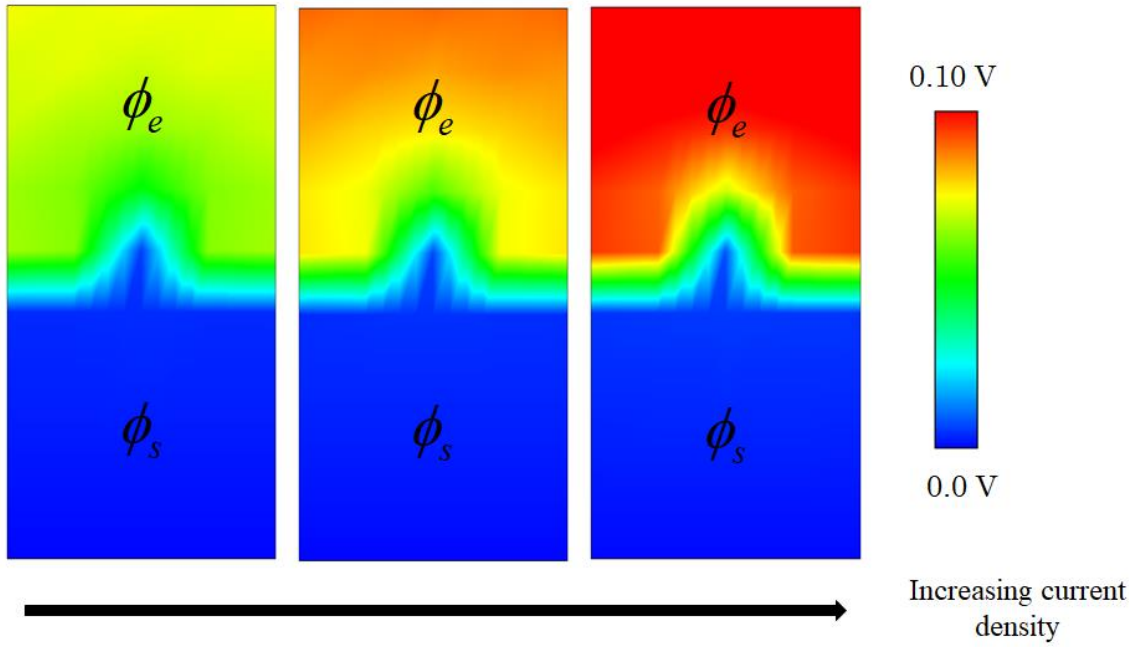

Figure 5.5 Electric field focuses Li^+ ions onto the central protrusion with more propensity as the current density is increased.

Figure 5.6 demonstrates the impact of through ion-channels number density on the corresponding potential profiles and deposition instability on a smooth and rough substrate respectively. The operating current density is 2 mA/cm^2 which is less than the limiting current density for this system. For the flat substrate shown in Figure 5.6 (a) and (b), increasing the ion-channel density has little impact on the electric fields and ion-flux lines. Li^+ ions move in a vertical route onto the metal substrate where the deposition happens. Since the substrate is perfectly flat, the Li^+ ions have equal proclivity towards all sites on the metal electrode and uniform deposition ensues. In contrast, in the presence of existing irregularities on the metal anode substrate the deposition nature changes. For the low ion channel density configuration shown in Figure 5.6 (c) where the channel width and protrusion width are non-conformal, there is a preferential influx of the Li^+ ions onto the protrusion as compared to the valley. This eventually leads to non-uniform deposition which can devolve into needle and fractal shaped dendrites. Figure 5.6 (d) exhibits the Li^+ path lines when the ion channel density is large enough such that there is conformity between the channel size and protrusion width. All current lines are now directed vertically downward and current density in each of the ion-channels is the same. Consequently, the ion channel number density boost assists flux homogenization on a rough substrate promoting uniform deposition.

Figure 5.7 (a) and (b) illustrate this further. As the ion channel-size, *W*, decreases, the current density ratio at the peak and the valley remains constant until the ion channel width becomes equal to the protrusion width, *w*.

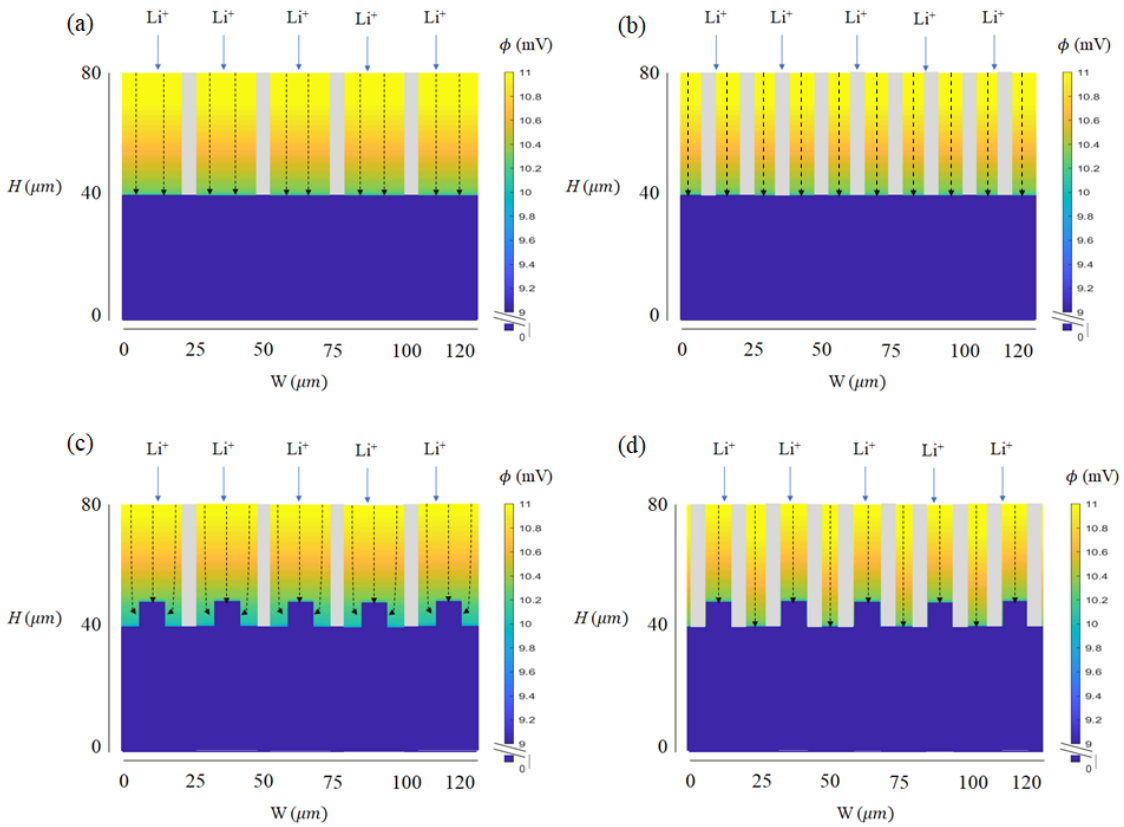

Figure 5.6 Potential contours and current flux lines on a smooth substrate with (a) low ion channel density and (b) high ion channel density. As the ion channel density increases, deposition stability remains the same. Current flux lines on a rough substrate with (c) low ion channel density and (d) high channel density. As the number density increases, flux homogenization is enhanced leading to stable deposition.

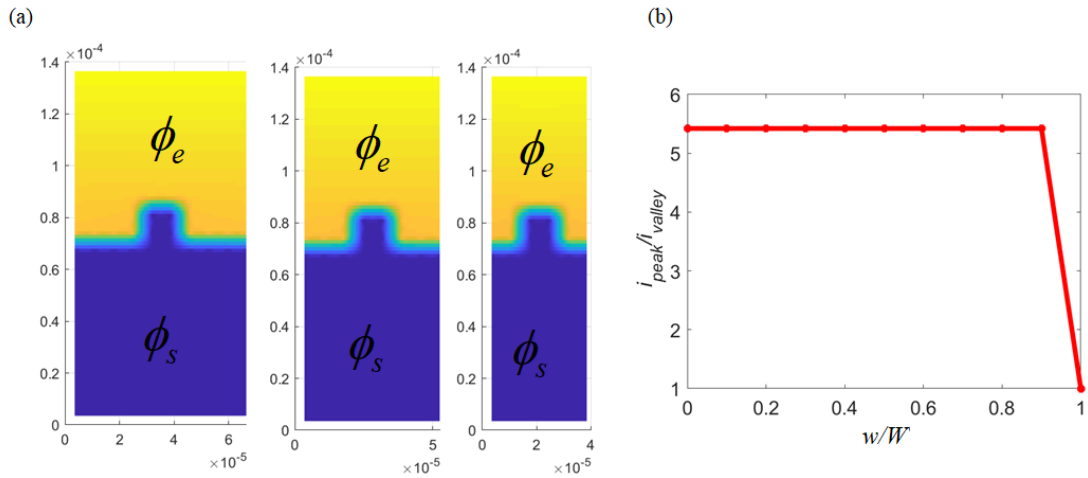

Figure 5.7 Impact of protrusion width to ion channel width ratio on (a) potential profiles and (b) deposition stability

Figure 5.8 gives the design window for the ion-channel dimensions with respect to the surface roughness of the Li metal substrate. Figure 5.8 (a) shows a schematic of the metal surface roughness and the ion channel. Figure 5.8 (b) and (c) show the contours for the peak vs valley current instability as a function of the applied current density, protrusion height to channel height ratio (*d/H*) and protrusion width to channel width ratio (*w/W*) respectively. For a protrusion width unequal to the ion-channel size, the current instability, i_{peak}/i_{valley} , increases as the metal anode surface roughness increases. For applied current densities, i_{app}, close to the limiting current density, i_{lim}, of the system, the instability rises precipitously. For protrusion heights, *d*, approximately 10% of the ion channel height, the instability magnitudes go up to 2 indicating that it is twice as likely to deposit at the protuberance than at the valley. Consequently, it is advisable to make the Li metal surface as smooth as possible to minimize the kinks. However, since achieving atomic scale roughness is infeasible, it is advisable to design the ion channel width to be conformal to the wavelength of the surface perturbation to minimize the current instability. This is amply evident from Figure 5.8 (c); the peak vs current instability is equal to one at all applied current densities only when the ion channel width is equal to the protrusion width. It is to be noted here that the applied current densities have been normalized by the applied current density of the system. Beyond the limiting current density, deposition is always unstable owing to the Sand's time limitation causing the concentration to drop to zero near to the metal electrode surface engendering unmitigated dendritic growth.

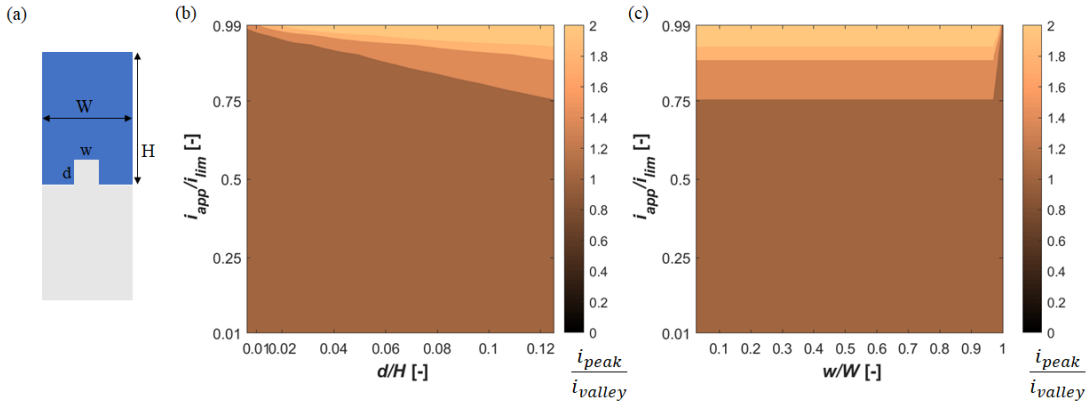

Figure 5.8 (a) Schematic of Li metal surface protrusion and ion channel dimensions. (b) Contour plot of current instability, i_{peak}/i_{valley}, as function of applied current density and protrusion height to channel height ratio. (c) Contour plot of current instability as function of applied current density and protrusion width to channel width ratio. Note that the applied current density is normalized by the limiting current density of the system.

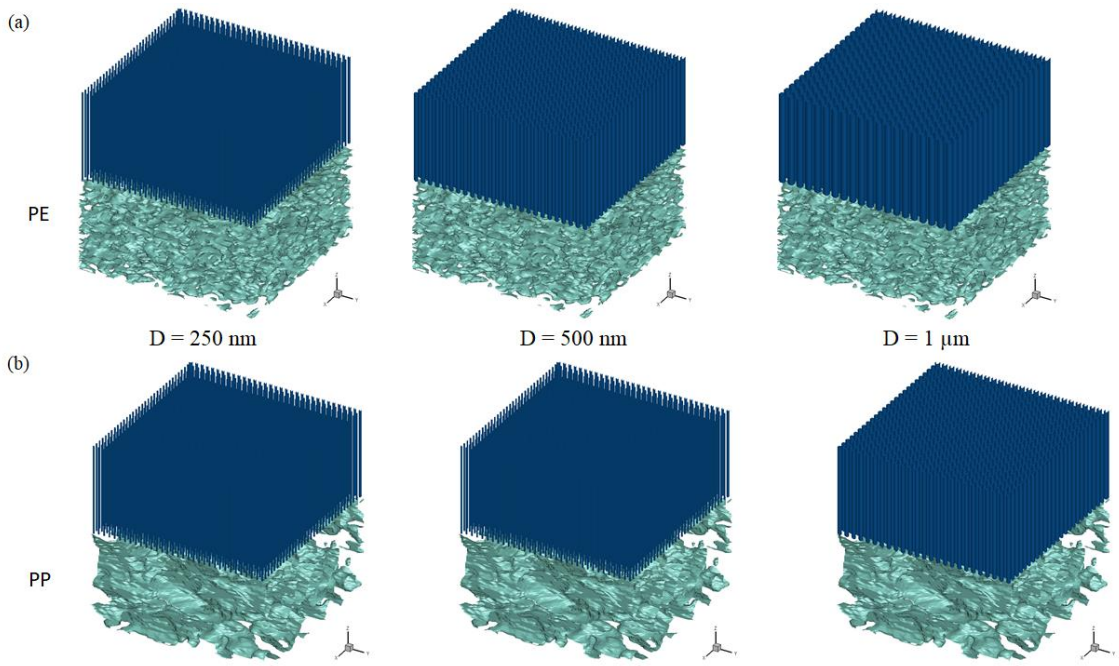

Figure 5.9 Bilayer separator architecture comprising of through ion channels and (a) Targray PE separator and (b) Celgard PP separator. Ion channel size increases from 250 nm to 1 µm as we move from left to right.

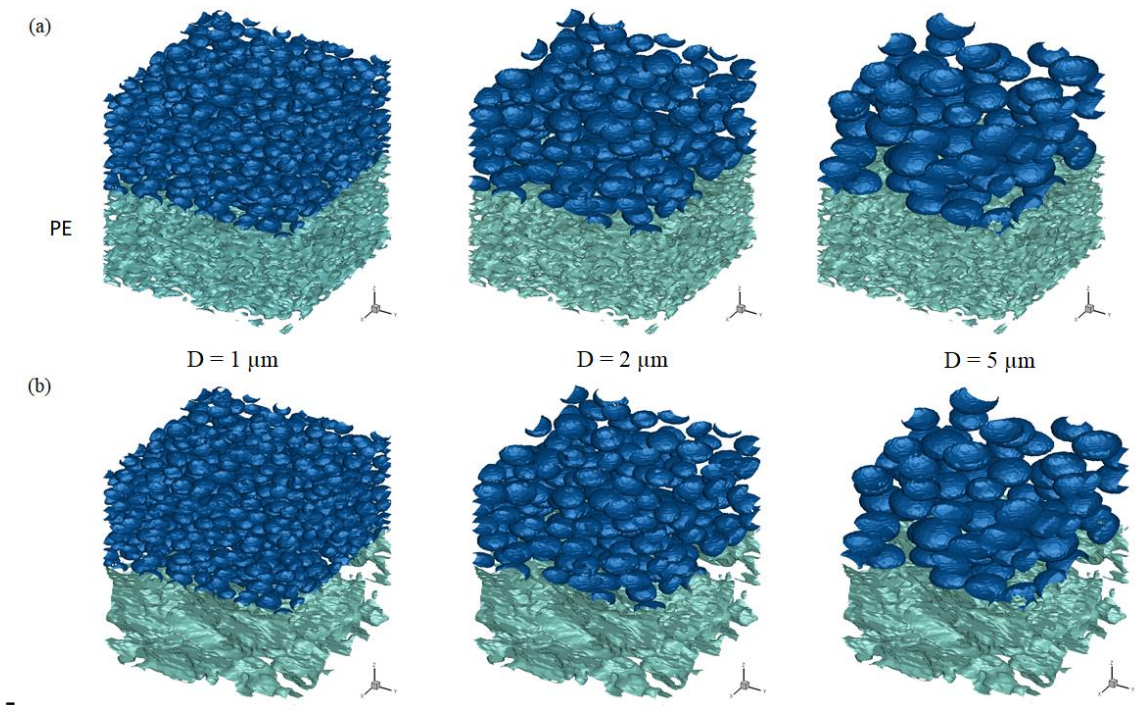

Figure 5.10 Bilayer separator architecture comprising of microspheres and (a) Targray PE separator and (b) Celgard PP separator. Microsphere size increases from 1 µm to 5 µm as we move from left to right.

Finally, we utilize our mesoscale model insights to aid in designing bilayer separator architectures that provide ion flux regulation alongside mechanical rigidity. To this effect, we combine the polyethylene (PE)/polypropylene (PP) separator with our flux regulating ion channels creating a bilayer architecture. The ion channel layer will face the metal anode and allow for ion flux regulation while the polymer structure will provide some mechanical strength. We use the virtual microstructure generation suite in GeoDict to build the ion-channel architectures and stitch it together with tomograms of the PP and PE separator available open source. Figure 5.9 displays the bilayer separator architecture comprising of through ion channels and PE/PP separator. We characterized the effective properties of this separator to find that the tortuosity of the ion-flux layer lies close to 1.4 for all the ion channel sizes investigated. Consequently, we propose using the ion channel size that provides closest conformity to the surface roughness of the Li metal. Generally, the Li metal surface roughness lies in the range of 200-600 nm; we delineate 200 nm diameter ion channels to be the optimal choice for dendrite suppression in lithium metal batteries. This also paves a way for rapid screening of separator architectures for ion-flux regulation. Figure

5.10 shows bilayer separator architecture combining the PE/PP separator with microspheres of varying sizes. The tortuosity of microsphere layer comes close to 1.6; showing it to be slightly inferior to the through ion-channel architecture.

5.4 Magnesium Electrodeposition

Li metal has high propensity for dendrite formation which can lead to deleterious side effects like internal short circuit inside the cell [249, 309-313]. This reduces the viability of using Li metal as an anode in LIBs. Consequently, other metal-ion chemistries are being investigated in detail as an alternative to LIBs.

Magnesium has been reported to be a suitable candidate for substituting lithium ion batteries [10, 288, 290, 314-319]. Owing to the divalent nature of the Mg^{2+} cation, its volumetric energy density can exceed that of LIBs. Experimental studies into Mg deposition reveal the formation of uniform structures as opposed to agglomerates, thereby, showing reduced predilection towards formation of dendritic structures [320, 321]. A theoretical first principles study investigating dendrite growth on magnesium ion battery anode unveils the possibility of faster surface diffusion characteristics leading to the formation of uniform deposits along the Mg (0001) plane [322]. However, anisotropy and large variation in magnitude of Mg self-diffusion coefficient has been reported in literature [316, 318, 323-325]. Magnesium exhibits hexagonal close packed unit cell structure which leads to diffusion anisotropy, parallel and perpendicular to the basal plane. Also, surface self-diffusion in itself cannot explain the deposition characteristics; the applied current density is an equally important parameter determining the nature of Mg deposits on Mg substrate. Consequently, investigation into deposition morphology requires considering both these parameters.

In this work, we have performed accurate quantification of the magnitude of Mg self-diffusion coefficient derived from experiments and theoretical studies. Dimensional analysis based on relative magnitudes of electrochemical reaction versus surface diffusion rates is done to delineate varying Mg deposition regimes based on electrodeposition operating conditions. Finally, Kinetic Monte Carlo simulations are performed, utilizing the computed self-diffusion and electrochemical reaction rates as inputs, to supplement the deposition methodology analysis presented earlier.

5.4.1 Methodology

Deposition morphology on a substrate can be determined from the relative magnitudes of the electrochemical reaction rate and the surface diffusion rate. For Mg deposition on Mg substrate, these parameters can be related to the experimental current density magnitude and the self-diffusion coefficient of Mg. The electrochemical reaction rate, k_e can be obtained from the experimental current density, J, through Equation (5.5).

$$k_e = \frac{Jd^2}{2F} N_a \tag{5.5}$$

Here d is the mean diffusion distance between lattice sites for magnesium, F is Faraday's constant and N_a is Avogadro's constants. The values for these parameters are enumerated in Table 5-1. The average current density magnitude utilized for Mg symmetric cell is, J_0 = 9.2 A/m^2. Since, the formation of Mg deposits can vary the interface morphology and consequently affect the current density at the substrate we have assumed an order of magnitude variation, $n = \frac{J}{J_0} = 0.1$ – 10, for the current density magnitude, i.e., from 0.92 A/m^2 to 92 A/m^2, when defining our electrode operating conditions. Also, magnesium exhibits a hexagonal close packed structure with lattice constants, a = 3.21 Å and c = 5.21 Å [326]. Consequently, we have assumed an average lattice cell dimension, d = 5 Å for our computations.

Table 5-1 Model Parameters.

Parameters		Values	Units
D	Lattice cell dimension	5	Å
J_0	Average current density	9.2	A/m^2
R	Gas constant	8.314	J/mol-K
F	Faraday constant	96,487	C/mol
N_a	Avogadro constant	6.022×10^{23}	1/mol
T	Operating temperature	300	K
ν	Vibration frequency	5×10^{12}	1/s

Surface diffusion rate, k_d, is computed using equation (5.6) and depends on the activation energy barrier for self-diffusion, E_{diff}, temperature, T and jumping frequency for Mg diffusion, ν. Literature reports average values of jumping frequency between 10^{12}~10^{13} s^{-1} [327]. Consequently, we use a value of $\nu = 5\times10^{12}$ s^{-1} for our computations. Here, k_B is the Boltzmann constant.

$$k_d = \nu \exp\left(\frac{-E_{diff}}{k_B T}\right) \tag{5.6}$$

Self-diffusion energy barrier, E_{diff}, determines the magnitude of the diffusion rate, and thus, needs to be determined accurately to mimic the Mg system. Low magnitudes of E_{diff} correlates to high values of diffusion rates and vice versa. In literature, generally values of diffusion energy barrier, E_{diff} [328], or diffusion coefficients, D, are reported [325, 329-331]. When the E_{diff} value is reported, Equation (5.6) is directly used to compute the self-diffusion rate. Alternatively, the diffusion coefficient can be related to the diffusion rate via the Einstein-Smoluchowski relation given in Equation (5.7) [325].

$$D = \frac{1}{2} k_d d^2 \tag{5.7}$$

Consequently, when the diffusion coefficient values are reported, Equation (5.7) is utilized to compute the self-diffusion rate, k_d, and energy barrier, E_{diff}. Experimental and theoretical values of diffusion coefficient, self-diffusion energy barrier and diffusion rate from literature have been computed at $T = 300$ K and tabulated in Table 5-2. Since magnesium has an HCP structure, diffusion can occur along the basal plane, $D_{\parallel}$, or perpendicular to the basal plane, $D_{\perp}$. Both these values are reported along with the averaged diffusivity value, D_{avg}, which is then utilized for the diffusion rates computation.

Arrhenius type experimental relations for self-diffusion in Mg have been reported by Shewmon [326], Combronde and Brebec [327] in the temperature range 468 °C – 635 °C and 500 °C - 630 °C respectively (Equation (5.8)).

$$D = D_0 \exp\left(\frac{-E_a}{RT}\right) \tag{5.8}$$

The relations are extrapolated to temperature of 300 K to obtain the self-diffusion coefficient at room temperature. First principle theoretical calculations using LDA and GGA have been performed by Ganeshan et al. [328], Zhang et al. [329] and the diffusion coefficients are reported in the temperature range 625 – 1000 K and 500 – 1000 K respectively. The applicability of Arrhenius equation is assumed based on the diffusivity-temperature dataset and linear regression analysis of ln (D) versus T is performed to obtain the Arrhenius constants, D_0 and E_a for these datasets. Subsequently, the diffusivity at 300 K is obtained from the regression correlation

Table 5-2 Reference values of self- diffusion coefficient, energy barrier and rate

References		$D_{\parallel}$ (m^2/s)	$D_{\perp}$ (m^2/s)	D_{avg} (m^2/s)	E_{diff} (eV)	k_d (s^{-1})
Shewmon (Expt.) [331]		3.4695×10^{-27}	3.7421×10^{-27}	3.6058×10^{-27}	1.2051	2.8846×10^{-8}
Combronde and Brebec (Expt.) [326]		1.8154×10^{-27}	1.3398×10^{-27}	3.1552×10^{-27}	1.2086	2.5242×10^{-8}
Ganeshan (Th.) [327]	LDA	9.9201×10^{-27}	4.9844×10^{-27}	7.4523×10^{-27}	1.1863	5.9618×10^{-8}
	GGA	2.2919×10^{-24}	1.1162×10^{-24}	1.7041×10^{-24}	1.0459	1.3633×10^{-5}
Zhang (Th.) [328]	LDA / GGA	7.2716×10^{-28}	6.5608×10^{-28}	6.9162×10^{-28}	1.2478	5.5330×10^{-9}
Jäckle (Th.) [329]	GGA	2.8840×10^{-7}	-	2.8840×10^{-7}	0.02	2.3072×10^{12}

5.4.2 Results and Discussion

Order of magnitude analysis is performed by defining the non-dimensional electrochemical Damköhler number, *Da*, as the ratio of the electrochemical reaction rate, k_e to the surface diffusion rate, k_d (given in Eq (41)).

$$Da = \frac{k_e}{k_d} \qquad (5.9)$$

Here, $Da \gg 1$ implies that the electrochemical reaction occurs at a much faster pace as compared to surface self-diffusion. This leads to the formation of dendritic structures since the deposited Mg will not have enough time to diffuse on the substrate. For $Da \sim 1$, formation of Mg islands should be observed due the equivalence of the reaction and self-diffusion rates. Finally, for $Da << 1$, Mg self-diffusion eclipses the reaction rate and uniform deposition is obtained.

Figure 5.11 shows the aforementioned regimes of deposition morphology for Mg as a function of the electrochemical reaction and surface diffusion rate. Different isovalues of the Damköhler number are represented by the contour colors. The magnesium electrode operating regime is shown enclosed in the white box based on the electrochemical reaction rates and surface diffusion rates. For the experiments performed, the electrochemical reaction rate ranges from 0.72 to 72 s^{-1}. Table 5-2 lists the Mg self-diffusion rates and corresponding activation energy barriers

available in literature. It can be observed that the diffusion coefficient magnitude exhibits a wide range of variation ranging from 10^{-7} to 10^{-28} m^2/s. This corresponds to extremely high (~10^{12} s^{-1}) to very low (~10^{-9} s^{-1}) diffusion rates. Consequently, we have around two orders of magnitude variation in reaction rate versus around twenty order of magnitude variation in the self-diffusion rate. This also gets reflected in the magnesium electrode operating zone (boundaries shown in white) in the electrodeposition phase map shown in Figure 5.11. The zone is elongated along the x-axis as compared to y-axis owing to the larger variation of self-diffusion rates. Damköhler number isovalues of 10^{-2} and 10^{2} are chosen to define the boundaries of dendritic, islands and film type deposition.

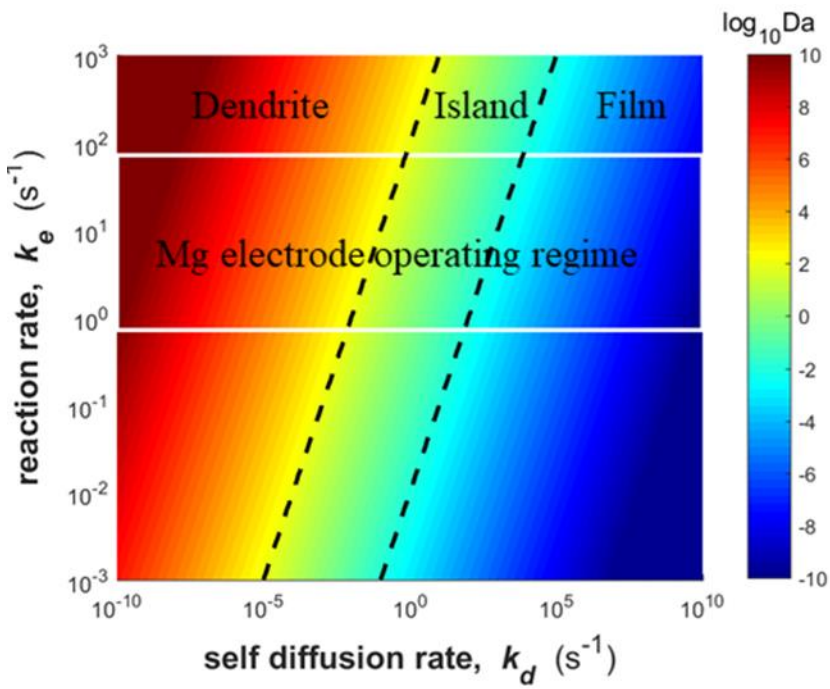

Figure 5.11 Deposition morphology phase map as a function of Damkohler number. Red zone corresponds to Da >>1 (dendrite morphology), green zone corresponds to Da ~1 (island morphology) and blue zone corresponds to Da << 1 (film morphology). Magnesium electrode operating zone is shown in the white box and morphology zone boundaries are shown by black lines.

5.5 Conclusions

In summary, we elucidate the proclivity of the formation of dendritic deposition morphology at high reaction rates and low surface diffusion rates during plating at metal electrodes. Surface diffusion is an intrinsic material property of the deposited metal while the reaction rate is

dependent on the operating conditions, the operational current density and the presence of surface heterogeneities on the metal substrate. The metal electrode surface roughness contributes to Li^+ ion flux directed to the peaks as opposed to the valleys contributing to unstable deposition fronts.

Given that dendrites result in detrimental performance of Li metal batteries, we provide a dendrite suppression strategy using vertically aligned though ion channels. It is found that the size of the channels, its width, height with respect to the surface roughness as well as the ion channel number density plays a key role in flux homogenization-based dendrite suppression. The confinement effect of the ion-channels plays a key role in controlling Li-ion transport towards uniform deposition. The usage of bilayer separators combining the mechanical rigidity of state-of-the-art polymeric separators along with ion flux regulating through ion channels can pave the way for Li metal batteries with long cycle life.

6. ELECTRODEPOSITION STABILITY OF METAL ELECTRODES WITH SOLID ELECTROLYTES

Relevant Publications and/or Working Papers

1. **A. Verma**, H. Kawakami, T. Kotaka, N. Ikeda, M. Shibata, K. Aotani, Y. Tabuchi, P.P. Mukherjee, *"Microstructure and Pressure Driven Electrodeposition Stability in Solid-State Batteries"*

6.1 Background

Lithium-ion batteries (LIBs) have become pervasive in small scale electronics and are gearing towards high energy, power applications like electric vehicles and grid energy storage [326]. Commercial LIBs with graphite anode, transition metal oxide cathodes and liquid electrolyte operate through shuttling of Li^+ ions between the intercalation hosts. Graphite (specific capacity ~ 372 mAh/g)[327] and metal oxide (specific capacity ~ 200 mAh/g)[328] host structure lowers the cell gravimetric/volumetric specific capacity, consequently, large battery packs comprising of several unit cells are required for high energy/power applications. The development of next generation lithium-ion batteries with enhanced energy and power density is predicated on utilization of pristine lithium metal anodes, which exhibit low reduction potential (-3.04 V) and high specific capacity (3870 mAh/g) [329]. In this configuration, entire anode mass contributes to the cell capacity precluding the inactive weight associated with the carbonaceous host. However, several problems plague the usage of Li metal anodes in LIBs. Immense volumetric fluctuations during the plating-stripping process coupled with heterogeneous metal nucleation and growth leads to solid electrolyte interphase (SEI) breakdown-reformation loop and dead lithium accumulation during each cycle contributing to rapid capacity fade.[325, 332] Uninhibited dendritic growth at the anode during charging poses a serious safety issue; dendritic growth through the porous separator in liquid electrolytes can reach the cathode causing internal short circuit-based failure of the metal battery system.[333]

Dendrite growth suppression using all solid-state batteries (ASSBs) comprising of solid electrolytes (SEs) providing a rigid barrier against Li deposition has emerged as a promising growth control strategy.[10, 334, 335] Solid electrolyte systems also offer improved safety, no leakage, non-flammability and a larger electrochemical window. During the past decade, several

SEs with ionic conductivity similar to liquid electrolytes have been developed [296, 335-338]. However, there are some bottlenecks afflicting the performance of solid-state batteries as well. High interfacial resistance due to low chemical/mechanical wettability, unstable nature of the metal-SE interface resulting in chemical/electrochemical decomposition based interphase formation and imperfect contact are major hindrances that need to be overcome[336, 339]. SE decomposition at the electrode/electrolyte interface leads to the formation of interphase layer while sluggish interfacial transport leads to the formation of Li-ion depletion zones[340, 341]. Imperfect contact between the metal-electrolyte interface leads to current focusing at junctions, reducing the interfacial charge transfer area considerably and result in large kinetic overpotentials[342]. Furthermore, stress evolution inside the SE resulting from heterogeneous deposition can surpass its material fracture strength, causing fracture, and impede the Li-ion transport in electrolyte appreciably.[343] The cathode-solid electrolyte composite also suffers from dynamic stress and fracture during cycling arising from diffusion-induced stress and contact mechanics[344, 345].

Polymer[118, 346-348], garnet[60, 116, 290, 306, 349, 350] and sulfide[351-353] electrolytes primarily comprise the array of SEs being investigated for applications in solid-state batteries to mitigate dendrite growth. Single-ion conductors with unity transference numbers (inorganic garnet, sulfide SEs) have attracted renewed interest recently[354]. While sulfide electrolytes like LPS generally exhibit glassy/amorphous structure[355, 356], garnet oxide electrolytes like LLZO exhibit polycrystalline structure[357, 358]. Polycrystalline structure of garnet electrolytes has been identified as the cause of unmitigated Li growth through the electrolyte beyond critical current densities (CCD) through preferential growth along the grain boundaries as observed in experiments[359]. Transgranular growth of Li has also been proposed, although, propagation through grain boundaries form majority of experimental findings. Single crystal SEs have exhibited penetration by Li dendrite as well.[360, 361] Experimentally, several strategies are being explored to ensure deposition stability with inorganic electrolytes including the use of electrochemically stable artificial interlayers juxtaposed between the Li metal and SE (eliminates interphase formation through metal-SE decomposition)[121, 258, 354, 362-365] and external mechanical “stack” pressure application (promotes interfacial contact reducing contact resistance)[258, 366-368] on the metal-SE system.

Electrodeposition at solid-solid interfaces is affected by interfacial stresses as demonstrated by the seminal theoretical work of Monroe and Newman [346]. Further analysis of Li-solid

polymer electrolyte systems using linear elasticity theory and stress-kinetics coupling was pioneered by Monroe and Newman; it was demonstrated that a SE with shear modulus twice that of Li metal was capable of suppressing dendrite growth [369]. This work was extended by Barai *et al.* incorporating ion transport through the SE and elastic-plastic deformation of lithium for solid polymer electrolyte [370]. The above analysis has been recently extended to solid inorganic electrolytes to account for the varying partial molar volumes of Li in polymer electrolyte vs solid inorganic electrolyte [12, 371]. A unifying theme of the above studies was the large interfacial stress magnitudes (gigapascals) impacting the deposition stability through ion flux redistribution towards/away from the metal protrusions. The impact of polycrystalline SE architecture on deposition stability and delineation of current focusing in the grain boundaries for nanometer-sized grains have been studied as well[114]. However, realistic SEs can be of the size of hundreds of microns with grain size lying in the micrometer range[115]. Furthermore, experimental data suggests that even for sufficiently high shear modulus electrolytes, Li metal penetration through the SE is unavoidable[93]. These findings necessitate detailed investigation of the mechanisms of growth and the correlation between the critical current density, transport–electrochemistry-mechanics complexations of the Li metal substrate and SE microstructure (grain boundaries, defects, pores, imperfect contact) under external pressure and varying thermal environments. There is a need for a coupled physics-based model to delineate stable operating regimes of the solid-state battery with inorganic SE under external pressure[372].

In this work, we use the modeling paradigm to elucidate the deposition stability of the metal-inorganic SE system cognizant of practical ASSB system physics. Firstly, the amorphous/polycrystalline microstructure of inorganic SEs comprising of grains, grain boundaries and voids is characterized to obtain the effective transport and mechanical parameters governing deposition dynamics. The effective property computations help in discerning the optimal microstructural configuration of the SE with superior transport and strength. Subsequently, we discern the impact of external pressure on the deposition characteristics. Stress in the metal-SE system under external pressure is directly correlated to the stack pressure magnitudes, lying primarily in the megapascal range. Consequently, the impact of stress-kinetics coupling on deposition stability is considerably reduced. Finally, we give the stability map for inorganic SE-Li metal system as a function of its mechanical and thermodynamic parameters (shear modulus ratio and molar volume ratio) for a wide range of operating conditions, namely, external pressure,

applied current density, surface roughness and working temperature. They provide good qualitative match to experimental datasets for the amorphous and polycrystalline LPS SE system.

6.2 Methodology

The schematic of the model geometry used for our computations is shown in Figure 6.1. The SE domain (blue) lies on top of the Li metal domain (grey) with perfect conformal contact. The metal-electrolyte surface roughness is represented by a sinusoidal interfacial perturbation allowing for the computation of stresses using linear elastic perturbation theory[117, 118, 121, 373]. The metal-electrolyte system is reduced to a two-dimensional geometry with isotropic mechanical and transport properties.

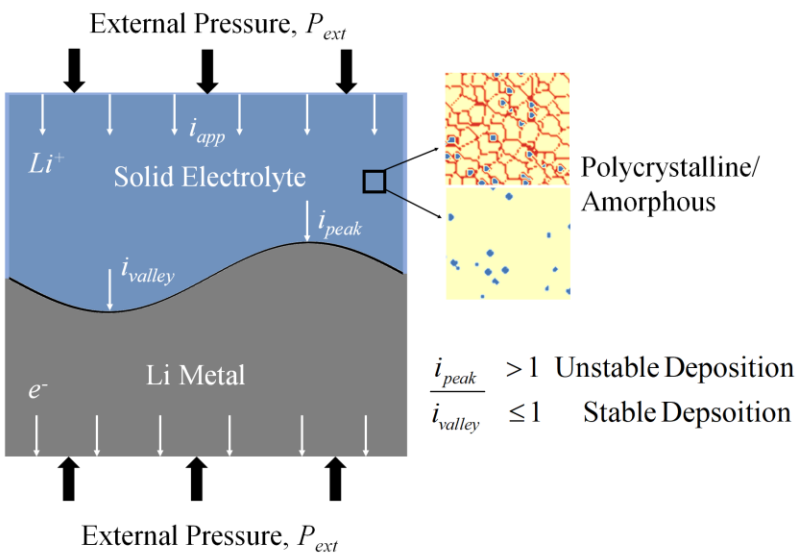

Figure 6.1 Schematic of the Li metal-solid electrolyte domain with a sinusoidal interfacial perturbation and perfect contact (left). Peaks and valleys correspond to the surface roughness of the metal-solid electrolyte domain. Current density from the counter electrode, i_{app}, redistributes through the polycrystalline/amorphous (right) solid electrolyte domain reaching the metal-electrolyte interface where the reduction of Li^+ ions to metallic lithium occurs. An interfacial current density distribution governed by the coupled electrolyte transport, interfacial curvature and external pressure induced interfacial stress is established. Stability descriptor, i_{peak} / i_{valley}, is used to distinguish the deposition regimes; i_{peak} and i_{valley} are the normal current densities at the peak and valley respectively. $i_{peak} / i_{valley} > 1$ implies preferential growth of the Li peaks as opposed to valleys (unstable deposition) and $i_{peak} / i_{valley} \leq 1$ corresponds to eventual flattening of the perturbation (stable deposition).

The applied external pressure generates mechanical stresses inside our system, with differing magnitudes at the peaks and the valleys. Lithium-ion flux from the SE corresponding to the applied current density, i_{app} , redistributes at the Li protrusions (peaks) and the Li depressions (valleys) of the interface in accordance with transport through the SE and interfacial stresses and the subsequent deposition stability can be characterized through the magnitude of the peak to valley current density ratio, i_{peak} / i_{valley} or i_p / i_v . This criterion is widely used in literature to understand deposition characteristics[372, 374-376]. A magnitude of $i_{peak} / i_{valley} > 1$ corresponds to preferential growth of the peaks as opposed to the valley resulting in an enhancement of surface roughness leading to unstable deposition. Conversely, a magnitude of $i_{peak} / i_{valley} \leq 1$ results in eventual flattening of the interfacial perturbation leading to stable deposition. The architecture of the SE, polycrystalline or amorphous, determine the effective transport and elastic properties, having an impact on the deposition stability. A polycrystalline architecture comprises of grains, grain boundaries and voids with different values of ionic conductivity and elastic constant attributed to each phase while an amorphous architecture can be characterized through the presence of grains and voids.

The analysis involves the following steps:

- Virtual generation of *polycrystalline* and *amorphous* SE microstructure for computation of effective transport and elastic constants.
- Effective property computation on the voxelated microstructure mesh with intrinsic properties attributed to each of the grain, grain boundary and void phase.
- Electrodeposition stability analysis on the SE-Li metal system cognizant of the external pressure-based stress considerations, stress-kinetics coupling at the metal-electrolyte interface and ionic transport through the SE.

6.2.1 Virtual Microstructure Generation and Effective Property Calculations

Figure 6.2 shows the representative microstructures for polycrystalline and amorphous SE system. A polycrystalline structure comprises of grains (G), grain boundaries (GB) and voids (V) while the amorphous structure consists of grains and voids[93, 377]. Experimentally, SEM images of the electrolyte can be used to characterize the grain and void size while the relative density values can

be used to compute the porosity of the electrolyte. The virtual microstructures are generated using the software suite DREAM.3D which allows for the screening of a wide range of grain size, void size, and void fractions[118]. Figure 6.2(a-i) exhibits the three-dimensional polycrystalline SE without voids and a grain size of 10 µm, while Figure 6.2(a-ii) displays a polycrystalline SE containing voids with a larger grain size of 20 µm. The voids are of size 4 µm with the pore volume fraction 25%. Figure 6.2(b) shows the front view of the polycrystalline SE with varying grain size, void size and porosity. The grains are shown in yellow, grain boundaries in red and voids in blue. As we move from the left to right, the grain size - void size - porosity varies from (b-i) 5 µm – 4 µm – 5%, (b-ii) 10 µm – 4 µm – 5%, (b-iii) 5 µm – 10 µm – 5% to (d) 5 µm – 4 µm – 20%. As the grain size increases, the grain boundary density decreases. As the void size increases, the number of voids for the same void volume decreases. Figure 6.2(c) shows the representative amorphous SE microstructure with varying void size and porosity. As we move from left to right, the void size – porosity varies from (c-i) 4 µm - 5%, (c-ii) 10 µm – 5% to (c-iii) 4 µm – 20%. There are no grain boundaries in the amorphous SE.

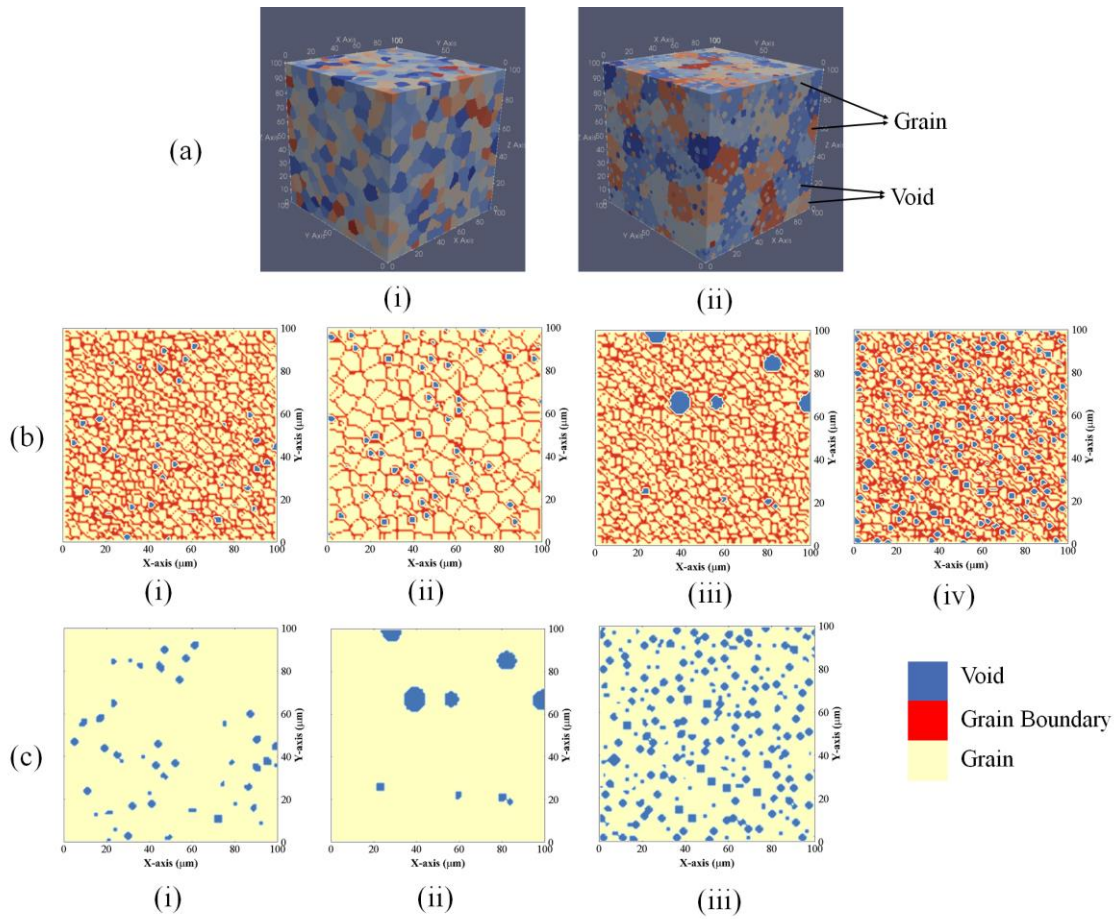

Figure 6.2 Visualization of solid electrolyte (SE) microstructure with grains, grain boundaries and voids. (a-i) Polycrystalline SE without voids and grain size 10 μm. (a-ii) Polycrystalline SE with voids of size 5 μm and grain size 20 μm. (b) Front view of polycrystalline SE with varying grain size, void size and void fraction. (b-i) 5 μm – 4 μm – 5%, (b-ii) 10 μm – 4 μm – 5%, (b-iii) 5 μm – 10 μm – 5% and (d) 5 μm – 4 μm – 20%. As the grain size increases, grain boundary density decreases. As void size increases, number of voids for the same void volume decreases. (c) Front view of amorphous SE with varying void size and void fraction. (c-i) 4 μm - 5%, (c-ii) 10 μm – 5%, (c-iii) 4 μm – 20%. There are no grain boundaries in amorphous SE.

Effective electrolyte properties are obtained by doing Direct Numerical Simulation (DNS) calculations on the reconstructed virtual SE microstructure. The effective electrolyte ionic conductivity and elastic modulus depends on arrangement of the grains, grain boundaries and voids and their instrinsic values. The DNS calculations involve the solution of Laplace equation on three-dimensional electrode microstructure grid with Dirichlet boundary conditions along the transport/stress direction and periodic boundary conditions on the other four faces. We assign a finite thickness to the grain boundary for the effective property computations on a voxelated mesh,

with the grain boundary thickness ranging from 10 nm to 100 nm[115]. The grain boundary thickness of 10 nm represents the closest analogue to the realistic structure. In-house codes are used to characterize the effective ionic conductivity and elastic constants. The representative elementary volume is ensured to be approximately 10 times the biggest feature size to ensure grid independence of the properties, and the voxel resolution is kept equal to the smallest feature size, namely, the grain boundary thickness. High performance computing was utilized to enable effective property computations for large grid sizes.

The effective ionic conductivity can be calculated by solving the Laplace's equation for electrolyte potential $\nabla.\left(\kappa_{SE,ref}\nabla\phi\right)=0$ with the indivdual phases assigned their intrinsic reference ionic conductivities.

$$\kappa_{SE,ref}\left(\vec{x}\right)=\begin{Bmatrix} \kappa_G \quad if\ \vec{x}\in G \\ 0.01\kappa_G \quad if\ \vec{x}\in GB \\ 0\ \ if\ \vec{x}\in V \end{Bmatrix} \tag{6.1}$$

$$\kappa_{SE,ref,x}^{eff}=\frac{L}{A\left(\phi_{right}-\phi_{left}\right)}\int_{\Omega_x}\kappa_{SE}\frac{\partial\phi}{\partial x}dydz \tag{6.2}$$

Here, the grain boundary conductivity is assigned an intrinsic value of 0.01 times the conductivity of the grain in accordance with density functional theory computations of grain boundary transport[59, 378]. They show that grain boundary transport of Li^+ is sluggish as compared to the Li^+ intragrain transport. The effective conductivities in the *y* and *z*-directions are computed in the usual fashion and an arithmetic mean is used to calculate the effective ionic conductivity of the full 3D structure, $\kappa_{SE,ref}^{eff}=\left(\kappa_{SE,ref,x}^{eff}+\kappa_{SE,ref,y}^{eff}+\kappa_{SE,ref,z}^{eff}\right)/3.0$ Similarly, the effective elastic modulus can be calculated by solving the Laplace's equation for displacement $\nabla.\left(E_{SE}\nabla u\right)=0$ with the indivdual phases assigned their intrinsic elastic modulus.

$$E_{SE}\left(\vec{x}\right)=\begin{Bmatrix} E_G \quad if\ \vec{x}\in G \\ 0.5E_G \quad if\ \vec{x}\in GB \\ 0\ \ if\ \vec{x}\in V \end{Bmatrix} \tag{6.3}$$

$$E_{x,eff}=\frac{L}{A\left(u_{right}-u_{left}\right)}\int_{\Omega_x}E_{SE}\frac{\partial u}{\partial x}dydz \tag{6.4}$$

Here, the grain boundary elastic modulus is assigned an intrinsic value of 0.5 times the elastic modulus of the grain in accordance with density functional theory computations by Seungho *et al*[379]. This complies with the grain boundary softening mechanism through which the dendrites can penetrate the SE.

6.2.2 Electrochemistry-Transport-Stress Model

Since, the garnet and sulfide electrolytes are single-ion conductors with immobile anionic species, Li^+ transport occurs only through migration and concentration gradients cannot develop inside the SE due to violation of electroneutrality[380]. Hence, the corresponding governing differential equation and boundary conditions for ion transport through the electrolyte domain take the following form.

$$\vec{\nabla}\cdot\left(\kappa_{SE}^{eff}\vec{\nabla}\phi_e\right)=0 \tag{6.5}$$

$$\begin{aligned}
&-\kappa_{SE}^{eff}\vec{\nabla}\phi_e = i_{app} && \text{at solid electrolyte - top interface}\\
&-\kappa_{SE}^{eff}\vec{\nabla}\phi_e = i_{BV} && \text{at solid electrolyte - Li metal interface}\\
&-\kappa_{SE}^{eff}\vec{\nabla}\phi_e = 0 && \text{at left and right boundaries}
\end{aligned} \tag{6.6}$$

$$\kappa_{SE}^{eff} = \kappa_{SE,ref}^{eff}\left[\frac{-E_{a,\kappa}}{R}\left(\frac{1}{T}-\frac{1}{T_{ref}}\right)\right] \tag{6.7}$$

Here, ϕ_e is electrolyte phase potential, i_{app} is the applied current density entering the SE domain. Ionic conductivity of the SE shows an Arrhenius dependence on the operating temperature T with activation energy $E_{a,\kappa}$ and reference values are given at T_{ref} = 25°C . i_{BV} is the electrochemical current density at the Li metal- electrolyte interface given by the modified Butler-Volmer kinetics,

$$i_{BV} = i_0 \exp\left[\left(1-\alpha_a\right)\frac{\Delta\mu_{e^-}}{RT}\right]\left[\exp\left(\frac{\alpha_a F}{RT}\eta\right)-\exp\left(-\frac{\alpha_c F}{RT}\eta\right)\right] \tag{6.8}$$

$$i_0 = i_{0,ref} \exp\left[-\frac{E_{a,i0}}{R}\left(\frac{1}{T}-\frac{1}{T_{ref}}\right)\right] \tag{6.9}$$

Here, i_0 is the exchange current density for the electrochemical reaction at the metal-electrolyte interface at absolute temperature T. It exhibits an Arrhenius dependence on the operating temperature with activation energy $E_{a,i0}$ and reference values are given at T_{ref} = 25°C. $\alpha_a, \alpha_c = 0.5$ are the anodic and cathodic charge transfer coefficients, F is Faraday's constant and R is the universal gas constant. Surface overpotential for the plating reaction is defined as, $\eta = \phi_s - \phi_e - U_{Li} + \left(\Delta\mu_{e^-} / F\right)$, where ϕ_s is the solid phase potential and U_{Li} is the open circuit potential of Li . Given that the open circuit potential of *Li* vs *Li* is equal to zero, this overpotential reduces to $\eta = \phi_s - \phi_e + \left(\Delta\mu_{e^-} / F\right)$. Furthermore, the Li metal electronic conductivity is sufficiently high (~10^7 S/m) allowing the solid phase potential to be set to zero all throughout the Li metal domain. The corresponding surface overpotential for the plating reaction now takes the form $\eta = -\phi_e + \left(\Delta\mu_{e^-} / F\right)$.

The stress-kinetics coupling is exemplified by the $\Delta\mu_e^-$ term which indicates the electrochemical potential change due to mechanical stress. The electrochemical potential change due to strain energy can be expressed in terms of the mechanical stress, $\overleftrightarrow{\sigma}$, and partial molar volumes of the lithium metal, $\bar{V}_{Li}$, and SE, $\bar{V}_{SE}$, as

$$\mu_e^- = -\frac{1}{2}\left(\bar{V}_{Li} + \bar{V}_{SE}\right)\left(\gamma\hat{\kappa} + \vec{n}.\left[\vec{n}.\left(\overleftrightarrow{\tau}_{Li} - \overleftrightarrow{\tau}_{SE}\right)\right]\right) + \frac{1}{2}\left(\bar{V}_{Li} - \bar{V}_{SE}\right)\left(p_{Li} + p_{SE}\right) \tag{6.10}$$

Here, γ is the surface energy, $\hat{\kappa}$ is the surface curvature of the Li metal-SE interface, $\vec{n}$ is the unit normal vector at the lithium-SE interface directed into the SE, $\overleftrightarrow{\tau}_{Li}$, $\overleftrightarrow{\tau}_{SE}$ are the interfacial deviatoric stress tensors in the metallic Li and SE phase respectively, and p_{Li} , p_{SE} are the interfacial hydrostatic stresses in the lithium and SE domain respectively. It is to be noted that compressive hydrostatic stress is assumed to be positive here, while the deviatoric stress tensors follow the usual sign convention, i.e., tensile stresses are positive and compressive stresses are negative. Surface energy contributions to the electrochemical potential change, $\Delta\mu_e^-$, have been

shown to be negligible in literature. It is evident that a computation of the electrochemical potential change term requires computation of mechanical stress magnitudes throughout the system.

The analysis of stresses generated due to external pressure on the SE-Li metal domain is carried out assuming quasistatic mechanical equilibrium since pressure waves travel at the speed of sound allowing for instantaneous equilibration. Correspondingly, the governing differential equation for mechanical stress take the following form

$$\nabla \cdot \overleftrightarrow{\sigma} = 0 \tag{6.11}$$

In accordance with the linear elastic perturbation theory analysis, elastic mechanics is assumed for both the Li metal and the SE:

$$\overleftrightarrow{\sigma} = -\frac{2\nu G}{1-2\nu}\operatorname{tr}\left(\overleftrightarrow{\epsilon}\right) - 2G\overleftrightarrow{\epsilon} \tag{6.12}$$

The top and bottom of the SE and Li metal domain are subjected to the constant external pressure boundary condition, $\overleftrightarrow{\sigma}\vec{n} = P_{ext}\vec{n}$, with the interfacial perturbation giving the displacement boundary condition at the interface, $u_y = A\cos\left(kx\right)$, alongside continuity of stress vector across the interface from force balance. The solution to the mechanical problem is computed by finding the Airy stress function which satisfies the biharmonic equation, $\Delta^4\varphi = 0$. The stress components can be calculated form the relations

$$\sigma_{xx} = \frac{\partial^2\varphi}{\partial y^2},\ \sigma_{yy} = \frac{\partial^2\varphi}{\partial x^2},\ \sigma_{zz} = -\frac{\partial^2\varphi}{\partial x\partial y} \tag{6.13}$$

The corresponding solution to the Airy stress functions takes the form:

$$\begin{aligned}\varphi_1 &= -\frac{|P_{ext}|}{2}\left(x^2 + \nu_{SE}y^2\right) + \frac{-|P_{ext}|A\cos(kx)\exp\left(-ky\right)\left(\alpha_{SE}y + \beta\right)}{k\left(G_{Li}\tilde{\kappa}_{SE} + G_{SE}\right)\left(G_{SE}\tilde{\kappa}_{Li} + G_{Li}\right)} \\ \varphi_1 &= -\frac{|P_{ext}|}{2}\left(x^2 + \nu_{Li}y^2\right) + \frac{|P_{ext}|A\cos(kx)\exp\left(ky\right)\left(\alpha_{Li}y - \beta\right)}{k\left(G_{Li}\tilde{\kappa}_{SE} + G_{SE}\right)\left(G_{SE}\tilde{\kappa}_{Li} + G_{Li}\right)}\end{aligned} \tag{6.14}$$

Here, the material specific constants are defined as

$$
\begin{aligned}
&\tilde{\kappa}_{SE} = \frac{3-\nu_{SE}}{1+\nu_{SE}},\ \tilde{\kappa}_{Li} = \frac{3-\nu_{Li}}{1+\nu_{Li}} \\
&\alpha_{SE} = k\left(1-\nu_{SE}\right)\left(G_{Li}-G_{SE}\right)\left(G_{SE}\tilde{\kappa}_{Li}+G_{Li}\right) \\
&\alpha_{Li} = k\left(1-\nu_{Li}\right)\left(G_{SE}-G_{Li}\right)\left(G_{Li}\tilde{\kappa}_{SE}+G_{SE}\right) \\
&\beta = 2G_{SE}^{2}\frac{1-\nu_{Li}}{1+\nu_{Li}} - 2G_{Li}^{2}\frac{1-\nu_{SE}}{1+\nu_{SE}} + 4G_{SE}G_{Li}\frac{\nu_{SE}-\nu_{Li}}{\left(1+\nu_{Li}\right)\left(1+\nu_{SE}\right)}
\end{aligned}
\tag{6.15}
$$

For a detailed derivation of the stress equations and the constitutive constants, the reader is referred to Angheluta et al.[381]

6.3 Results and Discussion

6.3.1 Electrolyte Microstructure Optimization

Figure 6.3 shows the contour maps of effective transport (ionic conductivity) and mechanical (elastic modulus) properties for the polycrystalline SE system as a function of the grain size, void size and porosity. Figure 6.3(a) and (b) give the effective ionic conductivity and Young's modulus for the grain boundary thickness $\delta = 10\,\text{nm}$. As the porosity increases for a fixed grain size, it is evident that the effective ionic conductivity decreases rapidly (see Figure 6.3(a)). For a porosity of 25%, the effective conductivity is reduced to 65% of the nominal value. The presence of voids hinders ion transport through the SE considerably and the Li^{+} ions must move along tortuous pathways around the voids. Conversely, the impact of grain size on effective ionic conductivity is significantly less as compared to porosity; for a fixed porosity, effective conductivity increases marginally as the grain size is increased from 1 micron to 25 microns and beyond 25 microns it remains approximately constant. This is because for grain boundary thickness $\delta = 10\,\text{nm}$, the corresponding grain boundary volume is less than 3% even for the smallest grain size of 1 μm. The grain boundary impedes ion transport as its ionic conductivity is 1% of the grain conductivity. However, its impact is seen only at very low grain sizes where the grain boundary density is the highest. As the grain size increases, the grain boundary density decreases with grain boundary volume <0.12% for grain size 25 μm and above. Consequently, grain size of 25 μm and above possess enough ion conduction pathways to increase its ionic conductivity to the nominal value. We see a similar trend with porosity and grain size for the effective Young's modulus in Figure 6.3 (b). The impact of porosity on Young's modulus is synonymous to its effect on ionic

conductivity. As the porosity increases, the SE becomes softer due to the presence of voids which do not provide any stiffness. The grain size effect on Young's modulus is significantly more negligible than on ionic conductivity. This is because grain boundary stiffness is approximately 50% of the grain stiffness while the corresponding ionic conductivity ratio is 0.01. Consequently, SE microstructure should be optimized for the effective ionic conductivity; a SE microstructure with good transport characteristics will automatically have adequate stiffness. The SE should be packed tightly to avoid void formation; a porosity less than 5% is desirable.

Figure 6.3 (c) and (d) exhibit the effective ionic conductivity and Young's modulus for the SE system when the grain boundary thickness is increased to 100 μm. Now we see a more discernible trend of ionic conductivity with grain size. As the grain size increases from 1 μm to 50 μm, there is a significant increase in ionic conductivity. Grain boundary volume for 1 μm grain size is approximately 23% which reduces to nearly 0.1% when the grain size is 50 μm. The polycrystalline SE has favorable transport and mechanical properties when the grain boundary density is miniscule. The contour plot of Young's modulus exhibits a similar trend. As porosity increases, stiffness decreases rapidly; as the grain size increases beyond 50 μm, the nominal Young's modulus is achieved.

Figure 6.3 (e) and (f) depict the void size impact on effective properties along with porosity for a grain boundary thickness of 10 nm. No discernible impact of void size is seen; there are minor variations in the effective ionic conductivity and stiffness with void size. Heuristically, void sizes should be kept as small as possible; the presence of large voids may lead to highly tortuous pathways and if a void is present close to the electrode-electrolyte interface, it may render that portion of the interface electrochemically inactive. Pore connectivity has an impact on the critical current density as well; SE with interconnected pores short circuits earlier as opposed to one with less connected pores.[378] For an optimal polycrystalline SE microstructure, the design criteria is outlined here: grain size $\geq 25\,\mu\text{m}$, void size $\leq 1\,\mu\text{m}$ and porosity $< 5\%$. If the grain boundary thickness increases to 100 nm, the grain size should be increased to 50 μm and above. The above criteria are valid for amorphous SEs as well.

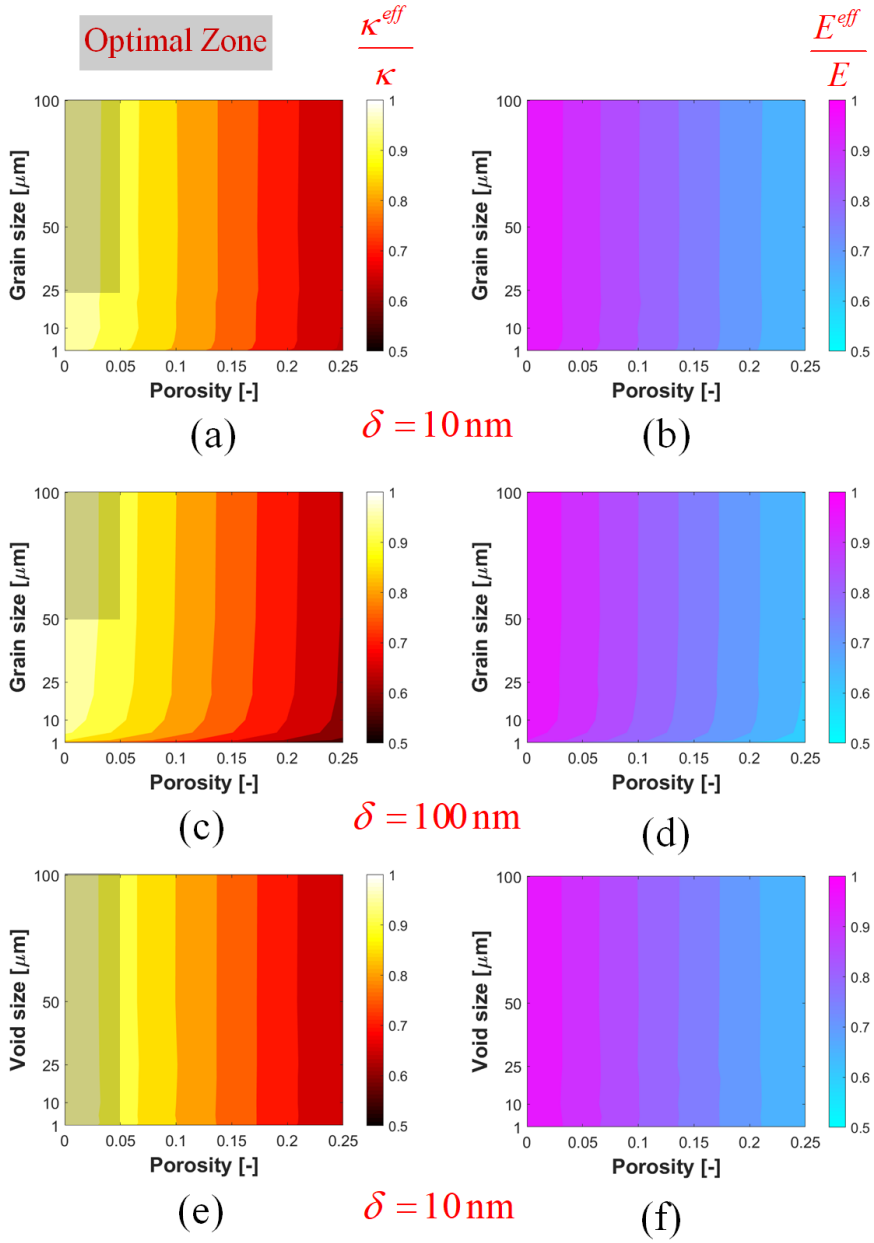

Figure 6.3 Effective transport and mechanical property computations for the polycrystalline solid electrolyte system. (a), (c) and (e) exhibit the effective ionic conductivity, κ^{eff} , and (b), (d) and (f) show the effective Young's modulus, E^{eff} , as a function of grain size, porosity, grain boundary thickness, δ , and void size. (a), (b) Effective property variation with grain size and porosity for $\delta = 10\,\text{nm}$. Rapid decrease in κ^{eff} and E^{eff} is seen with porosity increase while grain size has a relatively smaller impact. As grain size increases, the grain boundary density decreases resulting in enhanced transport, mechanics. (c), (d) Effective property variation with grain size and porosity for $\delta = 100\,\text{nm}$. As grain boundary thickness increases, it occupies more volume and impedes transport further. (e), (f) Effective property variation with void size and porosity for $\delta = 10\,\text{nm}$. Void size has negligible impact on effective properties.

6.3.2 Impact of External Pressure

Figure 6.4 shows the stress computations in the Li metal-SE domain for varying boundary conditions and interfacial surface roughness. Here, surface roughness, S_R, is related to the perturbation amplitude, A, as $S_R = 2A$. The Li metal and SE domain sizes are 100 μm×100 μm each; with a surface roughness of 1 μm and wavenumber, k= 6.2832×10^4 ensuring that $Ak << 1$. In particular, Figure 6.4 (a) displays the stress contours for the normal, (i) σ_{XX}, (ii) σ_{YY}, and shear stress components of the stress tensor, (iii) σ_{XY}, for the zero-displacement boundary condition at the top and bottom surfaces of SE and Li metal respectively. This configuration is taken from the Monroe and Newman[382] along with the stress solutions reported therein. It is interesting to note that the stress magnitudes for this configuration lies in the gigapascal range. Correspondingly, since the interfacial stress magnitudes are high, its impact on the chemical potential change due to stress, $\Delta\mu_{e^-}$ is significant. For the SE to Li shear modulus ratio, G_{SE}/G_{Li}, ranging from 0.0 to 3.0 and molar volume ratio, $V_{SE}/V_{Li} = 12.88$, the chemical potential change magnitudes is of the order of 100 kJ/mol for a surface roughness of 8 nm with $Ak = 0.4$.[120] The contributions of chemical potential change to the current density is further amplified because of the exponential nature of the corresponding term in the current density modified Butler-Volmer expression, $\exp\left[(1-\alpha_a)\frac{\Delta\mu_{e^-}}{RT}\right]$. Correspondingly, we can see the amplified stress effects on current density distribution resulting in redistribution of current flux away from the peaks for a shear modulus of the solid electrolyte twice that of the Li metal.

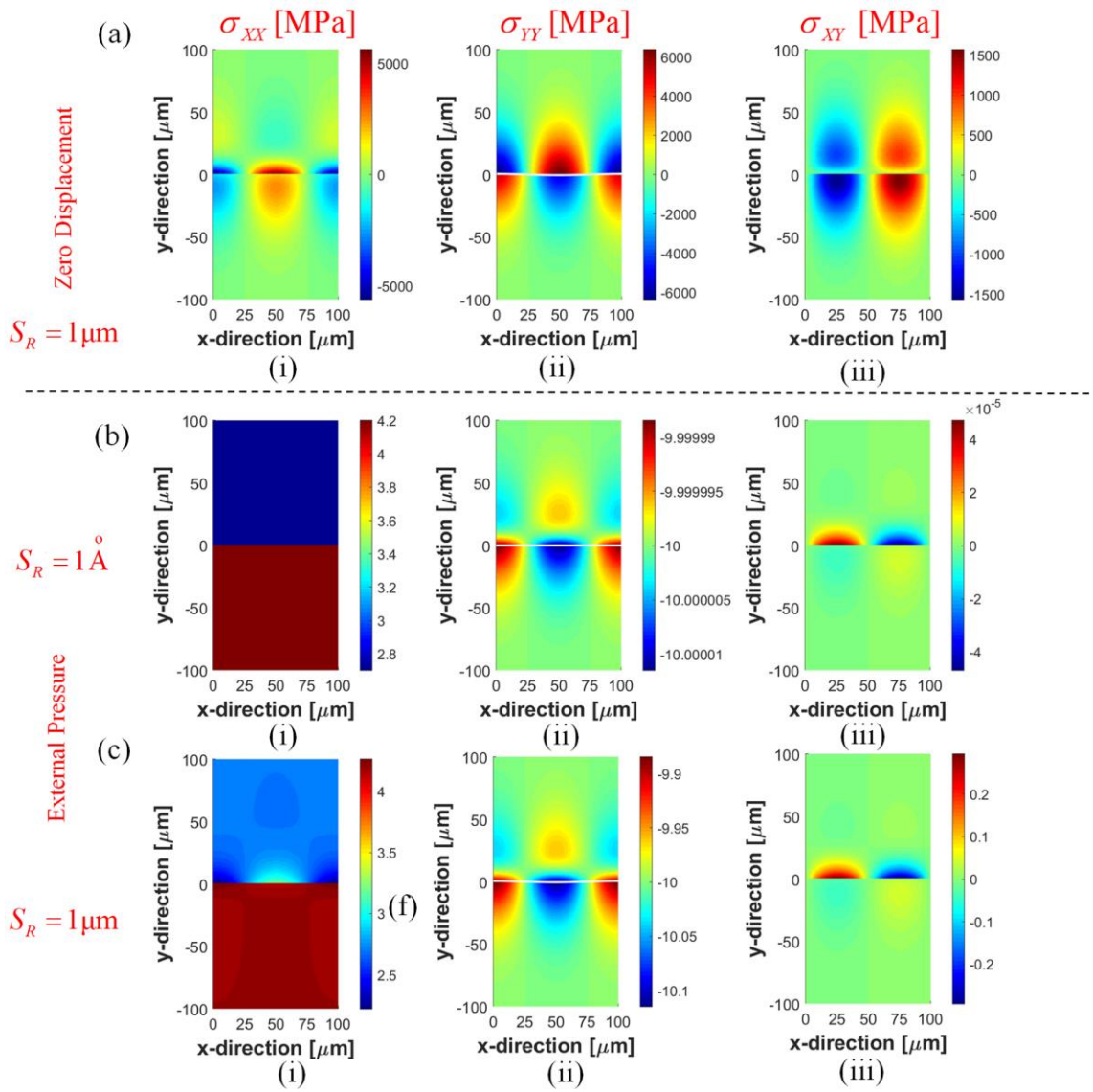

Figure 6.4 Stress contours in the Li metal – solid electrolyte domain for varying boundary conditions and interfacial perturbation amplitude, *A*. (a) Normal and shear stress for zero displacement boundary condition and $A = 1\mu\text{m}$. The stress magnitudes come in the range of gigapascals. (b) Normal and shear stress for external pressure boundary condition and $A = 1\,\text{Å}$ corresponding to a flat interface. σ_{YY} becomes equal to external pressure and shear stress tends to zero. (c) Normal and shear stress for external pressure boundary condition and $A = 1\mu\text{m}$. With external pressure, the stresses inside the system lie in the megapascal range, nearly three orders of magnitude smaller as compared to zero displacement boundary condition. Stress impact on reaction kinetics gets reduced considerably.

In contrast, Figure 6.4 (b) and Figure 6.4 (c) display the stress contours in the Li metal-SE domain under the external pressure boundary condition. The top and bottom surfaces of the SE and Li metal are subjected to 10 MPa pressure respectively. Figure 4(b) displays the stress contours for the normal, (i) σ_{XX}, (ii) σ_{YY}, and shear stress components of the stress tensor, (iii) σ_{XY}, for the 10 MPa external pressure and surface roughness of 1 Å. The miniscule surface roughness is chosen to check the fidelity of the stress solve; it nearly approximates a flat interface. For a flat interface, the *y*-direction normal stress should converge to the external pressure magnitude, which is exemplified in Figure 6.4 (b-ii). The σ_{YY} values lie close to -10 MPa throughout the solid electrolyte and Li metal, implying the compressive nature of the stress. At the far-field away from the interface, σ_{YY}, takes the external pressure value, matching the specified boundary conditions. Furthermore, a flat interface under normal loading should be devoid of shear stresses. The stress contours for σ_{XY} show this behavior with shear stress magnitudes of the order of 10^{-5} MPa. The *x*-direction normal stress shows a stress discontinuity at the interface which is to be expected.

Figure 6.4 (c) displays the stress contours for the normal, (i) σ_{XX}, (ii) σ_{YY}, and shear stress components of the stress tensor, (iii) σ_{XY}, for the 10 MPa external pressure and surface roughness of 1 µm. An increase in the perturbation amplitude changes the stress contours slightly, although, the *y*-direction normal stress still lies close to 10 MPa. An important point to note is that with the external pressure boundary condition, the stresses inside the system lie in the megapascal range close to the external pressure magnitude. This is nearly three orders of magnitude smaller as compared to the zero-displacement boundary condition. The corresponding chemical potential change is of the order of J/mol instead of kJ/mol. Subsequently, stress impact on reaction kinetics gets reduced considerably with the $\exp\left[\left(1-\alpha_a\right)\frac{\Delta\mu_{e^-}}{RT}\right]$ term taking values very close to 1. This implies that the impact of interfacial stress on heterogeneous current density distribution at the Li-SE interface is miniscule, and the major contributions to the deposition instability stem from the ion transport limitations. Furthermore, the surface overpotential for the plating reaction given by $\eta = -\phi_e + \left(\Delta\mu_{e^-} / F\right)$ can be further approximated to $\eta = -\phi_e$ since $\Delta\mu_{e^-} / F$ magnitudes are of the order of 10^{-4} V.

6.3.3 Impact of Operating Conditions

We now discern the impact of external pressure, current density, surface roughness and ambient temperature on the electrodeposition stability at the Li metal-solid electrolyte interface cognizant of the kinetic-transport-stress coupling. From our discussion on external pressure considerations, we have been able to deduce the relatively small impact of stress on the reaction current density. This allows us to decouple the stress and surface overpotential terms which can now be estimated separately to delineate the electrodeposition stability. The electrolyte potential difference, $\Delta\phi_e$, between the peak and the valley can be calculated using ion-transport considerations[383],

$$\Delta\phi_e = \frac{S_R i_{app}}{\kappa_{SE}^{eff}} \tag{6.16}$$

The peak and valley surface overpotentials, η_p and η_v respectively, can then be estimated using the following equations

$$\eta_v = \frac{2RT}{F}\ln\left(m+\sqrt{1+m^2}\right),\ m = \frac{i_{app}}{2i_0} \tag{6.17}$$

$$\eta_p = \eta_v + \Delta\phi_e \tag{6.18}$$

Finally, the electrodeposition stability parameter, i_p / i_v , is given by

$$\frac{i_p}{i_v} = \frac{\exp\left(\frac{1-\alpha_a}{RT}\mu_{e^-,p}\right)}{\exp\left(\frac{1-\alpha_a}{RT}\mu_{e^-,v}\right)} \cdot \left[\frac{\exp\left(\frac{\alpha_a F}{RT}\eta_p\right)-\exp\left(\frac{\alpha_a F}{RT}\eta_p\right)}{\exp\left(\frac{\alpha_a F}{RT}\eta_v\right)-\exp\left(\frac{\alpha_a F}{RT}\eta_v\right)}\right] = I_S \cdot I_T$$

$$0.95 < I_S < 1.05,\ I_T > 1 \tag{6.19}$$

Here, I_S denotes the stress contributions to the electrodeposition stability and I_T denotes the combined ionic transport and reaction overpotential contribution to the electrodeposition stability parameter. It is noteworthy that the while external pressure-based stress effects can increase/decrease the deposition stability depending on the shear modulus and molar volume ratio

values in a small window, ion transport effects will always contribute to a higher current density at the peak as compared to the valley.

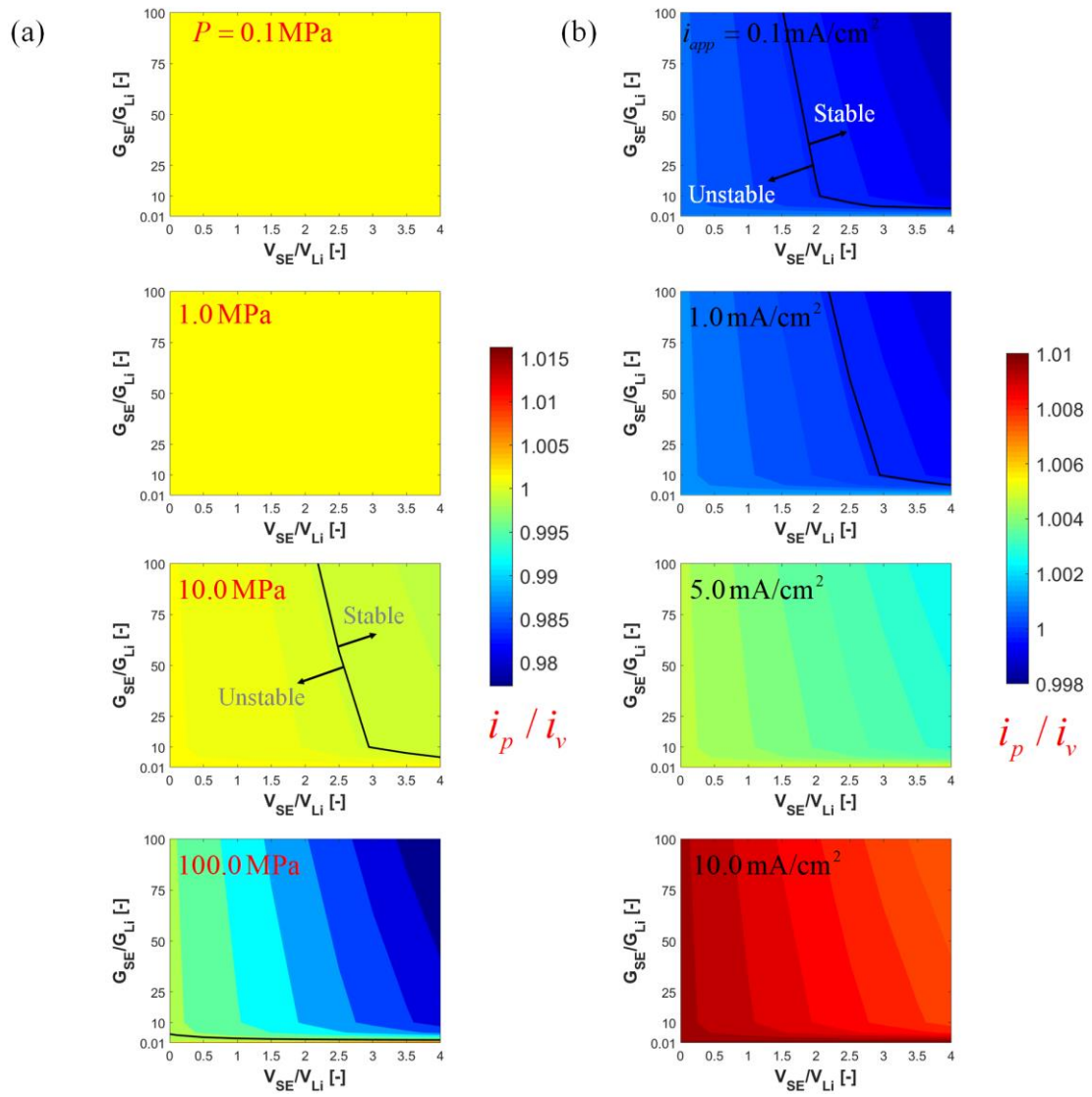

Figure 6.5 (a) Impact of external pressure and (b) current density on deposition stability as a function of the shear modulus and molar volume ratio. As external pressure is increased, deposition stability improves across all molar volume ranges. As current density is increased, transport and kinetic overpotentials increase, resulting in stable deposition only at low current densities.

Figure 6.5(a) delineates the impact of external pressure on electrodeposition stability parameter as a function of the SE to Li metal shear modulus and molar volume ratio. The shear modulus ratio is screened from 0.01 to 100 while the molar volume ratio is screened from 0 to 4. While changing the shear modulus and molar volume ratios, the Li metal electrode shear modulus,

Poisson's ratio and molar volume are kept constant to its intrinsic properties: 3.4 GPa, 0.42 and 1.3×10^{-5} m^3/mol respectively. The surface roughness is set to 500 nm, current density is 1 mA/cm^2 and operating temperature is 25°C. As we go from top to bottom, the external pressure is increased from 0.1 MPa to 100.0 MPa. At low pressures of 0.1 MPa and 1.0 MPa, the stress induced chemical potential change is insufficient to compensate for transport instability resulting in unstable deposition over the entire range of shear modulus and molar volume ratio. On further increase of the external pressure to 10.0 MPa and 100.0 MPa we see a clear demarcation of the stable and unstable zones. As the external pressure is increased, the stress induced deposition stability improves trumping the instability caused by transport. For 100.0 MPa external pressure, almost the entire range of molar volume and shear modulus ration moves to stable deposition regime. An interesting observation is the monotonic decrease of deposition stability as we go towards lower molar volume ratios. The effect of molar volume is more prominent as opposed to the shear modulus ratio, evidenced by the larger colour gradient along the horizontal axis. Under external pressure considerations, we no longer see the non-monotonic trend of deposition stability as a function of the molar volume reported in Ahmad *et al.*[384] which predicts an inversion of electrodeposition stability beyond $V_{SE}/V_{Li}=1$ stating that low shear modulus electrolytes for molar volume ratios < l and high shear modulus electrolytes for molar volume ratios > 1 are inherently stable . In literature, the molar volume of SE has been proposed to be zero; in this regime, we see that it is hard to maintain stable deposition even at high shear modulus ratios up to $G_{SE}/G_{Li}=50$.

Figure 6.5 (b) underscores the impact of applied current density on the deposition stability. Here, the external pressure is set to 10 MPa, surface roughness is 500 nm and ambient temperature is 25°C. As the current density is increased from 0.1 mA/cm^2 to 10.0 mA/cm^2, the transport instabilities are exacerbated due to high current rate engendering a wide potential difference between the peaks and the valleys, $i_{app}\uparrow, \Delta\phi_e\uparrow$. The stable zone shrinks as the current density is increased; stress is unable to divert the lithium flux away from the Li protrusions. The magnitude of the instability increases beyond 1 at current densities above 5.0 mA/cm^2. This exemplifies that it is difficult to ensure stable deposition at high current densities and provides a reasoning for the critical current density observations for solid electrolytes. As the current density keeps on increasing, the propensity of Li peaks to grow rapidly increases. Beyond a threshold current

density, the Li peak will grow unhindered and can reach the cathode through the grain boundaries fracture causing an internal short and failure of the ASSB.

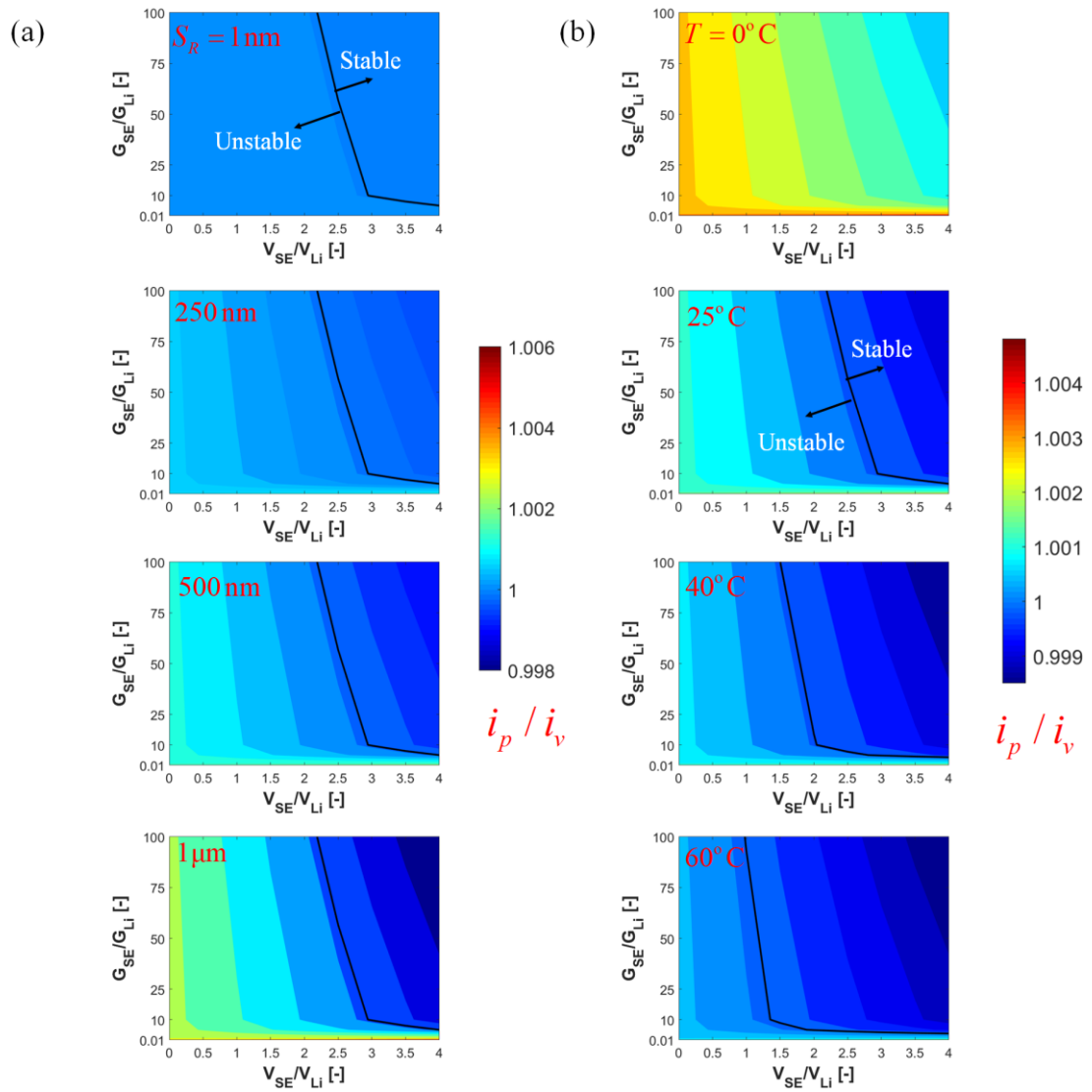

Figure 6.6 (a) Impact of surface roughness and (b) temperature on deposition stability as a function of the shear modulus and molar volume ratio. As surface pressure is increased, deposition stability improves across all molar volume ranges. As temperature is decreased, transport and kinetic overpotentials increase, resulting in stable deposition only at high temperatures.

Figure 6.6(a) exhibits the impact of the surface roughness on deposition stability keeping external pressure at 10 MPa, applied current density at 1 mA/cm^2 and operating temperature at 25°C. As the surface roughness at the metal-electrolyte interface increases, the transport

instabilities start to grow, $S_R \uparrow, \Delta\phi_e \uparrow$. The potential difference between the peak and the valley widens; increasing the transport instabilities. Interestingly, the stress effects can counter the transport instability rise at high molar volume ratios >3. The hydrostatic and deviatoric stress contributions redirect the Li^+ flux away from the peaks to the valleys at these ratios. For low molar volume ratios, the instability keeps on rising as the surface roughness is increased exhibiting a compounding effect of the transport and stress-based instability.

Finally, the impact of operating temperature on deposition stability is ascertained keeping the external pressure at 10 MPa, applied current density at 1 mA/cm^2 and surface roughness at 500 nm (see Figure 6.6(b)). The thermal environment is varied from 0 ^{o}C to 60°C. It is evident that low temperature operation is unsuited for stable deposition. The decrease in ionic conductivity and exchange current density at low temperatures results in sluggish transport and kinetics creating a compounding effect. As the temperature is increased, enhancement of both these parameters result in smaller surface overpotential variation between the peak and the valley which can be countered by stress effects. The stable zone grows as we move towards higher operating temperatures. Clearly, the SE-Li metal system is aided by thermal ramps. The flowability of the Li metal is also enhanced at high temperatures, improving contact area. A detailed insight into those effects requires elasto-plastic deformation of the Li metal as well incorporation of creep effects[115, 385].

6.3.4 Experimental Validation

The LPS solid electrolyte can exist in amorphous as well as crystalline form. We performed experiments to tabulate the overpotential for the Li plating reaction for Li|Li symmetric cells with crystalline and amorphous LPS operating under varying external pressure and ambient temperature and report it in Figure 6.7(a). It is evident that the performance of crystalline LPS at 60°C under 1.5 MPa external pressure is overshadowed by its counterpart operation at 100°C. This is directly correlated to the enhancement of the ionic conductivity and exchange current density at higher temperatures. A further drop in overpotential is seen when the amorphous LPS at 100°C under 1.5 MPa external pressure is subjected to an increase in pressure to 7 MPa. High pressure increases the interfacial contact and can decrease the surface roughness of the Li metal as well, improving the performance. A qualitative match is obtained between the experiments and the numerical model shown in Figure 6.7(b). The current instability parameter is the largest for the crystalline

LPS at 60°C followed by the crystalline LPS at 100°C under 1.5 MPa external pressure. This matches the experimental dataset for the overpotential decrease with temperature. Similarly, external pressure dataset shows a small decrease in deposition instability as the external pressure is increased from 1.5 MPa to 7.0 MPa at 100°C for amorphous LPS. The parameters are given in Table 6-1.

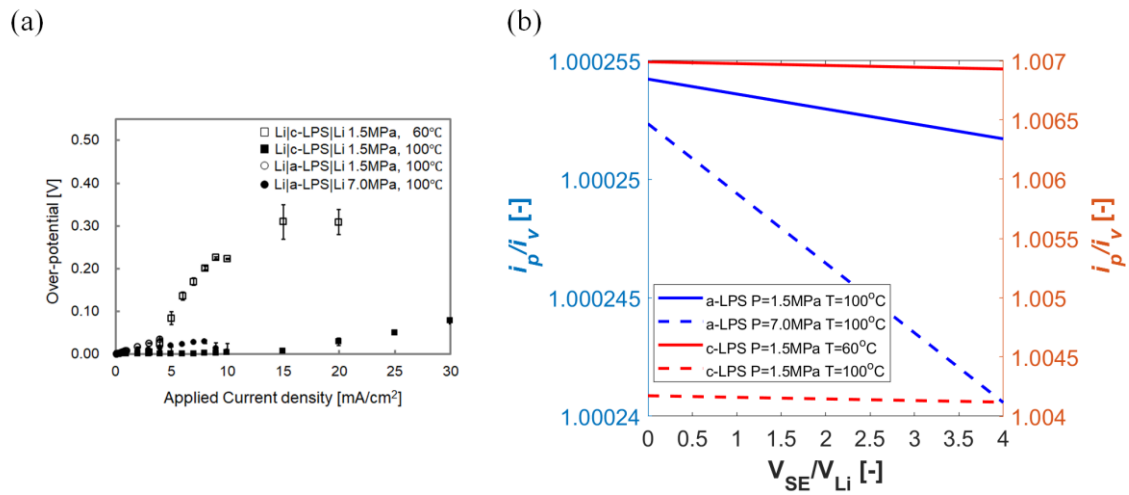

Figure 6.7 Comparison between experiments and model. As temperature and pressure increase, the deposition stability increases.

Table 6-1 List of mechanical, transport and kinetic parameters.

Name	Symbol	Unit	Value	Reference
Li Young's modulus	E_{Li}	GPa	9.0	[115]
Li shear modulus	G_{Li}	GPa	3.4	[302]
Li Poisson's ratio	ν_{Li}	-	0.42	[118]
Li partial molar volume	V_{Li}	m^3/mol	1.3×10^{-5}	[386]
LLZO Ionic conductivity	κ_{LLZO}	S/m	0.12	-
LLZO exchange current density	$i_{0,LLZO}$	A/m^2	5.5	[387]
Crystalline LPS Young's modulus	E_{LPS}	GPa	13	-
LPS Poisson's ratio	ν_{LPS}	-	0.29	[118]
Crystalline LPS conductivity	κ_{c-LPS}	S/m	0.03	-
Amorphous LPS conductivity	κ_{a-LPS}	S/m	0.04	-
LPS exchange current density	$i_{0,LPS}$	A/m^2	12.6	-
Activation energy for electrolyte transport	$E_{a,\kappa}$	kJ/mol	15	-
Activation energy for charge transfer	E_{a,i_0}	kJ/mol	12	-

6.4 Conclusion

In summary, we have devised the optimal solid electrolyte microstructure with beneficial transport and mechanical characteristics. Polycrystalline and amorphous solid electrolyte microstructure with grain size in excess of 25 μm, porosity <5% and void size <2 μm provides the optimal ionic conductivity and stiffness. Further, we developed an analytical model to discern the

stress-transport-electrochemistry coupling in the Li metal-solid electrolyte system under external pressure considerations. We revealed that the stress impact on reaction kinetics diminishes considerably in the presence of an external “stack” pressure as opposed to the zero displacement boundary conditions generally used in literature. Using linear elasticity perturbation theory, we developed an analytical formalism capable of predicting the electrodeposition stability at Li metal-SE interface under a wide range of operating conditions including external pressure, surface roughness, current density and ambient temperature. We provided a phase map for the stable regimes as a function of the SE to Li metal shear modulus ratio and SE to Li metal molar volume ratio. Interestingly, the stability regimes show monotonic trends towards deposition stability; as we go towards higher molar volume ratios and shear modulus ratios, deposition stability is enhanced. For high current operations, we need to operate the cell under higher external pressure, high temperature and smoothen out the surface features in order to ensure stable deposition.

7. SUMMARY AND OUTLOOK

Coupled electrochemistry-transport-mechanics modeling is essential towards delineating the degradation interactions in electrodes pertaining to pulverization, solid electrolyte interphase formation and lithium plating. A physics-based model has been developed which can help elucidate these coupled interactions and shed light on strategies to enhance the performance of the system. In particular, we have analyzed the impact of surface/SEI film on both low and high-volume expansion intercalation electrodes. Graphite and silicon show widely varying transport and electrochemical characteristics in conjunction with mechanics, and this work was able to capture the essential physics of both materials shedding light on the mechanism behind degradation in these electrodes along with surface/SEI film and thermal considerations. Metal-ion anodes, like lithium and magnesium, in the presence of both liquid and solid electrolytes, have also been investigated for their electrochemical-transport characteristics to provide a baseline for further studies into the mechanics interactions.

In the section below, pertinent science questions that could be answered through an extension of the current formalism have been identified. Solutions to these problems will greatly advance our understanding of degradation interactions in electrodes for energy storage.

7.1 Particle Morphology Impact on Degradation

Lithium-ion battery electrode particles show multiple configurations from spherical to platelet to irregular shaped. A three-dimensional framework can be developed to investigate the aforementioned coupled physics and ascertain the impact of realistic electrode particle structure on the microcracking, SEI formation and plating characteristics. The presence of surface irregularities on actual electrode particles is hypothesized to lead to hotspots for cracking and electrochemical reactions. As such, these computations will help reveal more insights into the relative influence of the aforementioned degradation modes. The framework can also be extended to include sodiation dynamics to explain decrepitation modes in sodium-ion batteries.

7.2 Machine Learning in Degradation Analytics

Large volume of degradation dataset can be generated through the physics-based coupled mechano-electrochemical modeling as a function of relevant operating (C-rate, temperature), geometrical (particle size, SEI thickness) and material parameters (Young's moduli, fracture threshold energy). Analysis of the datasets using machine learning algorithms can be constructed for a broad range of the aforementioned parameters. The relative impact of mechanical, electrochemical and chemical degradation will then be quantified for Li-ion and Li metal battery cycle life prognostics.

REFERENCES

1. Tarascon, J.-M. and M. Armand, *Issues and challenges facing rechargeable lithium batteries.* Nature, 2001. **414**(6861): p. 359-367.
2. Whittingham, M.S., *Lithium batteries and cathode materials.* Chemical reviews, 2004. **104**(10): p. 4271-4302.
3. Park, K.H., et al., *Design strategies, practical considerations, and new solution processes of sulfide solid electrolytes for all-solid-state batteries.* Advanced Energy Materials, 2018. **8**(18): p. 1800035.
4. Armand, M. and J.-M. Tarascon, *Building better batteries.* nature, 2008. **451**(7179): p. 652.
5. Daniel, C., *Materials and processing for lithium-ion batteries.* Jom, 2008. **60**(9): p. 43-48.
6. Dunn, B., H. Kamath, and J.-M. Tarascon, *Electrical energy storage for the grid: a battery of choices.* Science, 2011. **334**(6058): p. 928-935.
7. Cairns, E.J. and P. Albertus, *Batteries for electric and hybrid-electric vehicles.* Annual Review of Chemical and Biomolecular Engineering, 2010. **1**: p. 299-320.
8. Das, M.K., P.P. Mukherjee, and K. Muralidhar, *Porous Media Applications: Electrochemical Systems*, in *Modeling Transport Phenomena in Porous Media with Applications*. 2018, Springer. p. 93-122.
9. Birkl, C.R., et al., *Degradation diagnostics for lithium ion cells.* Journal of Power Sources, 2017. **341**: p. 373-386.
10. Xu, W., et al., *Lithium metal anodes for rechargeable batteries.* Energy & Environmental Science, 2014. **7**(2): p. 513-537.
11. Lin, D., Y. Liu, and Y. Cui, *Reviving the lithium metal anode for high-energy batteries.* Nature Nanotechnology, 2017. **12**: p. 194.
12. Kerman, K., et al., *practical challenges hindering the development of solid state Li ion batteries.* Journal of The Electrochemical Society, 2017. **164**(7): p. A1731.
13. Vetter, J., et al., *Ageing mechanisms in lithium-ion batteries.* Journal of power sources, 2005. **147**(1-2): p. 269-281.
14. Barré, A., et al., *A review on lithium-ion battery ageing mechanisms and estimations for automotive applications.* Journal of Power Sources, 2013. **241**: p. 680-689.
15. Broussely, M., et al., *Main aging mechanisms in Li ion batteries.* Journal of power sources, 2005. **146**(1-2): p. 90-96.
16. Yoshida, T., et al., *Degradation mechanism and life prediction of lithium-ion batteries.* Journal of The Electrochemical Society, 2006. **153**(3): p. A576-A582.
17. Chen, C.-F., P. Barai, and P.P. Mukherjee, *An Overview of Degradation Phenomena Modeling in Lithium-ion Battery Electrodes.* Current Opinion in Chemical Engineering, 2016. **13**: p. 82-90.
18. Christensen, J. and J. Newman, *Stress generation and fracture in lithium insertion materials.* Journal of Solid State Electrochemistry, 2006. **10**(5): p. 293-319.
19. Barai, P. and P.P. Mukherjee, *Stochastics of diffusion induced damage in intercalation materials.* Materials Research Express, 2016. **3**(10): p. 104001.
20. Kalnaus, S., K. Rhodes, and C. Daniel, *A study of lithium ion intercalation induced fracture of silicon particles used as anode material in Li-ion battery.* Journal of Power Sources, 2011. **196**(19): p. 8116-8124.

21. Harris, S.J., et al., *Mesopores inside electrode particles can change the Li-ion transport mechanism and diffusion-induced stress.* Journal of Materials Research, 2010. **25**(08): p. 1433-1440.
22. Grantab, R. and V.B. Shenoy, *Location- and Orientation-Dependent Progressive Crack Propagation in Cylindrical Graphite Electrode Particles.* Journal of the Electrochemical Society, 2011. **158**(8): p. A948-A954.
23. Verma, P., P. Maire, and P. Novák, *A review of the features and analyses of the solid electrolyte interphase in Li-ion batteries.* Electrochimica Acta, 2010. **55**(22): p. 6332-6341.
24. Kotak, N., et al., *Electrochemistry-Mechanics Coupling in Intercalation Electrodes.* Journal of The Electrochemical Society, 2018. **165**(5): p. A1064-A1083.
25. Deshpande, R.D. and D.M. Bernardi, *Modeling Solid-Electrolyte Interphase (SEI) Fracture: Coupled Mechanical/Chemical Degradation of the Lithium Ion Battery.* Journal of the Electrochemical Society, 2017. **164**(2): p. A461 - A474.
26. Ji, Y., Y.C. Zhang, and C.Y. Wang, *Li-Ion Cell Operation at Low Temperatures.* Journal of the Electrochemical Society, 2013. **160**(4): p. A636-A649.
27. Hasan, M.F., et al., *Analysis of the Implications of Rapid Charging on Lithium-Ion Battery Performance.* Journal of the Electrochemical Society, 2015. **162**(7): p. A1382-A1395.
28. Chen, C.-F., A. Verma, and P.P. Mukherjee, *Probing the Role of Electrode Microstructure in the Lithium-Ion Battery Thermal Behavior.* Journal of The Electrochemical Society, 2017. **164**(11): p. E3146-E3158.
29. Wang, C.Y., et al., *Lithium-Ion Battery Structure that Self-Heats at Low Temperatures.* Nature, 2016. **529**(7587): p. 515-+.
30. Smart, M.C. and B.V. Ratnakumar, *Effects of Electrolyte Composition on Lithium Plating in Lithium-Ion Cells.* Journal of the Electrochemical Society, 2011. **158**(4): p. A379-A389.
31. Lopez, C.F., J.A. Jeevarajan, and P.P. Mukherjee, *Characterization of Lithium-Ion Battery Thermal Abuse Behavior Using Experimental and Computational Analysis.* Journal of the Electrochemical Society, 2015. **162**(10): p. A2163-A2173.
32. Lopez, C.F., J.A. Jeevarajan, and P.P. Mukherjee, *Experimental Analysis of Thermal Runaway and Propagation in Lithium-Ion Battery Modules.* Journal of the Electrochemical Society, 2015. **162**(9): p. A1905-A1915.
33. Bandhauer, T.M., S. Garimella, and T.F. Fuller, *A Critical Review of Thermal Issues in Lithium-Ion Batteries.* Journal of the Electrochemical Society, 2011. **158**(3): p. R1-R25.
34. Arora, P., R.E. White, and M. Doyle, *Capacity fade mechanisms and side reactions in lithium-ion batteries.* Journal of the Electrochemical Society, 1998. **145**(10): p. 3647-3667.
35. Cheng, Y.T. and M.W. Verbrugge, *Application of Hasselman's Crack Propagation Model to Insertion Electrodes.* Electrochemical and Solid State Letters, 2010. **13**(9): p. A128-A131.
36. Deshpande, R., et al., *Diffusion Induced Stresses and Strain Energy in a Phase-Transforming Spherical Electrode Particle.* Journal of the Electrochemical Society, 2011. **158**(6): p. A718-A724.
37. Barai, P. and P.P. Mukherjee, *Stochastic analysis of diffusion induced damage in lithium-ion battery electrodes.* Journal of the Electrochemical Society, 2013. **160**(6): p. A955-A967.

38. Cheng, Y.T. and M.W. Verbrugge, *Diffusion-Induced Stress, Interfacial Charge Transfer, and Criteria for Avoiding Crack Initiation of Electrode Particles.* Journal of the Electrochemical Society, 2010. **157**(4): p. A508-A516.
39. Deshpande, R., et al., *Battery Cycle Life Prediction with Coupled Chemical Degradation and Fatigue Mechanics.* Journal of the Electrochemical Society, 2012. **159**(10): p. A1730-A1738.
40. Peled, E. and S. Menkin, *Review-SEI: Past, Present and Future.* Journal of the Electrochemical Society, 2017. **164**(7): p. A1703-A1719.
41. An, S.J., et al., *The state of understanding of the lithium-ion-battery graphite solid electrolyte interphase (SEI) and its relationship to formation cycling.* Carbon, 2016. **105**: p. 52-76.
42. Pinson, M.B. and M.Z. Bazant, *Theory of SEI Formation in Rechargeable Batteries: Capacity Fade, Accelerated Aging and Lifetime Prediction.* Journal of the Electrochemical Society, 2013. **160**(2): p. A243-A250.
43. Christensen, J., *Modeling Diffusion-Induced Stress in Li-Ion Cells with Porous Electrodes.* Journal of the Electrochemical Society, 2010. **157**(3): p. A366-A380.
44. Kerlau, M., J.A. Reimer, and E.J. Cairns, *Investigation of particle isolation in Li-ion battery electrodes using Li-7 NMR spectroscopy.* Electrochemistry Communications, 2005. **7**(12): p. 1249-1251.
45. Barre, A., et al., *A review on lithium-ion battery ageing mechanisms and estimations for automotive applications.* Journal of Power Sources, 2013. **241**: p. 680-689.
46. Lin, X.K., et al., *A Comprehensive Capacity Fade Model and Analysis for Li-Ion Batteries.* Journal of the Electrochemical Society, 2013. **160**(10): p. A1701-A1710.
47. Ning, G., B. Haran, and B.N. Popov, *Capacity fade study of lithium-ion batteries cycled at high discharge rates.* Journal of Power Sources, 2003. **117**(1-2): p. 160-169.
48. Ning, G., R.E. White, and B.N. Popov, *A generalized cycle life model of rechargeable Li-ion batteries.* Electrochimica Acta, 2006. **51**(10): p. 2012-2022.
49. Christensen, J. and J. Newman, *A mathematical model for the lithium-ion negative electrode solid electrolyte interphase.* Journal of the Electrochemical Society, 2004. **151**(11): p. A1977-A1988.
50. Ploehn, H.J., P. Ramadass, and R.E. White, *Solvent diffusion model for aging of lithium-ion battery cells.* Journal of the Electrochemical Society, 2004. **151**(3): p. A456-A462.
51. Harris, S.J., et al., *Mesopores inside electrode particles can change the Li-ion transport mechanism and diffusion-induced stress.* Journal of Materials Research, 2010. **25**(8): p. 1433-1440.
52. Christensen, J. and J. Newman, *A mathematical model of stress generation and fracture in lithium manganese oxide.* Journal of the Electrochemical Society, 2006. **153**(6): p. A1019-A1030.
53. Zhang, X., W. Shyy, and A.M. Sastry, *Numerical simulation of intercalation-induced stress in Li-ion battery electrode particles (vol 154, pg A910, 2007).* Journal of the Electrochemical Society, 2007. **154**(12): p. S21-S21.
54. Barai, P. and P.P. Mukherjee, *Mechano-Electrochemical Model for Acoustic Emission Characterization in Intercalation Electrodes.* Journal of the Electrochemical Society, 2014. **161**(11): p. F3123-F3136.
55. Qi, Y. and S.J. Harris, *In Situ Observation of Strains during Lithiation of a Graphite Electrode.* Journal of the Electrochemical Society, 2010. **157**(6): p. A741-A747.

56. Wang, H.F., et al., *TEM study of electrochemical cycling-induced damage and disorder in LiCoO2 cathodes for rechargeable lithium batteries.* Journal of the Electrochemical Society, 1999. **146**(2): p. 473-480.
57. Woodford, W.H., Y.M. Chiang, and W.C. Carter, *Electrochemical Shock in Ion-Intercalation Materials with Limited Solid-Solubility.* Journal of the Electrochemical Society, 2013. **160**(8): p. A1286-A1292.
58. Zhao, K.J., et al., *Fracture of electrodes in lithium-ion batteries caused by fast charging.* Journal of Applied Physics, 2010. **108**(7).
59. Cheng, L., et al., *Effect of microstructure and surface impurity segregation on the electrical and electrochemical properties of dense Al-substituted Li 7 La 3 Zr 2 O 12.* Journal of Materials Chemistry A, 2014. **2**(1): p. 172-181.
60. Cheng, L., et al., *Effect of surface microstructure on electrochemical performance of garnet solid electrolytes.* ACS applied materials & interfaces, 2015. **7**(3): p. 2073-2081.
61. Cheng, Y.-T. and M.W. Verbrugge, *Evolution of stress within a spherical insertion electrode particle under potentiostatic and galvanostatic operation.* Journal of Power Sources, 2009. **190**(2): p. 453-460.
62. Xu, J.G., et al., *Electrode Side Reactions, Capacity Loss and Mechanical Degradation in Lithium-Ion Batteries.* Journal of the Electrochemical Society, 2015. **162**(10): p. A2026-A2035.
63. Narayanrao, R., M.M. Joglekar, and S. Inguva, *A Phenomenological Degradation Model for Cyclic Aging of Lithium Ion Cell Materials.* Journal of the Electrochemical Society, 2013. **160**(1): p. A125-A137.
64. Chaboche, J.L.a.J.L., *Mechanics of solid materials.* Cambridge University

Press, 1990.
65. Xu, B.-X., Y. Zhao, and P. Stein, *Phase field modeling of electrochemically induced fracture in Li-ion battery with large deformation and phase segregation.* GAMM-Mitteilungen, 2016. **39**(1): p. 92 - 110.
66. Han, S., et al., *Numerical study of grain boundary effect on Li+ effective diffusivity and intercalation-induced stresses in Li-ion battery active materials.* Journal of Power Sources, 2013. **240**: p. 155-167.
67. Zhang, X., A.M. Sastry, and W. Shyy, *Intercalation-Induced Stress and Heat Generation within Single Lithium-Ion Battery Cathode Particles.* Journal of the Electrochemical Society, 2008. **155**(7): p. A542 - A552.
68. Park, J., W. Lu, and A.M. Sastry, *Numerical simulation of stress evolution in lithium manganese dioxide particles due to coupled phase transition and intercalation.* Journal of The Electrochemical Society, 2011. **158**(2): p. A201-A206.
69. Malavé, V., et al., *A computational model of the mechanical behavior within reconstructed LixCoO2 Li-ion battery cathode particles.* Electrochimica Acta, 2014. **130**: p. 707-717.
70. Rahani, E.K. and V.B. Shenoy, *Role of plastic deformation of binder on stress evolution during charging and discharging in lithium-ion battery negative electrodes.* Journal of The Electrochemical Society, 2013. **160**(8): p. A1153-A1162.
71. Roberts, S.A., et al., *A Framework for Three-Dimensional Mesoscale Modeling of Anisotropic Swelling and Mechanical Deformation in Lithium-Ion Electrodes.* Journal of the Electrochemical Society, 2014. **161**(11): p. F3052 - F3059.
72. Mendoza, H., et al., *Mechanical and Electrochemical Response of a LiCoO2 Cathode using Reconstructed Microstructures.* Electrochemica Acta, 2016. **190**: p. 1 - 15.

73. Chen-Wiegart, Y.-c.K., et al., *3D morphological evolution of Li-ion battery negative electrode LiVO2 during oxidation using X-ray nano-tomography.* Electrochemistry Communications, 2012. **21**: p. 58-61.
74. Chen-Wiegart, Y.-c.K., et al., *3D analysis of a LiCoO2–Li (Ni1/3Mn1/3Co1/3) O2 Li-ion battery positive electrode using x-ray nano-tomography.* Electrochemistry Communications, 2013. **28**: p. 127-130.
75. Ebner, M., et al., *X-ray tomography of porous, transition metal oxide based lithium ion battery electrodes.* Advanced Energy Materials, 2013. **3**(7): p. 845-850.
76. Pietsch, P., et al., *Quantifying microstructural dynamics and electrochemical activity of graphite and silicon-graphite lithium ion battery anodes.* Nature communications, 2016. **7**: p. 12909.
77. Pietsch, P. and V. Wood, *X-ray tomography for lithium ion battery research: A practical guide.* Annual Review of Materials Research, 2017. **47**: p. 451-479.
78. Hutzenlaub, T., et al., *Three-dimensional reconstruction of a LiCoO2 Li-ion battery cathode.* Electrochemical and Solid-State Letters, 2011. **15**(3): p. A33-A36.
79. Hutzenlaub, T., et al., *Three-dimensional electrochemical Li-ion battery modelling featuring a focused ion-beam/scanning electron microscopy based three-phase reconstruction of a LiCoO2 cathode.* Electrochimica Acta, 2014. **115**: p. 131-139.
80. Zielke, L., et al., *A Combination of X-Ray Tomography and Carbon Binder Modeling: Reconstructing the Three Phases of LiCoO2 Li-Ion Battery Cathodes.* Advanced Energy Materials, 2014. **4**(8).
81. Zielke, L., et al., *Three-Phase Multiscale Modeling of a LiCoO2 Cathode: Combining the Advantages of FIB–SEM Imaging and X-Ray Tomography.* Advanced Energy Materials, 2015. **5**(5).
82. Larcher, D. and J.M. Tarascon, *Towards greener and more sustainable batteries for electrical energy storage.* Nature Chemistry, 2014. **7**: p. 19.
83. Chen, C.-F., P. Barai, and P.P. Mukherjee, *Diffusion Induced Damage and Impedance Response in Lithium-Ion Battery Electrodes.* Journal of The Electrochemical Society, 2014. **161**(14): p. A2138-A2152.
84. Chen, C.-F. and P.P. Mukherjee, *Probing the morphological influence on solid electrolyte interphase and impedance response in intercalation electrodes.* Physical Chemistry Chemical Physics, 2015. **17**(15): p. 9812-9827.
85. Choi, J.W. and D. Aurbach, *Promise and reality of post-lithium-ion batteries with high energy densities.* 2016. **1**: p. 16013.
86. Wood, K.N., M. Noked, and N.P. Dasgupta, *Lithium Metal Anodes: Toward an Improved Understanding of Coupled Morphological, Electrochemical, and Mechanical Behavior.* ACS Energy Letters, 2017. **2**(3): p. 664-672.
87. Liu, Z. and P.P. Mukherjee, *Mesoscale Elucidation of Surface Passivation in the Li–Sulfur Battery Cathode.* ACS Applied Materials & Interfaces, 2017. **9**(6): p. 5263-5271.
88. Liu, Z., et al., *Li2S Film Formation on Lithium Anode Surface of Li–S batteries.* ACS Applied Materials & Interfaces, 2016. **8**(7): p. 4700-4708.
89. Girishkumar, G., et al., *Lithium−Air Battery: Promise and Challenges.* The Journal of Physical Chemistry Letters, 2010. **1**(14): p. 2193-2203.
90. Wu, F., et al., *Perspectives for restraining harsh lithium dendrite growth: Towards robust lithium metal anodes.* Energy Storage Materials, 2018. **15**: p. 148-170.

91. Zhang, S.S., *Problem, Status, and Possible Solutions for Lithium Metal Anode of Rechargeable Batteries.* ACS Applied Energy Materials, 2018. **1**(3): p. 910-920.
92. Chen, K.-H., et al., *Dead lithium: mass transport effects on voltage, capacity, and failure of lithium metal anodes.* Journal of Materials Chemistry A, 2017. **5**(23): p. 11671-11681.
93. Barai, P., K. Higa, and V. Srinivasan, *Lithium dendrite growth mechanisms in polymer electrolytes and prevention strategies.* Physical Chemistry Chemical Physics, 2017. **19**(31): p. 20493-20505.
94. Hallinan, D.T., et al., *Lithium Metal Stability in Batteries with Block Copolymer Electrolytes.* Journal of The Electrochemical Society, 2013. **160**(3): p. A464-A470.
95. Chen, S., et al., *High-Voltage Lithium-Metal Batteries Enabled by Localized High-Concentration Electrolytes.* Advanced Materials, 2018. **30**(21): p. 1706102.
96. Ding, F., et al., *Dendrite-Free Lithium Deposition via Self-Healing Electrostatic Shield Mechanism.* Journal of the American Chemical Society, 2013. **135**(11): p. 4450-4456.
97. Miao, R., et al., *Novel dual-salts electrolyte solution for dendrite-free lithium-metal based rechargeable batteries with high cycle reversibility.* Journal of Power Sources, 2014. **271**: p. 291-297.
98. Cheng, X.-B., et al., *Dendrite-Free Lithium Deposition Induced by Uniformly Distributed Lithium Ions for Efficient Lithium Metal Batteries.* Advanced Materials, 2016. **28**(15): p. 2888-2895.
99. Zhang, Y., et al., *High-capacity, low-tortuosity, and channel-guided lithium metal anode.* Proceedings of the National Academy of Sciences, 2017. **114**(14): p. 3584-3589.
100. Wang, S.-H., et al., *Stable Li Metal Anodes via Regulating Lithium Plating/Stripping in Vertically Aligned Microchannels.* Advanced Materials, 2017. **29**(40): p. 1703729.
101. Yan, K., et al., *Selective deposition and stable encapsulation of lithium through heterogeneous seeded growth.* Nature Energy, 2016. **1**: p. 16010.
102. Khurana, R., et al., *Suppression of Lithium Dendrite Growth Using Cross-Linked Polyethylene/Poly(ethylene oxide) Electrolytes: A New Approach for Practical Lithium-Metal Polymer Batteries.* Journal of the American Chemical Society, 2014. **136**(20): p. 7395-7402.
103. Cheng, X.-B. and Q. Zhang, *Dendrite-free lithium metal anodes: stable solid electrolyte interphases for high-efficiency batteries.* Journal of Materials Chemistry A, 2015. **3**(14): p. 7207-7209.
104. Peled, E., D. Golodnitsky, and G. Ardel, *Advanced Model for Solid Electrolyte Interphase Electrodes in Liquid and Polymer Electrolytes.* Journal of The Electrochemical Society, 1997. **144**(8): p. L208-L210.
105. Yu, X. and A. Manthiram, *Electrode–Electrolyte Interfaces in Lithium–Sulfur Batteries with Liquid or Inorganic Solid Electrolytes.* Accounts of Chemical Research, 2017. **50**(11): p. 2653-2660.
106. Hao, F., et al., *Mesoscale Elucidation of Solid Electrolyte Interphase Layer Formation in Li-Ion Battery Anode.* The Journal of Physical Chemistry C, 2017. **121**(47): p. 26233-26240.
107. Cheng, X.-B., et al., *A Review of Solid Electrolyte Interphases on Lithium Metal Anode.* Advanced Science, 2016. **3**(3): p. 1500213-n/a.
108. Bieker, G., M. Winter, and P. Bieker, *Electrochemical in situ investigations of SEI and dendrite formation on the lithium metal anode.* Physical Chemistry Chemical Physics, 2015. **17**(14): p. 8670-8679.

109. Leung, K., et al., *Stability of Solid Electrolyte Interphase Components on Lithium Metal and Reactive Anode Material Surfaces.* The Journal of Physical Chemistry C, 2016. **120**(12): p. 6302-6313.
110. Aurbach, D., *Review of selected electrode–solution interactions which determine the performance of Li and Li ion batteries.* Journal of Power Sources, 2000. **89**(2): p. 206-218.
111. Hahn, M., et al., *A Dilatometric Study of Lithium Intercalation into Powder-Type Graphite Electrodes.* Electrochemical and Solid-State Letters, 2008. **11**(9): p. A151-A154.
112. Cheng, E.J., A. Sharafi, and J. Sakamoto, *Intergranular Li metal propagation through polycrystalline Li 6.25 Al 0.25 La 3 Zr 2 O 12 ceramic electrolyte.* Electrochimica Acta, 2017. **223**: p. 85-91.
113. Zhang, X., W. Shyy, and A.M. Sastry, *Numerical simulation of intercalation-induced stress in Li-ion battery electrode particles.* Journal of the Electrochemical Society, 2007. **154**(10): p. A910-A916.
114. Monroe, C. and J. Newman, *The effect of interfacial deformation on electrodeposition kinetics.* Journal of The Electrochemical Society, 2004. **151**(6): p. A880-A886.
115. Monroe, C. and J. Newman, *The impact of elastic deformation on deposition kinetics at lithium/polymer interfaces.* Journal of The Electrochemical Society, 2005. **152**(2): p. A396-A404.
116. Barai, P., K. Higa, and V. Srinivasan, *Impact of external pressure and electrolyte transport properties on lithium dendrite growth.* Journal of The Electrochemical Society, 2018. **165**(11): p. A2654-A2666.
117. Ahmad, Z. and V. Viswanathan, *Role of anisotropy in determining stability of electrodeposition at solid-solid interfaces.* Physical Review Materials, 2017. **1**(5): p. 055403.
118. Barai, P., et al., *Mechanical Stress Induced Current Focusing and Fracture in Grain Boundaries.* Journal of The Electrochemical Society, 2019. **166**(10): p. A1752-A1762.
119. Raj, R. and J. Wolfenstine, *Current limit diagrams for dendrite formation in solid-state electrolytes for Li-ion batteries.* Journal of Power Sources, 2017. **343**: p. 119-126.
120. Yu, S. and D.J. Siegel, *Grain boundary softening: A potential mechanism for lithium metal penetration through stiff solid electrolytes.* ACS applied materials & interfaces, 2018. **10**(44): p. 38151-38158.
121. Porz, L., et al., *Mechanism of lithium metal penetration through inorganic solid electrolytes.* Advanced Energy Materials, 2017. **7**(20): p. 1701003.
122. Ahmad, Z. and V. Viswanathan, *Stability of electrodeposition at solid-solid interfaces and implications for metal anodes.* Physical review letters, 2017. **119**(5): p. 056003.
123. Sendek, A.D., et al., *Holistic computational structure screening of more than 12000 candidates for solid lithium-ion conductor materials.* Energy & Environmental Science, 2017. **10**(1): p. 306-320.
124. Dawson, J.A., et al., *Atomic-scale influence of grain boundaries on Li-ion conduction in solid electrolytes for all-solid-state batteries.* Journal of the American Chemical Society, 2017. **140**(1): p. 362-368.
125. Mathiesen, N.R., et al., *Charge Transport in Alkali-Metal Superoxides: A Systematic First-Principles Study.* Chemistry of Materials, 2019. **31**(21): p. 9156-9167.
126. Hao, F. and P.P. Mukherjee, *Mesoscale Analysis of the Electrolyte-Electrode Interface in All-Solid-State Li-Ion Batteries.* Journal of The Electrochemical Society, 2018. **165**(9): p. A1857-A1864.

127. Hao, F., W. Wang, and P.P. Mukherjee, *Electrochemical-Reaction-Driven Interfacial Stress in a Solid-Solid Layered Architecture.* Physical Review Applied, 2019. **11**(3): p. 034038.
128. Thackeray, M.M., C. Wolverton, and E.D. Isaacs, *Electrical energy storage for transportation—approaching the limits of, and going beyond, lithium-ion batteries.* Energy & Environmental Science, 2012. **5**(7): p. 7854-7863.
129. Nelson, P., et al. *Advanced lithium-ion batteries for plug-in hybrid-electric vehicles*. in *Proceedings from the 23rd Electric Vehicle Symposium. See also URL http://www. transportation. anl. gov/pdfs/HV/461. pdf*. 2007.
130. Divya, K. and J. Østergaard, *Battery energy storage technology for power systems—An overview.* Electric Power Systems Research, 2009. **79**(4): p. 511-520.
131. Magasinski, A., et al., *High-performance lithium-ion anodes using a hierarchical bottom-up approach.* Nature materials, 2010. **9**(4): p. 353.
132. Nitta, N. and G. Yushin, *High-capacity anode materials for lithium-ion batteries: choice of elements and structures for active particles.* Particle & Particle Systems Characterization, 2014. **31**(3): p. 317-336.
133. Wang, Y. and G. Cao, *Developments in nanostructured cathode materials for high-performance lithium-ion batteries.* Advanced Materials, 2008. **20**(12): p. 2251-2269.
134. Fergus, J.W., *Recent developments in cathode materials for lithium ion batteries.* Journal of Power Sources, 2010. **195**(4): p. 939-954.
135. Yoshio, M., H. Wang, and K. Fukuda, *Spherical Carbon-Coated Natural Graphite as a Lithium-Ion Battery-Anode Material.* Angewandte Chemie, 2003. **115**(35): p. 4335-4338.
136. Chen, J., *Recent progress in advanced materials for lithium ion batteries.* Materials, 2013. **6**(1): p. 156-183.
137. Croy, J.R., et al., *Quantifying Hysteresis and Voltage Fade in xLi2MnO3●(1-x) LiMn0. 5Ni0. 5O2 Electrodes as a Function of Li2MnO3 Content.* Journal of The Electrochemical Society, 2014. **161**(3): p. A318-A325.
138. Dahn, J., *Phase diagram of Li x C 6.* Physical Review B, 1991. **44**(17): p. 9170.
139. Chan, C.K., et al., *High-performance lithium battery anodes using silicon nanowires.* Nature nanotechnology, 2008. **3**(1): p. 31.
140. Idota, Y., et al., *Tin-based amorphous oxide: a high-capacity lithium-ion-storage material.* Science, 1997. **276**(5317): p. 1395-1397.
141. Obrovac, M. and L. Christensen, *Structural changes in silicon anodes during lithium insertion/extraction.* Electrochemical and Solid-State Letters, 2004. **7**(5): p. A93-A96.
142. Obrovac, M., et al., *Alloy design for lithium-ion battery anodes.* Journal of The Electrochemical Society, 2007. **154**(9): p. A849-A855.
143. Beaulieu, L., et al., *Reaction of Li with alloy thin films studied by in situ AFM.* Journal of The Electrochemical Society, 2003. **150**(11): p. A1457-A1464.
144. Huggins, R. and W. Nix, *Decrepitation model for capacity loss during cycling of alloys in rechargeable electrochemical systems.* Ionics, 2000. **6**(1-2): p. 57-63.
145. Zhao, K., et al., *Fracture of electrodes in lithium-ion batteries caused by fast charging.* Journal of Applied Physics, 2010. **108**(7): p. 073517.
146. Deshpande, R., Y.-T. Cheng, and M.W. Verbrugge, *Modeling diffusion-induced stress in nanowire electrode structures.* Journal of Power Sources, 2010. **195**(15): p. 5081-5088.

147. Cheng, Y.-T. and M.W. Verbrugge, *Diffusion-induced stress, interfacial charge transfer, and criteria for avoiding crack initiation of electrode particles.* Journal of the Electrochemical Society, 2010. **157**(4): p. A508-A516.
148. Barai, P., et al., *Mechano-Electrochemical Interaction Gives Rise to Strain Relaxation in Sn Electrodes.* Journal of The Electrochemical Society, 2016. **163**(14): p. A3022-A3035.
149. Singh, G. and T.K. Bhandakkar, *Analytical Investigation of Binder's Role on the Diffusion Induced Stresses in Lithium Ion Battery through a Representative System of Spherical Isolated Electrode Particle Enclosed by Binder.* Journal of The Electrochemical Society, 2017. **164**(4): p. A608-A621.
150. Chen, C.-F., et al., *Scaling relations for intercalation induced damage in electrodes.* Electrochimica Acta, 2016. **204**: p. 31-49.
151. Barai, P. and P.P. Mukherjee, *Mechano-electrochemical stochastics in high-capacity electrodes for energy storage.* Journal of The Electrochemical Society, 2016. **163**(6): p. A1120-A1137.
152. Takahashi, K., et al., *Mechanical degradation of graphite/PVDF composite electrodes: a model-experimental study.* Journal of The Electrochemical Society, 2016. **163**(3): p. A385-A395.
153. Yao, Y., et al., *Improving the cycling stability of silicon nanowire anodes with conducting polymer coatings.* Energy & Environmental Science, 2012. **5**(7): p. 7927-7930.
154. Hao, F. and D. Fang, *Diffusion-induced stresses of spherical core-shell electrodes in lithium-ion batteries: the effects of the shell and surface/interface stress.* Journal of The Electrochemical Society, 2013. **160**(4): p. A595-A600.
155. Wang, C., et al., *Self-healing chemistry enables the stable operation of silicon microparticle anodes for high-energy lithium-ion batteries.* Nat Chem, 2013. **5**(12): p. 1042-1048.
156. Zhang, S., K. Xu, and T. Jow, *EIS study on the formation of solid electrolyte interface in Li-ion battery.* Electrochimica acta, 2006. **51**(8): p. 1636-1640.
157. Tasaki, K. and S.J. Harris, *Computational study on the solubility of lithium salts formed on lithium ion battery negative electrode in organic solvents.* The Journal of Physical Chemistry C, 2010. **114**(17): p. 8076-8083.
158. Deshpande, R.D. and D.M. Bernardi, *Modeling Solid-Electrolyte Interphase (SEI) Fracture: Coupled Mechanical/Chemical Degradation of the Lithium Ion Battery.* Journal of The Electrochemical Society, 2017. **164**(2): p. A461-A474.
159. SAKAI, M., K. URASHIMA, and M. INAGAKI, *Energy principle of elastic-plastic fracture and its application to the fracture mechanics of a polycrystalline graphite.* Journal of the American Ceramic society, 1983. **66**(12): p. 868-874.
160. Nukala, P.K.V., S. Zapperi, and S. Šimunović, *Statistical properties of fracture in a random spring model.* Physical Review E, 2005. **71**(6): p. 066106.
161. Shenoy, V., P. Johari, and Y. Qi, *Elastic softening of amorphous and crystalline Li–Si phases with increasing Li concentration: a first-principles study.* Journal of Power Sources, 2010. **195**(19): p. 6825-6830.
162. Guo, M., G. Sikha, and R.E. White, *Single-particle model for a lithium-ion cell: Thermal behavior.* Journal of The Electrochemical Society, 2011. **158**(2): p. A122-A132.
163. Qi, Y., et al., *Threefold increase in the Young's modulus of graphite negative electrode during lithium intercalation.* Journal of The Electrochemical Society, 2010. **157**(5): p. A558-A566.

164. Bruce, G.C. and L. Marcoux. *Large lithium ion batteries for aerospace and aircraft applications*. in *Applications and Advances, 2001. The Sixteenth Annual Battery Conference on*. 2001. IEEE.
165. Marsh, R., et al., *Li ion batteries for aerospace applications.* Journal of power sources, 2001. **97**: p. 25-27.
166. Diercks, D.R., et al., *Evidence for anisotropic mechanical behavior and nanoscale chemical heterogeneity in cycled LiCoO2.* Journal of the electrochemical society, 2014. **161**(11): p. F3039-F3045.
167. Kummer, M., et al., *Silicon/polyaniline nanocomposites as anode material for lithium ion batteries.* Journal of the Electrochemical Society, 2014. **161**(1): p. A40-A45.
168. Green, M., et al., *Structured silicon anodes for lithium battery applications.* Electrochemical and Solid-State Letters, 2003. **6**(5): p. A75-A79.
169. Gowda, S.R., et al., *Three-dimensionally engineered porous silicon electrodes for Li ion batteries.* Nano letters, 2012. **12**(12): p. 6060-6065.
170. Limthongkul, P., et al., *Electrochemically-driven solid-state amorphization in lithium-silicon alloys and implications for lithium storage.* Acta Materialia, 2003. **51**(4): p. 1103-1113.
171. Liu, X.H., et al., *Size-dependent fracture of silicon nanoparticles during lithiation.* Acs Nano, 2012. **6**(2): p. 1522-1531.
172. Cho, J., *Porous Si anode materials for lithium rechargeable batteries.* Journal of Materials Chemistry, 2010. **20**(20): p. 4009-4014.
173. Lee, S.W., et al., *Fracture of crystalline silicon nanopillars during electrochemical lithium insertion.* Proceedings of the National Academy of Sciences, 2012. **109**(11): p. 4080-4085.
174. Zhao, K., et al., *Inelastic hosts as electrodes for high-capacity lithium-ion batteries*. 2011, AIP.
175. Deshpande, R., et al., *Battery cycle life prediction with coupled chemical degradation and fatigue mechanics.* Journal of the Electrochemical Society, 2012. **159**(10): p. A1730-A1738.
176. Xu, J., et al., *Electrode side reactions, capacity loss and mechanical degradation in lithium-ion batteries.* Journal of The Electrochemical Society, 2015. **162**(10): p. A2026-A2035.
177. Bucci, G., et al., *Measurement and modeling of the mechanical and electrochemical response of amorphous Si thin film electrodes during cyclic lithiation.* Journal of the Mechanics and Physics of Solids, 2014. **62**: p. 276-294.
178. Huang, S., et al., *Stress generation during lithiation of high-capacity electrode particles in lithium ion batteries.* Acta materialia, 2013. **61**(12): p. 4354-4364.
179. Zhao, K., et al., *Large plastic deformation in high-capacity lithium-ion batteries caused by charge and discharge.* Journal of the American Ceramic Society, 2011. **94**(s1).
180. Song, T., et al., *Arrays of sealed silicon nanotubes as anodes for lithium ion batteries.* Nano letters, 2010. **10**(5): p. 1710-1716.
181. Soni, S.K., et al., *Diffusion mediated lithiation stresses in Si thin film electrodes.* Journal of the Electrochemical Society, 2012. **159**(9): p. A1520-A1527.
182. Chen, L., et al., *A phase-field model coupled with large elasto-plastic deformation: application to lithiated silicon electrodes.* Journal of The Electrochemical Society, 2014. **161**(11): p. F3164-F3172.

183. Soni, S.K., et al., *Stress mitigation during the lithiation of patterned amorphous Si islands.* Journal of the Electrochemical Society, 2011. **159**(1): p. A38-A43.
184. Higa, K. and V. Srinivasan, *Stress and strain in silicon electrode models.* Journal of The Electrochemical Society, 2015. **162**(6): p. A1111-A1122.
185. Bhandakkar, T.K. and H. Gao, *Cohesive modeling of crack nucleation under diffusion induced stresses in a thin strip: Implications on the critical size for flaw tolerant battery electrodes.* International Journal of Solids and Structures, 2010. **47**(10): p. 1424-1434.
186. Bhandakkar, T.K. and H. Gao, *Cohesive modeling of crack nucleation in a cylindrical electrode under axisymmetric diffusion induced stresses.* International Journal of Solids and Structures, 2011. **48**(16): p. 2304-2309.
187. Bathe, K.-J., *Finite element procedures*. 2006: Klaus-Jurgen Bathe.
188. Reddy, J.N., *An Introduction to Nonlinear Finite Element Analysis: with applications to heat transfer, fluid mechanics, and solid mechanics*. 2014: OUP Oxford.
189. Qi, Y., et al., *Lithium concentration dependent elastic properties of battery electrode materials from first principles calculations.* Journal of The Electrochemical Society, 2014. **161**(11): p. F3010-F3018.
190. Johari, P., Y. Qi, and V.B. Shenoy, *The mixing mechanism during lithiation of Si negative electrode in Li-ion batteries: an ab initio molecular dynamics study.* Nano letters, 2011. **11**(12): p. 5494-5500.
191. Pharr, M., Z. Suo, and J.J. Vlassak, *Measurements of the fracture energy of lithiated silicon electrodes of Li-ion batteries.* Nano letters, 2013. **13**(11): p. 5570-5577.
192. Verma, A., et al., *Galvanostatic intermittent titration and performance based analysis of LiNi0. 5Co0. 2Mn0. 3O2 cathode.* Journal of The Electrochemical Society, 2017. **164**(13): p. A3380-A3392.
193. Chen, X., et al., *Virus-enabled silicon anode for lithium-ion batteries.* ACS nano, 2010. **4**(9): p. 5366-5372.
194. Zhang, H. and P.V. Braun, *Three-dimensional metal scaffold supported bicontinuous silicon battery anodes.* Nano letters, 2012. **12**(6): p. 2778-2783.
195. Verma, A. and P.P. Mukherjee, *Mechanistic analysis of mechano-electrochemical interaction in silicon electrodes with surface film.* Journal of The Electrochemical Society, 2017. **164**(14): p. A3570-A3581.
196. Li, J., et al., *Asymmetric Rate Behavior of Si Anodes for Lithium-Ion Batteries: Ultrafast De-Lithiation versus Sluggish Lithiation at High Current Densities.* Advanced Energy Materials, 2015. **5**(6): p. 1401627.
197. Liu, X.H., et al., *Self-limiting lithiation in silicon nanowires.* Acs Nano, 2013. **7**(2): p. 1495-1503.
198. Ryu, I., et al., *Size-dependent fracture of Si nanowire battery anodes.* Journal of the Mechanics and Physics of Solids, 2011. **59**(9): p. 1717-1730.
199. McDowell, M.T., et al., *Novel size and surface oxide effects in silicon nanowires as lithium battery anodes.* Nano Letters, 2011. **11**(9): p. 4018-4025.
200. Grantab, R. and V.B. Shenoy, *Pressure-gradient dependent diffusion and crack propagation in lithiated silicon nanowires.* Journal of the Electrochemical Society, 2012. **159**(5): p. A584-A591.
201. Ashuri, M., Q. He, and L.L. Shaw, *Silicon as a potential anode material for Li-ion batteries: where size, geometry and structure matter.* Nanoscale, 2016. **8**(1): p. 74-103.

202. Teki, R., et al., *Nanostructured silicon anodes for lithium ion rechargeable batteries.* Small, 2009. **5**(20): p. 2236-2242.
203. Wen, Z., et al., *Silicon nanotube anode for lithium-ion batteries.* Electrochemistry Communications, 2013. **29**: p. 67-70.
204. Liu, X.H., et al., *Anisotropic swelling and fracture of silicon nanowires during lithiation.* Nano letters, 2011. **11**(8): p. 3312-3318.
205. Chandrasekaran, R., et al., *Analysis of lithium insertion/deinsertion in a silicon electrode particle at room temperature.* Journal of the Electrochemical Society, 2010. **157**(10): p. A1139-A1151.
206. Chandrasekaran, R. and T.F. Fuller, *Analysis of the lithium-ion insertion silicon composite electrode/separator/lithium foil cell.* Journal of The Electrochemical Society, 2011. **158**(8): p. A859-A871.
207. Garrick, T.R., et al., *Modeling volume change due to intercalation into porous electrodes.* Journal of The Electrochemical Society, 2014. **161**(8): p. E3297-E3301.
208. Garrick, T.R., et al., *Modeling volume change in dual insertion electrodes.* Journal of The Electrochemical Society, 2017. **164**(11): p. E3552-E3558.
209. Pereira, D.J., J.W. Weidner, and T.R. Garrick, *The Effect of Volume Change on the Accessible Capacities of Porous Silicon-Graphite Composite Anodes.* Journal of The Electrochemical Society, 2019. **166**(6): p. A1251-A1256.
210. Swamy, T. and Y.-M. Chiang, *Electrochemical charge transfer reaction kinetics at the silicon-liquid electrolyte interface.* Journal of The Electrochemical Society, 2015. **162**(13): p. A7129-A7134.
211. Ji, Y., Y. Zhang, and C.-Y. Wang, *Li-ion cell operation at low temperatures.* Journal of The Electrochemical Society, 2013. **160**(4): p. A636-A649.
212. Srinivasan, V., *Model-experimental studies on next-generation Li-ion materials.* OVT Merit Review, 2009.
213. Ding, N., et al., *Determination of the diffusion coefficient of lithium ions in nano-Si.* Solid State Ionics, 2009. **180**(2-3): p. 222-225.
214. Baggetto, L., et al., *On the electrochemistry of an anode stack for all-solid-state 3D-integrated batteries.* Journal of Power Sources, 2009. **189**(1): p. 402-410.
215. Xie, J., et al., *Li-ion diffusion in amorphous Si films prepared by RF magnetron sputtering: A comparison of using liquid and polymer electrolytes.* Materials Chemistry and Physics, 2010. **120**(2-3): p. 421-425.
216. Li, J., et al., *Potentiostatic intermittent titration technique for electrodes governed by diffusion and interfacial reaction.* the Journal of Physical Chemistry C, 2011. **116**(1): p. 1472-1478.
217. Pharr, M., et al., *Kinetics of initial lithiation of crystalline silicon electrodes of lithium-ion batteries.* Nano letters, 2012. **12**(9): p. 5039-5047.
218. Sethuraman, V.A., V. Srinivasan, and J. Newman, *Analysis of electrochemical lithiation and delithiation kinetics in silicon.* Journal of the Electrochemical Society, 2013. **160**(2): p. A394-A403.
219. Mai, W., A. Colclasure, and K.A. Smith, *A Novel Reformulation of the Pseudo2D Battery Model Coupling Large Deformations at Particle and Electrode Levels*. 2019, National Renewable Energy Lab.(NREL), Golden, CO (United States).

220. Wu, H., et al., *Stable Li-ion battery anodes by in-situ polymerization of conducting hydrogel to conformally coat silicon nanoparticles.* Nature communications, 2013. **4**: p. 1943.
221. Ahmed, S., et al., *Enabling fast charging–A battery technology gap assessment.* Journal of Power Sources, 2017. **367**: p. 250-262.
222. Keyser, M., et al., *Enabling fast charging–Battery thermal considerations.* Journal of Power Sources, 2017. **367**: p. 228-236.
223. Meintz, A., et al., *Enabling fast charging–Vehicle considerations.* Journal of Power Sources, 2017. **367**: p. 216-227.
224. Burnham, A., et al., *Enabling fast charging–Infrastructure and economic considerations.* Journal of Power Sources, 2017. **367**: p. 237-249.
225. Besenhard, J., et al., *Binary and ternary Li-alloys as anode materials in rechargeable organic electrolyte Li-batteries.* Solid State Ionics, 1986. **18**: p. 823-827.
226. Inaba, M., et al., *In situ Raman study on electrochemical Li intercalation into graphite.* Journal of The Electrochemical Society, 1995. **142**(1): p. 20-26.
227. Yang, J., M. Winter, and J. Besenhard, *Small particle size multiphase Li-alloy anodes for lithium-ionbatteries.* Solid State Ionics, 1996. **90**(1-4): p. 281-287.
228. Funabiki, A., et al., *Stage Transformation of Lithium-Graphite Intercalation Compounds Caused by Electrochemical Lithium Intercalation.* Journal of The Electrochemical Society, 1999. **146**(7): p. 2443-2448.
229. Padhi, A.K., K.S. Nanjundaswamy, and J.B. Goodenough, *Phospho-olivines as positive-electrode materials for rechargeable lithium batteries.* Journal of the electrochemical society, 1997. **144**(4): p. 1188-1194.
230. Wang, B., et al., *Characterization of Thin-Film Rechargeable Lithium Batteries with Lithium Cobalt Oxide Cathodes.* Journal of The Electrochemical Society, 1996. **143**(10): p. 3203-3213.
231. Zhang, S.S., *A review on electrolyte additives for lithium-ion batteries.* Journal of Power Sources, 2006. **162**(2): p. 1379-1394.
232. Ryan, E.M. and P.P. Mukherjee, *Mesoscale modeling in electrochemical devices—A critical perspective.* Progress in Energy and Combustion Science, 2019. **71**: p. 118-142.
233. Mistry, A.N., K. Smith, and P.P. Mukherjee, *Electrochemistry coupled mesoscale complexations in electrodes lead to thermo-electrochemical extremes.* ACS applied materials & interfaces, 2018. **10**(34): p. 28644-28655.
234. Mistry, A.N., K. Smith, and P.P. Mukherjee, *Secondary-phase stochastics in lithium-ion battery electrodes.* ACS applied materials & interfaces, 2018. **10**(7): p. 6317-6326.
235. Downie, L., et al., *In situ detection of lithium plating on graphite electrodes by electrochemical calorimetry.* Journal of The Electrochemical Society, 2013. **160**(4): p. A588-A594.
236. Bitzer, B. and A. Gruhle, *A new method for detecting lithium plating by measuring the cell thickness.* Journal of Power Sources, 2014. **262**: p. 297-302.
237. Petzl, M. and M.A. Danzer, *Nondestructive detection, characterization, and quantification of lithium plating in commercial lithium-ion batteries.* Journal of Power Sources, 2014. **254**: p. 80-87.
238. Birkenmaier, C., et al., *Lithium plating on graphite negative electrodes: Innovative qualitative and quantitative investigation methods.* Journal of The Electrochemical Society, 2015. **162**(14): p. A2646-A2650.

239. Burns, J., D. Stevens, and J. Dahn, *In-situ detection of lithium plating using high precision coulometry.* Journal of The Electrochemical Society, 2015. **162**(6): p. A959-A964.
240. Arora, P., M. Doyle, and R.E. White, *Mathematical Modeling of the Lithium Deposition Overcharge Reaction in Lithium-Ion Batteries Using Carbon-Based Negative Electrodes.* Journal of The Electrochemical Society, 1999. **146**(10): p. 3543-3553.
241. Rangarajan, S.P., Y. Barsukov, and P.P. Mukherjee, *In operando signature and quantification of lithium plating.* Journal of Materials Chemistry A, 2019. **7**(36): p. 20683-20695.
242. Jansen, A.N., et al., *Low-temperature study of lithium-ion cells using a Li y Sn micro-reference electrode.* Journal of Power Sources, 2007. **174**(2): p. 373-379.
243. Park, G., et al., *The study of electrochemical properties and lithium deposition of graphite at low temperature.* Journal of power sources, 2012. **199**: p. 293-299.
244. Tippmann, S., et al., *Low-temperature charging of lithium-ion cells part I: Electrochemical modeling and experimental investigation of degradation behavior*. Journal of Power Sources, 2014. **252**: p. 305-316.
245. Remmlinger, J., et al., *Low-temperature charging of lithium-ion cells Part II: Model reduction and application.* Journal of Power Sources, 2014. **254**: p. 268-276.
246. Petzl, M., M. Kasper, and M.A. Danzer, *Lithium plating in a commercial lithium-ion battery–A low-temperature aging study.* Journal of Power Sources, 2015. **275**: p. 799-807.
247. Cannarella, J. and C.B. Arnold, *The effects of defects on localized plating in lithium-ion batteries.* Journal of The Electrochemical Society, 2015. **162**(7): p. A1365-A1373.
248. Gallagher, K.G., et al., *Optimizing areal capacities through understanding the limitations of lithium-ion electrodes.* Journal of The Electrochemical Society, 2016. **163**(2): p. A138-A149.
249. Aurbach, D., et al., *A short review of failure mechanisms of lithium metal and lithiated graphite anodes in liquid electrolyte solutions.* Solid state ionics, 2002. **148**(3-4): p. 405-416.
250. López, C.M., J.T. Vaughey, and D.W. Dees, *Morphological transitions on lithium metal anodes.* Journal of The Electrochemical Society, 2009. **156**(9): p. A726-A729.
251. Bai, Y.-J., et al., *Excellent long-term cycling stability of La-doped Li 4 Ti 5 O 12 anode material at high current rates.* Journal of Materials Chemistry, 2012. **22**(36): p. 19054-19060.
252. Zhang, Z., et al., *Hydrothermal synthesis of Zn-doped Li 4 Ti 5 O 12 with improved high rate properties for lithium ion batteries.* Ceramics International, 2013. **39**(6): p. 6139-6143.
253. Zhang, Y., et al., *Influence of Sc 3+ doping in B-site on electrochemical performance of Li 4 Ti 5 O 12 anode materials for lithium-ion battery.* Journal of power sources, 2014. **250**: p. 50-57.
254. Wang, P., et al., *Enhanced lithium storage capability of sodium lithium titanate via lithium-site doping.* Journal of Power Sources, 2015. **297**: p. 283-294.
255. Wang, P., et al., *Improved lithium storage performance of lithium sodium titanate anode by titanium site substitution with aluminum.* Journal of Power Sources, 2015. **293**: p. 33-41.
256. Liu, H.-p., et al., *High rate cycling performance of nanosized Li 4 Ti 5 O 12/graphene composites for lithium ion batteries.* Electrochimica Acta, 2016. **192**: p. 38-44.

257. Mu, D., et al., *Nano-sized Li 4 Ti 5 O 12/C anode material with ultrafast charge/discharge capability for lithium ion batteries.* Journal of Alloys and Compounds, 2016. **671**: p. 157-163.
258. Luo, W., et al., *Transition from superlithiophobicity to superlithiophilicity of garnet solid-state electrolyte.* Journal of the American Chemical Society, 2016. **138**(37): p. 12258-12262.
259. Zhang, P., et al., *High Rate Capability of Lithium Chromium Titanium Oxide Hierarchical Mesoporous Microspheres Anode Materials Synthesized by a One-Pot Co-Precipitation for Lithium Ion Batteries.* Journal of The Electrochemical Society, 2016. **163**(9): p. A1920-A1926.
260. Zheng, H., et al., *A comprehensive understanding of electrode thickness effects on the electrochemical performances of Li-ion battery cathodes.* Electrochimica Acta, 2012. **71**: p. 258-265.
261. Du, Z., et al., *Understanding limiting factors in thick electrode performance as applied to high energy density Li-ion batteries.* Journal of Applied Electrochemistry, 2017. **47**(3): p. 405-415.
262. Leng, Y., et al., *Electrochemical Cycle-Life Characterization of High Energy Lithium-Ion Cells with Thick Li (Ni0. 6Mn0. 2Co0. 2) O2 and Graphite Electrodes.* Journal of The Electrochemical Society, 2017. **164**(6): p. A1037-A1049.
263. Wang, Q., et al., *Thermal runaway caused fire and explosion of lithium ion battery.* Journal of power sources, 2012. **208**: p. 210-224.
264. Srinivasan, V. and C. Wang, *Analysis of electrochemical and thermal behavior of Li-ion cells.* Journal of The Electrochemical Society, 2003. **150**(1): p. A98-A106.
265. Ge, H., et al., *Investigating lithium plating in lithium-ion batteries at low temperatures using electrochemical model with NMR assisted parameterization.* Journal of The Electrochemical Society, 2017. **164**(6): p. A1050-A1060.
266. Fraunhofer, I., *GeoDict.* Homepage of the GeoDict software, 2011. **16**.
267. Wiegmann, A., *GEODICT: virtual microstructure simulator and material property predictor*. 2016, ed.
268. Wang, C.-Y., et al., *A fast rechargeable lithium-ion battery at subfreezing temperatures.* Journal of The Electrochemical Society, 2016. **163**(9): p. A1944-A1950.
269. Wang, C.-Y., et al., *Lithium-ion battery structure that self-heats at low temperatures.* Nature, 2016. **529**(7587): p. 515.
270. Yang, X.-G., G. Zhang, and C.-Y. Wang, *Computational design and refinement of self-heating lithium ion batteries.* Journal of Power Sources, 2016. **328**: p. 203-211.
271. Ji, Y. and C.Y. Wang, *Heating strategies for Li-ion batteries operated from subzero temperatures.* Electrochimica Acta, 2013. **107**: p. 664-674.
272. Yang, X.-G., et al., *Fast charging of lithium-ion batteries at all temperatures.* Proceedings of the National Academy of Sciences, 2018. **115**(28): p. 7266-7271.
273. Liu, Z., P.B. Balbuena, and P.P. Mukherjee, *Revealing charge transport mechanisms in Li2S2 for Li–sulfur batteries.* The journal of physical chemistry letters, 2017. **8**(7): p. 1324-1330.
274. Mistry, A. and P.P. Mukherjee, *Precipitation–Microstructure Interactions in the Li-Sulfur Battery Electrode.* The Journal of Physical Chemistry C, 2017. **121**(47): p. 26256-26264.
275. Girishkumar, G., et al., *Lithium− air battery: promise and challenges.* The Journal of Physical Chemistry Letters, 2010. **1**(14): p. 2193-2203.

276. Jung, H.-G., et al., *An improved high-performance lithium–air battery.* Nature chemistry, 2012. **4**(7): p. 579.
277. Cheng, X.B., et al., *A review of solid electrolyte interphases on lithium metal anode.* Advanced Science, 2016. **3**(3).
278. Rosso, M., et al., *Dendrite short-circuit and fuse effect on Li/polymer/Li cells.* Electrochimica Acta, 2006. **51**(25): p. 5334-5340.
279. Sacci, R.L., et al., *Nanoscale imaging of fundamental Li battery chemistry: solid-electrolyte interphase formation and preferential growth of lithium metal nanoclusters.* Nano letters, 2015. **15**(3): p. 2011-2018.
280. Gao, Y., et al., *Interfacial chemistry regulation via a skin-grafting strategy enables high-performance lithium-metal batteries.* Journal of the American Chemical Society, 2017. **139**(43): p. 15288-15291.
281. Qian, J., et al., *High rate and stable cycling of lithium metal anode.* Nature communications, 2015. **6**: p. 6362.
282. Ishikawa, K., et al., *Crystal orientation dependence of precipitate structure of electrodeposited Li metal on Cu current collectors.* Crystal Growth & Design, 2017. **17**(5): p. 2379-2385.
283. Steiger, J., et al., *Comparison of the growth of lithium filaments and dendrites under different conditions.* Electrochemistry Communications, 2015. **50**: p. 11-14.
284. Tu, Z., et al., *Nanoporous polymer-ceramic composite electrolytes for lithium metal batteries.* Advanced Energy Materials, 2014. **4**(2).
285. Shin, W.-K., A.G. Kannan, and D.-W. Kim, *Effective suppression of dendritic lithium growth using an ultrathin coating of nitrogen and sulfur codoped graphene nanosheets on polymer separator for lithium metal batteries.* ACS applied materials & interfaces, 2015. **7**(42): p. 23700-23707.
286. Orsini, F., et al., *In situ SEM study of the interfaces in plastic lithium cells.* Journal of power sources, 1999. **81**: p. 918-921.
287. Dollé, M., et al., *Live scanning electron microscope observations of dendritic growth in lithium/polymer cells.* Electrochemical and solid-state letters, 2002. **5**(12): p. A286-A289.
288. Kim, W.-S. and W.-Y. Yoon, *Observation of dendritic growth on Li powder anode using optical cell.* Electrochimica acta, 2004. **50**(2-3): p. 541-545.
289. Ghassemi, H., et al., *Real-time observation of lithium fibers growth inside a nanoscale lithium-ion battery.* Applied Physics Letters, 2011. **99**(12): p. 123113.
290. Harry, K.J., et al., *Detection of subsurface structures underneath dendrites formed on cycled lithium metal electrodes.* Nature materials, 2014. **13**(1): p. 69-73.
291. Zeng, Z., et al., *Visualization of electrode–electrolyte interfaces in LiPF6/EC/DEC electrolyte for lithium ion batteries via in situ TEM.* Nano letters, 2014. **14**(4): p. 1745-1750.
292. Chang, H.J., et al., *Correlating microstructural lithium metal growth with electrolyte salt depletion in lithium batteries using 7Li MRI.* Journal of the American Chemical Society, 2015. **137**(48): p. 15209-15216.
293. Chang, H.J., et al., *Investigating Li microstructure formation on Li anodes for lithium batteries by in situ 6Li/7Li NMR and SEM.* The Journal of Physical Chemistry C, 2015. **119**(29): p. 16443-16451.

294. Tang, C.-Y. and S.J. Dillon, *In situ scanning electron microscopy characterization of the mechanism for Li dendrite growth.* Journal of The Electrochemical Society, 2016. **163**(8): p. A1660-A1665.
295. Yoshimatsu, I., T. Hirai, and J.i. Yamaki, *Lithium electrode morphology during cycling in lithium cells.* Journal of the Electrochemical Society, 1988. **135**(10): p. 2422-2427.
296. Bai, P., et al., *Transition of lithium growth mechanisms in liquid electrolytes.* Energy & Environmental Science, 2016. **9**(10): p. 3221-3229.
297. Barton, J. and J.M. Bockris, *The electrolytic growth of dendrites from ionic solutions.* Proc. R. Soc. Lond. A, 1962. **268**(1335): p. 485-505.
298. Diggle, J., A. Despic, and J.M. Bockris, *The mechanism of the dendritic electrocrystallization of zinc.* Journal of The Electrochemical Society, 1969. **116**(11): p. 1503-1514.
299. Chazalviel, J.-N., *Electrochemical aspects of the generation of ramified metallic electrodeposits.* Physical review A, 1990. **42**(12): p. 7355.
300. Yamaki, J.-i., et al., *A consideration of the morphology of electrochemically deposited lithium in an organic electrolyte.* Journal of Power Sources, 1998. **74**(2): p. 219-227.
301. Monroe, C. and J. Newman, *Dendrite growth in lithium/polymer systems a propagation model for liquid electrolytes under galvanostatic conditions.* Journal of The Electrochemical Society, 2003. **150**(10): p. A1377-A1384.
302. Akolkar, R., *Mathematical model of the dendritic growth during lithium electrodeposition.* Journal of Power Sources, 2013. **232**: p. 23-28.
303. Akolkar, R., *Modeling dendrite growth during lithium electrodeposition at sub-ambient temperature.* Journal of Power Sources, 2014. **246**: p. 84-89.
304. Liang, L. and L.-Q. Chen, *Nonlinear phase field model for electrodeposition in electrochemical systems.* Applied Physics Letters, 2014. **105**(26): p. 263903.
305. Cogswell, D.A., *Quantitative phase-field modeling of dendritic electrodeposition.* Physical Review E, 2015. **92**(1): p. 011301.
306. Harry, K.J., et al., *Influence of electrolyte modulus on the local current density at a dendrite tip on a lithium metal electrode.* Journal of The Electrochemical Society, 2016. **163**(10): p. A2216-A2224.
307. Barai, P., K. Higa, and V. Srinivasan, *Effect of initial state of lithium on the propensity for dendrite formation: A theoretical study.* Journal of The Electrochemical Society, 2017. **164**(2): p. A180-A189.
308. Gireaud, L., et al., *Lithium metal stripping/plating mechanisms studies: A metallurgical approach.* Electrochemistry communications, 2006. **8**(10): p. 1639-1649.
309. Li, Z., et al., *A review of lithium deposition in lithium-ion and lithium metal secondary batteries.* Journal of power sources, 2014. **254**: p. 168-182.
310. Valøen, L.O. and J.N. Reimers, *Transport properties of LiPF6-based Li-ion battery electrolytes.* Journal of The Electrochemical Society, 2005. **152**(5): p. A882-A891.
311. Liu, G. and W. Lu, *A Model of Concurrent Lithium Dendrite Growth, SEI Growth, SEI Penetration and Regrowth.* Journal of The Electrochemical Society, 2017. **164**(9): p. A1826-A1833.
312. Efrima, S., *Morphology of Quasi-Two-Dimensional Electrodeposits A Generalized Wagner Number.* Langmuir, 1997. **13**(13): p. 3550-3556.
313. Braun, T. and D. Schwartz, *Localized electrodeposition and patterning using bipolar electrochemistry.* Journal of The Electrochemical Society, 2015. **162**(4): p. D180-D185.

314. Nishikawa, K., et al., *In situ observation of dendrite growth of electrodeposited Li metal.* Journal of The Electrochemical Society, 2010. **157**(11): p. A1212-A1217.
315. Nishikawa, K., et al., *Li dendrite growth and Li+ ionic mass transfer phenomenon.* Journal of electroanalytical chemistry, 2011. **661**(1): p. 84-89.
316. Aurbach, D., Y. Cohen, and M. Moshkovich, *The study of reversible magnesium deposition by in situ scanning tunneling microscopy.* Electrochemical and Solid-State Letters, 2001. **4**(8): p. A113-A116.
317. Besenhard, J.O. and M. Winter, *Advances in Battery Technology: Rechargeable Magnesium Batteries and Novel Negative-Electrode Materials for Lithium Ion Batteries.* ChemPhysChem, 2002. **3**(2): p. 155-159.
318. Zhao, Q.S., et al., *Reversibility of electrochemical magnesium deposition from tetrahydrofuran solutions containing pyrrolidinyl magnesium halide.* Electrochimica Acta, 2011. **56**(18): p. 6530-6535.
319. Muldoon, J., et al., *Electrolyte roadblocks to a magnesium rechargeable battery.* Energy & Environmental Science, 2012. **5**(3): p. 5941-5950.
320. Yoo, H.D., et al., *Mg rechargeable batteries: an on-going challenge.* Energy & Environmental Science, 2013. **6**(8): p. 2265-2279.
321. Doe, R.E., et al., *Novel, electrolyte solutions comprising fully inorganic salts with high anodic stability for rechargeable magnesium batteries.* Chemical communications, 2014. **50**(2): p. 243-245.
322. Mohtadi, R. and F. Mizuno, *Magnesium batteries: Current state of the art, issues and future perspectives.* Beilstein journal of nanotechnology, 2014. **5**: p. 1291.
323. Bucur, C.B., et al., *Confession of a magnesium battery.* J. Phys. Chem. Lett, 2015. **6**(18): p. 3578-3591.
324. Massé, R.C., E. Uchaker, and G. Cao, *Beyond Li-ion: electrode materials for sodium-and magnesium-ion batteries.* Science China Materials, 2015. **58**(9): p. 715-766.
325. Jäckle, M. and A. Groß, *Microscopic properties of lithium, sodium, and magnesium battery anode materials related to possible dendrite growth.* The Journal of chemical physics, 2014. **141**(17): p. 174710.
326. Shewmon, P., *Self-diffusion in magnesium single crystals.* JOM, 1956. **8**(8): p. 918-922.
327. Combronde, J. and G. Brebec, *Anisotropie d'autodiffusion du magnesium.* Acta Metallurgica, 1971. **19**(12): p. 1393-1399.
328. Ganeshan, S., L. Hector, and Z.-K. Liu, *First-principles study of self-diffusion in hcp Mg and Zn.* Computational Materials Science, 2010. **50**(2): p. 301-307.
329. Zhang, L.-J., et al., *Atomic self-diffusion anisotropy of HCP metals from first-principles calculations.* Computational Materials Science, 2017. **128**: p. 236-242.
330. Baraille, I., et al., *Comparison between Hartree-Fock and Kohn-Sham electronic and structural properties for hexagonal-close-packed magnesium.* Journal of Physics: Condensed Matter, 1998. **10**(48): p. 10969.
331. Dathar, G.K.P., et al., *Calculations of Li-ion diffusion in olivine phosphates.* Chemistry of Materials, 2011. **23**(17): p. 4032-4037.
332. Tarascon, J.-M. and M. Armand, *Issues and challenges facing rechargeable lithium batteries*, in *Materials For Sustainable Energy: A Collection of Peer-Reviewed Research and Review Articles from Nature Publishing Group*. 2011, World Scientific. p. 171-179.

333. Peled, E., et al., *Improved Graphite Anode for Lithium-Ion Batteries Chemically Bonded Solid Electrolyte Interface and Nanochannel Formation.* Journal of The Electrochemical Society, 1996. **143**(1): p. L4-L7.
334. Liu, S., L. Xiong, and C. He, *Long cycle life lithium ion battery with lithium nickel cobalt manganese oxide (NCM) cathode.* Journal of Power Sources, 2014. **261**: p. 285-291.
335. Fujimura, K., et al., *Accelerated Materials Design of Lithium Superionic Conductors Based on First-Principles Calculations and Machine Learning Algorithms.* Advanced Energy Materials, 2013. **3**(8): p. 980-985.
336. Inaguma, Y., et al., *High ionic conductivity in lithium lanthanum titanate.* Solid State Communications, 1993. **86**(10): p. 689-693.
337. Thangadurai, V., S. Narayanan, and D. Pinzaru, *Garnet-type solid-state fast Li ion conductors for Li batteries: critical review.* Chemical Society Reviews, 2014. **43**(13): p. 4714-4727.
338. Chen, S., et al., *Sulfide solid electrolytes for all-solid-state lithium batteries: structure, conductivity, stability and application.* Energy Storage Materials, 2018. **14**: p. 58-74.
339. Bates, J., et al., *Thin-film lithium and lithium-ion batteries.* Solid State Ionics, 2000. **135**(1): p. 33-45.
340. Dudney, N.J., *Solid-state thin-film rechargeable batteries.* Materials Science and Engineering: B, 2005. **116**(3): p. 245-249.
341. Murugan, R., V. Thangadurai, and W. Weppner, *Fast lithium ion conduction in garnet-type Li7La3Zr2O12.* Angewandte Chemie International Edition, 2007. **46**(41): p. 7778-7781.
342. Kamaya, N., et al., *A lithium superionic conductor.* Nature materials, 2011. **10**(9): p. 682-686.
343. Luntz, A.C., J. Voss, and K. Reuter, *Interfacial challenges in solid-state Li ion batteries*. 2015, ACS Publications.
344. Basappa, R.H., T. Ito, and H. Yamada, *Contact between garnet-type solid electrolyte and lithium metal anode: influence on charge transfer resistance and short circuit prevention.* Journal of The Electrochemical Society, 2017. **164**(4): p. A666-A671.
345. Santhanagopalan, D., et al., *Interface limited lithium transport in solid-state batteries.* The journal of physical chemistry letters, 2013. **5**(2): p. 298-303.
346. Zhu, Y., X. He, and Y. Mo, *First principles study on electrochemical and chemical stability of solid electrolyte–electrode interfaces in all-solid-state Li-ion batteries.* Journal of Materials Chemistry A, 2016. **4**(9): p. 3253-3266.
347. Fleig, J. and J. Maier, *The impedance of imperfect electrode contacts on solid electrolytes.* Solid State Ionics, 1996. **85**(1-4): p. 17-24.
348. Bucci, G., et al., *Modeling of internal mechanical failure of all-solid-state batteries during electrochemical cycling, and implications for battery design.* Journal of Materials Chemistry A, 2017. **5**(36): p. 19422-19430.
349. Koerver, R., et al., *Chemo-mechanical expansion of lithium electrode materials–on the route to mechanically optimized all-solid-state batteries.* Energy & Environmental Science, 2018. **11**(8): p. 2142-2158.
350. Maslyn, J.A., et al., *Growth of lithium dendrites and globules through a solid block copolymer electrolyte as a function of current density.* The Journal of Physical Chemistry C, 2018. **122**(47): p. 26797-26804.

351. Fu, K.K., et al., *Flexible, solid-state, ion-conducting membrane with 3D garnet nanofiber networks for lithium batteries*. Proceedings of the National Academy of Sciences, 2016. **113**(26): p. 7094-7099.
352. Park, K., et al., *Electrochemical nature of the cathode interface for a solid-state lithium-ion battery: interface between LiCoO2 and garnet-Li7La3Zr2O12*. Chemistry of Materials, 2016. **28**(21): p. 8051-8059.
353. Fu, K., et al., *Transient behavior of the metal interface in lithium metal–garnet batteries.* Angewandte Chemie International Edition, 2017. **56**(47): p. 14942-14947.
354. Swamy, T., et al., *Lithium metal penetration induced by electrodeposition through solid electrolytes: example in single-crystal Li6La3ZrTaO12 garnet.* Journal of The Electrochemical Society, 2018. **165**(16): p. A3648.
355. Han, X., et al., *Negating interfacial impedance in garnet-based solid-state Li metal batteries.* Nature materials, 2017. **16**(5): p. 572-579.
356. Lau, J., et al., *Sulfide solid electrolytes for lithium battery applications.* Advanced Energy Materials, 2018. **8**(27): p. 1800933.
357. Yu, C., et al., *Unravelling li-ion transport from picoseconds to seconds: bulk versus interfaces in an argyrodite li6ps5cl–li2s all-solid-state li-ion battery.* Journal of the American Chemical Society, 2016. **138**(35): p. 11192-11201.
358. Zhang, Z., et al., *Interface re-engineering of Li10GeP2S12 electrolyte and lithium anode for all-solid-state lithium batteries with ultralong cycle life.* ACS applied materials & interfaces, 2018. **10**(3): p. 2556-2565.
359. Famprikis, T., et al., *Fundamentals of inorganic solid-state electrolytes for batteries.* Nature materials, 2019: p. 1-14.
360. Jung, Y.S., et al., *Issues and challenges for bulk-type all-solid-state rechargeable lithium batteries using sulfide solid electrolytes.* Israel Journal of Chemistry, 2015. **55**(5): p. 472-485.
361. Tatsumisago, M., F. Mizuno, and A. Hayashi, *All-solid-state lithium secondary batteries using sulfide-based glass–ceramic electrolytes.* Journal of power sources, 2006. **159**(1): p. 193-199.
362. Ni, J.E., et al., *Room temperature elastic moduli and Vickers hardness of hot-pressed LLZO cubic garnet.* Journal of Materials Science, 2012. **47**(23): p. 7978-7985.
363. Sharafi, A., et al., *Characterizing the Li–Li7La3Zr2O12 interface stability and kinetics as a function of temperature and current density.* Journal of Power Sources, 2016. **302**: p. 135-139.
364. Shao, Y., et al., *Drawing a soft interface: an effective interfacial modification strategy for garnet-type solid-state Li batteries.* ACS Energy Letters, 2018. **3**(6): p. 1212-1218.
365. Luo, W., et al., *Reducing interfacial resistance between garnet-structured solid-state electrolyte and Li-metal anode by a germanium layer.* Advanced Materials, 2017. **29**(22): p. 1606042.
366. Liu, B., et al., *Garnet solid electrolyte protected Li-metal batteries.* ACS applied materials & interfaces, 2017. **9**(22): p. 18809-18815.
367. Tsai, C.-L., et al., *Li7La3Zr2O12 interface modification for Li dendrite prevention.* ACS applied materials & interfaces, 2016. **8**(16): p. 10617-10626.
368. Van Den Broek, J., S. Afyon, and J.L. Rupp, *Interface-Engineered All-Solid-State Li-Ion Batteries Based on Garnet-Type Fast Li+ Conductors.* Advanced Energy Materials, 2016. **6**(19): p. 1600736.

369. Wang, M.J., R. Choudhury, and J. Sakamoto, *Characterizing the Li-Solid-Electrolyte Interface Dynamics as a Function of Stack Pressure and Current Density.* Joule, 2019. **3**(9): p. 2165-2178.
370. Jow, T. and C. Liang, *Interface between solid anode and solid electrolyte-effect of pressure on Li/LiI (Al2O3) interface.* Solid State Ionics, 1983. **9**: p. 695-698.
371. Zhang, X., et al., *Rethinking How External Pressure Can Suppress Dendrites in Lithium Metal Batteries.* Journal of The Electrochemical Society, 2019. **166**(15): p. A3639-A3652.
372. Qingsong, T., et al., *Modeling of Electro-deposition and Mechanical Stability at Li Metal/Solid Electrolyte Interface during Plating in Solid-State Batteries.* arXiv preprint arXiv:1910.13922, 2019.
373. Sharafi, A., et al., *Controlling and correlating the effect of grain size with the mechanical and electrochemical properties of Li 7 La 3 Zr 2 O 12 solid-state electrolyte.* Journal of Materials Chemistry A, 2017. **5**(40): p. 21491-21504.
374. Timoshenko, S.P. and J.M. Gere, *Theory of elastic stability*. 2009: Courier Corporation.
375. Tikekar, M.D., L.A. Archer, and D.L. Koch, *Stability analysis of electrodeposition across a structured electrolyte with immobilized anions.* Journal of The Electrochemical Society, 2014. **161**(6): p. A847-A855.
376. McMeeking, R.M., et al., *Metal electrode surfaces can roughen despite the constraint of a stiff electrolyte.* Journal of The Electrochemical Society, 2019. **166**(6): p. A984-A995.
377. Choudhury, S., *Confining electrodeposition of metals in structured electrolytes*, in *Rational Design of Nanostructured Polymer Electrolytes and Solid–Liquid Interphases for Lithium Batteries*. 2019, Springer. p. 59-79.
378. Yu, S. and D.J. Siegel, *Grain boundary contributions to Li-ion transport in the solid electrolyte Li7La3Zr2O12 (LLZO).* Chemistry of Materials, 2017. **29**(22): p. 9639-9647.
379. David, I.N., et al., *Microstructure and Li-Ion Conductivity of Hot-Pressed Cubic Li7La3Zr2O12.* Journal of the American Ceramic Society, 2015. **98**(4): p. 1209-1214.
380. Groeber, M.A. and M.A. Jackson, *DREAM. 3D: a digital representation environment for the analysis of microstructure in 3D.* Integrating materials and manufacturing innovation, 2014. **3**(1): p. 5.
381. Lacaille, V., et al., *Finite element analysis of the grain size effect on diffusion in polycrystalline materials.* Computational materials science, 2014. **95**: p. 187-191.
382. Dawson, J.A., et al., *Atomic-scale influence of grain boundaries on Li-ion conduction in solid electrolytes for all-solid-state batteries.* Journal of the American Chemical Society, 2018. **140**(1): p. 362-368.
383. Vargas-Barbosa, N.M. and B. Roling, *Dynamic Ion Correlations in Solid and Liquid Electrolytes: How Do They Affect Charge and Mass Transport?* ChemElectroChem, 2019.
384. Angheluta, L., E. Jettestuen, and J. Mathiesen, *Thermodynamics and roughening of solid-solid interfaces.* Physical Review E, 2009. **79**(3): p. 031601.
385. Shen, F., et al., *Effect of pore connectivity on Li dendrite propagation within LLZO electrolytes observed with synchrotron X-ray tomography.* ACS Energy Letters, 2018. **3**(4): p. 1056-1061.
386. Masias, A., et al., *Elastic, plastic, and creep mechanical properties of lithium metal.* Journal of materials science, 2019. **54**(3): p. 2585-2600.
387. LePage, W.S., et al., *Lithium mechanics: roles of strain rate and temperature and implications for lithium metal batteries.* Journal of The Electrochemical Society, 2019. **166**(2): p. A89-A97.

VITA

EDUCATION

Purdue University

2017 - current PhD in *Mechanical Engineering* GPA: 4**.00/4.00**

Texas A&M University, USA

2015-2017 PhD in *Mechanical Engineering* GPA: **4.00/4.00**

Indian Institute of Technology Kanpur, India

2012 – 2014 Master of Technology in *Fluid and Thermal Sciences* (Mechanical Engineering) GPA: **8.75/10.00**

Birla Institute of Technology and Science Pilani, Pilani Campus, India

2008 – 2012 Bachelor of Engineering in *Mechanical Engineering* GPA: **7.59/10.00**

RESEARCH EXPERIENCE

Doctoral Research

Multimodal Degradation Interactions in Electrodes for Energy Storage

Graduate Research Assistant, Energy & Transport Sciences Laboratory

Advisor: Dr. Partha P. Mukherjee (Purdue: Fall '17 onwards, A&M: Fall '15 – Summer '17)

Keywords: Li-ion, Porous electrode theory, Electrode pulverization, Lithium plating, Solid electrolyte

Internship

National Renewable Energy Laboratory, Group: Energy Storage, Department: Transportation

June 2019 – August 2019

Principal Investigator: Dr. Kandler Smith

Duties: Development of Coupled Mechano-Electrochemical Model for Damage Evolution in Intercalation Anodes

National Renewable Energy Laboratory, Group: Energy Storage, Department: Transportation

June 2016 – August 2016

Principal Investigator: Dr. Kandler Smith

Duties: Characterization of Graphite and NCM523 battery electrode materials: Experiments and Modelling using Multi Scale Multi Domain (MSMD) model

Project Associate

July 2014 – July 2015.

OpenFOAM® Simulations of Phase Change Material Melting Process in a Heated Enclosure

Principal Investigator: Dr. Malay Kumar Das & Dr. Sameer Khandekar (IIT Kanpur)

Duties: Validation of experimental results obtained using simulation of melting process on OpenFOAM®

Master's Thesis

OpenFOAM® simulations of Rising Hydrogen Bubble in Water Splitting Reactor

Supervisor: Dr. Malay Kumar Das (IIT Kanpur)

Keywords: Surface tension, Volume of Fluid, Surface Compression, Rising Bubble Benchmark

Journal Publications

1. **A. Verma,** A. Franco, P.P. Mukherjee, "*Mechanistic Elucidation of Si Particle Morphology on Electrode Performance*", Journal of Electrochemical Society **165** (15), A3852-A3860 **(2019)**
2. **A. Verma,** T. Kotaka, Y. Tabuchi, P.P. Mukherjee, "*Mechano-Electrochemical Interaction and Degradation in Graphite Electrode with Surface Film"*, Journal of Electrochemical Society **165** (10), A2397-A2408 **(2018)**
3. **A. Verma,** P.P. Mukherjee**,** "*Mechanistic Analysis of Mechano-Electrochemical Interaction in Silicon Electrodes with Surface Film"*, Journal of Electrochemical Society **164** (14), A3570-A3581 **(2017)**
4. **A. Verma**, K. Smith, S. Santhanagopalan, D. Abraham, K.P.C. Yao, P.P. Mukherjee, "*Galvanostatic Intermittent Titration and Performance Based Analysis of* $LiNi_{0.5}Co_{0.2}Mn_{0.3}O_2$ *Cathode"*, Journal of Electrochemical Society **164** (13), A3380-A3392 **(2017)**
5. R. Davidson, **A. Verma**, D. Santos, F. Hao, C. Fincher, S. Xiang, J. van Buskirk, K. Xie, M. Pharr, P. P. Mukherjee, S. Banerjee, "*Mapping Mechanisms and Growth Regimes of Magnesium Electrodeposition at High Current Densities"*, Materials Horizons, DOI: 10.1039/C9MH01367A **(2019)**
6. R. Davidson, **A. Verma**, D. Santos, F. Hao, C. Fincher, S. Xiang, J. van Buskirk, K. Xie, M. Pharr, P. P. Mukherjee, S. Banerjee, "*Formation of Magnesium Dendrites during Electrodeposition"*, ACS Energy Letters, **4**, 375-376 **(2019)**
7. F. Hao, **A. Verma**, P.P. Mukherjee, "*Cationic Shield Mediated Electrodeposition Stability in Metal Electrodes*", Journal of Material Chemistry A, **7**, 18442-18450 **(2019)**
8. F. Hao, **A. Verma**, P.P. Mukherjee, "*Mechanistic Insight into Dendrite-SEI Interactions for Lithium Metal Electrodes*", Journal of Material Chemistry A, **6**, 19664-19671 **(2019)**
9. F. Hao, **A. Verma**, P.P. Mukherjee, "*Electrodeposition stability of metal electrodes*", Energy Storage Materials, **20**, 1-6 **(2019)**
10. A. Mistry, **A. Verma**, P.P. Mukherjee, "*Controllable Electrode Stochasticity Self-heats Lithium-ion Batteries at Low Temperatures*", Energy Storage Materials, **11** (30), 26764-26769 **(2019)**
11. F. Hao, **A. Verma**, P.P. Mukherjee, "*Mesoscale Complexations in Lithium Electrodeposition*", ACS Applied Materials and Interfaces, **10** (31), 26320-26327 **(2018)**
12. C-F. Chen., **A. Verma**, P.P. Mukherjee., "*Probing the Role of Electrode Microstructure in the Lithium-ion Battery Thermal Behavior*", Journal of Electrochemical Society **164** (11), E3146 – E3158 **(2017)**.
13. D.E. Galvez-Aranda, **A. Verma**, K. Hankins, J.M. Seminario, P.P. Mukherjee, P.B. Balbuena, "*Chemical and Mechanical Degradation and Mitigation Strategies for Si Anodes: Multiscale Modeling*", Journal of Power Sources, **419**, 208-218 **(2019)**
14. P. Huang, **A. Verma**, D. Juarez-Robles, Q. Wang, P.P. Mukherjee, J. Sun, "*Probing the*

cooling effectiveness of phase change materials on lithium-ion battery thermal response under overcharge condition", Applied Thermal Energy **132,** 521-530 **(2018)**

15. N. Kotak, P. Barai, **A. Verma**, A. Mistry, P.P. Mukherjee, "*Electrochemistry-Mechanics Coupling in Intercalation Electrodes*", Journal of Electrochemical Society **165** (5), A1064-A1083 **(2018)**
16. J. B. Grunewald, A. Mistry, **A. Verma**, N. Goswami, P.P. Mukherjee, T. F. Fuller, "Mesoscale Physics in the Catalyst Layer of Proton Exchange Membrane Fuel Cells: a Critical Perspective", Journal of Electrochemical Society, **166** (7), F3089-F3092 **(2019)**
17. B. Mondal, C.F. Lopez, **A. Verma**, P.P. Mukherjee, "*Vortex generators for active thermal management in lithium-ion battery systems*", International Journal of Heat and Mass Transfer **124**, 800-815 **(2018)**
18. P. Huang, H. Chen, **A. Verma**, Q. Wang, P.P. Mukherjee, J. Sun, "Non-dimensional Analysis of the Criticality of Li-ion Battery Thermal Runaway Behavior", Journal of Hazardous Materials, **369**, 268-278 **(2019)**
19. A. Saraswat, R. Bhattacharjee, **A. Verma**, M.K. Das, S. Khandekar "*Investigation of diffusional transport of heat and its enhancement in phase-change thermal energy storage systems*", Applied Thermal Engineering **111**, 1611-1621 **(2017)**.

Manuscripts under review

1. **A. Verma**, H. Kawakami, T. Kotaka, N. Ikeda, M. Shibata, K. Aotani, Y. Tabuchi, P.P. Mukherjee, *"Microstructure and Pressure Driven Electrodeposition Stability in Solid-State Batteries"*
2. (joint first author) B.S. Vishnugopi, **A. Verma**, P.P. Mukherjee, *"Fast Charge of Lithium-Ion Batteries via Electrode Engineering*"
3. (joint first author) F. Hao, **A. Verma**, W. Wang, B.S. Vishnugopi, P.P. Mukherjee, *"Ion Channel Assisted Uniform Deposition in Li Metal Batteries*"
4. B.S. Vishnugopi, **A. Verma**, P.P. Mukherjee, "*A Level Set Method for Modeling Electrodeposition Morphology*"
5. C. Hawkins, **A. Verma**, W. Horbinski, R. Weeks, P.P. Mukherjee, L. Whittaker-Brooks, "*Decreasing the ion-diffusion pathways for the intercalation of multivalent cations into one-dimensional TiS2 nanobelt arrays*"
6. Z. Ahmed, **A. Verma**, P.P. Mukherjee, Z.A. Talib, V. Keast, J.L.Y. Chyi, S.W. Donne, "*Mechanistic Analysis of Li^+ Diffusion Mechanisms in Spinel Cathodes via Step Potential Electrochemical Spectroscopy (SPECS) and GITT*"
7. K. Hatzell, X. Chen, C. Cobb, N. Dasgupta, M. Dixit, L. Marbella, M. McDowell, P. Mukherjee, **A. Verma**, V. Viswanathan, A. Westover, W. Zeier, "Challenges in lithium metal anodes for solid state batteries"
8. B.S. Vishnugopi, F. Hao, **A. Verma**, P.P. Mukherjee, "*Electrodeposition in Binary Metal Anode Systems*"
9. B.S. Vishnugopi, F. Hao**, A. Verma**, P.P. Mukherjee, "*Double-Edged Effect of Temperature on Lithium Dendrites*"
10. B.S. Vishnugopi, F. Hao**, A. Verma**, P.P. Mukherjee, "*The Impact of Surface Diffusion Pathways on Electrodeposition Morphology*"

Conference Proceedings

1. **Verma, A.**, Das, M.K., "*Latent Heat Thermal Energy Storage in a Heated Semi-Cylindrical Cavity: Numerical Analysis and Comparison with Experiments*", Proceeding of the 23rd National & 1st International ISHMT-ASTFE Heat and Mass Transfer Conference (2015).
2. **Verma, A.**, Babu R., Das, M. K., 2014, "*Modeling of a Single Bubble Rising in a Water Column*", Proceedings of 5th International and 41st National Conference on Fluid Mechanics and Fluid Power (2014).
3. Mistry, A., **Verma, A.**, Das, M. K., "*Modeling of Polymer Electrolyte Membrane (PEM) Fuel Cell Cathode with Agglomerate Catalyst Layer*", Proceedings of Fortieth National Conference on Fluid Mechanics and Fluid Power (2013).

Book Chapters

1. (under review) P. P. Mukherjee, **A. Verma**, A. Mistry "*Polymer Electrolyte Membrane Fuel Cells*", in *Energy Storage and Conversion*
2. (under review) P. P. Mukherjee, A. Mistry, **A. Verma**, "*Electrochemical Energy System Fundamentals*", in *Energy Storage and Conversion*
3. (under review) P. P. Mukherjee, A. Mistry, **A. Verma**, "*Lithium-ion Battery*", in *Energy Storage and Conversion*
4. P. P. Mukherjee, **A. Verma**, and A. Mistry, "*Mesoscale Interactions of Transport Phenomena in Polymer Electrolyte Fuel Cells",* in *Modeling Transport Phenomena in Porous Media with Applications*, eds. M. K. Das, P. P. Mukherjee, K. Muralidhar, Springer (2017)
5. P. P. Mukherjee, A. Mistry and **A. Verma**, "*Porous Media Applications: Electrochemical Systems",* in *Modeling Transport Phenomena in Porous Media with Applications*, eds. M. K. Das, P. P. Mukherjee, K. Muralidhar, Springer Porous Media Applications: Electrochemical Systems (2017)

Conference Presentations and Technical Reports

1. (upcoming) **Verma A.**, Mukherjee, P.P., "*Mechanistic Elucidation of Electrodeposition Stability at Metal-Solid Electrolyte Interfaces*", TMS, San Diego, CA (2020)
2. (upcoming) **Verma A.**, Mukherjee, P.P., "*Electrodeposition Stability at Metal-Solid Electrolyte Interfaces*", GRC, Ventura, CA (2020)
3. (upcoming) **Verma A.**, Mukherjee, P.P., "*Electrodeposition Stability at Metal-Solid Electrolyte Interfaces*", GRS, Ventura, CA (2020)
4. **Verma A.**, Mukherjee, P.P., "*Microstructure Ramifications on Electrodeposition in Solid-State Electrolytes*", 236th Meeting of Electrochemical Society, Atlanta, GA (2019)
5. **Verma A.**, Mukherjee, P.P., "*Mechanistic Investigations of Interfacial Stochasticity in Lithium Metal Anodes*", 235th Meeting of Electrochemical Society, Dallas, TX (2019)
6. **Verma A.**, Mukherjee, P.P., "*Mechanistic Understanding of Multi-modal Degradation in Li-ion Battery Electrodes*", TMS, San Antonio, TX (2019)
7. **Verma A.**, Mukherjee, P.P., "*Machine Learning Based Understanding Of Lithium-ion Battery Performance Decay*", IMECE, Pittsburgh, PA (2018)

8. **Verma A.**, Mukherjee, P.P., "*Analyzing Multi-Modal Degradation Interplay in Li-Ion Battery Electrodes*", 233rd Meeting of Electrochemical Society, Seattle, WA (2018)
9. **Verma, A.**, Mukherjee, P.P., "*Coupled Mechano-Electrochemical Interactions in Silicon Anode with Solid Electrolyte Interphase Layer",* 232nd Meeting of Electrochemical Society, National Harbor, MD (2017)
10. **Verma A.**, Mistry A., Mukherjee, P.P., "*Electrode Level Implications in Sub-Zero Temperature Operation of Li-ion cells*", IMECE, Tampa, FL (2017),
11. Mukherjee, P.P., Hao, F., **Verma, A.**, Mistry, A., "*Mesoscale Understanding of Lithium Electrodeposition*", AiMES 2018, Cancun, Mexico (2018)
12. Smith, K., Santhanagopalan S., Yang, C., Graf P., Usseglio-Viretta, F., Li Q., Finegan, D., Pesaran A., Yao, K.P.C, Abraham, D., Dees, D., Jansen A., Mukherjee P.P., Mistry A., **Verma, A**., Lamb J., Darcy, E., "*Computational Design of Batteries from Materials to Systems*", Advanced Automotive Battery Conference, San Francisco, CA, NREL/PR-5400-68770 (2017)
13. Smith K., Usseglio-Viretta F., Graf, P., Santhanagopalan S., Yao, K.P.C., Abraham D., Dees, D., Jansen A., Mukherjee P., Mistry A., **Verma A**., "*Microstructure Characterization and Modeling for Improved Electrode Design*", VTO Annual Merit Review, Washington DC, NREL/PR- 68323 (2017)
14. Mistry, A., **Verma, A.**, Mukherjee, R. and Mukherjee P.P., "*Image-based Reconstruction and Statistical Characterization of the Li-ion Battery Electrode Microstructure*", 229th Meeting of Electrochemical Society, San Diego, CA (2016).
15. Mistry, A., **Verma, A.**, Juarez-Robles, D. and P. P. Mukherjee, "*How Electrode Processing Affects Li-ion Battery Performance?",* Material Challenges in Alternative and Renewable Energy, Clearwater, FL (2016).

Peer Reviewer

1. Journal of Electronic Packaging (ASME: American Society of Mechanical Engineers)
2. Journal of the Electrochemical Energy Storage and Conversion (ASME: American Society of Mechanical Engineers)
3. ASME IMECE 2019 Conference.
4. IEEE ITherm 2017 & 2018 conference

Professional Affiliations

1. Electrochemical Society (ECS)
2. American Society of Mechanical Engineering (ASME)
3. The Minerals, Metals and Materials Society (TMS)

Awards and Honors

1. Ward A. Lambert Graduate Teaching Fellowship, Mechanical Engineering, Purdue University, Term: Spring 2019, Fall 2019
2. Travel Grant, the Minerals, Metals and Materials Society (TMS) Spring 2019
3. Session Chair, Summer Undergraduate Research Fellowship 2018 Symposium, Purdue University
4. Student Volunteer at the 236th Electrochemical Society Meeting 2019 and 232nd Electrochemical Society Meeting 2017
5. Google Scholar Citations: 189, h-index: 9, i10-index: 9. *https://scholar.google.com/citations?user=eDyVwf0AAAAJ&hl=en&oi=ao*

TEACHING EXPERIENCE

Teaching Assistantships at Purdue University

1. Lambert Teaching Fellow, Fall 2019: *Heat and Mass Transfer* (ME 315), class strength – 64. In-class instructor for the entire semester (~40 lectures). Tasks encompassed preparation of in-class quizzes as well as exam questions.
2. Lambert Teaching Fellow, Spring 2019: *Heat and Mass Transfer* (ME 315), class strength – 80. Assisted in preparation of exam questions and was in-class lecturer for a total of 6 lectures out of approximately 40.
3. Spring 2018: *Numerical Methods in Heat, Mass and Momentum Transfer* (ME 608), class strength – 40

Teaching Assistantships at Indian Institute of Technology Kanpur

1. Spring 2014: *Fluid Mechanics* (ME 231) class strength – 115
2. Fall 2013: *Energy Systems II* (ME 401) class strength – 105

Student Mentoring

1. Akshay Parag Biniwale, M.S. Mechanical Engineering, Purdue University 2019. "*Mechanistic Analysis of Sodiation in Electrodes*"
2. Richa Naik, B. Tech., IIT Madras, Summer 2018. *"Machine Learning Enabled Screening of Metal-Ion Batteries*"
3. Pranjal Ketan Jhaveri, B. Tech IIT Bombay, Summer 2018. *"Machine Learning Enabled Degradation Analysis of Lithium-Ion Batteries*"
4. Srivatasa Chakravarthy, M.S. Mechanical Engineering, Texas A&M University 2017. "*Thermodynamically Consistent Analysis for Lithium-Ion Batteries*"

MISCELLANEOUS

Relevant Courses

Fundamentals of Energy Storage, Advanced Transport Phenomenon, Computational Fluid Dynamics, Flow and Heat Transfer in Porous Media, Heat Transfer, Turbulence, Virtual Instrumentation, Statistical Thermodynamics

*Coursera Courses**:***

1. Algorithms: Design and Analysis, Part 1 & Part2, Stanford University
2. High Performance Scientific Computing, University of Washington

PhD Qualifying/Area Exam Passed: Heat Transfer, Thermodynamics (at Texas A&M University), Mathematics (at Purdue University)

Test Scores

ELPE: Listening: 91, Reading: 99, Oral: 80
GRE**:** Quantitative: 163, Verbal: 159, Total: 322/340, Writing: 4.5/6
TOEFL: Listening: 26, Reading: 29, Speaking: 27, Writing: 26, Total: 108/120

Programming Expertise

FEniCS, OpenFOAM, C/C++, Fortran 90/95, python, MATLAB, LabVIEW, COMSOL, LaTeX

Extra-curricular Activities:

Coordinating events in technical festivals

e.g., helped organize a two days conference *IITK Student Research Convention 2014* for undergraduate and graduate students of IIT Kanpur on Aug, 9th-10th, 2014

PUBLICATIONS

The list of publications based on my dissertation research (accepted before Feb 1, 2020) is provided below.

A. Verma, A. Franco, P.P. Mukherjee, "*Mechanistic Elucidation of Si Particle Morphology on Electrode Performance*", Journal of Electrochemical Society **165** (15), A3852-A3860 **(2019)**

A. Verma, T. Kotaka, Y. Tabuchi, P.P. Mukherjee, "*Mechano-Electrochemical Interaction and Degradation in Graphite Electrode with Surface Film"*, Journal of Electrochemical Society **165** (10), A2397-A2408 **(2018)**

A. Verma, P.P. Mukherjee**,** "*Mechanistic Analysis of Mechano-Electrochemical Interaction in Silicon Electrodes with Surface Film"*, Journal of Electrochemical Society **164** (14), A3570-A3581 **(2017)**

A. Verma, K. Smith, S. Santhanagopalan, D. Abraham, K.P.C. Yao, P.P. Mukherjee, "*Galvanostatic Intermittent Titration and Performance Based Analysis of* $LiNi_{0.5}Co_{0.2}Mn_{0.3}O_2$ *Cathode"*, Journal of Electrochemical Society **164** (13), A3380-A3392 **(2017)**

R. Davidson, **A. Verma**, D. Santos, F. Hao, C. Fincher, S. Xiang, J. van Buskirk, K. Xie, M. Pharr, P. P. Mukherjee, S. Banerjee, "*Mapping Mechanisms and Growth Regimes of Magnesium Electrodeposition at High Current Densities"*, Materials Horizons, DOI: 10.1039/C9MH01367A **(2019)**

R. Davidson, **A. Verma**, D. Santos, F. Hao, C. Fincher, S. Xiang, J. van Buskirk, K. Xie, M. Pharr, P. P. Mukherjee, S. Banerjee, "*Formation of Magnesium Dendrites during Electrodeposition"*, ACS Energy Letters, **4**, 375-376 **(2019)**

F. Hao, **A. Verma**, P.P. Mukherjee, "*Cationic Shield Mediated Electrodeposition Stability in Metal Electrodes*", Journal of Material Chemistry A, **7**, 18442-18450 **(2019)**

F. Hao, **A. Verma**, P.P. Mukherjee, "*Mechanistic Insight into Dendrite-SEI Interactions for Lithium Metal Electrodes*", Journal of Material Chemistry A, **6**, 19664-19671 **(2019)**

F. Hao, **A. Verma**, P.P. Mukherjee, "*Electrodeposition stability of metal electrodes*", Energy Storage Materials, **20**, 1-6 **(2019)**

A. Mistry, **A. Verma**, P.P. Mukherjee, "*Controllable Electrode Stochasticity Self-heats Lithium-ion Batteries at Low Temperatures*", Energy Storage Materials, **11** (30), 26764-26769 **(2019)**

F. Hao, **A. Verma**, P.P. Mukherjee, "*Mesoscale Complexations in Lithium Electrodeposition*", ACS Applied Materials and Interfaces, **10** (31), 26320-26327 **(2018)**

C-F. Chen., **A. Verma**, P.P. Mukherjee., "*Probing the Role of Electrode Microstructure in the Lithium-ion Battery Thermal Behavior*", Journal of Electrochemical Society **164** (11), E3146 – E3158 **(2017)**.

D.E. Galvez-Aranda, **A. Verma**, K. Hankins, J.M. Seminario, P.P. Mukherjee, P.B. Balbuena, "*Chemical and Mechanical Degradation and Mitigation Strategies for Si Anodes: Multiscale Modeling*", Journal of Power Sources, **419**, 208-218 **(2019)**

P. Huang, **A. Verma**, D. Juarez-Robles, Q. Wang, P.P. Mukherjee, J. Sun, "*Probing the cooling effectiveness of phase change materials on lithium-ion battery thermal response under overcharge condition*", Applied Thermal Energy **132,** 521-530 **(2018)**

N. Kotak, P. Barai, **A. Verma**, A. Mistry, P.P. Mukherjee, "*Electrochemistry-Mechanics Coupling in Intercalation Electrodes*", Journal of Electrochemical Society **165** (5), A1064-A1083 **(2018)**

J. B. Grunewald, A. Mistry, **A. Verma**, N. Goswami, P.P. Mukherjee, T. F. Fuller, "Mesoscale Physics in the Catalyst Layer of Proton Exchange Membrane Fuel Cells: a Critical Perspective", Journal of Electrochemical Society, **166** (7), F3089-F3092 **(2019)**

B. Mondal, C.F. Lopez, **A. Verma**, P.P. Mukherjee, "*Vortex generators for active thermal management in lithium-ion battery systems*", International Journal of Heat and Mass Transfer **124**, 800-815 **(2018)**

P. Huang, H. Chen, **A. Verma**, Q. Wang, P.P. Mukherjee, J. Sun, "Non-dimensional Analysis of the Criticality of Li-ion Battery Thermal Runaway Behavior", Journal of Hazardous Materials, **369**, 268-278 **(2019)**